Development of graphene-based sensors for scanning Hall microscopy and imaging of vortex matter in unconventional superconductors

Collomb, David

Award date:
2021

Awarding institution:
University of Bath

Development of graphene-based sensors for scanning Hall microscopy and imaging of vortex matter in unconventional superconductors

Collomb, David

Award date:
2021

Awarding institution:
University of Bath

Development of graphene-based sensors for scanning Hall microscopy and imaging of vortex matter in unconventional superconductors

submitted by

David Collomb

for the degree of Doctor of Philosophy

of the

University of Bath

Department of Physics

December 2020

Abstract

The isolation of graphene in 2004 started a new development in the field of condensed matter physics and materials science to use graphene's impressive electronic properties and mechanical versatility to improve upon existing electrical devices. One of several types of key devices that graphene could become incorporated into is the Hall-effect magnetic field sensor. Within this project CVD graphene Hall probes with wire widths from 1.5μm down to 50nm have been fabricated and characterised to explore the possibility of replacing III-V semiconductor-based 2D electron gas Hall probes that are the current standard in scanning Hall probe microscopy. The minimum detectable field of the graphene Hall probes was estimated by measuring their Hall coefficients, and characterising the low frequency electronic noise between 1Hz and 1kHz using a dynamic spectrum analyser. The minimum detectable field was mapped as a function of wire width, carrier density and current density. This revealed that it can be optimised by increasing the current density, with performance improvements being particularly pronounced in devices with micrometer-scale dimensions. The minimum detectable field can also be tuned by back gating the devices on a Si/SiO2 substrate, allowing the carrier density and type to be controlled. In this way, the minimum detectable field can be substantially improved by reducing the carrier density close to the charge neutrality point. In practice its dependence on the wire width is surprisingly weak. However, a large increase in the minimum detectable field is seen when the width drops below 85nm, associated with a drop in mobility as edge roughness-induced charge scattering begins to dominate. To improve the minimum detectable field, graphene devices passivated by HSQ and encapsulated in exfoliated hBN flakes have been fabricated and characterised. Passivation by HSQ yields a small improvement in the electrical mobility as estimated from Hall measurements, while the biggest improvements are found by encapsulation with hBN. This improvement in mobility substantially improves the minimum detectable fields, with encapsulated devices exhibiting an order of magnitude better detection limit than unencapsulated CVD graphene. Resistance versus back gate voltage measurements on devices encapsulated with hBN also show significantly lower extrinsic doping levels than unencapsulated devices, thus removing the need to gate such devices to achieve optimal carrier densities near the CNP. These encouraging results reveal that encapsulated graphene is a promising material for the sensors of the next generation of high resolution scanning Hall probe microscopes.

Scanning Hall probe microscopy with a GaAs/AlGaAs 2D electron gas-based Hall probe has been used to explore the unique interplay between superconductivity and ferromagnetism in the Fe-based material, $RbEuFe_4As_4$. Quantitative magnetic images of superconducting vortices allows the direct extraction of the superconducting penetration depth from the vortex profiles as a function of temperature. This reveals a pronounced increase in the penetration depth near the magnetic transition temperature, in good agreement with a recently developed model describing the change in superfluid density as a result of the ordering of the magnetic moments. This shows that there is a significant interplay between the two types of order within the material, yet the exchange interaction between superconducting and magnetic sublattices is still weak enough that both are able to coexist. Scanning Hall probe microscopy has also been used to characterise the vortex pinning landscape in second generation GdBaCuO high temperature superconducting tapes. Local Hall probe magnetometry was employed to estimate the critical current, while topographic and magnetic imaging reveals that the films contain strong distinct vortex pinning sites. Comparing magnetic and topographic images reveals that these are most likely linked to the GdO second phases formed during thin film growth, as opposed to grain boundaries and normal

CuO phases that protruding from the surface of the superconducting layer. This suggests that the engineering of high critical current tapes should focus on optimising the film microstructure and pinning sites during growth, rather than the addition of extra artificial pinning post-growth sites.

Acknowledgments

I would like to in particular express my gratitude to my supervisor Prof. Simon Bending for his constant support, his patience, his knowledge and his never ending enthusiasm. I do not believe words here can describe the worth of his sincere supervision; perhaps the best thing to say is that he has imparted skills, support and mentality that will not be forgotten.

Special thanks to Dr Penglei Li who has imparted invaluable knowledge and experience to me, who has been an excellent colleague on a challenging project and perfect company in the lab and office. Additionally a special thanks and great appreciation to Dr Estefani Marchiori Pereira for her assistance, advice and indispensable friendship during her time at Bath and beyond. I would like to extend my thanks to all the great friends I made during my time at Bath and the time spent together.

I would like to thank funding from the Lloyd's Register Foundation ICoN project led by Prof Themis Podromakis and Angela Westley, and the unique learning opportunities they provided.

I also have huge tremendous respect, indebtedness and appreciation for all the technical staff (Dr. Stephen Wedge, Dr. Sivapathasundaram Sivaraya, Clare Cambridge, Wendy Lambson, Edwina Wilkinson, Martin Fullick, Joe Mills and Paul Reddish) who not only provided vital assistance and taught me new skills, but also imparted their positive attitudes and acted as sources of comfort and perseverance in the face of unknown challenges. I certainly won't forget cleanroom colleagues Robert Armstrong, Pierre-Marie Coulon and Pierre Chausse for their advice and for injecting a little extra fun into lengthy cleanroom sessions.

Finally, but perhaps most importantly, I am very thankful for the support provided by my family, especially my parents Pascale and Norbert. I am also fortunate to have an amazing partner, Rita Mendes Da Silva, who provided unrivalled support to me, and reminded me what is truly important. Their patience, and unconditional love helped me through challenging times when I needed help and support the most.

Abbreviations

HTS	High temperature superconductor	TEM	Transmission electron microscope
SHPM	Scanning Hall probe microscopy	SEM	Scanning electron microscope
CVD	Chemical vapour deposition	MOKE	Magneto-optical Kerr effect
MFM	Magnetic force microscopy	EBL	Electron beam lithography
AFM	Atomic force microscopy	SSQUID	Scanning superconducting quantum interference device
sNVM	Scanning nitrogen vacancy magnetometery	NV	Nitrogen vacancy
ST	Scanning Tunnelling	STM	Scanning tunnelling microscope
DP	Dirac point	Exf	Exfoliated
hBN	Hexagonal boron nitride	2G-HTS	2^{nd} generation high temperature superconductor
SiC	Silicon carbide		
PMMA	Poly(methylmethacrylate)	PLD	Pulsed laser deposition
PDMS	Polydimethylsiloxane	MOD	Metal organic deposition
MOCVD	Metal organic chemical vapour deposition	RCEDR	Reactive co-evaporation by deposition and reaction
RCECDR	Reactive co-evaporation by cyclic deposition & reaction	APC	Artificial pinning center
		AG	Abrikosov-Gor'kov
RE	Rare earth	IPA	Isopropanol
DLW	Direct laser writer	DI	Deionised
RIE	Reactive ion etch	TMAH	Tetramethyl ammonium hydroxide
ICP	Inductively coupled plasma		
EDX	Energy dispersive x-ray analysis	RF	Radio frequency
		HSQ	Hydrogen silsesquioxane
SMU	Source-measurement unit	TLM	Transmission line measurements
DSA	Dynamic signal analyser		
AFHPM	Atomic force Hall probe microscope	ER	Edge roughness
		HF	Hydrofluoric acid

Contents

List of Figures

List of Tables

1 Introduction

1.1 Motivation

Avoiding the need for the use of the more expensive cryogen, liquid Helium, High Temperature Superconductors (HTS) open up the way for cost-effective applications of superconductivity, such as use in upcoming fusion power plants, lossless transport of energy from remote sources and magnetic levitation tracks [1, 2, 3]. A magnetic field penetrates into a type II material in the form of flux lines. As the magnetic field increases these can start to move, resulting in loss of the superconducting state, introducing electrical resistance. This can be overcome by pinning the vortices. However, much work is still needed in order to find optimal defect densities for the pinning of magnetic vortices to maximise the current-carrying capacity of HTS tapes without degrading their critical temperatures, T_c. Magnetic imaging methods such as magnetic force microscopes (MFM) and Scanning Hall Probe Microscopey (SHPM) have been developed to accurately map localised magnetic fields at the surfaces of superconductors and other magnetic materials. These maps can be used to characterise current flows around microscopic material defects with resolutions down to the nanoscale, making imaging tools a vital tool for the task of optimising HTS tapes.

High temperature superconducting tapes are not the only topic of interest in the field of contemporary superconductivity. The coexistence of superconductivity and magnetism is not yet fully understood, while the rapid expansion of material growth systems and techniques means that more materials with this property are being added to the list each year. Under normal circumstances this coexistence should not be possible since the opposite spin pairing of the Cooper pairs responsible for superconductivity is not compatible with parallel electron spin alignment responsible for ferromagnetism. Understanding why superconductivity survives in these materials could open the door to a vast array of landscape-changing technologies such as superspintronic and fluxonic devices. Here again, the ability of magnetic imaging to map local magnetic fields will allow key superconducting parameters to be extracted and correlated with the local ferromagnetism across a wide range of temperatures.

Since the first isolation of graphene in 2004, efforts have been made to realise devices that take advantage of its impressive electronic transport properties [4]. While progress is being made, 14 years later graphene is still not routinely used material in everyday technologies. This is due to limitations on scaleable graphene fabrication, performance reductions introduced by fabrication procedures as well as the choice of substrate. Work on graphene has opened up interest in other 2D materials, such as hexagonal Boron Nitride, as well as the development of new fabrication techniques to unlock graphene's full potential. Graphene can now be readily grown on copper by Chemical Vapour Deposition (CVD) for large scale production, but, the electronic quality is still appreciably worse than that of exfoliated graphene [5]. Reduction in performance can be attributed not only to defects and grain boundaries introduced during growth, but also to the transfer methods. Polymer-based transfer methods can leave behind residues in addition to causing cracks and other forms of damage in the graphene sheet [5]. It has recently been shown that dry transferred graphene can exhibit mobilities close to that of exfoliated graphene, highlighting the key

importance of the transfer method [6]. Nevertheless, even unencapsulated CVD graphene has excellent physical properties which can be taken advantage of. Progressing towards smaller wire widths Hall probes can greatly improve the spatial resolution of a scanning Hall probe system (SHPM), which is easier to fabricate from such a thin layered and versatile material. Graphene's two dimensional nature also allows the active layer to be much closer to the surface of the scanned material as compared to the embedded active layer of previous common Hall Probe structure. Furthermore, the high mobility, and low carrier concentration of graphene should allow high magnetic sensitivity and low enough noise levels to obtain very low minimum detectable fields, B_{min}. Hence, for many reasons graphene is a very attractive material for fabricating nanoscale Hall sensors.

The objective of this project is firstly to expand the reach of SHPM by developing high magnetic field sensitivity nanoscale graphene Hall sensors for ambient operation. Two main sensor parameters will be investigated and optimised: the minimum detectable field and the spatial resolution. To optimise the sensors, various fabrication methods, e.g. graphene transfer protocols, device designs and device architectures (e.g. encapsulation) and various sources of graphene, will be explored and the physics understood. Issues of scalability and fabrication versatility also need to be addressed if these sensors are to be used as the active components of an SHPM. The subsequent objectives of the project are to use SHPM to study two unconventional superconducting materials. The first of these is a material which has recently reignited interest in coexistence phenomena between superconductivity and ferromagnetism. The quantitative high resolution capabilities of SHPM allow it to directly probe the superconducting properties of $RbEuFe_4As_4$ above and below the ferromagnetic transition temperature, enabling us to validate a recently-developed theoretical model constructed to describe these unique hybrid materials [7]. The second material studied was GdBaCuO, a high temperature superconducting cuprate present in high critical current second generation high temperature superconducting tapes produced by SuNAM [8]. Once again, SHPM can be used to image discrete vortices, allowing us to understand the vortex pinning landscape and extract information about key superconducting parameters.

1.2 Thesis outline

This thesis describes the research undertaken to develop and fabricate the next generation of SHPM sensors based on graphene to; enable the optimisation of HTS tapes, unravel the mechanisms behind unconventional superconductivity and, more generally, to pave the way for high resolution room temperature magnetic imaging of novel magnetic materials and devices. The report begins in chapter 2 by describing the current magnetic imaging landscape through a comparison of the figures-of-merit of contemporary magnetic imaging methods. It then develops the theoretical work underpinning graphene electronics, different sources of graphene and potential avenues for future graphene Hall probe devices in chapter 3. Chapter 4 explains the theory behind the superconducting materials studied in this project, focusing on the fundamental theories of superconductivity and then expanding into vortex pinning and the effect of local magnetism in superconducting materials. After covering the theoretical basics, the thesis describes the methods used for fabricating, characterising and utilising our graphene-based sensors, as well as the details of SHPM

operation in chapter 5. Following this, chapter 6 discusses the results of our exploration of CVD graphene-based Hall probes for SHPM. This chapter is split into two subsections, the first being an investigation into the performance of nanoscale CVD Hall sensors on a silicon dioxide substrate while the second section looks at performance improvements achieved by capping the CVD graphene with an electron beam resist material known as HSQ. In this chapter we also explore graphene devices that are encapsulated between two exfoliated hBN flakes. We show that even after the wet transfer of the CVD graphene, the performance of encapsulated Hall probes is at least an order of magnitude better than their unencapsulated counterparts. Finally the SHPM imaging technique is utilised in chapter 7 to directly explore the effect of local magnetism on the superconducting parameters in the Fe-based superconductor, $RbEuFe_4As_4$. These data are used to validate and fit a recently-developed model to describe the suppression of superconductivity in ferromagnetic superconducting materials. Chapter 8 describes investigations of the vortex pinning behaviour in a high temperature superconducting tape provided by the Korean manufacturer SuNAM. In these measurements we observe a clear difference in the vortex structure compared to the more conventional one seen in chapter 8, highlighting the significant impact artificial pinning sites have on the superconductor. The thesis concludes in chapter 9 with a summary of the key findings and suggestions for future research building on the results of this project.

2 Introduction to magnetic imaging and scanning Hall probe microscopy

2.1 Introduction to Magnetic Imaging

Humans have benefited from a natural ability to interact with the world around them via their five basic senses. However, they lack an intrinsic magnetic sense. Using their ingenuity, humans have over time developed various magnetic sensors based on a vast variety of effects such as the Hall effect, magnetoresistance effect or the magneto optical Kerr effect. Magnetic sensors have an impressively wide range of important modern day applications, including their use in position sensing in automobiles, oil and mineral exploration, weather prediction and even archaeology.

However, magnetic sensors do not just need to sense a magnetic field in one point in space. By raster scanning a magnetic sensor such as a Hall probe across an area and collecting the sensed magnetic field at each point, one can form a magnetic field map, essentially forming a magnetic image. Magnetic imaging has a variety of uses: identifying defects and studying cracks and soldering joints for non-destructive testing of industrial manufacturing processes [9]; studying biological samples for non-invasive medical diagnosis [10]; furthering our understanding of physical phenomena such as superconductivity and magnetism in materials [11, 12] and optimising material or device properties such as the critical current in high temperature superconductors.

With so many magnetic imaging techniques available, it can be challenging to know which technique is optimal for a given application. A low minimum detectable field, B_{min}, is generally desired in order to be able to produce more precise magnetic maps/images. This

becomes especially important when the features of interest have a particularly weak magnetic signal. Since the field of research covered by this thesis is nanoscience, this naturally makes spatial resolution another important figure of merit when choosing an appropriate imaging technique. In cases where magnetic features may move on short timescales, temporal resolution may also be an important figure of merit. However in for the work described in this thesis, i.e., magnetic features such as domain walls and pinned magnetic vortices, temporal resolution is not a relevant figure of merit. There are also other practical requirements including: the operating temperature and environment (e.g., gas and pressure); how invasive the technique is to magnetic materials and how easy to use the technique is.

The following sub-section explores imaging techniques which are currently used for the magnetic imaging of materials, especially for room temperature applications where, for example, candidate spintronic devices are expected to operate in [13, 14, 15]. The subsection will conclude with a general comparison between the techniques for the purposes of the research described in this thesis.

2.1.1 Lorentz Force Microscopy

Lorentz electron microscopy offers the highest spatial resolution, typically down to 2nm [16]. This is due to the use of fine electron beams which are deflected by the local magnetic induction. This can be simply understood in terms of the action of the Lorentz force on electrons as they pass through the magnetic flux. The magnetic contrast is then achieved in a transmission electron microscope (TEM). This not only allows for high spatial resolution but also a good temporal resolution. The major disadvantages are that the sample must be thinner than a couple of hundred nanometres. If the sample is not already of the required thickness, this can involve heavy physical processing of the material, possibly damaging or distorting any magnetic structures one may be trying to view. The sample is also placed in the high magnetic field of the objective lens, which can distort or destroy any magnetic structures of interest [16]. Finally, it is very difficult to be able to extract quantitative information from Lorentz microscopy, however, the technique is still very effective in studying the dynamics of magnetic structures.

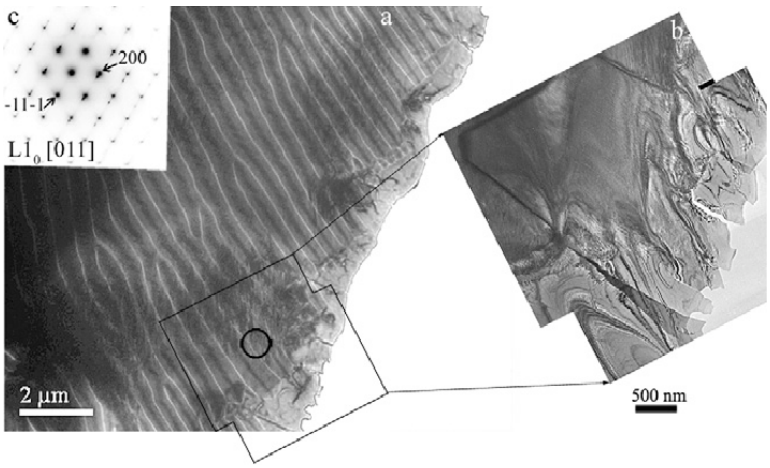

Figure 1: A Lorentz force micrograph of magnetic domains in an annealed $Co_{38}Ni_{33}Al_{29}$ sample [17].

2.1.2 Bitter Decoration

The Bitter decoration method was the first used to image ferromagnetic structures, and later was the first technique used to resolve an Abrikosov vortex lattice [18, 19]. It utilises dispersed fine magnetic particles on the sample, often generated by evaporation or liquid suspension, which migrate under the field gradient to the regions of highest magnetic field. This creates a pattern that mirrors the underlying magnetic structure of the sample. This pattern can then be imaged in a scanning electron microscope (SEM) [18]. This method is restricted in spatial resolution by the particle size (usually ≈10nm), but is more severely limited by being only appropriate for use at low magnetic fields below 10mT, especially for studies of vortices where at higher fields the extended vortex field profile begin to overlap and magnetic gradients quickly decrease. It is also hard to reuse the sample for further applications due to the dispersed magnetic particles van der Waals bonded onto it, which are often difficult to remove. The technique is also purely qualitative and provides no quantitative information about the underlying magnetic structure.

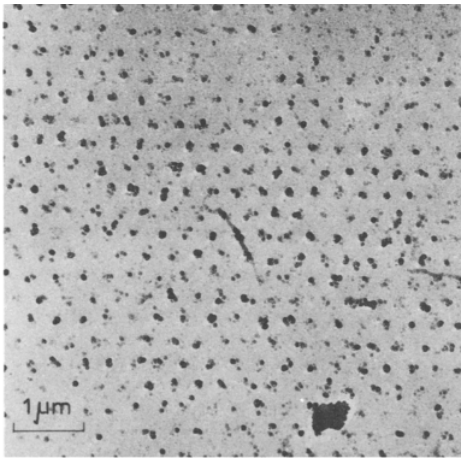

Figure 2: SEM image of Bitter decoration of an Abrikosov vortex lattice in a Lead-Indium rod using Cobalt particles [19].

2.1.3 Magneto optics

The magneto-optical Kerr effect microscope (MOKE) relies on the interaction between the electro-magnetic field of incident photons and a magnetised sample surface. Typically, a sample is coated or brought into touching contact with a magneto-optically active film. Light that is reflected from a magnetic surface is modified via the Faraday rotation of the polarisation, creating a contrast between regions of differing magnetic field [20]. The effect can be understood by considering an elastically bound carrier which is driven into a circular motion by the rotating electric field of the circular polarised wave passing through it. When a magnetic field is present perpendicular to this circular motion, an additional Lorentz force will be felt by the carrier. The force can act either inwards or outwards, yields two different values of polarisation. This causes a difference in propagation velocity between the two polarisations. A linearly polarised wave can be described as the superposition of two circularly polarised waves, shown by,

$$E_{lin}(z) = E^{+}_{cir}(z) + E^{-}_{cir}(z) = \frac{E_0}{2}[\exp^{-ikz} + \exp^{ikz}]. \tag{1}$$

After traversing the medium of thickness d which the carrier inhabits, the beams accumulate equal and opposite phase changes of δ. The phase of the linearly polarized light is therefore rotated by an amount δ,

$$E_{lin}(d) = E_0 cos(kd)\exp(i\delta). \tag{2}$$

This is equivalent to a Faraday rotation for small angles equal to,

$$\delta = \pm V_{Ver} dH, \tag{3}$$

where V_{Ver} is the Verdet constant for the medium and H is the applied field. This rotation can then be visualised using a crossed polariser. Although simple, very fast and non-invasive, these methods are not very competitive in terms of both spatial and magnetic resolution when compared with scanning probe magnetic imaging techniques as well as TEM/SEM

magnetic imaging [11]. MOKE is still widely used to today, having recently been used to image magnetism down to the monolayer limit in 2D materials [21]. MOKE had been ultimately limited by the diffraction limit which, depending in the lenses used could limit spatial resolution to a few micrometres. So higher numerical apertures and lower probe wavelengths would yield higher spatial resolutions, as in accordance with what is known as Sparrow's criterion, where the spatial resolution is directly related to the probe wavelength divided by the numerical aperture. Because of this, spatial resolutions and details can vary significantly depending on the apparatus and can be magnification dependent where even the camera system's individual cell size may limit the spatial resolution [22].

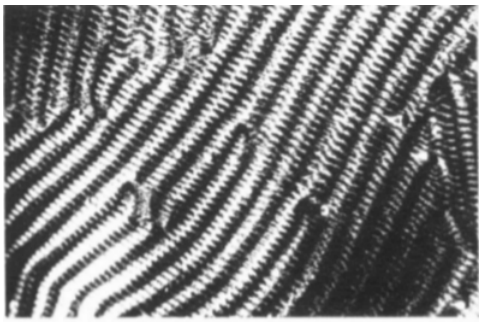

Figure 3: Domains in a of $Fe_{78}Si_9B_{13}$ metallic glass composition imaged by MOKE microscopy. The horizontal length is 100μm. [23].

2.1.4 Magnetic Force Microscopy

One of the main competitors in room temperature magnetic imaging is magnetic force microscopy (MFM). This relies on the long-range force from the sample's stray magnetic field causing a deflection in a magnetic-coated atomic force microscopy (AFM) tip (a technique described in more detail in chapter 5). This is usually performed with the tip raised well above the height typically used for a topographic scan, so only the long range magnetic interactions affect the tip motion. A major advantage of this approach is that it can achieve high spatial resolution, depending on tip quality - even at room temperature [24].

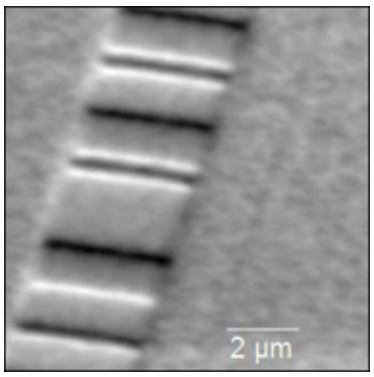

Figure 4: An example MFM image of a CoCrTa Hard Disk.

Common pitfalls to this technique include: the stray magnetic field of the tip which can be invasive to the material under study; a relatively poor magnetic field resolution, typically limited to $10^{-5}T/\sqrt{Hz}$; the final image can contain artefacts due to electrostatic and frictional forces and the difficulty to obtain quantitative data which would require the precise knowledge of the magnetisation state of the tip (usually unknown) [25, 26, 27]. The field resolution is related to the minimum force felt on the tip by the sample's stray magnetic field, as well as considering any other topographical or electrical coupling. The magnetic component is related to the magnetic moment provided by the magnetic material and shape, where a lower moment should result in a higher sensitivity. But a detailed estimation of the force resolution can become complicated when one considers that the image is a convolution of both the sample and probe's magnetic properties, hence one also has to consider the effects between sample and probe when determining the sensitivity. Despite these pitfalls, MFM is an easily accessible technique, usable not only at room temperature but also in ambient conditions. This allows it to be used on a plethora of materials such as biological samples, more sensitive soft non-biological materials and in continued research into novel ferromagnetic and anti-ferromagnetic materials [28].

2.1.5 Scanning superconducting quantum interference device (SSQUID)

Although not operating at room temperature (only reaching as high as the T_c of a high temperature superconductor), Scanning Superconducting Quantum Interference Devices (SSQUIDs) should be given a mention due to their non-invasive operation and ultra-low minimum detectable fields. An SSQUID contains two Josephson junctions in a superconducting loop. Once in close proximity to a sample, the sample's stray field penetrates the SQUID loop. When above the critical current, I_c, of the superconducting loop the difference in voltage between the electrodes is given by [29],

$$V = \frac{R}{2}(I^2 - (2I_c cos(\pi\frac{\Phi}{\Phi_0}))^2), \tag{4}$$

where R is the resistance between the electrodes, I is the current, Φ is the total magnetic flux through the ring and Φ_0 is the flux quantum. The voltage hence oscillates sinusoidally with respect to the amount of flux going through the loop, meaning that only the change

in magnetic field from a known value can be measured. In practice the penetration of magnetic flux is usually compensated by using a field coil to apply a separate magnetic field parallel to the device to keep a constant voltage across the electrodes. The strength of the field being measured will then be equal to the strength of the bias magnetic field passing through the SQUID [30]. While scanning, the strength of the compensating magnetic field is controlled by feedback electronics, with the field strength recorded along with the position of the probe to produce the final magnetic image.

The magnetic resolution of SSQUID imaging can easily reach the nano-Tesla range, while with optimisation it is capable of reaching the pico-Tesla range [31]. However, early probes were limited to spatial resolutions of 80μm. Over time, with development of SQUIDs-on-tips, resolutions have reduced dramatically to some tens of nanometers, due to the possibility to position the sensing component within a few nanometers of the sample (avoiding the rapid decay of the magnetic signal away from the sample surface) [32]. The significant drawback comes with the need for low operating temperatures, generally liquid helium temperatures with a few capable of imagine at the liquid nitrogen temperatures [33].

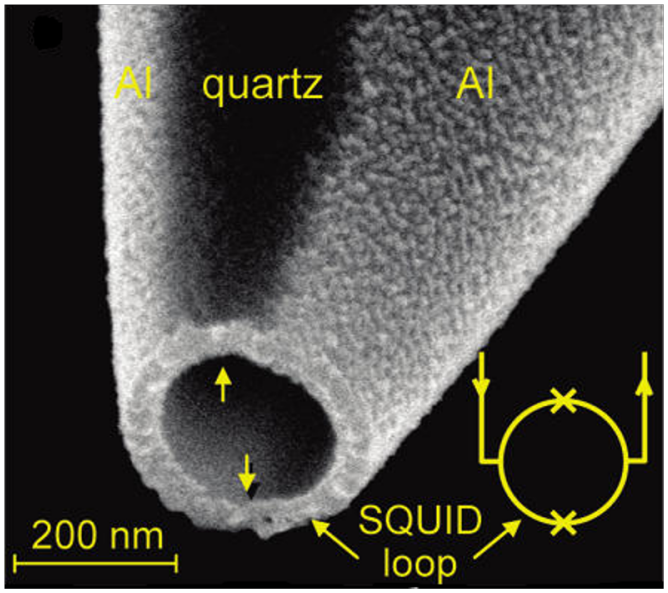

Figure 5: A scanning electron micrograph of a high spatial resolution SQUID-on-a-tip [34].

2.1.6 Scanning Nitrogen Vacancy Centre Magnetometry (sNVM)

A recent entry to the field is scanning Nitrogen Vacancy (NV) centre Magnetometery technique (sNVM). This microscope takes a standard Nitrogen vacancy centre magnetometer and integrates it onto the end of an AFM tip. A nitrogen vacancy centre is a molecular defect in diamond consisting of a Nitrogen substituted in the diamond lattice with an adjacent carbon vacancy. It is also known as a colour centre as this vacancy absorbs photons

in the visible light wavelength range and then emits photons in a broad range [35]. These defects can exist naturally but can also be controllably created by implanting the diamond with nitrogen ions. The diamond can then be annealed at high temperatures (800°C) so that the carbon vacancies migrate until they meet the implanted nitrogen ions. The NV center has 6 electrons when negatively charged. Of these, four of them form pairs and the remaining two are unpaired, forming spin triplet ground state. These triplets are zero field-split into $m_s = 0$ and $m_s = \pm 1$, separated by about 2.9 GHz [36]. In the presence of a non-zero magnetic field along the NV axis, the $m_s = \pm 1$ states are split further. By measuring the amount of Zeeman splitting, one can then measure the magnetic field. Figure 6 shows two examples of magnetic imaging using NV centres.

This technique has very impressive resolutions, both magnetic and spatial, owing to the near atomic size sensing component being on-tip and using the AFM surface tracking technique to approach and scan across the sample. Spatial resolutions are typically in the deep submicron to nanoscale resolutions, while magnetic field resolutions range in the micro- to nano-Tesla range at room temperature. Although strides have been made to make the combined optical and scanning probe system an easier to use turn-key technique, current limitations include the lower temporal resolutions and the higher fabrication costs of diamond tipped probes.

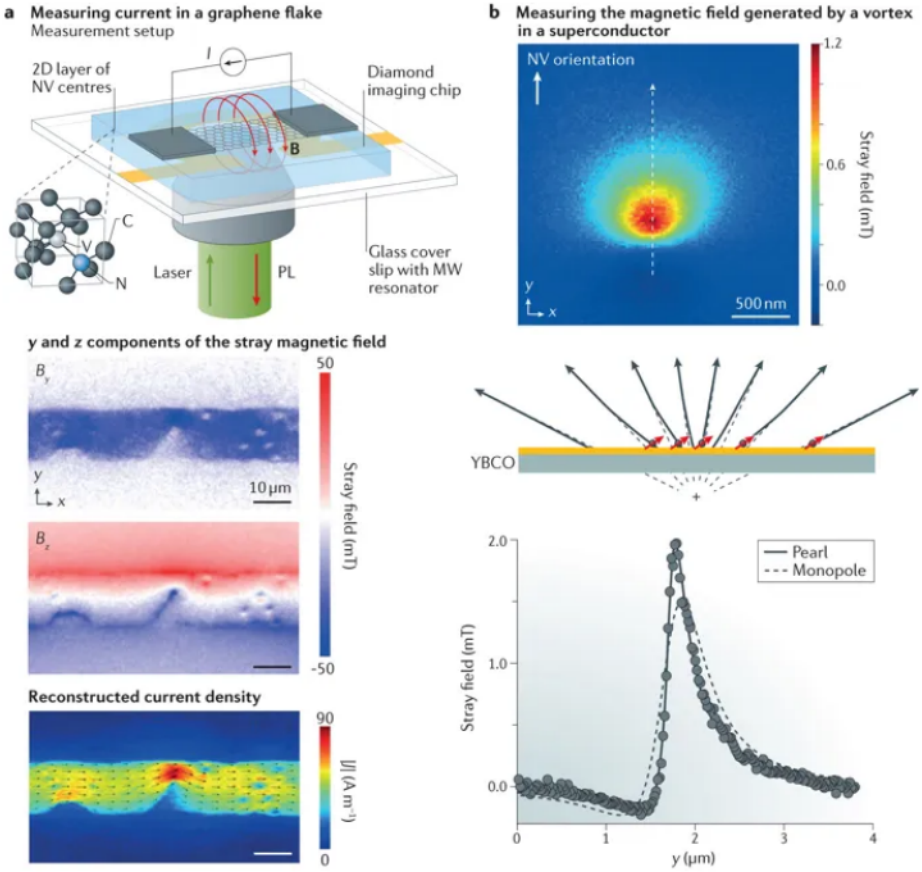

Figure 6: An example of sNVM imaging. In **a**), a graphene flake is exfoliated on a near-surface layer of NV centres (20nm sample-sensor separation). The current density is then re-constructed from the stray magnetic field image. In **b**), a superconducting vortex in YBCO is imaged using a similar set-up at cryogenic temperatures [37].

2.1.7 Scanning Hall Probe microscopy

Once integrated with a surface tracking method, a Hall probe magnetometer can raster scan across a surface and measure and record the magnetic field at each position. The tracking method may be either based on a Scanning Tunnelling (ST) tip fabricated via deposition of a gold thin film over the corner of the chip in close proximity to the active sensor (a few μm), or employing an SiO_2 tip and using a quartz tuning fork to enable AFM tracking [38, 39]. Such a Hall probe-tip device can be mounted onto a piezoelectric scanner tube, similar to other Scanning Probe Microscopes (SPM) like AFM and Scanning Tunnelling Microscopy (STM), to enable its three dimensional motion. An example of an SHPM chip with the Hall cross positioning with respect to the ST tip is shown in fig7.

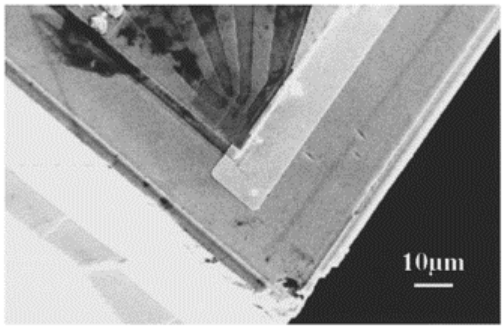

Figure 7: An SEM image of a Hall probe integrated with an ST tip for surface tracking [38].

The probe is tilted 1-2 degrees with respect to the sample plane to minimise the distance between the Hall probe and the sample surface. In ST tracking SHPM, the probe is approached to the sample until a tunnel current is established, the probe is then scanned over the sample keeping the tunnel current constant by adjusting the scan height to accommodate changes in topography in a feedback loop(as for standard STM operation). An alternative approach is to lift the probe up 100nm above the surface of the sample after a tunnel current is detected and to scan in a faster ($\approx$10 frames/s) 'flying-mode'. This is often preferred in order to minimise the chance of a tip-sample crash. Depending on the piezoelectric transducers used, the scan area can be as small as 25μm x 25μm at 77K, with the area becoming smaller still as the temperature falls [38]. The SHPM does not necessarily need to be approached using the scanning tunnelling mode, but can also be approached in the same fashion as an AFM using the corner of a silicon chip as a make-shift tip to detect surface forces [39]. The Hall probe produces a negligible stray field, generally much smaller than earth's field itself, meaning that SHPM is relatively non-invasive to the sample it is scanning. Knowledge of the Hall coefficient, R_H, of the material of the Hall probe also allows for quantitative data to be extracted from the image. The spatial resolution of the technique is typically limited by the electronic size of the Hall cross. In materials such as graphene this is approximately equal to the width of the Hall cross leads, while in GaAs-based Hall probes this is usually estimated to be a little smaller than the physical wire width due to edge wall depletion effects [38]. Spatial resolutions range between 50nm and 1μm are readily achieved. The minimum detectable field of an SHPM sensor is determined by the following equation,

$$B_{min} = \frac{V_n}{I_H R_H}, \tag{5}$$

where V_n is the voltage noise at a select frequency and I_H is the drive current of the Hall device. Minimum detectable fields at room temperature can reach down to the nano-Tesla range, more than capable of studying room temperature superconductors, should they ever be discovered.

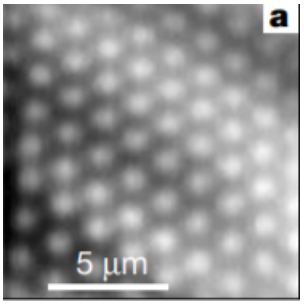

Figure 8: An example SHPM image of a superconducting Abrikosov vortex lattice in the high temperature superconducting material, BSCCO [40].

2.1.8 Comparison between techniques

To compare the different techniques one can plot the minimum detectable field as a function of spatial resolution. The best imaging techniques will be found towards the bottom left of this plot. As one can see from 9, sNVM performs exceptionally well and is currently leading the field overall, only being outperformed in spatial resolution by Lorentz microscopy. For Lorentz microscopy, the environment, the expensive TEM system and the requirements on the sample make it a much less accessible and highly invasive technique. MFM also performs exceptionally in terms of spatial resolution. However it lacks somewhat in terms of magnetic resolution, while its greatest pitfall is the invasiveness of the tip, a problem that other techniques such as SHPM, Magneto-optical imaging and sNVM do not have. Despite its great promise, an issue surrounding sNVM imaging is the minimum sensor-sample separation it can attain due NV centres only being stable a few nanometers inside the diamond lattice [37]. Furthermore, sNVM has a frequency limit of around 100GHz which can limit the field range the technique can image to just a couple of Tesla [37]. SHPM leads the main pack of imaging techniques when considering both magnetic and spatial resolution. Combining further improvements in spatial resolution and magnetic resolution using new material combinations, such as graphene and hBN, with the ease and simplicity of Hall effect measurements gives SHPM plenty of room to rival sNVM. SHPM can also be made just as accessible as MFM by using AFM tracking and approach techniques with a scanning Hall sensor [39].

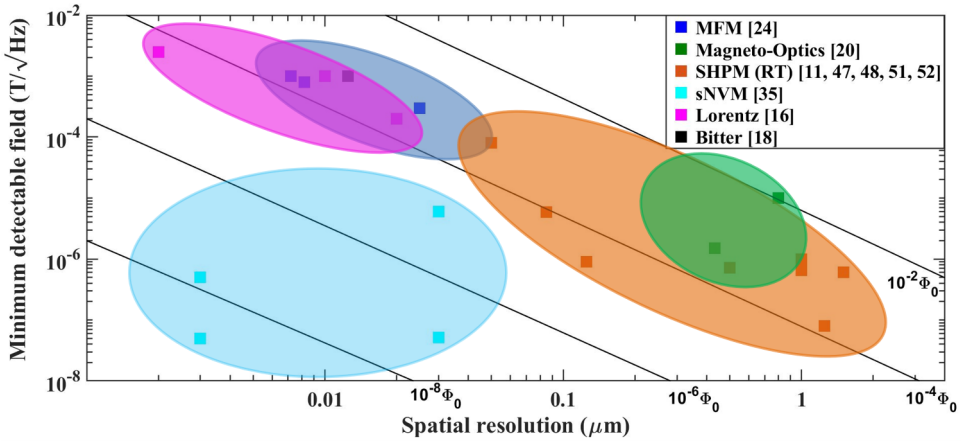

Figure 9: A plot of the minimum detectable fields and spatial resolutions, X_{min}, of room temperature magnetic imaging techniques. The diagonal lines represent the equivalent flux sensitivity ($B_{min} \times X_{min}^2$) expressed in fractions of a superconducting flux quantum Φ_0=h/2e.

2.2 The SHPM in detail

The scanning Hall probe microscope was first designed and built in 1958 by Kronick using a Bismuth Hall sensor on a glass substrate [41]. These Hall sensors were fairly large, up to 100μm with a sample-sensor separation of the order of 50μm [41]. Since then, Hall sensors sizes and sample-sensor separations have reduced while minimum detectable fields have also decreased. With these improvements, the technique has become widely commercialised and used in both basic research and industrial applications. This section covers the technique in more detail. It starts with a description of the principle effect used to measure the local stray magnetic fields, before outlining the key figures of merit of an SHPM Hall probe. This finishes with a brief review of the currently available Hall probes and their performances.

2.2.1 The Hall effect

The SHPM makes use of the Hall effect to detect local stray magnetic fields from the materials under study. Charge carriers in a conductor under zero magnetic field follow straight paths between collisions with impurities etc. In a magnetic field perpendicular to the sample, the paths taken are curved due to the Lorentz force, F_L, experienced by the carriers. This results in charges building up on one side of the material causing a charge imbalance. This separation of charges creates an electric field whose electric force, F_E, balances the Lorentz force steady state. This is described by the following equation,

$$F = F_L + F_E = 0. \tag{6}$$

By substituting the Hall electric field, E_H, electric charge, q, drift velocity, ν and the magnetic field, B for the two forces one obtains,

$$qE_H = -q\nu \times B. \tag{7}$$

In the case that E_H, ν and B are perpendicular this becomes,

$$E_H = -\nu B. \tag{8}$$

Figure 10 illustrates the Hall effect in a cuboid shaped sample with dimensions $t \times w \times L$ with t being the sample thickness, w being the wire width and L being the sample length [42].

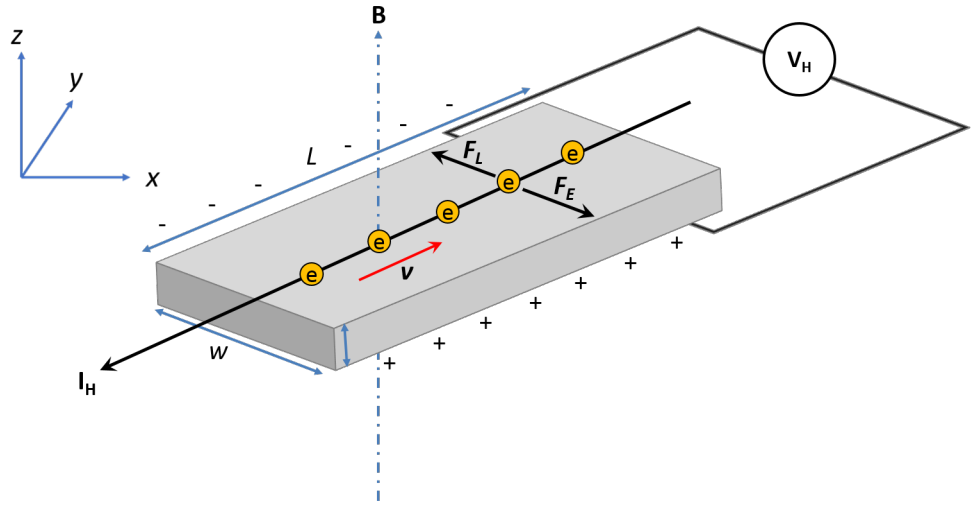

Figure 10: The basic illustration of the Hall effect in a cuboid shaped sample showing the electric and magnetic field forces (F_L and F_E) acting on the negatively charged electron carriers in a perpendicular magnetic field, B.

When a current, I_H, flows along the length of the conductor, one can re-write equation 8 in terms of the potential (the Hall voltage), V_H, as,

$$V_H = \frac{I_H B}{ntq}, \tag{9}$$

where n the carrier concentration. In the case of an atomically thin sample such as graphene, t can be neglected. In the case of an atomically thin sample such as graphene, t is generally combined with n to create a 2D carrier density, n_{2d}. The magnetic sensitivity, R_H, also known as the Hall co-efficient can then be obtained by,

$$R_H = \frac{V_H t}{IB} = -\frac{1}{n_{2d} e}. \tag{10}$$

Using this relationship it becomes straightforward to calculate the Hall coefficient of a Hall probe by applying a known magnetic field and recording the measured Hall voltage. In a semiconductor however, this picture is not entirely accurate, as contributions can come from both holes and electrons. Taking these into account in a simple two band model leads to,

$$R_H = \frac{p - nb^2}{e(p + nb^2)}, \tag{11}$$

where b is

$$b = \frac{\mu_e}{\mu_h}. \tag{12}$$

with μ_e and μ_h being the electron and hole mobilities respectively. Returning to a one band picture, the Hall effect gives us precise insight into semiconductor performance, namely, via calculation of the mobility from the Hall co-efficient and the conductivity, σ, using,

$$\mu = \sigma R_H. \tag{13}$$

The estimation of mobility is conventionally done with devices in a Hall bar configuration in which the material under study is in a rectangular shape of known dimensions with current and voltage leads at known separations along the bar. The known separations allows one to accurately calculate the conductivity for this Hall mobility calculation. Standard Hall probe devices are in the form of a Greek cross, as shown in figure 11. Two opposite leads provide source and drain for the Hall current, while the other two leads running perpendicular to the current leads measure the Hall voltage.

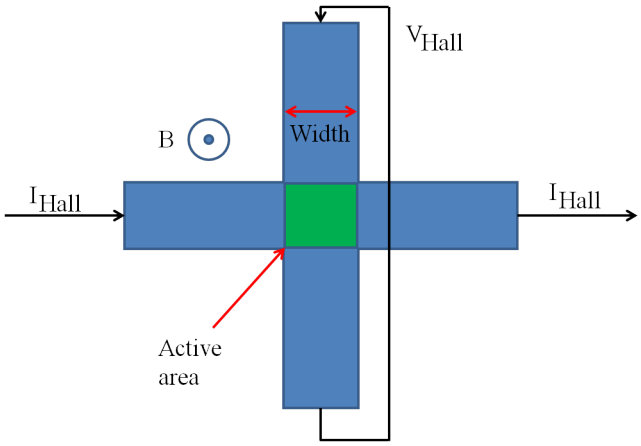

Figure 11: Illustration of a Greek cross for Hall measurements, two Hall crosses in series can be used for mobility measurements as described in this section. I_{Hall} is the Hall drive current, while V_{Hall} is the measured transverse voltage and B the magnetic field applied perpendicular to the Hall cross.

2.2.2 Hall probe figures of merit

When choosing a material as the Hall probe component one has to consider the figures of merit of an SHPM. Two of these have been touched upon in chapter 2.1.7, the spatial resolution and the minimum detectable field. As previously mentioned, the spatial resolution is typically determined to be equivalent to the size of the active area of the Hall cross, as illustrated in fig 11. This is usually equal to the wire-width, w. Hence, a graphene Hall cross with a wire width of 50nm yields a maximum spatial resolution of 50nm. In practice this value can be significantly higher if the tip-sensor separation is not also minimised. With this in mind optimal materials should be those whose spatial resolution is not limited by edge wall depletion effects and it should also be easy to pattern the material into the Hall

cross shape. It should be noted that in some cases the spatial resolution is of the order of the characteristic magnetic length scales of superconductivity, λ_L. This means there is significant signal broadening which needs to be accounted for when making comparisons with theory.

A more challenging figure of merit to optimise is the minimum detectable field, B_{min}. Recalling equation 5, one can see that the minimum detectable field depends on both the magnetic sensitivity and the voltage noise of the material. The Hall coefficient is much easier to understand, as can be seen from equation 10, and is related to the charge carrier concentration of a material. This means that in order to optimise R_H, one should choose a conductor with a low carrier concentration, yielding a high magnetic sensitivity. The voltage noise, on the other hand, depends on the measurement frequency of the device. At frequencies above a $1/\mathrm{f}$ corner frequency, the voltage noise is determined by the Johnson-Nyquist noise, caused by the thermal agitation of charge carriers and described by,

$$V_n^J = \sqrt{4Rk_BT\Delta f}, \tag{14}$$

with R being the channel resistance, k_B is the Boltzmann constant, T is the temperature and Δf is the measurement bandwidth. Johnson noise, also called thermal noise, is noise generated by thermal agitation of the charge carriers. In contrast to Johnson noise, $1/f$ noise is currently thought to be due to fluctuations in charge carrier number and/or mobility [43]. Figure 12 illustrates the difference between low frequency noise and Johnson-Nyquist noise as a function of frequency in a Hall device.

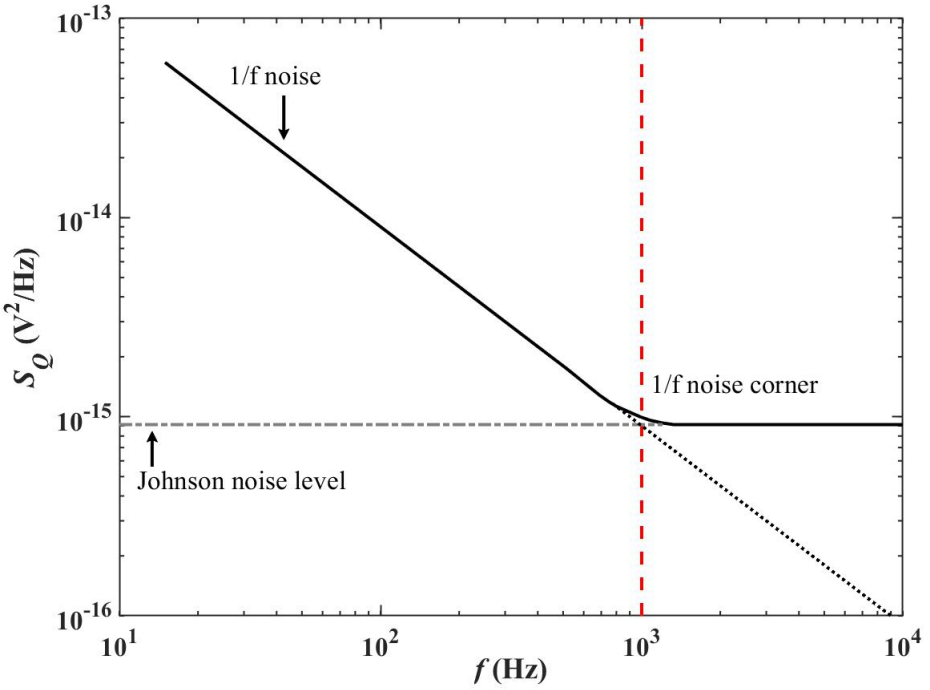

Figure 12: Voltage noise power versus frequency indicating the dependence of low frequency and high frequency noise on measurement frequency. The dotted red line indicates the $1/f$ noise corner (the transition between the two regimes). The dotted gray and black lines show the Johnson noise level and the $1/f$ trend respectively. Note that the crossover from $1/f$ to Johnson noise is not abrupt as indicated by the black line.

By substituting in equations 14, 13 and 10 into equation 5 the minimum detectable field at high measurement frequencies becomes,

$$B^J_{min} = \frac{1}{I_H}\sqrt{\frac{n}{\mu}}\sqrt{\frac{4Lek_BT\Delta f}{w}}, \tag{15}$$

where L is the lead-to-lead length, k_B is the Boltzmann constant, Δf is the measurement bandwidth, T is the temperature and e is the charge of the electron. In the high frequency regime one would hence expect the minimum detectable field to increase with increasing carrier concentration and decrease with increasing mobility. However the bandwidth of the device may be reduced due to the resistance-capacitance constant. Because of the inverse relationship of field resolution to current shown in equation 15, the optimum condition to measure in the high frequency regime would be ideally up to the breakdown current density of the device, this has as of yet not been shown to change even in the linear transport regime. Since the target is room temperature operation, T is fixed at 300K.

In the low frequency limit the transverse voltage noise can be described using the conduc-

tivity fluctuation model proposed by L. K. J. Vandamme et al. [44]

$$V_n^{1/f} = I_H \rho_{xx} \sqrt{\frac{\alpha}{AFfn}}, \tag{16}$$

where ρ_{xx} is the longitudinal resistivity, α is a material dependent dimensionless constant usually on the order of 10^{-3}, A is the contact-free surface area, f is the measurement frequency in the low frequency regime and F is a geometric factor usually dependent on the aspect ratio of the Hall cross. In the case of a Hall cross with aspect ratio of 5:1, the value of F is 1 [44]. Performing a similar substitution as for the high frequency regime, we obtain a low frequency minimum detectable field of [45],

$$B_{min}^{1/f} = \frac{1}{\sqrt{n}e\mu} \sqrt{\frac{\alpha \Delta f}{AFf}}. \tag{17}$$

In contrast to the high frequency limit, the minimum detectable field in the low frequency regime is directly inversely proportional to the square root of carrier density. However, depending on the relationship between mobility and carrier density, it could still be more beneficial to have a higher carrier concentration. One should keep in mind that the transition between low and high frequency noise regimes is not a sudden change, but rather a gradual crossover. This means that in close vicinity to the noise corner, the value of B_{min} may find itself between the two limits described by equations 15 and 17. For an SHPM, Hall probes are typically operated at fairly low frequencies up to 1kHz to minimise the influence of parasitic lead capacitances. The lead capacitance is typically dominated by the miniature coaxial cables with an approximate capacitance of 100pmF/m. Consequently, it is likely that these devices are often operating in the low frequency noise regime, hence the focus of the hunt for a new Hall probe material should be one with minimal low frequency noise. This requires looking towards materials with high mobilities and low defect activity at edges and surfaces.

Finally, an often overlooked parameter is the Hall offset voltage. One should note that the measured Hall voltage also includes an offset voltage, the Hall voltage in the absence of a magnetic field due to misalignment of voltage contacts or material inhomogeneity. This Hall offset should ideally be minimised to prevent saturation of preamplifiers when amplifying Hall voltage signals. Hence an additional figure of merit is how low the Hall offset voltage can be. For optimally patterned probes the causes of the Hall offset resistance are generally linked to inhomogeneous current flows inside the semiconducting material [46].

2.2.3 Comparison and analysis of previous Hall probe architectures

Before searching for a new material for the SHPM Hall probe, it is important to first identify which materials are currently leading the way in terms of each figure merit. This sub-section covers, in tabular format, a history of previous noteworthy Hall probe devices including their figures of merit.

Type N/A	R_H (Ω/T)	B_{min} $(\mu T/\sqrt{H_z})$	Frequency (H_z)	Conditions N/A	Size $(\mu$m)
AlGaAs/InGaAs/GaAs [47]	N/A	15	100	Vacuum	1
GaAs/AlGaAs [48]	2600	41	N/A	Vacuum	0.8
InSb [49]	370	0.72	201	Vacuum	0.5
InSb [50]	300	0.08	N/A	Vacuum	1
Bismuth [51]	1.81	100	30	Vacuum	0.1
Bismuth [48]	3.3	38	N/A	Vacuum	2.8
Bismuth [52]	4	80	1000	Vacuum	0.05

Table 1: A summary of the performance of previous room temperature (300K) Hall probe devices reported in literature. Since the focus of this research is on room temperature operation, data at low temperature devices are omitted. The drive current has also been left out due to the very different currents used for different materials and device sizes.

The best competitor in terms of spatial resolution are the Bismuth probes. However the minimum detectable fields struggle to come close to those of other probes. Bismuth also has further disadvantages. The fabrication of small probes is challenging due to the requirement of thin film deposition and etching/lift off. Bismuth is also relatively unstable in air, degrading quickly over time [51]. In terms of minimum detectable fields, the InSb and even improved GaAs based probes perform very well. However one of the major pitfalls for GaAs based probes is the surface charge depletion effects which severely limits the possibility of effective devices when reducing the physical wire width. Meanwhile, InSb based probes suffer from the formation of dead layers during the reactive ion etching step. Furthermore, these devices typically have their active layer buried beneath the epilayer surface, further increasing the probe-sample separation [49].

3 Graphene-based Hall probes

The Hall probes in Table 1 of chapter 2 can still be beaten in performance. Probes with attractive minimum detectable fields generally have large wire widths that are too large for high resolution imaging, while those with small wire widths have exhibit significantly degraded minimum detectable fields. The solution to this problem that is explored in this thesis is to fabricate Hall probes from graphene. This chapter introduces graphene and its unique properties that make it particularly applicable to Hall probe technologies. We show why graphene has attracted so much interest since its isolation in 2003 [4], yet graphene still has its shortcomings for a variety of reasons and these will be explored here. Faced with these limitations, this chapter looks into the potential of graphene beyond a single layer, the alternative sources of graphene and the possible improvement of graphene based Hall probe devices through encapsulation.

3.1 Introduction to graphene

Graphene, a 2D monolayer of sp^2-bonded carbon atoms, was first theoretically studied in 1974 by Wallace [53]. It was later isolated in 2003 by Geim and Novoselov when they realised that thinner graphite flakes could be found on the Scotch tape that had for many years been used to obtain cleaner graphite flakes [4]. This method of obtaining graphene has since become known as the 'Scotch-tape' method, but is better formally known as the micromechanical exfoliation method. The big attraction of graphene comes from its superior electronic transport properties that make it a promising material for the next generation of nanoscale electronic devices. Its other properties such as its mechanical and thermal robustness give it the required versatility for use in a vast range of environments, thus unlocking a wide array of practical uses.

The rhombus-shaped unit cell of graphene contains two carbon atoms sitting at non-equivalent sites, which one can designate A and B, as seen in figure 13.

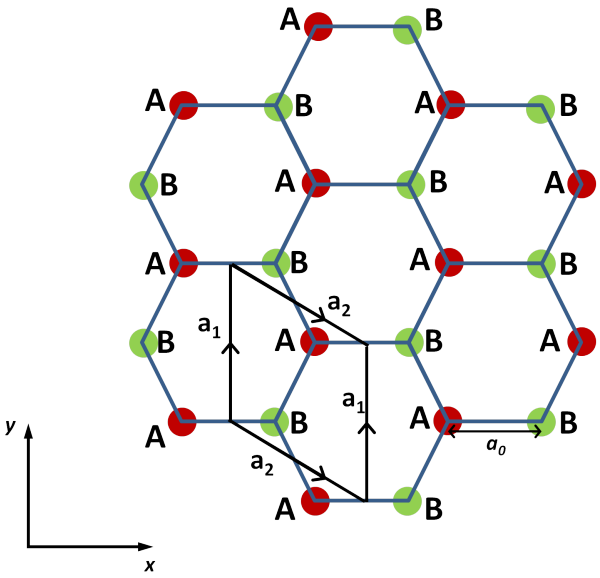

Figure 13: The lattice structure of graphene where A and B are the non-equivalent atomic sites which form graphene's unit cell. The unit cell has the indicated rhombus shape which is defined by two lattice vectors, $\mathbf{a}_1$ and $\mathbf{a}_2$.

The hexagonal lattice vectors in the x,y plane, $\mathbf{a_1}$, $\mathbf{a_2}$ can be written as

$$\mathbf{a_1} = \left(\frac{a_0\sqrt{3}}{2}, \frac{a_0}{2}, \right), \tag{18}$$

$$\mathbf{a_2} = \left(\frac{a_0\sqrt{3}}{2}, -\frac{a_0}{2}, \right), \tag{19}$$

where a_0 is the in-plane lattice constant of 0.246nm. The carbon atoms bond through a process called hybridisation whereby the mixing of atomic orbitals forms new hybrid orbitals. Here, one 2s atomic orbital hybridises with two 2p atomic orbitals giving three hybridised sp^2 orbitals. These are occupied by three out the four sp^2 electrons, forming what are known as the σ-bonds. The remaining electron occupies the p_z orbital which forms a half-filled delocalised π-band.

The reciprocal lattice vectors are:

$$\mathbf{b_1} = \frac{2\pi}{3a_0}\begin{pmatrix}1\\ \sqrt{3}\end{pmatrix}, \tag{20}$$

$$\mathbf{b_2} = \frac{2\pi}{3a_0}\begin{pmatrix}1\\ -\sqrt{3}\end{pmatrix}. \tag{21}$$

These are used to define the hexagonal reciprocal lattice with two non-equivalent points, K and K', also known as the Dirac points (DPs) of graphene. The band structure can be calculated taking into account two p_z electrons per graphene unit cell. The tight binding model calculation by P.R. Wallace in 1947 found that the energy bands were described by

$$E(k_x, k_y) = \pm\gamma_0\sqrt{1 + 4cos\frac{k_x a}{2}cos\frac{ak_y\sqrt{3}}{2} + 4cos^2\frac{k_x a}{2}}, \tag{22}$$

where the positive and negative signs correspond to the π bonding and π^* anti-bonding orbitals [53], and the wave vectors are k_x and k_y [54]. Plots of this equation are shown in figure 14, where at the centre of the Brillouin zone (denoted as Γ) the bands are separated by a finite energy gap, whereas they touch in a cusp at the K and K' points. The unique structure at these points leads to the categorisation of graphene as a zero band gap semiconductor [53].

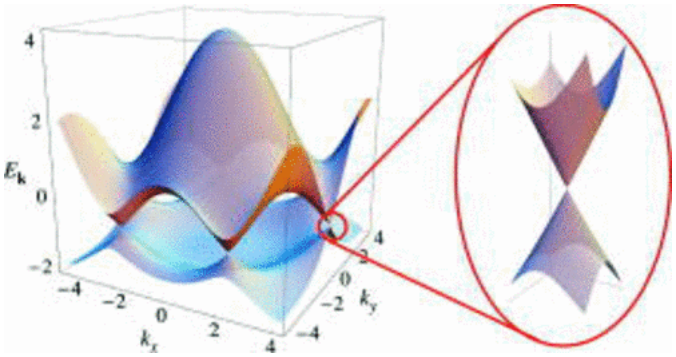

Figure 14: The electronic dispersion in one cell of the honeycomb lattice. Left: energy spectrum with finite values of the nearest and next-nearest neighbour hopping energies. Right: a blow up of the energy bands close to one of the DPs [55].

In the vicinity of the K points, the energy dispersion relation is described by

$$E(\mathbf{k}') = \pm\hbar\nu_F, \tag{23}$$

where the $\pm$ relates to the conductance and valance bands respectively and ν_f is the Fermi velocity given by

$$\nu_F = \frac{a_0 \gamma_0 \sqrt{3}}{2\hbar} \approx 10^6 m/s. \tag{24}$$

This linear energy dispersion makes the electrons and holes near this point (also called Dirac Fermions) behave like relativistic massless particles, but ones that move with ν_F instead of the speed of light. In pristine graphene the Fermi energy is located at $E = 0$. This can be tuned between the valence or conduction band by some form of doping. Usually this is achieved by electrostatic gating, which will be described in chapter 5.

Graphite and multilayer graphene can be obtained by stacking these graphene sheets on top of each other, stabilised by van der Waals interactions. The separation between parallel layers is typically 0.335nm. The exact method of stacking multilayer graphene and graphite stacks will affect their electronic structure. For bilayer graphene, the layers are normally Bernal stacked, or AB stacked. In this case atoms A_1 and A_2 overlap (the numbers referring to separate planes), while the atoms B_1 and B_2 are positioned at the vacant hexagon centres in the other layer. This leads to a quadratic E-k dispersion in the electronic structure near the band edge, but a zero band gap. For trilayer graphene, there are two different possibilities. The first is ABA Bernal stacking, in which a bilayer stack is capped by a third layer that mirrors the first layer. This results in an electronic structure which is a combination of the linear and quadratic dispersion of monolayer and bilayer graphene. The second stacking order is ABC, where the third layer is now stacked with the same displacement relative to the second layer as the second layer has relative to the first. The electronic structure in this case is described by a cubic dispersion. Sketches of the stacking and energy dispersion are shown in figure 15 The details of the stacking structure become important in the presence of an electric field; devices made out of bilayer graphene or ABC stacked multilayer graphene will open up a band gap. For ABA stacked multilayer devices, a semimetallic band overlap forms.

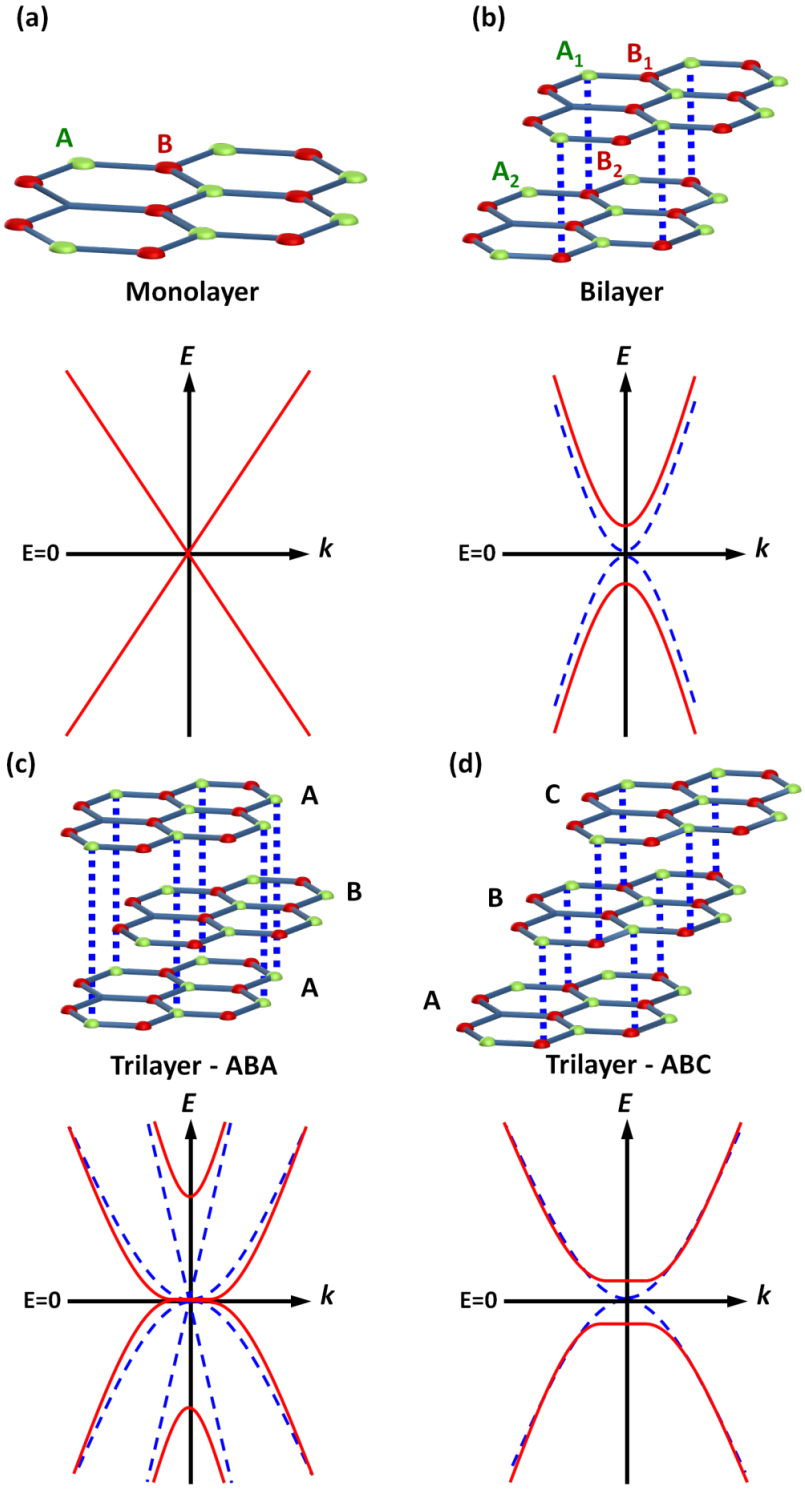

Figure 15: Diagram of the crystal structure and energy dispersion for (a) monolayer, (b) bilayer, (c) ABA stacked trilayer and (d) ABC stacked trilayer graphene. The dashed lines are the band structures without an applied electric field across the layers, while the solid lines are with a field.

3.1.1 Electronic properties of graphene

Graphene has been proposed for use in a vast array of electronic applications including: wearable electronics, touchscreens, spintronics and solar cells [56, 57, 58, 59]. Each application would look to exploit certain properties that graphene has, such as its robustness to stress or strain, or the preservation of electron spins over long distances and times. Since there is a lot to discuss about graphene's remarkable physical properties, this section will only look at the electronic properties of graphene from the perspective of building Hall sensors.

The quality of electronic devices made from graphene can be characterised in several ways. The three key values for almost any electronic device are the: the carrier mobility, the conductivity and the residual doping level. The relation between current and electric field is given by

$$E_x = J_x \cdot \rho_{xx}, \tag{25}$$

where $\rho_{xx} = m/(ne^2\tau)$ with n being the carrier density, m the charge carrier mass and τ the average scattering time of the charge carriers. Replacing the mass with $m = |\mathbf{p}|/\nu_F$, the conductivity can be written as,

$$\frac{1}{\rho_{xx}} = \frac{2e^2\tau\nu_F\sqrt{\pi n}}{h}, \tag{26}$$

where again τ is the average time between two momentum scattering events. There are several factors that govern τ depends on many factors, including; inhomogeneous charge distributions in the substrate, surface contamination, electron-phonon coupling at higher temperatures and strain [60, 61, 62]. The longitudinal resistivity of a 2D material is defined in terms of the measured longitudinal resistance, Rxx, as,

$$\rho_{xx} = R_{xx}\frac{w}{L}, \tag{27}$$

where W is is the width and L the length of the channel. The electrical conductivity measures how easily charge can flow in a system and is described in graphene by,

$$\sigma_{xx} = ne\mu, \tag{28}$$

where μ is the carrier mobility, which is a measure of how easily a charge carrier moves in response to an electric field in the system [63]. Another indicator of material quality is the mean free path, given by,

$$l_{mfp} = \mu\sqrt{n\pi}\frac{\hbar}{e}. \tag{29}$$

In very short graphene devices, the mobility becomes limited by device size, as the contact-related scattering becomes the dominant factor. The carriers are considered classically ballistic when $L << l_{mfp}$, and diffusive in the opposite limit $L >> l_{mfp}$.

Aside from the mobility, one also needs to optimise the carrier concentration. The semimetallic 2D nature of graphene means that the carrier concentration can be low enough to achieve high room temperature magnetic sensitivities. Furthermore, graphene can be exfoliated or

transferred onto a substrate such as n^+-Si/$SiO_2$to allow for the tuning of the carrier concentration by applying a back gate voltage. As one sweeps the back gate voltage and measures resistance, the DP can usually be identified with the resistance maximum. Should the extrinsic doping of graphene push it far away from the DP, one can generally use a back gate to reduce the carrier concentration close to zero. The change in carrier concentration per back gate voltage, V_{bg}, applied is given by,

$$\delta n = \frac{\epsilon_r \epsilon_0 V_{bg}}{de}, \tag{30}$$

where the relative permittivity, ϵ_r, is 3.9 for SiO_2 and d is the dielectric thickness, typically 90nm or 300nm.

In addition to the magnetic sensitivity, the electronic noise is an important parameter for graphene Hall devices. Electronic noise in Hall devices has been explored in chapter 2.2.2 in terms of figure-of-merits for Hall probe devices. Understanding noise sources in graphene can hence help us form optimise Hall probe devices. When operating at frequencies above the 1/f noise corner frequency (c.f., figure 12) our understanding is clear that temperature and lead-to-lead resistance are the main factors influencing the electronic noise (i.e., thermal Johnson noise). When operated below the corner frequency, the noise is dominated by so-called $1/f$ noise. The origins of and mechanisms for $1/f$ noise remain the source of much debate today [43]. Researchers have come to realise that the noise cannot be attributed to a single physical mechanism, and is instead due to the combination of several effects. The 2D nature of graphene means that conduction electrons are exposed to traps near the surface of the substrate such as silicon dioxide, suggesting that carrier-number fluctuations will play a strong role. These traps could be anything from oxide defect traps to chemical impurities on the surface, both of which have been highlighted as key players [64]. Traps capture carriers and re-emit them back to the channel, leading to carrier fluctuations which typically have a Lorentzian spectral density:

$$S_I(f) = \frac{S_0}{1 + (2\pi f \tau_{trap})^2}, \tag{31}$$

where τ_{trap} is the time constant of the particular trap and S_0 is the frequency-independent limiting term observed at $f << (2\pi\tau_{trap})^{-1}$. The overlap of closely positioned Lorentzians due to sources with different lifetimes generally results in an overall $1/f$ dependence over a fairly broad frequency range. If one type of trap with a specific time constant dominates a generation-recombination 'bulge' appears in the $1/f$ region centred on $f_c = 1/2\pi\tau$. Mobility fluctuations are a second source of noise that is linked to the capture and release of charged carriers on traps. The traps act as scattering centres with fluctuating cross sections and again the superposition of many individual sources with different time constants generally leads to an overall $1/f$ frequency [43].

Since the purpose of this thesis is to study the capabilities of nanoscale graphene Hall sensors, the size of the device should also be considered and the role it plays in device performance. The size dependence has been well studied and reveals an inverse dependence of B_{min} on the wire width [64, 65]. Device resistance tend to increase as the size of the

device reduces because strongly scattering edges make up a larger fraction of the nanostructure area, leading to an adverse effect on the mobility [66]. Recalling the relationship between mobility and noise derived in chapter 2.2.2, a lower mobility would result in higher noise, hence a lower signal-to-noise ratio. The effect in very small graphene devices can be attributed to the line edge roughness (ER), causing additional scattering which decreases the device carrier mobility and increasing the noise. Unfortunately, the edge roughness can typically be as large as a few nanometres after top-down etching of the graphene channels, something that is often unavoidable for more intricate device designs. The edge disorder can be reduced by treating the edges and recent studies have shown that immersion in a low concentration of hydrofluoric acid (HF) can improve the mobility of graphene nanoribbons [67]. A Corbino disk is where the current flows from a central disk shaped anode to a surrounding annular electrode on the outside of the material under study. This essentially edgeless device would be an ideal method to compare with a conventional Hall bar to study the edge effects in detail. However, it should be noted that practically, a deep sub-micron Corbino disk would be an incredibly challenging device to fabricate. A lot of research remains to be done to fully optimising nanodevice performance, be that by improving fabrication procedures (e.g., controlled etching), by modification of the edges, or by changes to the device architecture such as through encapsulation.

3.1.2 Graphene beyond a single layer

At first sight, single layer graphene would appear to be the most preferred materials choice as compared to bilayer or other multilayers. However, some research reports suggest that using a device of containing more layers may provide lower minimum detectable fields for the same spatial resolution [68, 69, 43]. The reasons for this are still unclear, and there is still plenty of room for more research in this area. A long-standing question in regard to $1/f$ noise, is if the noise is generated on the surface or in the 'bulk' of the conductors. Due to graphene's 2D nature, it is an interesting choice of material to study this question. Recent research suggests that surface noise dominates in very thin samples, before crossing over to 'bulk' noise after $\sim$7 layers [68]. The results of this research are shown in figure 16, where a bulk noise model and a surface noise model are compared. It is clear that a thicker sample has lower $1/f$ noise, something which could be exploited for Hall sensor development. The study also found that noise in multilayers increased as more carriers are electrostatically induced, leading to an increase in contribution of surface noise due to a decrease of the surface resistance and possible increased surface-roughness scattering. This would suggest a different carrier density dependence compared to single layer graphene [68]. The difference in the dependence of noise on carrier concentration has also been observed elsewhere and has been suggested to be due to the difference in band structure, suggesting this is caused by a bandgap-opening as carrier concentration increases [69, 70, 71, 72]. Research by Lin and Avouris also reveals good prospects for bilayer graphene nanoscale devices [73]. They discover that $1/f$ noise is strongly suppressed in nanoribbon bilayer graphene due to the better screening of potential fluctuations caused by impurity charges [73].

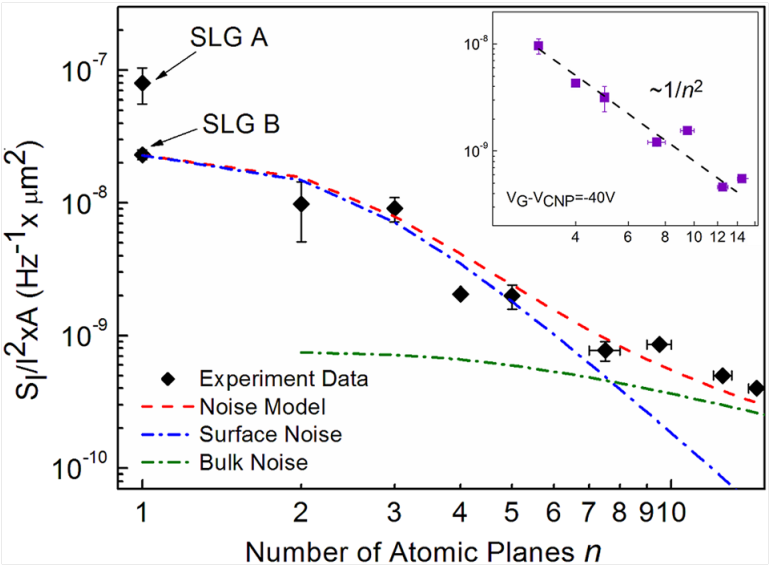

Figure 16: Normalized noise spectral density, $S_I(f)/I^2 \times A$, of different numbers of layers of graphene near the DP. The surface and bulk noise models are plotted separately for comparison. The inset shows the normalized noise spectral density when a high gate bias is applied, where surface contributions are more prevalent [68].

Systematic research into how many layers of graphene is best for a Hall sensor is very limited. No accurate comparison or optimisation using any tuneable parameters has been made as a function of sample thicknesses, for example, magnetic sensitivity and noise as a function of electrostatic gating. A more intensive investigation of this could open the door for much easier fabrication of high resolution Hall probes should multiple layers prove to be just as good, or better, than a single layer.

3.1.3 Encapsulation

A desire to encapsulate graphene between two other layers comes in part from the needing limit the impacts of substrate and environment on graphene sensor performance. Encapsulation also enables extra device functionality, for example allowing a top gate to be added for band-gap control [74, 75, 76]. In this thesis we are most interested in looking to see if graphene's electronic performance for nanoscale Hall sensors can be significantly improved by encapsulation. Since the recent explosion in the number of members of the 2D materials family, in addition to the various polymers and organic materials one can combine with graphene, the choice of which materials to choose to improve graphene's properties has become enormous [4]. However, we can use the specific requirements of the graphene devices we are fabricating to signpost the way to find the optimum materials for encapsulation.

Hall probes for SHPM need to have a high signal-to-noise ratio, hence they need to have high magnetic sensitivity, R_H, and low electronic noise, V_n. Ideally the noise to be optimised is low frequency noise, $V_n^{1/f}$, should be minimised since SHPMs are often operated

at low measurement frequencies where 1/f noise dominates (c.f. chapter 2.2.2). The goal of encapsulating Hall probe devices should be; to reduce low frequency noise and increase the magnetic sensitivity. This could achieved by; reducing the impact of the substrate on charge trapping (i.e., reduced noise), modification of edges (c.f., chapter 3.1.1), eliminating contaminant adsorption during fabrication and/or operation, and reduced surface roughness. So far research from countless other groups has shown that hexagonal boron nitride is a promising encapsulation material for Hall probe devices [77, 43, 78]. Hexagonal boron nitride, more commonly known as hBN, has the same 2D hexagonal structure as graphene, but differs in that a unit cell is composed of two different atoms, boron and nitrogen [79]. The material has excellent dielectric and thermal properties, making it a very suitable substrate for electronic applications [80].

The origins of the positive effects of encapsulating graphene are still unclear, but studies have pointed towards: hBN's smooth surface, minimal defect densities, the spatial separation from charge traps in the substrate oxide and protection from environmental and fabrication process contaminants leading to a reduction the formation of electron hole 'puddles' near the DP [81, 78, 82, 83]. Figure 17 demonstrates the ability of hBN encapsulation to reduce low frequency noise. As one can see, the noise can be reduced by a factor of ten as compare to bare graphene on Si/SiO_2 [82]. This shows exceptional promise for improved sensor performance in devices that incorporate these fabrication techniques.

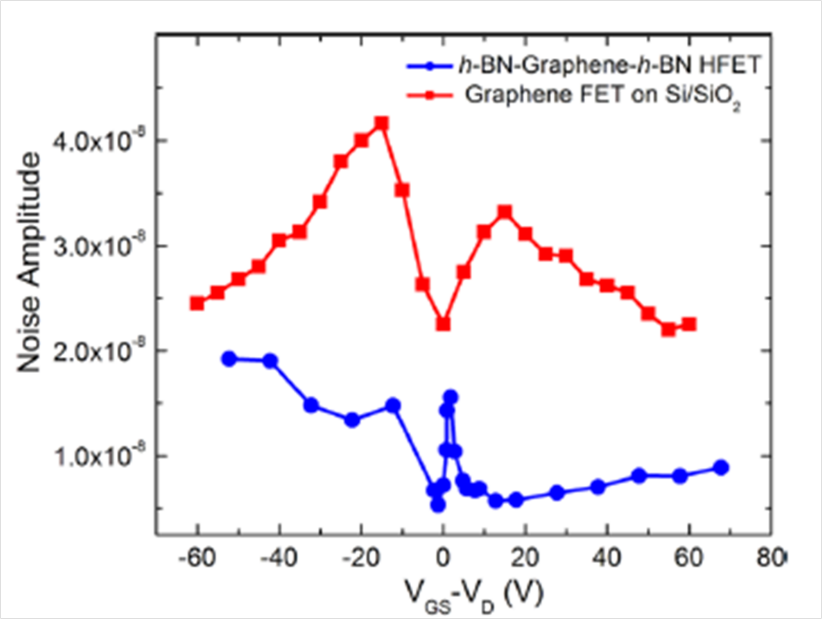

Figure 17: Results of experiments on exfoliated graphene, comparing the noise amplitude as a function of carrier concentration for an hBN-encapsulated and an unencapsulated FET on a Si/SiO_2 substrate [82].

Scanning tunnelling microscopy studies have shown that graphene on hBN has significantly less pronounced electron-hole puddles as compared to graphene placed directly on SiO_2,

which can greatly improve the magnetic sensitivity [84]. Unfortunately, when it comes to the noise levels in nanoscale devices, hBN-encapsulation has yet not been demonstrated to show much of an improvement [85]. This indicates that edge scattering plays a limiting role in transport in nanoribbons.

These heterostructures are typically made by the dry transfer (i.e., without use of solvents) pick-up of graphene on SiO_2, which is then dropped back down onto another hBN flake [86]. The technique used to achieve this in this project will be described in chapter 5.3.2. Another hBN layer can be placed on top afterwards to achieve full encapsulation. Contacting the device is no longer possible using the traditional top contacts, and edge contacts are required instead. These make contact solely at the 1D edge of the graphene flake exposed in the sidewall of the heterostructure after etching. This has been shown to yield low contact resistances due to the joint benefits of avoiding a polymer-degraded surface and shorter bond lengths [87].

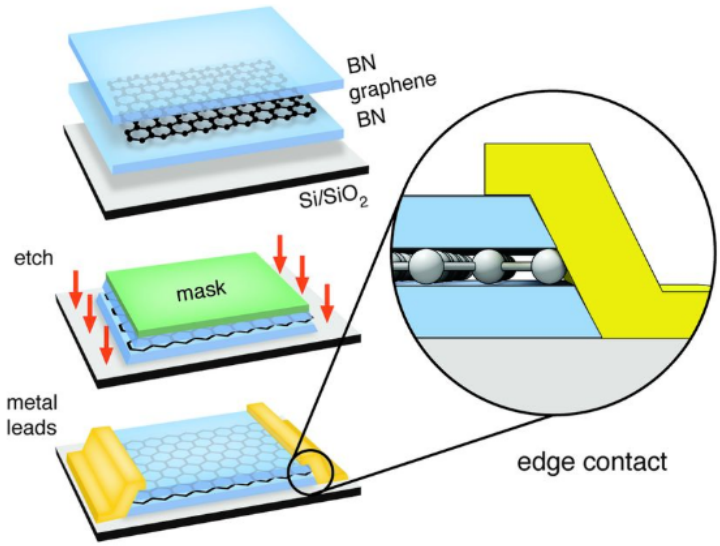

Figure 18: A schematic diagram of the process for making edge contacts to hBN-encapsulated graphene first reported by *Wang et al,*. [87].

3.1.4 Sources of graphene

There are a few different ways to obtain graphene. One has been discussed at the beginning of this chapter, i.e., via micromechanical exfoliation of graphite. The exact details of this process can be read in chapter 5.3.1. The other common method of obtaining graphene is to grow it. Molecular beam epitaxy has a strong track record in growing other semiconducting materials [88], and has recently been used to grow good quality graphene on a hBN substrate [89]. Epitaxial graphene can also be grown on the surface of silicon carbide (SiC) and also shows excellent performance as a Hall sensor [65]. However, in the latter case it is difficult to remove the graphene from the growth substrate, limiting the ability to control the carrier concentration in devices.

An alternative production method is chemical vapour deposition (CVD). Graphene grown via CVD can achieve large-area, high quality films. It is also inexpensive, and can readily be transferred from its growth substrate [90]. CVD grown graphene involves the thermal decomposition of a hydrocarbon source on a heated substrate. A careful choice of substrate (in graphene's case usually copper, nickel or platinum) can catalytically enhance this reaction. After decomposition, the carbon will diffuse across the heated substrate. The substrate is then allowed to cool at a controlled rate, during which the carbon will aggregate on the surface to form graphene sheets. The process often automatically terminates once the substrate is covered by the first carbon sheet [91]. However, mechanically exfoliated graphene has superior properties to that produced by other methods. CVD graphene has been shown to have noticeably higher low frequency noise and much lower magnetic sensitivity than exfoliated flakes [92, 93]. This is speculated to be due to a combination of different reasons such as; increased graphene stress, more surface adsorbates from the transfer processes, higher defect densities and granular polycrystalline growth [94, 93, 43, 70, 95].

Whether the graphene is exfoliated or grown, in most cases flakes eventually need to be built into a 2D material heterostructure or transferred onto another substrate. In the case of CVD grown graphene, it is common to spin and bake a polymeric layer, e.g., poly(methyl methacrylate) (PMMA), on top of the graphene layer to act as a temporary support [5]. The growth substrate is then etched away and the polymer/Graphene floats to the top of the etchant solution, is collected, and then dropped down onto the chosen substrate. At this point the polymeric layer is removed, however this degrades the graphene quality significantly due to remaining polymer residues [96]. To transfer CVD graphene without damaging the growth substrate and to maintain its electronic performance, dry transfer techniques have been developed [6]. One can weaken the Copper-graphene adhesion energy by oxidising the underlying copper and then using a vdW-based pick-up to delaminate the graphene [97, 6]. The transfer of exfoliated graphene itself has also evolved, from using PMMA/polydimethylsiloxane (PDMS) to using hBN as a transfer substrate [98, 86]. The ability pick-up and drop down 2D materials on two different substrates revolved around the adhesion energy. Pick-up using a hBN layer becomes favourable due to the strong Van der Waals forces between the hBN and graphene layers, which are typically greater than the adhesion forces between the graphene and its substrate. The application of heat can alter the adhesion forces and shift the balance in favour of picking up. Once dropped down, the polymer stack used to support the hBN layer can be dissolved or peeled away, leaving behind a finished heterostructure [86]. The specific transfer methods used in this project will be described later in chapter 5.

3.1.5 Nanoscale graphene devices

Up to this point graphene appears to be a promising candidate for high performance Hall sensors. To see if the theory lines up with practice, Table 2 summarises what has been achieved in this area so far.

Type N/A	R_H (Ω/T)	B_{min} $(\mu T/\sqrt{H_z})$	Frequency (H_z)	Conditions N/A	Size (μm)
All Exf hBN/Gr/hBN [92]	4100	0.05	3000	Vacuum	3
CVDhBN/CVDGr [99]	1650	0.05	300	Vacuum	50
CVDGr/ExfhBN [100]	345	N/A	N/A	Vacuum	2
All CVD hBN/Gr/hBN [77]	97	400	3000	Air	75
Epitaxial graphene [101]	87	0.095	1000	Air	150
Epitaxial graphene [65]	640	49.3	3300	Vacuum	0.5
Epitaxial graphene [65]	711	3.9	3300	Vacuum	5
CVD graphene [102]	1800	20	1000	Vacuum	1.5
CVD graphene [103]	2093	0.1	3000	Vacuum	50
CVD graphene [104]	1200	43	50000	Vacuum	5
ExfhBN/CVDGr/ExfhBN [105]	2270	N/A	N/A	Vacuum	5

Table 2: A summary of the key room temperature figures-of-merit of graphene-based Hall probe devices previously reported in the literature (excluding the results of this project). Exfoliated is abbreviated to Exf. Details of the drive current are omitted due to the drastically different current densities used when characterising different device sizes and types before their breakdown.

It is important to that the quoted value of the B_{min} is listed here. These are sometimes quoted at higher measurement frequencies than would be used in applications such as SHPM. Another factor to consider is the physical size of the devices made as there is a substantial difference in noise values of larger, multi-micron sized devices compared to smaller, sub-micron sizes. Even if the full frequency noise spectrum is reported, sometimes the bandwidth of the measurement instrumentation is too narrow, artificially suppressing noise levels at higher frequencies. In other cases the trace is too noisy (possibly due limited averaging) to accurately read from.

Despite issues with quoted figures-of-merit, the noise values for encapsulated (and even unencapsulated) graphene sensors are impressive; promising the ability for smaller devices to easily beat the performance of existing Bi and InSb devices. Furthermore, there are encouraging signs that the drive current can be increased far enough to achieve a substantial reduction in B_{min} [101].It is also worth noting that some of these reported works have also not optimised B_{min} as a function of n and the drive current.

This chapter has explored the properties of graphene. As the SHPM looks to establish itself in the realm of room temperature imaging, a better Hall sensor made from graphene offer promise of reduced low frequency noise and a higher magnetic sensitivity than previously used materials. It also has highly versatile material for nanofabrication with the potential to achieve deep sub-micron spatial resolution because it is not buried beneath a surface epilayer. These last aspects could be crucial in making SHPM a highly competitive technique for room temperature microscopy.

4 Superconductivity and vortex matter

It would be no surprise that the notion of zero electrical resistance baffled the first scientists who discovered it. Still to this day, the idea that we can transport electrical power from point A to point B without losses could still be science fiction in the minds of many. Indeed, there are numerous practical challenges still to be overcome for superconductivity to become more than just another lab test subject. As will be described in this chapter, barriers such as incredibly low operating temperatures, immature material growth techniques and material brittleness limits superconducting materials for ever day usage. While this thesis certainly won't solve many of superconducting material's application challenges, the research described attempts to make vital micro-steps towards optimising superconducting tape growth, specifically, their current carrying capacity. At a more fundamental level, the research work investigates another avenue of hybrid magnetic-superconductors which could further our understanding of superconductivity and extend its range of applications. This chapter will introduce the topic of superconductivity from its first discovery through to the modern plethora of superconducting materials. The chapter then hones in on the main focus of this thesis by introducing high temperature superconductors, vortex matter and pinning as well as curious recent examples of magnetic superconductors.

4.1 Introduction to superconductivity

In 1911, Kamerlingh Onnes first found that mercury had zero resistivity below 4.2K. Repeating this for some of the other elements and alloys, he found a similar behaviour. This temperature became known as the critical temperature, T_c, which varied by material [106]. He also found that the breakdown of this zero resistivity state occurred when going beyond certain applied critical current densities, $J_c(T, H)$, and critical magnetic fields, $H_c(T)$ [107]. When the external field destroying the superconductivity was removed the superconductivity returned. This critical field, however, depended on the orientation of the field with respect to the material (usually with respect to its crystallographic axes). Likewise, the critical current density can vary vastly depending on the microscopic and structural properties. Some of these properties will be explored in further detail later in this chapter. A sketch of a typical resistance-temperature curve is shown in figure 19.

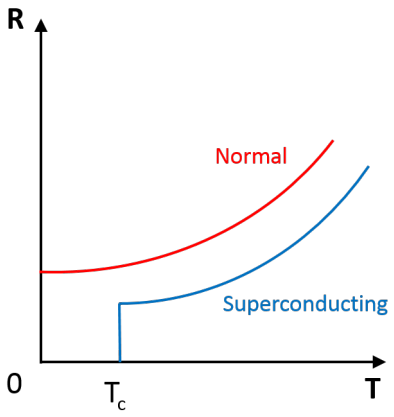

Figure 19: A simple sketch of a superconductor's resistance-temperature relationship. Below T_c, the resistance drops to zero. An example of a non-superconducting material is shown in red with no resistance drop to zero.

When $T > T_c$, these materials are in their normal state, whereby the resistivity at high temperatures increases as temperature increases due to dominant phonon scattering. At lower temperatures, scattering from the likes of impurities and lattice dislocations becomes dominant, flattening off the resistivity curve. Unfortunately, the properties of a material in its normal state give little indication as to whether it will be able to superconduct at lower temperatures. This made the search to find a microscopic theory for superconductivity a lot more challenging. Scientists would later be surprised that the complexity of superconductivity and the huge number of families of superconducting materials would lead them on a quest that is still very active to this day.

4.1.1 The Meissner effect

The zero resistance property of superconductors was not the only characteristic one. In 1933, Meissner and Ochsenfeld discovered that the magnetic flux of an applied external magnetic field ($H < H_c$) is expelled from the interior of the material below a certain temperature. This eventually became known as the Meissner effect and occurs regardless of whether the field is applied before or after the cooling the material below T_c. Within classical electromagnetism in contrast Lenz's law (the direction of an induced current is always so that it opposes the change in the magnetic field that produces it), dictates that induced currents are formed to produce a field directly opposing the external applied one, effectively dB/dT = 0 for a perfect conductor. The Meissner effect is illustrated by figure 20, where in (b) the magnetic induction is forced to distort and curve around the superconducting material. It is important to note at this stage the difference between magnetic induction, B, and the magnetic field, H. These are related by,

$$B = \mu_0 H + \mu_0 M = \mu_0(1 + \chi)H, \tag{32}$$

where μ_0 is the permeability of a vacuum, M is the magnetisation of a sample and χ is the magnetic susceptibility. The magnetisation is hence proportional to the field and

susceptibility [108].

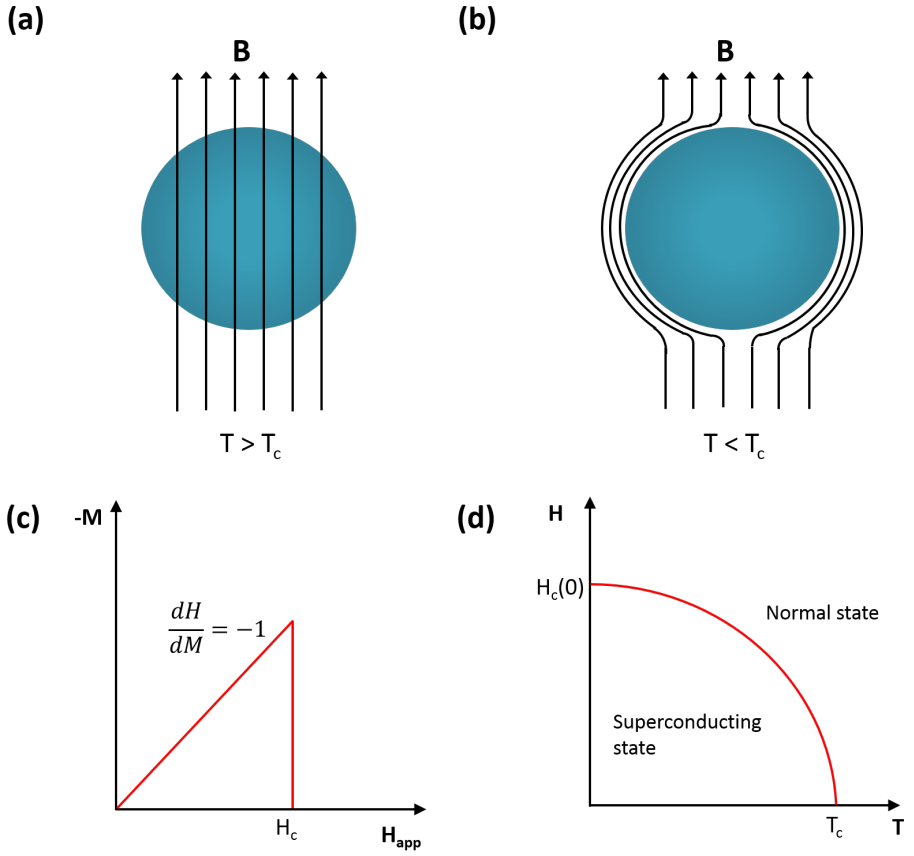

Figure 20: A sketch showing the Meissner effect in superconductors. In (a) is shown the magnetic field as it would be when the material is in its normal state, while in (b) it is shown as it would be when the material is in its superconducting state. The graph in (c) shows an example of the magnetisation behaviour of a superconducting material. The gradient of the line below H_c reflects the ideal case where M = -H. The plot (d) shows the temperature dependence of H_c.

In figure 20 (d), the temperature dependence has been plotted according to the following phenomenological approximation,

$$H_c(T) = H_c(0)\left[1 - \left(\frac{T}{T_c}\right)^2\right], \tag{33}$$

where $H_c(0)$ denotes the critical field at zero temperature. In the Meissner state, superconductors exhibit perfect diamagnetism, such that the magnetic susceptibility, $\chi = -1$, up to H = H_c. This means that our equation for the magnetic induction becomes,

$$B = \mu_0 H + \mu_0 M = 0, \tag{34}$$

and the field has been completely expelled.

4.1.2 London theory

Not long after the work by Meissner and Ochsenfeld, the London brothers introduced the superconducting penetration depth, λ_L, the length scale over which the magnetic field can vary within a superconductor, as a partial solution for the microscopic theory of superconductivity [109]. This means that the flux density at the boundary of the superconductor does not fall abruptly to zero, and instead gradually decays within the region where the screening currents flow. These currents cannot naturally be explained via Maxwell's equations and required the London brothers to seek modifications of them. Their new model was based upon there being a mix of two types of electron density; the normal part, n_n, and the superconducting part, n_s. The superconducting electron density experiences zero scattering resulting in the microscopic force equation having no dissipative term,

$$m\frac{d\nu_s}{dt} = eE. \tag{35}$$

In this equation, ν_s is the superconducting electron velocity, e is the electron charge , m is the electron mass and E is the electric field. The first London equation is then derived by substituting the modified force equation with the supercurrent density equation, $J_s = n_s e \nu_s$. This becomes,

$$E = \frac{m}{e^2 n_s}\frac{dj_s}{dt}. \tag{36}$$

This equation displays the eventual consequence of a zero resistance material with an applied electric field: constant acceleration. The second London equation is found by taking the curl of the first equation, and substituting Maxwell's 3$^{\text{rd}}$ equation

$$\nabla \times E = -\frac{\delta B}{\delta t}. \tag{37}$$

After substituting Maxwell's 4$^{\text{th}}$ equation,

$$\nabla \times B = \mu_0 J_{s]}. \tag{38}$$

this leads to,

$$-\frac{m}{\mu_0 n_s e^2}\nabla^2 \times \frac{\delta B}{\delta t} = \frac{\delta B}{\delta t}. \tag{39}$$

The London brothers then assumed that the above equation also applied to B itself, leading them to the following equation,

$$\nabla^2 B = \frac{B}{\lambda_L^2}. \tag{40}$$

The penetration depth, λ_L was defined as,

$$\lambda_L = \sqrt{\frac{m}{\mu_0 n_s e^2}}. \tag{41}$$

By considering a superconductor of infinite size in *x* and *z*, and with a superconducting/normal boundary at $y = 0$, and in an applied field in the *y* axis, equation 40 becomes,

$$\frac{\delta^2 B_z}{\delta y^2} = \frac{B_z(y)}{\lambda_L^2}. \tag{42}$$

The solution to this is,

$$B_z(y) = B_{app} \exp^{-\frac{y}{\lambda_L}} . \tag{43}$$

This essentially means that external magnetic fields decay exponentially into a superconductor over the length scale of λ_L. This is best shown via a sketch in figure 21. Typical values of the penetration depth are in the tens to hundreds of nanometeres at zero temperature.

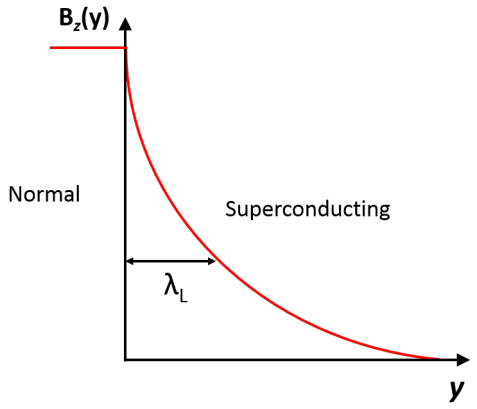

Figure 21: A sketch showing the exponential decay of an externally applied magnetic field over a length scale, λ_L into a superconductor occupying a region $y > 0$, with the normal region at $y < 0$.

From this relationship, the supercurrent can be calculated as,

$$J_s(y) = \frac{B_{app}}{\mu_0 \lambda_L} \exp^{-\frac{y}{\lambda_L}} \hat{z} . \tag{44}$$

This makes it clear that the magnetisation opposing and expelling the external field is generated by the surface layer of screening currents, showing how the London equations describe the Meissner effect. The temperature dependence of the London penetration depth is often approximated by,

$$\lambda_L = \frac{\lambda_L(0)}{\sqrt{1 - \left(\frac{T}{T_c}\right)^4}}. \tag{45}$$

However, the precise dependence of the penetration depth follow various relationships, depending on the superconducting material. This will be picked up again later in this chapter and in the results chapter 7.

4.1.3 Ginzburg-Landau theory

The London theory does not take into account the spatial variation of the superconducting charge carriers in a superconducting sample. With the discovery of materials with normal/superconducting domains near H = H_c, Ginzburg and Landau attempted to construct a mathematical model describing superconductors by considering the free energy near its

superconducting transition in terms of an order parameter, ψ, which can also be thought of as a macroscopic quantum mechanical wavefunction [110, 111]. The order parameter is used to describe the density of the superconducting electrons according to,

$$n_s = |\psi|^2 . \tag{46}$$

The superelectron density varies with temperature, dropping to zero at T_c. Near Tc, the density of superelectrons is small enough that it can be used as an expansion parameter in a Taylor series expansion of the free energy density of the system,

$$F(\psi) \approx F(\psi_0) + \frac{dF(\psi_0}{d\psi}(\psi - \psi_0) + \frac{1}{2!}\frac{d^2F(\psi_0)}{d\psi^2}(\psi - \psi_0)^2 + ..., \tag{47}$$

where $\psi_0 = \psi(T_c)$. Noting at T_c, ψ_0 is zero then the free energy at T_c is the same as that of the normal state, F_n. By ignoring higher order terms and making the following substitutions,

$$\alpha(T) = \frac{d^2F(0)}{d\psi^2}, \tag{48}$$

$$\beta(T) = \frac{d^4F(0)}{d\psi^4}, \tag{49}$$

equation 47 can be re-written as,

$$F_s = F_n + \alpha(T)\,|\psi|^2 + \frac{1}{2}\beta(T)\,|\psi|^4 . \tag{50}$$

Here, F_s is the free energy density of the superconducting state and must be a minimum at the transition point, therefore the odd powers in the expansion are removed. By equating $|\psi|^2$ with the superelectron density, n_s at temperature T is rewritten as,

$$n_s = -\frac{\alpha(T)}{\beta(T)}. \tag{51}$$

A minimum in energy below T_c can only be achieved if the sign of $\alpha(T)$ changes at the transition. Ginzburg-Landau theory can be extended via the additions of more terms. The first additional term is the kinetic energy term to account for spatial variations in the order parameter. A second term is added to account for the magnetic field energy. This yields,

$$F_s(r,T) = F_n + \alpha(T)\,|\psi|^2 + \frac{1}{2}\beta(T)\,|\psi|^4 + \frac{1}{2m^*}\,|(i\hbar\nabla - q_sA)\psi|^2 + \frac{1}{2}\mu_0H^2. \tag{52}$$

In the case of superconductivity, q_s is e^*, the effective electron mass of a Cooper pair also equal to $2e$. Hence the mass m^* is also equal to $2m$. The magnetic vector potential is given by A, described via $B = \nabla \times A$. Since the premise of Ginzburg-Landau theory is lowering of the overall system energy when undergoing a transition into the superconducting state, minimising equation 52 with respect to $\psi(r)$ and $A(r)$ is the next step. This leads to two Ginzburg-Landau equations:

$$\alpha\psi + \beta\,|\psi|^2\,\psi + \frac{1}{2m^*}(-i\hbar\nabla - e^*A)^2\psi = 0, \tag{53}$$

and

$$J_s = -\frac{ie^*\hbar}{2m^*}(\psi^*\nabla\psi - \psi\nabla\psi^2) - \frac{e^{*2}}{m^*}\psi^*\psi A. \tag{54}$$

Equation 53 describes the spatial variation of n_s while equation 54 is a quantum mechanical description of the supercurrent. The spatial variation of ψ in a superconductor is mitigated by the contribution of the condensation energy. The length scale over which ψ can vary is limited by the coherence length, $\xi_s(T)$. This can be defined using equation 53 when magnetic fields and currents are zero giving,

$$\alpha\psi + \beta\left|\psi\right|^3\psi - \frac{\hbar^2}{2m^*}\frac{d^2\psi}{dx^2} = 0, \tag{55}$$

From a dimensional analysis of this, one can define the coherence length as,

$$\xi_s = \sqrt{\frac{\hbar^2}{2m^*\left|\alpha\right|}}. \tag{56}$$

The subsequent variation of the density of superconducting charge carriers over the length scale ξ_s is shown graphically in figure 22. Upon substituting the equation for n_s as a function of α and β, into the London penetration depth equation (equation 41), one can see that both the coherence length and the penetration depth exhibit the same dependence of $|\alpha|$ which will be reflected in the same temperature dependence near T_c,

$$\lambda_L = \sqrt{\frac{m_e\beta}{2\left|\alpha\right|\mu_0 e^2}}. \tag{57}$$

The ratio of the penetration depth to the coherence length is called the GL parameter, given by,

$$\kappa = \frac{\lambda}{\xi_s}. \tag{58}$$

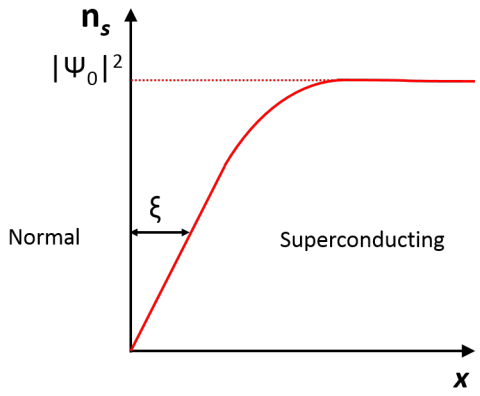

Figure 22: The variation of n_s over the coherence length, ξ_s, at a superconducting-normal interface.

The surface energy at the normal-superconducting phase interface adds an extra contribution to the free energy which is proportional to the total area of the boundary. The net interface energy per unit area is given approximately by,

$$\iota = \frac{1}{2}\mu_0 H_c^2(\xi_s - \lambda_L). \tag{59}$$

Here it becomes clear that there are two scenarios when $\lambda_L << \xi_s$ and $\lambda_L >> \xi_s$, i.e. when $\kappa < 1$ and $\kappa > 1$ respectively. This gives us two type of superconductors, type I ($\kappa < 1$) and type II ($\kappa > 1$), which will be described later.

4.1.4 BSC theory

Ginzburg-Landau theory was then taken by Bardeen-Cooper-Schieffer (BCS) to another level by describing the conduction electrons as a nearly free electron gas, bound together by an electron-phonon interaction [112]. They constructed Cooper pair states composed of bound pairs of electrons, each having spin and momentum of equal magnitude but opposite sign, on the assumption that this would be the most energetically favourable configuration for the system. One would expect a mutual repulsion within the pair, however this is overcome by the distortion of the surrounding lattice. The fast moving electrons will attract the lattice ions leaving behind a local region of higher positive charge density. This will attract a second electron which essentially becomes indirectly bound as a result its own interaction with this positive charge cloud. The electron separation in the pair is defined by a characteristic distance, the BCS coherence length.

However, so far our discussion just treats two electrons in isolation. BCS theory remedies this by constructing a many body state of Cooper pairs with different wavevectors, assuming the only interactions that matter are those within the Cooper pairs themselves. When multiple Cooper pairs are taken into account, the number of available pairing states ($\mathbf{K}\downarrow, -\mathbf{K}\uparrow$) becomes constrained. The many electron wavefuntion (ψ) was proposed by BCS as a product of many Cooper pair wavefunctions,

$$\psi(r_1, r_2..., r_n, k_1, k_2..., k_n) = \phi(r_1, r_2, k_1, k_2)\phi(r_3, r_4, k_3, k_4)...\phi(r_{n-1}, r_n, k_{n-1}, k_n). \tag{60}$$

where **r** is the position vector (*x, y, z*), k_n is the wavevector of the electron, ϕ is the wavefunction of the two particles scattering repeatedly subject to the conservation of momentum, and $n/2$ is the total number of Cooper pairs. As for a normal Schroedinger wavefunction, this gives the probability of finding one electron at r_1 at the same time as another at r_2, unconstrained by momentum. Maximising the number of pairs in equation 60 lowers the energy of the system significantly. By having all Cooper pairs in the same state with the same energy appears on the face of it to violate the Pauli exclusion principle. Hence the Cooper pairs are better thought of as composite particles, being represented by one coherent wavefunction throughout the whole superconducting material.

A key parameter of superconductors is the binding energy of the Cooper pairs (the energy required to destroy the pairing). This binding energy explained previously measured energy gaps of superconductors as well as their zero resistivity whereby Cooper pairs cannot scatter

off the lattice if the lattice phonons are below a certain threshold energy [113]. When a material is cooled below T_c, the lattice vibrations drop below this threshold, resulting in the zero resistance state.

4.1.5 Unconventional superconductors

Thus far in deriving BCS theory we have only considered a wavefunction containing the spatial component of the electron pair. A more complete picture would also be the combination of the spatial and spin components (σ), so that the wavefunction now becomes,

$$\Psi = \psi(r_1, r_2..., r_n, k_1, k_2..., k_n) \cdot \Phi(s_1, s_2..., s_n). \tag{61}$$

A Cooper pair, being thought of like a boson, can have a spin of S=0 or 1. The pair wavefunction describes the probability of finding one electron with respect to the position of the second electron of the pair, while an atomic orbital is the probability of finding an electron with respect to the nucleus. Thus making an analogy with atomic orbitals, a BCS ground state with a net zero angular momentum would be termed an s-wave (l=0). In this case, the s-orbital is spatially symmetric meaning that the spin component of the wave function should be anti-symmetric such that we have anti-parallel spins making S=0 (spin-singlets). This pairing is what defines conventional superconductors.

By now considering other odd (l=1,3,...) and even (l=0,2,...) angular momenta we see that we can form more spin-singlet and also spin-triplet (S=1) states. The 2D real space distributions of the bound states of l=1 to 3 are shown in figure 23. As one can see, the probability densities at the origin of non-zero angular momenta are zero. AAs previously described, the strong electron-electron repulsion is overcome by electron-phonon coupling in BCS theory, but in non s-wave materials the electronic interactions still play a role. This is what leads to $l > 0$ materials being called unconventional superconductors, as the role the electron-electron interactions is important and still not fully understood (and because these were discovered later than s-wave superconductors).

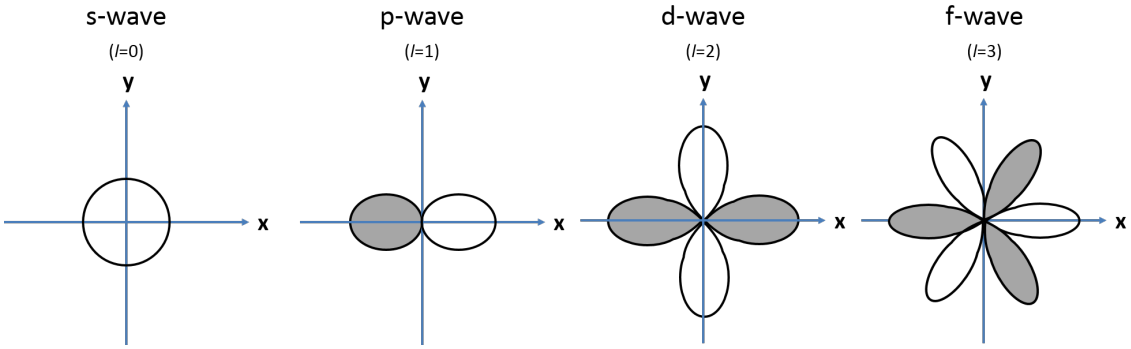

Figure 23: A sketch of the 2D real space distributions of the microscopic Cooper pair wavefunctions. The unshaded and shaded areas denote different signs of the wavefunction.

4.1.6 Type-I and Type-II superconductors

So far in this chapter, superconductors have been described as having just a superconducting and a normal state. However, in reality many superconductors do not behave like this. Superconductors can be split into two families, type-I superconductors and type-II superconductors. Type-II superconductors are particularly important since nearly all technologically important materials, including all known high temperature superconductors (HTS), are type-II superconductors.

In type I superconductors, supercurrents only flow at the surface, and their superconductivity is quickly destroyed under weak fields. Type-I superconductors without demagnetising effects are as described in section 4.1.1, where they enter a Meissner state up until a critical field H_c. Type-II superconductors, on the other hand, exhibit two states with two distinct critical fields, the lower critical field, H_{c1}, and the upper critical field H_{c2}. When below H_{c1}, the superconductor is in the Meissner state, and when above H_{c2} the superconductor returns to the normal state. In between the two critical fields ($H_{c1} < H < H_{c2}$), the superconductor enters a mixed state, where it contains an array of non-superconducting vortex cores. This is sketched in figure 24 as well as figure 25 where the temperature-dependent magnetisation is shown. Type-II superconductors are usually compounds, unlike type-I superconductors which are usually pure metals. Furthermore, for type-I superconductors typically $\lambda_L << \xi_s$ and for a type-II superconductor typically $\lambda_L >> \xi_s$. The precise crossover was determined to be $\kappa = 1/\sqrt{2}$ [114]. This means that the Ginzburg-Landau parameter (c.f. equation 58) can be used to indicate which type a superconductor is. When $\kappa < 1/\sqrt{2}$ superconductivity comes to a more abrupt end (as is reflected by the short penetration depth) while for the case of $\kappa > 1/\sqrt{2}$, the superconducting/normal interface lowers the overall system energy. For fields applied up to H_{c2}, the superconducting-normal area is maximised by the nucleation of an increasing number of quantised flux tubes. These penetrate the sample at certain sites to lower the magnetostatic energy, allowing superconductivity to survive to much higher fields compared to type-I superconductors. The normal cores are then surrounded by circulating supercurrents that shield the magnetic field. This brings us to the next subsection of this chapter where we discuss vortex matter in greater detail and explain how studying vortex matter is key to understanding the high current properties of superconducting materials.

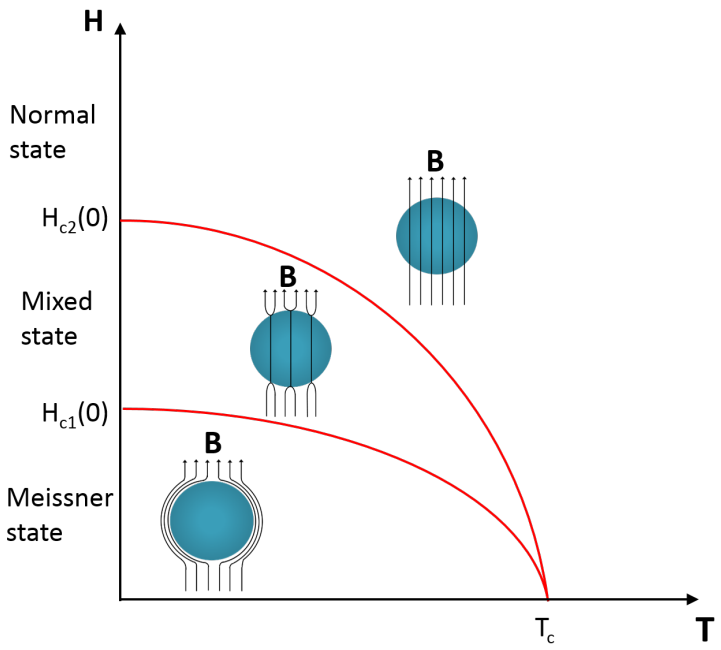

Figure 24: A sketch showing the temperature dependence of the two critical fields along with a diagram of the field distribution in each case.

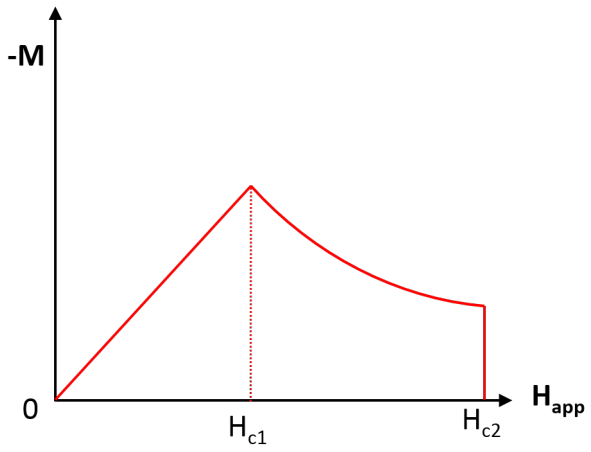

Figure 25: A sketch showing the temperature-dependent magnetisation of a type-II superconductor.

4.2 Vortex matter and vortex pinning

Before delving into vortex matter and vortex pinning it is first necessary to understand flux quantisation, something that was touched upon in the previous section. Vortices are often located on non-superconducting regions arising from extrinsic effects such as crystal

impurities, defects or intrinsic geometric effects such as strong demagnetisation factors. A vortex along with its vortical current is shown in figure 26.

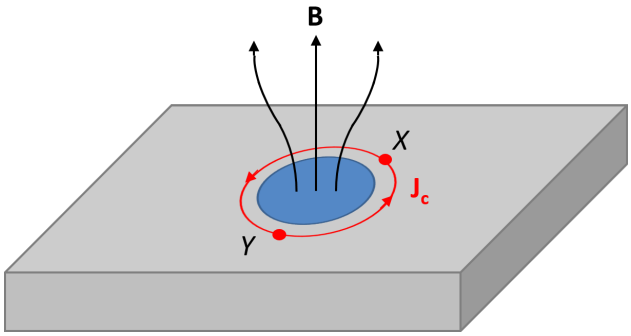

Figure 26: A sketch of a normal region in a superconducting sample. The vortex core is shown by the blue region along with the supercurrent in red. The resultant field is shown by the black arrows.

The vortical currents are represented by the following form of the order parameter,

$$\psi = |\psi| \exp^{\frac{i(P\cdot r)}{\hbar}}. \tag{62}$$

Inserting this into the second Ginzburg-Landau equation, simplifying, and assuming H=0, one can describe the vortical current as,

$$J_s = \frac{q_s P}{m_s} n_s, \tag{63}$$

where where P is the canonical momentum, $P = \hbar\nabla\phi(r)$. Between two points, *X* and *Y*, a closed loop of current will have a phase difference, $\Delta\phi$. In the presence of a magnetic field one has to add an extra component to the phase difference via the vector potential, A, where $B = \nabla \times A$. Upon substitution from equation 63 , this results in a phase difference between two points of,

$$\Delta\phi(X,Y) = \frac{m_s}{\hbar n_s q_s}\int_x^Y J_s \cdot dl. + \frac{q_s}{\hbar}\int_x^Y A \cdot dl \tag{64}$$

Due to the single value nature of quantum mechanical order parameter in Ginzburg-Landau theory, the overall phase difference must always be an integer multiple of 2π. Here *l* is an infinitesimally short section of the current path between *X* and *Y*. Thus the phase difference around the entire loop is

$$\Delta\phi = \frac{m_s}{\hbar n_s q_s}\oint J_s \cdot dl. + \frac{q_s}{\hbar}\oint A \cdot dl = n \cdot 2\pi. \tag{65}$$

By then using Stoke's theorem and the fact that the surface integral $B \cdot dS$ is equal to the total flux enclosed, one obtains the fluxoid quantisation condition,

$$\Phi = n\Phi_0 - \frac{m_s}{n_s q_s^2}\oint J_s \cdot dl, \tag{66}$$

where the flux quantum is $\Phi_0 = h/q_s$. By assuming that as one moves further away from the vortex core, the super current density reduces to zero we achieve true flux quantisation. Hence,

$$\Phi = n\Phi_0. \tag{67}$$

4.2.1 Vortices in type-II superconductors

One can show that the critical fields of a type-II superconductor depend on the penetration depth and coherence length according to,

$$H_{c1} = \frac{\Phi_0}{4\pi\lambda_L^2}, \tag{68}$$

and,

$$H_{c2} = \frac{\Phi_0}{4\pi\xi_s^2}. \tag{69}$$

When multiple vortices are close to one another, the supercurrents of one flow past the core of another, causing a repulsive Lorentz force. In 1957, Abrikosov demonstrated using Ginzburg-Landau theory that in an ideal type-II superconducting sample, the vortex lattice should form a square structure, as this is expected to have the lowest energy. This was eventually confirmed using the Bitter decoration method [114, 19]. Abrikosov actually got this initial prediction wrong, it turns out that it forms a triangular lattice. This triangular Abrikosov vortex lattice is shown in figure 27 (a) while the microscopic structure of a vortex core can be seen in (b).

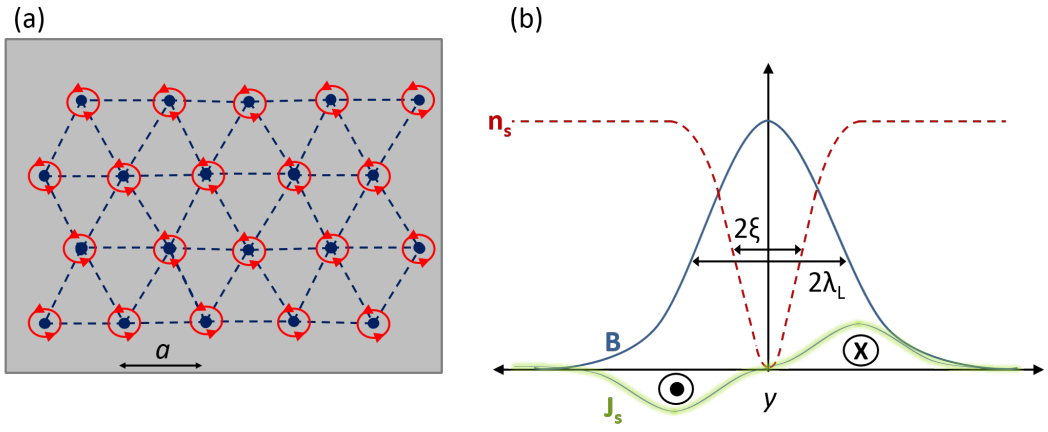

Figure 27: (a): An Abrikosov vortex lattice with lattice spacing denoted by a. (b): Sketch of the microscopic structure of a vortex.

The lattice parameter, a, is determined via,

$$a = \sqrt{\frac{\sqrt{3}\Phi_0}{2B}}. \tag{70}$$

From this it is clear that the number of vortices increases and their spacing decreases with increasing applied field until the upper critical field is reached. Generally the lowest energy state is when each vortex core contains one single flux quantum, Φ_0. Each vortex core contains one flux quantum as it is energetically favourable if the superconductor generates a superconductor/normal conductor interface above the lower critical magnetic field. This is achieved when the smallest quantum state is reached, this being plus or minus 1.

The London description of a vortex is not physically accurate since it has no analogue of the coherence length, causing the field and the supercurrent density to become singular at the vortex core. J. R. Clem proposed his own more realistic Ginzburg-Landau model based on the introduction of a variational coherence length [115]. Here Clem assumed a trial function for the magnitude of the normalised order parameter with the form,

$$f^{Clem} = \left(\frac{\rho}{R}\right)^{1/2}, \tag{71}$$

where ρ is the radial co-ordinate, $R = (\rho^2 + \xi_\nu^2)$ and ξ_ν is the variational coherence length [115]. Solving Ampere's law and the second Ginzburg-Landau equation, Clem obtained new bounded expressions for the magnetic flux density and the supercurrent density,

$$B^{Clem} = \frac{\phi_0}{2\pi\lambda\xi_\nu}\frac{K_0\left(\frac{R}{\lambda}\right)}{K_1\left(\frac{\xi_\nu}{\lambda}\right)}, \tag{72}$$

and

$$J_s^{Clem} = \frac{\phi_0}{8\pi^2\lambda^2\xi_\nu}\frac{\rho}{R}\frac{K_1\left(\frac{R}{\lambda}\right)}{K_1\left(\frac{\xi_\nu}{\lambda}\right)}, \tag{73}$$

where $K_n(x)$ is a modified Bessel function [115]. This function is later used to quantitatively fit imaged vortex profiles to obtain values of the penetration depth and superfluid density.

4.2.2 Vortex motion and pinning

In an ideal type-II superconductor, vortices will move in response to the Lorentz force arising from transport currents. In practice, however, type-II superconductors contain many defects, impurities, second phases, grain boundaries and dislocations which act as pinning centres for the vortices. These restrain the vortices and oppose the Lorentz force. Their role is crucial in applications of high temperature superconductors as pinning maintains high critical current densities. If this were not the case vortices would they dissipate energy (e.g., due to eddy currents in the normal cores) as they move, causing finite resistance and dissipation. Hence, for high Jc applications, the density and the size of the pinning sites need to be optimised. Usually, the optimum size is when the the defect dimension is of the same order as the vortex core. If the defect is smaller than the coherence length, the core may spread out over several defect sites, averaging their effect and reducing the pinning force. Pinning forces can be understood by carefully analysing the motion resulting from the Lorentz force. The current-induced Lorentz force per unit length on a flux line is given by,

$$F_p = J \times \Phi_0, \tag{74}$$

A resistance is then generated due to the motion of the vortex via,

$$E = B\Phi_0 J/\eta, \tag{75}$$

where η is the vortex viscosity. One can now see that at the critical current density, the Lorentz force will exceed the pinning force and vortices will start to move. The maximum possible supercurrent density, or better called the pair breaking critical current density, can be determined by analysing the relationship between the supercurrent density and Cooper pair velocity,

$$\nu_s = \frac{J_s}{n_s q_s} = \frac{J_s}{|\psi|^2 q_s}. \tag{76}$$

Comparing this with the following result that can be derived from the Ginzburg-Landau equations (52 and 54),

$$\nu_s = \frac{1}{m_s}(\hbar\nabla\phi - q_s A), \tag{77}$$

and rewriting the kinetic energy term with ν_s eventually yields a simpler form of equation 52,

$$F_s = F_n + \alpha\,|\psi|^2 + \frac{1}{2}\beta(T)\,|\psi|^4 + \frac{1}{2m_s}\nu_s^2\,|\psi|^2 + \frac{1}{2}\mu_0 H^2. \tag{78}$$

Substituting for n_s using equation 46 and minimising with respect to n_s one obtains an expression for the supercurrent density in terms of ν_s,

$$J_s = q_s\left(\frac{|\alpha| - \frac{1}{2}m_s\nu_s^2}{\beta}\right)\nu_s. \tag{79}$$

Finding when it is maximum (i.e. when $\frac{dJ_s}{d\nu_s} = 0$) yields the critical current density J_c,

$$J_c = q_s\frac{2\,|\alpha|}{3\beta}\left(\frac{2\,|\alpha|}{3m_s}\right)^{1/2}. \tag{80}$$

However, the pair breaking critical current only applies in type I superconductors without vortices. In principle, perfect, defect free type II superconductor should not be able carry any supercurrent at all, i.e., J_c=0. However, in real materials with pinning the minimum force per unit length required to 'depin' a vortex is,

$$F_p = J_c \times \Phi_0. \tag{81}$$

The overall dependence on current density is well illustrated by the sketch shown in figure 28.

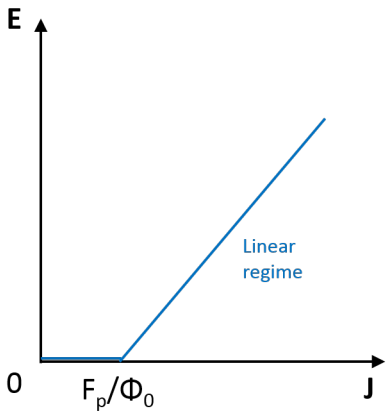

Figure 28: Sketch of voltage versus current density for a type II superconductor showing the linear 'flux-flow' regime once the pinning force is exceeded by the Lorentz force.

From an energy perspective, each vortex has an energy, ϵ, per unit length given by,

$$\epsilon = \ln(\lambda_L/\xi_s)(\phi_0/4\pi\lambda_L)^2, \tag{82}$$

The presence of pinning sites reduce the overall vortex energy, such that vortices become pinned in the bottom of these potential energy wells.

Even if $J < J_c$, vortices are still subject to thermal fluctuations that can cause them to jump out of and between pinning sites, also called flux creep, which leads to finite dissipation. Hence, even when the Lorentz force is smaller than the pinning force, a vortex can still be driven into a motion. This can be explained via the vortex viscosity that opposes the force once the Lorentz force exceeds the pinning force.

$$F_\eta = \eta\nu_v = F_L - F_p. \tag{83}$$

Making further substitutions,

$$\nu_v = (J - J_c) \times \frac{\phi_0}{\eta}, \tag{84}$$

where η is the vortex viscosity. This flux flow effect is also responsible for the time relaxation of persistent currents flowing around a superconducting loop. P.W. Anderson devised a theory for flux creep in type II superconductors by considering the flux motion as a thermally activated process [116]. When there is no force applied on the system (i.e. $J = 0$), the forward vortex jump rate in one direction, P_{jump}, can be characterised using a barrier height U_0 via,

$$P_{jump} = \exp^{\left(\frac{U_0}{K_B T}\right)}, \tag{85}$$

where k_B is the Boltzmann constant. The probability of moving in all directions is the same, hence $< P >= 0$. However in the presence of a force, this 'tilts' the energy landscape such that there is a change in barrier height in different directions from the action, fx_{jump},

$$P^{net}_{jump} \propto \exp^{-\left(\frac{U_0 - fx_{jump}}{K_B T}\right)} - \exp^{-\left(\frac{U_0 + fx_{jump}}{K_B T}\right)}. \tag{86}$$

One can then estimate the induced electric field as,

$$E \propto x_{jump} B \exp^{\left(\frac{U_0}{K_B T}\right)} sinh\left(\frac{U_0}{K_B T}\frac{J}{J_c}\right), \tag{87}$$

where B is the internal magnetic field. Thus we see that there is an additional flux creep regime when $J \approx J_c$ in a V-J relationship which is shown in figure 29.

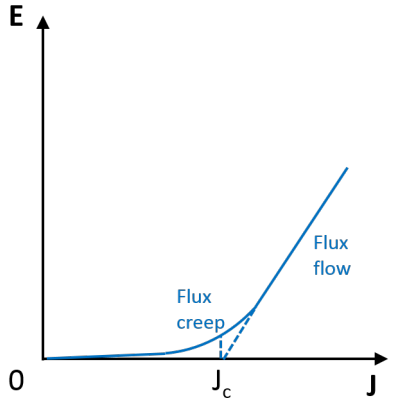

Figure 29: A sketch of the E-J relationship when now considering thermally activated flux creep in addition to flux flow.

In samples with strong pinning, magnetization is typically irreversible as the flux entry and exit into a sample of finite size is delayed and flux is trapped even at $H = 0$ (giving rise to a finite remnant magnetisation, $\pm M_{rem}$ is non zero at $H = 0$). By assuming,

$$J_c = \frac{1}{\mu_0}\nabla \times B, \tag{88}$$

and in a slab-shaped sample with the field applied perpendicular to the transport current and the direction of flux density gradients we derive

$$\frac{dB}{dx} = -\mu_0 J_c, \tag{89}$$

We see that the magnetic induction always has a constant slope in a region of constant critical current. The effect of this is best illustrated by the sketch shown in figure 30.

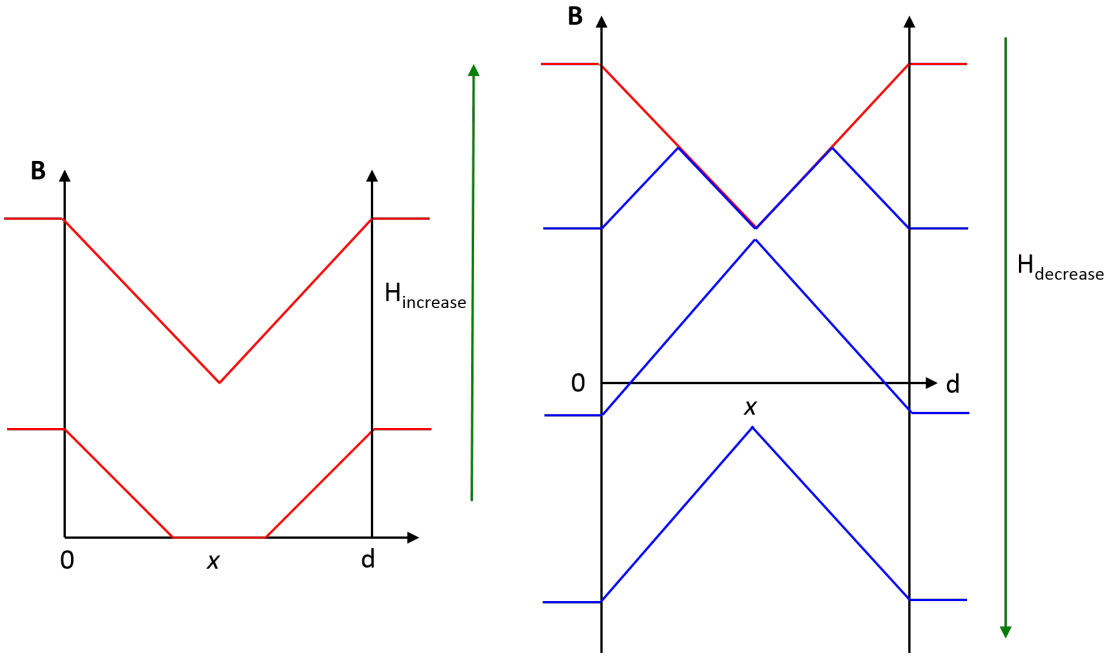

Figure 30: Sketch of flux entry (left) and flux exit (right) in a superconductor with strong pinning. Slopes are equal to $\pm\mu_0 J_c$ while outside the central superconducting region the horizontal lines are drawn at $\mu_0 H$.

This model, known as the Bean critical state model, can in principle also be used to estimate the critical current density for an infinitely long cylinder,

$$J_c = \frac{3\Delta M}{2R}, \tag{90}$$

where R is the cylinder radius and ΔM is the height of the saturated $M - H$ magnetisation loop [117]. When taking images of finite size superconductors it is hence important to consider the cooling history and edge effects on the field profiles. Research on vortex pinning has become a huge field within the superconducting and materials growth community. Hence the effectiveness of different vortex pinning configurations will be explored in further detail later in this chapter in the context of maximising J_c in high temperature superconducting tapes.

4.3 High temperature superconductors (HTS)

A plethora of HTS materials have been discovered and can generally be split into different families, some having already found a variety of applications such as magnetic resonance imaging machines, magnetic levitation train tracks, thin film electronic devices (sensors etc), and energy transportation and storage [118]. While there are other superconductors with higher critical temperatures such as hydrogen sulfide with a T_c of 203K, these only have high critical temperatures under very high pressures which is beyond the scope of this thesis, hence will not be discussed further here [119]. Magnesium diboride (MgB_2) is a

relatively cheap HTS material that is easy to work with and has a T_c of 39K [120]. The most recently discovered HTS materials family is the iron pnictide or Fe-based superconductors [121], currently claiming to reach critical temperatures up to the 109K in FeSe [122]. The family of main focus in this thesis is the cuprate family, with a T_c reaching up up to 133K in a mercury-based structure (which would allow lossless energy transportation if living at night time on the moon!) [123]. The most commonly studied cuprates are $YBa_2Cu_3O_{7-x}$ (YBCO) and $Bi_2Sr_2Ca_{n-1}Cu_nO_{2n+4+x}$ (BSSCO), however, a lesser well known one used in tapes manufactured by SuNaM is $GdBa_2Cu_3O_{7-y}$ (GdBCO) with a T_c of around 94K [8, 124]. This subsection covers the basics of HTS materials with a particular orientation towards HTS material applications for HTS tapes – that is large scale manufactured HTS materials for high current applications (e.g. power and magnet applications). A timeline of the discovery of superconducting (including HTS) materials is shown in figure 31.

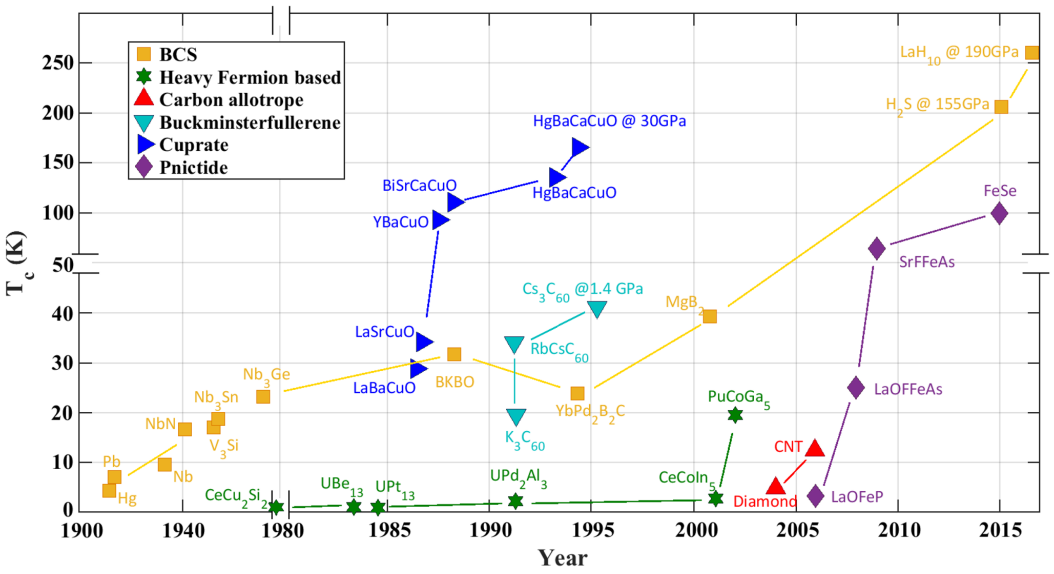

Figure 31: Timeline of the discovery of key superconducting materials and their critical temperatures since the first demonstration of the phenomena in 1911 [125].

4.3.1 Structure of HTS materials

The cuprate superconductors (including GBCO) have crystal structures very similar to the perovskite materials with orthorhombic symmetry, the structure of the unit cell of GBCO, which was determined from X-ray diffraction measurements, is shown in figure 32 which was determined through X-ray diffraction measurements [126]. The structure is comprised of a succession of CuO_2 planes lying normal to the c axis, which contain mobile charge carriers where the supercurrents flow. Thus, cuprates have high electrical conductivity in the CuO_2 planes, while normal to these planes it is very poor, resulting in high anisotropy. The physical properties are hence highly two dimensional. These are then separated by CuO and Gd/Ba-containing layers which act as charge reservoirs. A further intriguing property of YBCO-type ceramics is that the vortex structure will depend intimately on the orientation

of the magnetic field with respect to the layered structures, having a pronounced impact on the superconducting properties [127].

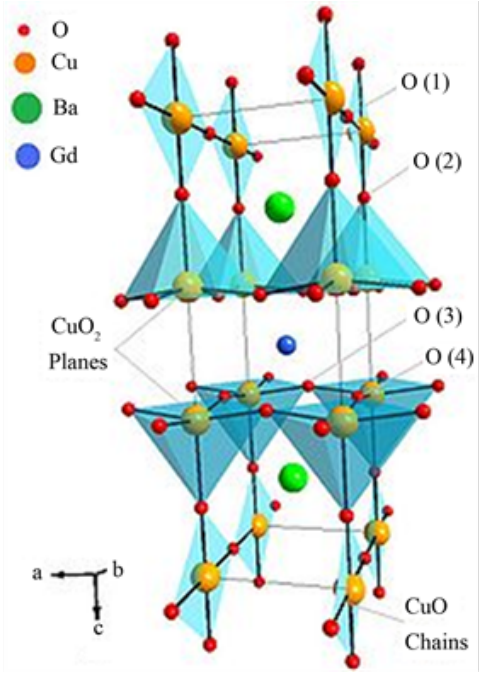

Figure 32: The unit cell structure of GBCO as determined from X-ray diffraction measurements [126].

Despite over 30 years since its discovery, a good understanding of high temperature superconductivity remains elusive. Trends as a function of pressure and chemical composition were rapidly found dues to altering the doping fraction [128]. The large crystalline anisotropy also results in anisotropy in the vortices and screening currents that depends on the relative orientation of the applied external magnetic field. Magnetic fields in the H_{ab} plane tend to produce a highly elongated rhombic lattice of 'Josephson' vortices typically centered in the normal spaces between the CuO_2 planes. Magnetic fields along the c-axis produce the typical Abrikosov vortex lattice. Although, some cuprates, such as those based on bismuth and mercury, have their vortices 'broken down' into pancake vortices, usually when the CuO_2 planes have a separation greater than $2\xi_s$. This results in a more 2D model of the flux lines being required rather than a 3D one. This also has an effect on the measured values of ξ_s and λ. In the case of tilted fields, both in-plane and out-of-plane vortex forms coexist. Tuning the lattice structure is possible by carefully altering the fields in the c- and ab-planes, as shown by P. J. Curran et al. in figure 33 where a variety of lattice structures was obtained [129].

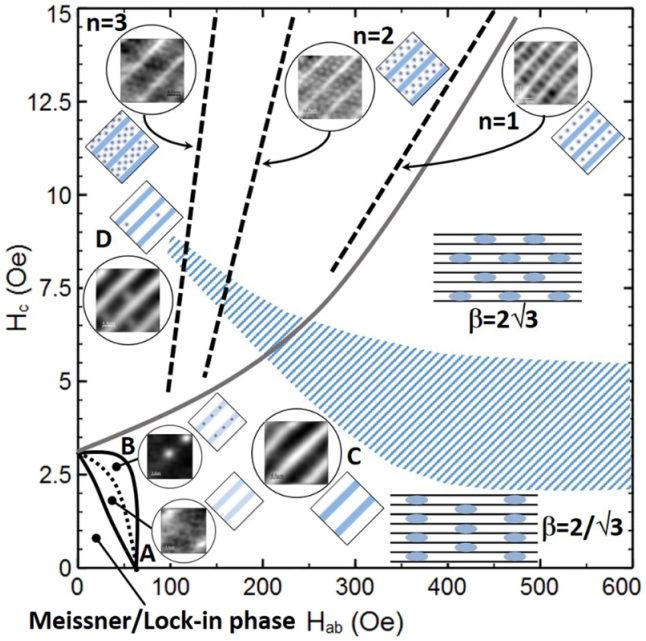

Figure 33: Phase diagram of the composite vortex lattice with applied field component, H_{ab}, on the horizontal axis and applied field component, H_c, on the y axis. Insets of SHPM images and sketches can be seen for specific field parameter at T=85K [129].

4.3.2 HTS tape fabrication

Despite the fact that the subject of this thesis is not the growth/fabrication of HTS tapes, it is important to gain insight into the possibilities and limitations of current HTS materials and how this affects the current methods of optimising J_c of these tapes. Hence a basic overview will be given in this subsection on the growth and fabrication of HTS tapes. In this case GBCO will once again be the focus.

The most recent development in superconducting applications is that of 2^{nd} generation high temperature superconducting tapes (2G-HTS). These are more often grown epitaxially on a structure of supporting layers, as opposed to first generation wires which were usually Bi-2223-based systems made via a 'powder-in-tube' method. This technique has allowed the use of YBCO, which can retain its higher current-carrying ability in larger magnetic fields than its cousin; BSSCO [130, 131].

2G-HTS tapes are grown by several major manufacturers including; AMSC, SuperOx, Bruker, SuNaM, Shanghai superconductor and Fujikura. Each has their own unique method of fabricating them on a large scale. The technique used is important, not just from a scalable production and competitive cost perspective, but studies have suggested that the fabrication process and the substrates used play an important role in the pinning mechanism/structure, and hence, on J_c [132]. Various methods such as pulsed laser deposition (PLD), metal organic deposition (MOD), metal organic chemical vapor deposition

(MOCVD) and reactive co-evaporation by cyclic deposition and reaction (RCECDR) are being utilised. SuNaM employ a reactive co-evaporation by deposition and reaction (RCE-DR) approach for the growth of the GBCO layer in their tapes, which provides them with a very high J_c of more than $4MA/cm^2$ at 77K under self-field conditions [8]. The precise structure of these tapes is shown in figure 34. Pinning can be controlled during the growth process by altering the growth material composition. In SuNaM tapes the optimum balance between Gd_2O_3, BaO and Cu_xO leads to what is currently thought to be the optimum pinning via measurements of J_c [8]. SuNaM attribute this to the concentration of Gd_2O_3 secondary phases, pO_2 composition and nanoparticle size [133]. The top protective layer of pure Ag makes it much easier to expose the GBCO layer for experimental studies, compared to other tapes which uses a multi-compound solder between the superconducting layer and protective layer.

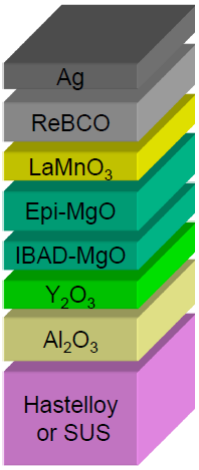

Figure 34: Schematic diagram of a SuNaM GBCO tape with all layers indicated. Fabrication is usually performed from bottom to top via various steps [8].

4.3.3 HTS vortex matter

The properties of vortex matter can change depending on the conditions imposed on the material, such as temperature and externally applied magnetic field. In type-II superconductors such as the cuprates, this allows vortices to undergo phase transitions between thermodynamic states. These are typically induced by vortex-vortex interactions, thermal fluctuations, anisotropic behaviour and system disorder [127]. In an HTS superconductor there are two distinct states, one which is the magnetically irreversible zero-resistance solid vortex phase and another reversible liquid phase with dissipative currents [127]. In a perfect superconducting crystal, the solid phase is where an Abrikosov lattice forms, sparser than the liquid state, and separated by a melting line from the liquid state. In HTS materials, the vortex lattice will melt when the mean displacement from thermal fluctuations is on the order of the lattice constant a such that: $\xi_s < r_{dp}(T) < a$, where r_{dp} is the characteristic length of the disorder potential. At the melting temperature this takes the form $r_{dp} \approx \langle u^2 \rangle_{th}^{1/2}$, where $\langle u^2 \rangle_{th}^{1/2}$ denotes the mean thermal displacement of an individual

vortex. In a vortex liquid the vortex tubes fluctuate so that they average out the effect of the disorder potential; meaning that the liquid cannot be pinned. This makes the liquid phase highly non-ideal for HTS applications. The irreversibility line, as shown in figure 35, can be shifted by optimising the type and density of defects in the system. In the ideal case, this line should be brought as close as possible to H_{c2} since the dissipationless regime is desired [127].

Further glassy states have also been suggested to exist at low temperatures. In a material with weak and random disorder points, defects like oxygen vacancies and electron irradiation produce a vortex glass. A Bose glass on the other hand is formed when a material has correlated disorder, e.g. columnar defects due to heavy ion irradiation and 2D planar defects [127]. The characteristics of a vortex glass state that make them 'glassy' is their finite-temperature freezing transition where the relaxation times extend to macroscopic time scales. The primary feature of the vortex-glass phase is the quenching of the dynamical degrees of freedom into a specific state. This means that the vortices become immobile and the resistivity at vanishing driving force is zero, essentially ticking the box of a 'true' superconductor.

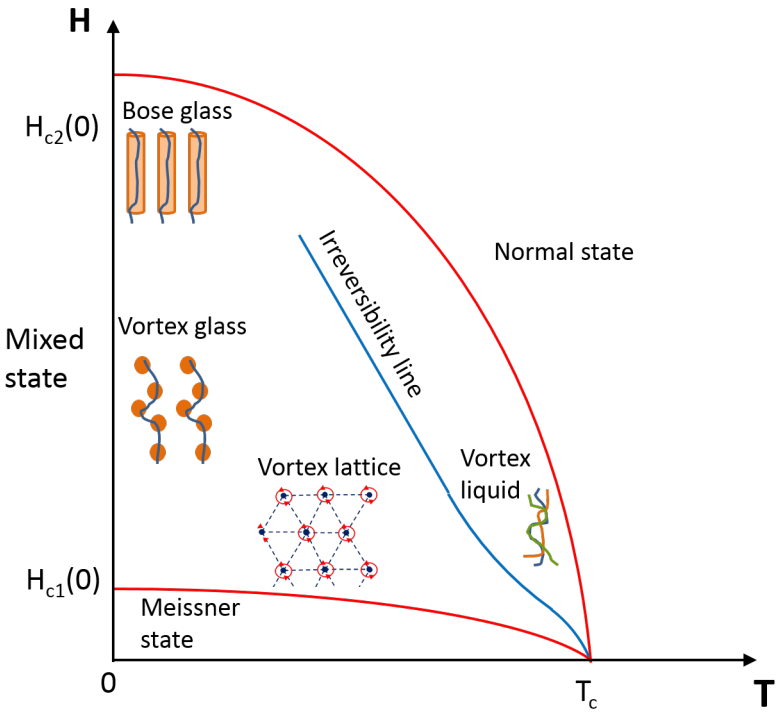

Figure 35: Sketch of the typical vortex H-T phase diagram in cuprate superconductors.

4.3.4 Vortex pinning in HTS tapes

Maximising the current-carrying capacity of tapes/wires means increasing the critical current density, J_c. As previously explored, this is ultimately limited theoretically by carrier-pair dissociation at very high values of current density (the maximum theoretical current density any superconductor could ever carry). The critical current density in this section is the vortex-based critical current, which is typically several orders of magnitude smaller than the depairing critical current density and is based on different criterion discussed. Here we will discuss some of these criterion that the type-II HTS superconductors are affected by. The reason for focusing specifically on I_c and not broadly the current carrying capacity is because by increasing film thickness, J_c is actually found to decrease. Hence, up to now HTS tape superconducting layers have been kept around about $2\mu m$ in thickness [130]. Currently experimentally measured values of J_c are still far below the pair-breaking limit [134]. This can be attributed to a variety of reasons including: cracks and voids in the crystal, thickness inhomogeneity, poor grain stitching during growth (grain orientation angle) and (often by extension), the movement of vortices [135].

Factors that a manufacturer of tapes may want to consider in terms of tape engineering are: the pinning energy of the sites and their size, shape and density. The pinning force is dependent not only on the size and shape, but also on the composition and interaction with the rest of the material. The cumulative effect of adding multiple pinning sites can also be difficult to model, generally one notes a trend whereby J_c increases until a certain density, past which J_c will decrease. There are a very wide variety of defects that can be used for vortex pinning, and each type has its own subset of properties to play with. Defects which can be used to improve (or potentially hinder) the performance of the tapes, include: Irradiation for nano-sized defects, changing the density of dislocations, surface deformation, impurities distributed in the bulk of the superconductor and rare-earth substitution [130]. It has also been suggested that local ionic magnetic moments may affect the pinning mechanism [136]. With the impact of pinning on J_c, studying the effects of pinning sites is possibly the single most important factor in developing HTS tapes for applications. The various different types of defects for pinning is well summarised visually by S. R. Foltyn in the sketch 36 [130]. Pinning sites that have been artificially introduced into a superconductor are often known as artificial pinning centers (APCs). Sadly, because of the overall effect and interplay between the many types of defects, it is almost futile to precisely predict F_p and hence J_c of any postulated system. Hence one relies heavily upon experimental experience in cataloguing the effects of the various pinning centers.

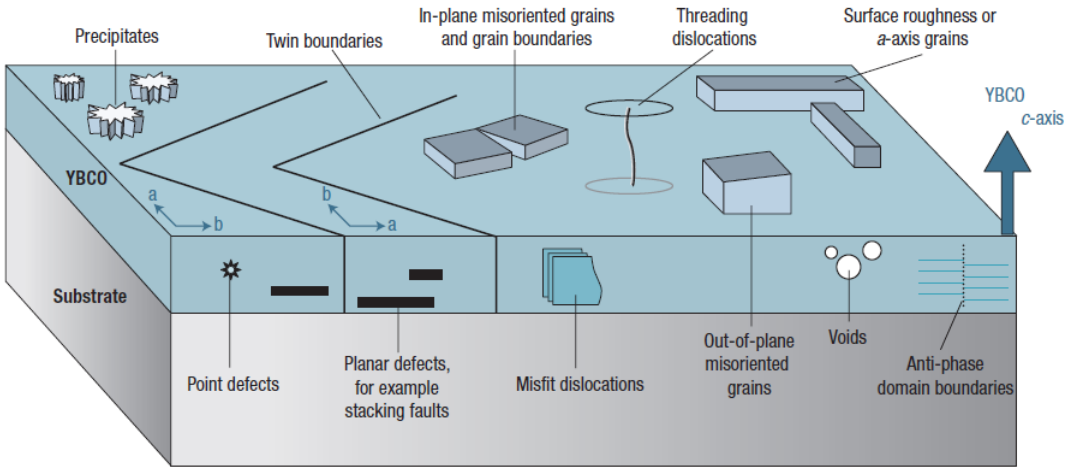

Figure 36: Sketch of the typical defects responsible for pinning in cuprate superconductors, usually anything that locally supresses the order parameter on a scale of 0.1-1nm is an ideal candidate [130].

There are different possible types of vortex pinning centers in a superconductor which depend on the origin of pinning and the conditions the superconductor is exposed to. One can sort pinning centers by their dimensionality. Zero dimensional pinning sites are usually aforementioned oxygen vacancies or point defects (defects usually smaller than ξ_s^3). Dislocations or columnar defects are known as one dimensional centres, grain boundaries as two dimensional ones and nanoparticles or local straining as three dimensional ones. Figure 37 illustrates this pinning center dimensionality. Pinning centers also have anisotropy or isotropy, whose impact then depends on the orientation of the applied field. Local strains, oxygen vacancies and nanoparticles usually behave equally in all field directions, but, dislocations or grain boundaries can be very anisotropic.

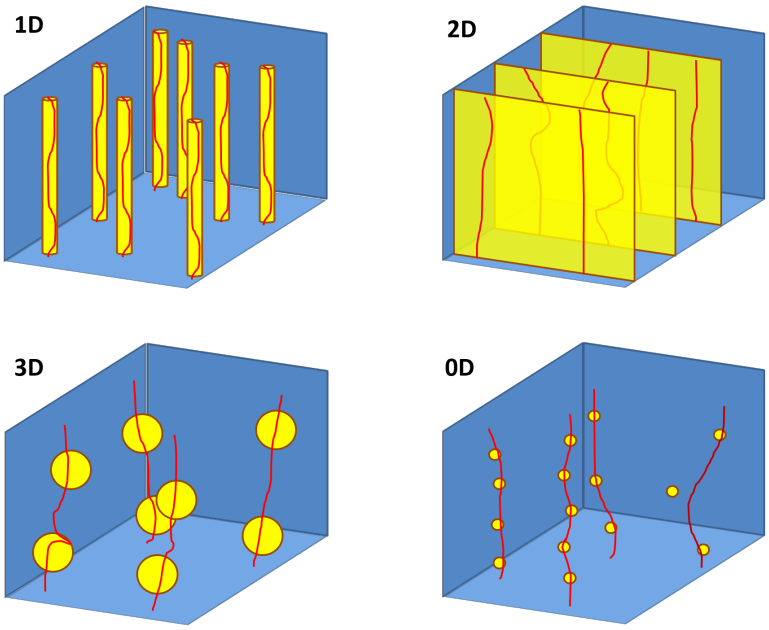

Figure 37: Schematic representation of the dimensionality of different pinning centers.

Pinning centers can also be characterised into weak and strong pinning centers. These can be evaluated via the temperature dependence of J_c. For weak pinning sites such as oxygen vacancies the weak collective pinning model predicts the following expression [127],

$$J_c^{weak}(T) = J_c^{weak}(0)\exp^{-\frac{T}{T_{weak}}}, \tag{91}$$

where $J_c^{weak}(0)$ is the weak pinning contribution at T=0K and T_{weak} is the vortex pinning energy of such defects measured in Kelvin. On the other hand, for a strong pinning site, the model proposes [137],

$$J_c^{strong}(T) = J_c^{strong}(0)\exp^{-3\left(\frac{T}{T_{strong}}\right)^2}, \tag{92}$$

where, $J_c^{strong}(0)$ is the strong pinning contribution at T=0K and T_{strong} is the vortex pinning energy of such defects measured in Kelvin. The subtle differences between them shows that strong pinning centers are more effective at high temperatures. This presents us with a 'pinning-type' phase diagram. The most prominent type of strong pinning to date is pinning by columnar defects as they have been shown to work the most effectively under high temperature and low field conditions [127]. However at low temperatures and high fields, thermal effects are at their lowest, meaning that even weak pinning centers are 'active'. This leads to a different pinning regime to that at high temperature and low fields where we see a shift from a columnar regime to a more isotropic smaller 'point-like' regime. In between high and low fields and temperatures, the regime becomes mixed since weak pinning centers become 'inactive' if the temperature is too high, while the field is too high for one vortex to occupy a single pinning site. Assuming the presence of both pinning types - anisotropic columnar and isotropic three dimensional defects - the pinning regime

becomes a superposition of both of these. Here, the vortex energy is better minimised due to the lower activation energy path the interspersed three dimensional defects provide for vortices moving between columnar defects [138].

4.3.5 Magnetic superconductors: the effect of local magnetism on superconductivity

New discoveries are constantly adding to the growing wealth of fascinating phenomena in high T_c materials discovered are not the only ones of interest. Superconductors with a magnetic transition above or below a superconducting transition are very rare since, in principle ferromagnetism should destroy superconductivity. Recalling the fact that Cooper pairs generally have opposite spins in a spin-singlet pair, this would generally be incompatible with the spin alignment characteristic of the ferromagnetic state. Despite this, some scientists thought it would be a good idea to search for some form of coexistence, e.g., work on $ErRh_4B_4$ by W. A. Fertig. Fertig discovered a material with a superconducting transition temperature, only to see it return to the normal state at a lower temperature. This was explained by the long-range ordering of the magnetic moments of the Er^{3+} ions at low temperatures [139]. Since then, other materials were discovered which exhibited a similar behaviour [140]. It was well known before this that rare earth (RE) impurities that exhibit ferromagnetic exchange interactions drastically affected the superconducting properties when embedded in a host superconductor, usually by reducing T_c [140]. Abrikosov–Gor'kov (AG) theory attempts to describe this in terms of a second order phase transition from the normal to the superconducting state,

$$ln\left(\frac{T_c}{T_{c0}}\right) = \psi(1/2) - \psi\left(1/2 + 0.14\frac{a}{a_{cr}}\frac{T_{c0}}{T_c}\right), \tag{93}$$

where T_{c0} is the non-perturbed superconducting transition temperature and a is the pair-breaking parameter proposed by AG which is proportional to the exchange interaction parameter, γ (the interaction between the ferromagnetic exchange field and the Cooper pair). Uranium-based superconductors allowed these questions to be explored when a superconducting transition was discovered just below a ferromagnetic transition [141]. Thus, being a true superconducting-ferromagnet, i.e. where the superconducting transition is below the Curie temperature. S. S. Saxena and co-authors suggested that the same electrons are both ferromagnetic and superconducting, which prompted a move away from viewing superconductivity as being due to a lattice interaction towards a magnetic interaction [141]. These authors suggested this material is not a spin-singlet superconductor, rather a spin-triplet one. However, this is still to be definitely proven despite plausible agreement with developed models.

On the other hand, materials which exhibit a magnetic transition below the superconducting transition temperature also exist, better known as a ferromagnetic-superconductors. This brings us closer to the material of interest in this thesis, which is the $EuFe_4As_4$ family [142]. This has re-ignited the debate on whether spin-singlet superconductivity can exist in the presence of local-moment ferromagnetism. In the $EuFe_4As_4$ compounds, the magnetic moments and the superconducting electrons probably occupy separate sublattices, which

is proposed to allow the existence of superconductivity in spite of the high concentration of localized magnetic moments (i.e., the exchange field between the two subsystems is very weak). This is also noticeable in the very weak effect the Eu-sublattice has on the overall T_c of the compound, in stark contrast with previous findings and the predictions of AG theory [140, 7]. Currently our understanding of this effect stops here and hence new research, especially into studying what happens on the surface of these materials, is needed to complete it. These materials may not just prove to be useful in advancing our understanding of superconductivity, but also open the door to rather exciting applications. By combining ferromagnetism with superconductivity, one can envisage new superspintronic devices that exhibit the functionalities of spintronics with no dissipation!

5 Experimental techniques

The following section describes the vast array of experimental techniques used throughout this thesis' research, including the SHPM imaging technique, nanofabrication techniques and topography and chemical characterisation techniques.

5.1 Operation of an SHPM

The research work described in this thesis not only looks at improving the Hall probe component of an SHPM, but also will use an SHPM to study novel ferromagnetic-superconducting materials and vortex matter in high critical current high temperature superconducting tapes. This section describes in further detail the operation of an SHPM to help gain a better understanding of the design of future Hall probe chips and to describe the preparation and imaging of superconducting samples for the SHPM. Figure 38 shows the general schematic diagram of an SHPM system.

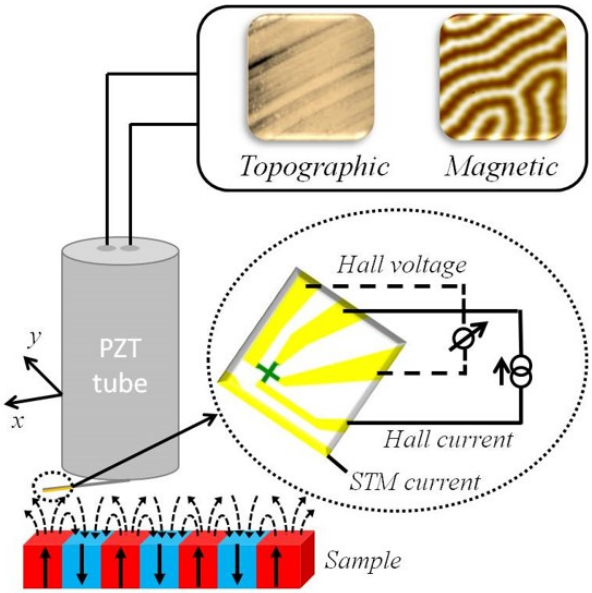

Figure 38: Schematic diagram of an SHPM system including the sample and insert components and the controlling and the PC that controls it.

5.1.1 SHPM cryostat and design

An SHPM can utilise both an AFM and an STM approach. The research undertaken on superconductors in this thesis use the STM approach which requires a mechanically stable enclosure to be able to approach to within a few nanometers, but imposes few restrictions on the gas environment. As such, an SHPM system includes not just the Hall probe but also the positioners which move the Hall probe to be able to achieve nanoscale resolution motion. The other important component of the SHPM system is the cryostat. Performing SHPM on superconductors requires low temperatures and liquid cryogens are generally needed to keep the sample at and below its critical temperature. Finally, the amount of flux trapped in a superconductor may need to be controlled, hence an external magnetic field must be applied. This sub-section describes the SHPM insert system including its piezoelectric positioners and the housing of the SHPM: the cryostat.

The three key components of the SHPM can be considered to be the sample puck, the Hall probe and the x-y-z motion piezoelectric transducers (in our case a slider and a tube scanner). All of these are located on the SHPM head, whose position on the SHPM insert is noted in figure 14. Once fabricated, the Hall probe is mounted on a bespoke package which has six connection. Two of these are for the Hall voltage leads, another two for the current leads, one for the tip and one acting as a spare lead which could be used for other applications such as a gate voltage. For an AFM tracked SHPM, the tip lead can be freed up for use in combination with the other free lead for applications such as the addition of quartz tuning fork sensor or a field excitation coil for Hall probe susceptometry [143]. The package design with a Hall probe bonded to it can be seen in figure 39 (a). The Hall probe is securely fixed with low temperature epoxy to the package and wire bonded.

Electrical contact is made using the spring loaded pins pushing onto the respective contacts on the rear of the Hall probe package. This is then mounted so as to oppose the sample by being screwed onto the end of the piezoelectric scanner tube. The sample is likewise fixed to the sample puck using conducting silver paint as shown in figure 39 (b). The silver paint ensures that a sample bias voltage can be established and a tip-sample tunnel current formed. As shown in 39 (c), the probe-sample tilt angle can be optimised via the three fine-threaded alignment screws. Before inserting the SHPM insert into the cryostat, the sample bias to the sample puck needs to be connected, as shown in figure 39.

The separation between the tip and sample can be altered using the two piezoelectric transducers. These enable nanometer positioning resolution to a high degree of accuracy. The piezoelectric effect dictates that certain materials become mechanically stressed or strained when they are exposed to an electric field, usually by applying a voltage between two electrodes on the material. In the case of SHPM, the main piezo is in the form of a tube, as shown in figure 38. This tube has been segmented into four quadrants allowing for different voltages to be applied to them [144]. It is important to note that the piezoelectric coefficient falls as a function of temperature approximately linearly. For our system the maximum scan range at 300K is 57.08μm x 57.08μm, compared to the smallest range at 4.2K being 7.42μm x 7.42μm. The same scaling relationship operates for the piezeoelectric slider used for coarse approach in the z direction, meaning that each z step is smaller at lower temperatures. It is hence important to calibrate the lift-off height (final probe-sample separation) and image size carefully at each temperature when performing image analysis. The fastest scan time at all temperatures using the full available range is roughly 4 minutes for our system. All these parameters depend upon the length of the scanner tube, the diameter of the tube, its wall thickness, the piezoelectric coefficients of the piezomaterial, and the maximum applied voltages.

While the SHPMs in our laboratory use piezos, it is possible for the scanner motion to be driven by motors and micrometer screws [50]. his gives the microscope a significantly larger scan area (in the millimeter range), but with a much larger pixel size in the micron range (due to the larger step sizes) [50]. Using this approach involves a trade-off between scan range and positioning resolution, for example, a centimeter scan range microscope can have a positioning resolution of 200nm [145].

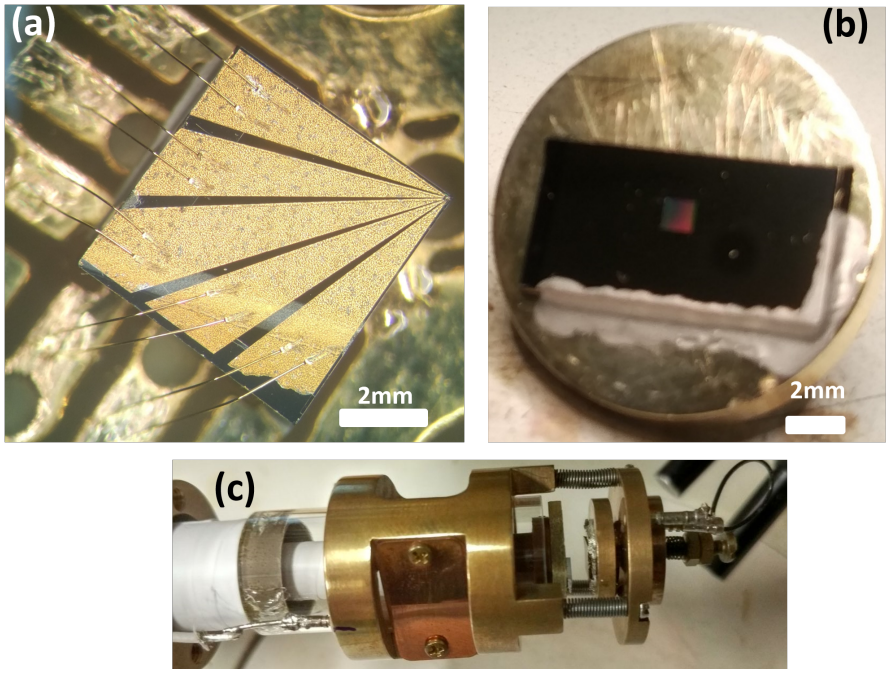

Figure 39: Various images of the components of an SHPM head. In panel (a), the Hall probe i shown affixed and wire bonded to the SHPM printed circuit board. In (b), a sample is shown fixed on the SHMP sample puck with Ag paint, and (c), is an image of the microscope ensemble onto which both probe and sample are attached.

Furthermore, studies of various material systems such as Skyrmions and superconductors require an externally applied magnetic field. This demands an integrated magnetic field coil in our SHPM system. An inert gas or ultra-high vacuum is also needed for a stable tunnel current to be formed. This is all achieved within the SHPM cryostat, a labelled example of the one used in our laboratory is shown in figure 40 **A** along with a schematic in **B**. The electromagnets are solenoids would from copper or Nb/Ti superconducting wire, and surround the neck of the cryostat (where the sample and probe sit). These electromagnets typically supply in the range of tens of mT for Cu wires up to tens of T for superconducting wires. In the cryostat shown here there is both an in-plane and out-of-plane electromagnet whereby the in-plane one can be rotated around the axis of the cryostat by 360 degrees. In cases where high fields are needed, a superconducting solenoid has been installed inside the cryostat. To efficiently keep the sample cool, the cryostat is equipped with an outer vacuum jacket which must be pumped out to 10^{-6}mbar pressure for good thermal isolation. Likewise, once the insert is inserted and properly sealed with an O-ring and clamp, the isolated sample space should be pumped free of air and back-filled with an atmosphere of inert Helium gas. This is to prevent the high piezo voltage breakdown, which depends non-monotonically on gas pressure. The sample space is repeatedly purged with Helium gas to ensure maximal purity in the sample space. It is important to note that the sample space should be back-filled with Helium gas every time the temperature has been lowered,

due to considerations of the ideal gas law.

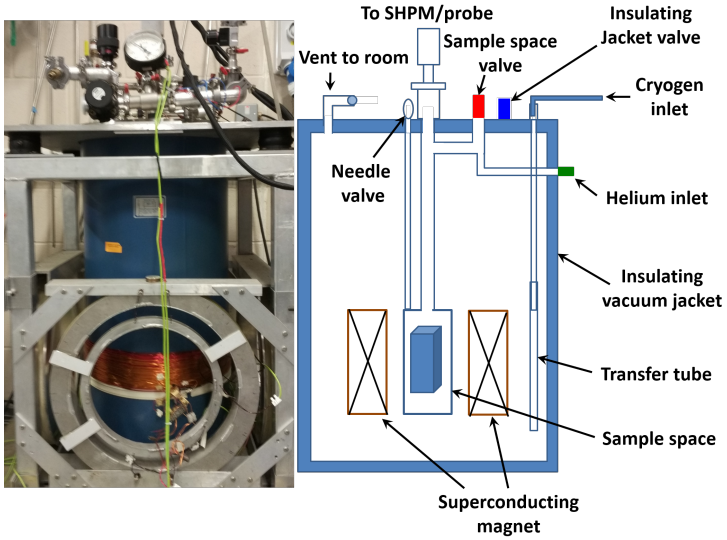

Figure 40: **A**: Photograph of one of the cryostat systems used in this project for SHPM. Pneumatic pads provide vibration isolation.**B**: A schematic of the cryostat interior as viewed from the side. The sample space is coupled to the cryogenic bath via a heat exchanger.

The cryostats used accept both liquid Helium and liquid Nitrogen. Liquid nitrogen is supplied from a commercially-filled Dewar via a flexible bellows-type transfer tube into the transfer port. The cryogen bath simply fills and the system cools. A needle valve is used to bleed a small amount of cold cryogen through the heat exchanger to control the sample space temperature. For experiments requiring liquid Helium, efficient filling first requires the cryostat to be as cold as possible. Once the sample space has been cooled using liquid Nitrogen (this is often monitored by a temperature sensor in the sample space), all of the liquid Nitrogen needs to be removed. This is achieved by using the gas vent port to pressurise the cryogen bath, with Nitrogen gas for example, and the liquid Nitrogen is expelled via the transfer port. Due to the high latent heat of liquid Nitrogen, it is essential that all liquid is gone before filling with liquid Helium, otherwise the cryostat may never reach base temperature. Once this is achieved, liquid Helium may be used to fill the bath, this time the gas vent valve is connected to a Helium recovery system for possible collection.

5.1.2 Sample preparation

Not all samples to be imaged are electrically conducting, allowing a tunnelling current to form between it and the tip. In this case samples are often coated in gold. If samples are also suspected of having poorly-conducting surface oxides, they are often coated as a safety measure to ensure stable tunnelling. Once mounted as described in the previous sub-section, the title angle can be set. The tilt angle between the sample and probe is very important as this contributes to the probe-sample separation. Figure 41 illustrates how the separation is impacted by the set tilt angle, as well as the fabricated tip-probe distance.

With the height, *Z*, of the tip above the sample and the probe-sample separation, *D*, the actual height, Z_{tot}, between the probe and the sample needs to take into account via the title angle, $sin(\alpha)$. This is given to be $Z_{tot} = H + Dsin(\alpha)$. Using this, along with the hall probe wire width, *w*, the absolute spatial resolution can be given by $\sqrt{w^2 + Z_{tot}^2}$. Since the probe and sample are monitored visually under a binocular microscope, the coarse motion transducer can be operated manually without experiencing a sample-probe crash during alignment. During cooldown, the probe-sample separation is usually kept in the range of a few hundred micrometres to avoid any thermal contraction resulting in a possible crash.

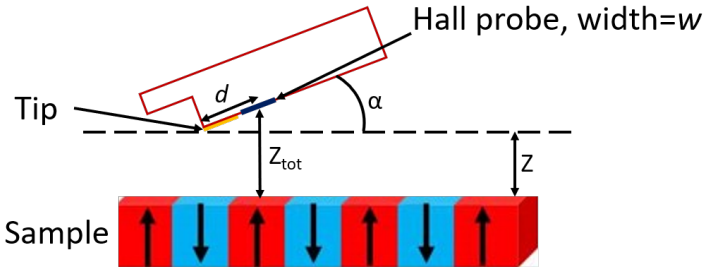

Figure 41: Illustration of the probe-sample distance dictated by the tip-sample separation, the tilt angle and the tip-probe separation.

5.1.3 Sample approach and imaging

Once the insert is placed into the cryostat and all the necessary conditions are met as described in the earlier sub-sections, the probe can now be approached to the sample. The probe is approached via a stick–slip coarse approach mechanism. An automatic approach process is used involving feedback from the tunnel current amplitude. During the approach and imaging, the sample is biased, usually with +0.2V with respect to the STM tip, and the tunnel current, I_t, is monitored. Once the tunnel current exceeds a target value, for example 1nA, the approach halts. Outside of the approach cycle, if this current is reached the head automatically retracts to a height where I_t no longer exceeds this target current. The automatic approach consists of scanner tube extension and retraction steps, bringing the probe closer to the sample. After full extension without the target tunnel current being met, the scanner tube makes one coarse approach step. This cycle is repeated until the target current is reached, and the approach procedure automatically terminates. Once the automatic approach is halted, a small lift-off is given on the piezo tube (usually 3-5V in the controller menu, where 20V = full range, depending on the expected sample topography). The edges of the scan area are then slowly scanned to check for higher topographical features. If a tunnel current exceeding the target is detected, the probe is lifted up a bit more. This process is repeated until the entire perimeter is checked with no tunnel current detected.

Once approached, the sample can be imaged in one of two modes: flying mode and tracking mode. Both of these are illustrated in figure 42. Flying mode involves the raster scanning the probe above the sample after having lifted off a fixed height above the surface (this

could range between 10s of nanometers to a micron). Flying mode is advantageous in that it is faster and greatly reduces the probability of a probe-sample crash which would cause irreversible damage to the probe and sample. However, due to the increased probe-sample separation, both the spatial and magnetic resolution are negatively impacted. Tracking mode, on the other hand, is operated using the full capabilities of a scanning tunnelling or atomic force tip. By maintaining a fixed sample-probe separation using the tunnel current in a feedback loop, the probe can scan without hitting the surface. This achieves the greatest resolution. However, often for samples with complex topography this gives a high chance of a probe-sample crash. Finally, the slow scanning due to running the feedback loop means temporal resolution is sacrificed in tracking mode.

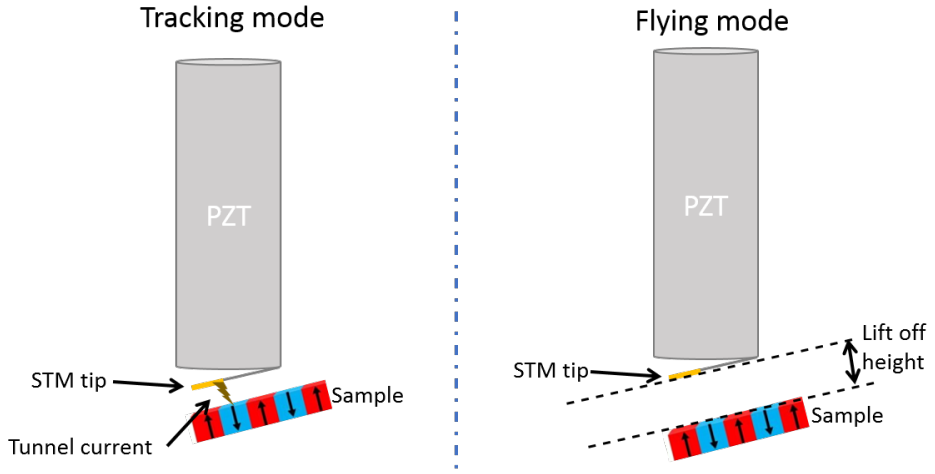

Figure 42: Illustration of the two different operation modes of an SHPM: flying and tracking mode.

5.2 Substrate preparation

The crucial supporting platform for all devices is the substrate. In the case of all of the samples prepared in this project, the substrate is either Si or Si/SiO_2. Silicon dioxide is frequently used due to the various benefits it offers. It plays an important role in the optical identification of monolayer or thin flake graphene and hBN flakes exfoliated onto the substrate (c.f. chapter 5.3.1). Usually a 300nm or 90nm SiO_2 thickness is best for this purpose due to the maximum optical interference it provides [146]. The oxide layer also acts as a dielectric gate in back-gated devices, c.f., the results chapters to see the typical range of doping density that can be achieved this way. Which side is the correct side to use? This is quite a straightforward question to answer. Wafers are usually polished on one side and rough on the other side, so the device side is the one that mirrors light. Wafers of Si and SiO_2 are characterised not only by the thickness of the oxide layer, but also the wafer resistivity, typically in the range of 0.01-0.02Ωcm.

Substrate dicing: Larger substrates may need to diced into smaller pieces. This procedure is also the same as the one used once a wafer of devices has passed through all fabrication

steps and needs to be diced up into individual chips. A diamond scribing tool is used to make scribe lines where we want to cut the wafer. For example, we have may have a 10cm circular wafer of Si/SiO_2 that we want to break up into 10mm$\times$10mm samples. To do this we make a square lattice of scribe lines with a 10mm periodicity using a manual micrometer stage. The scribing station uses vacuum chuck to ensure that the chip does not move while this is being performed. It is also important to consider that for Si substrates, one needs to scribe along the crystallographic axes to ensure a clean cleave. Usually these can be identified from the polished flats at the wafer edge, and scribe lines must be carefully aligned to these. This can be accurately achieved using the manual angle adjustment control on the scribing station. During operation the diamond-tipped scribing tool drops to the level of the surface of the chip, and is then drawn manually across the wafer to form the scribe line. This process is repeated for all scribe lines, while lines in the perpendicular direction can be made after turning the wafer using the 90 degree rotation mechanism. The final size of individual devices after scribing depends on the dimensions of the package used. This is smallest for the leadless packages requiring chip sizes to be 3.75mm $\times$ 3.75mm. Cleaving is then achieved by applying a small force on both ends of the wafer to be split into two, supporting one half on a glass slide with the scribe line running along one edge of it.

Substrate cleaning: Having a very clean substrate, whether a 'blank' substrate or one with an incomplete device present, is very important to ensure a strong metal-surface adhesion, a higher exfoliation yield and to avoid chemical contaminants from affecting any etch reactions and/or device performance. A simple three step process is used to clean most substrates, the only difference being how much sonication power is used, if any. In some cases, such as sample with weakly adhered CVD or exfoliated 2D materials, a cleaning step is avoided as solvents can cause them to delaminate. For the best exfoliation yield, an oxygen plasma clean is used to further remove surface adsorbents [147]. In figure 43, the simple 'wet' cleaning process is shown using trichloroethylene acetone and isopropanol (IPA). Trichloroethylene is an effective degreasing agent while Acetone effectively removes polymer residues, e.g., to strip commonly used resists like Polymethyl methacrylate (PMMA). IPA is a very pure general solvent that evaporate quickly, leaving very little residue. Sonication involves placing the beaker in a water-filled ultrasonic bath which agitates the solvent particles. This increases the rate of polymer, residue or other contaminant removal, and can also increase the rate of lift-off. However, if one already has important features on the substrate, it is important to keep the sonication power low, or to use none at all.

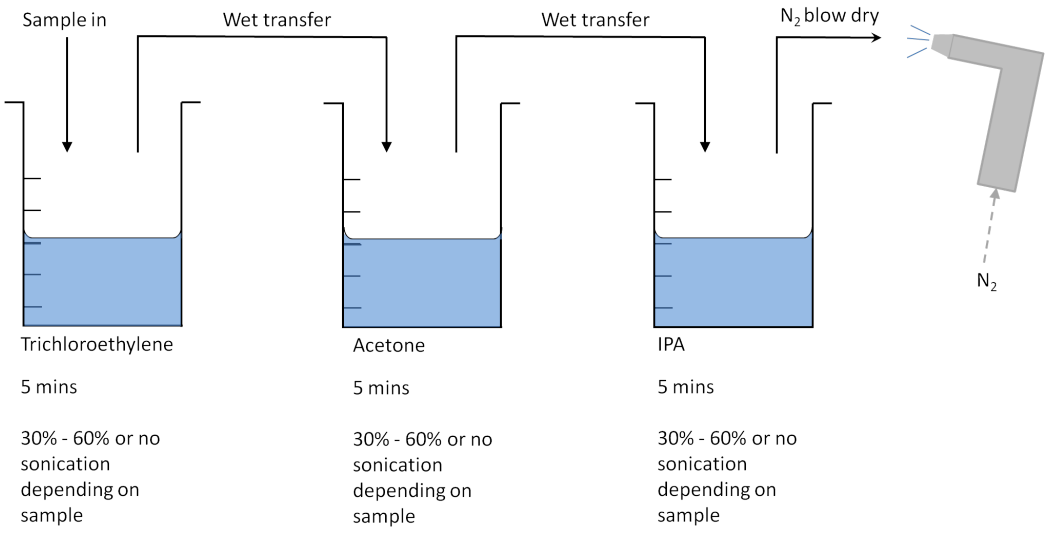

Figure 43: A schematic flow diagram of the generic substrate cleaning procedure, with a short nitrogen blow dry at the end of each step cleaning steps.

5.3 Nanofabrication of devices

A variety of different devices were fabricated during the course of this project. Hall cross arrays and bars were fabricated from CVD graphene and exfoliated graphene/hBN. SHPM devices were fabricated from exfoliated flakes. Hall cross arrays are simply an array of 8 Hall crosses each with their own pair of voltage contacts and one pair of current contacts servicing the entire array. This ensures the economical use of purchased CVD material and exfoliated flakes. We have also used 'easy-transfer' CVD graphene from Graphenea to transfer graphene onto pre-patterned gold contacts. Encapsulated devices were fabricated with hBN flakes using a dry transfer rig. This section is dedicated to describing the methods used to fabricate these aforementioned devices. Only the generic use of each technique is described here and any innovative applications of them are described in the appropriate results chapters.

5.3.1 Mechanical exfoliation of flakes

Also known as the 'Scotch tape' method, the mechanical exfoliation of flakes (in our case graphene/graphite and hBN) involves using sticky, low residue Nitto tape to cleave flakes from larger crystals [4]. Graphene was obtained via mechanical exfoliation of graphenium, 1.0 - 1.8 mm, flakes. Two or three of these were stuck on the sticky side of the blue Nitto tape. The tape was then folded over onto itself and subsequently rapidly unfolded. This process was repeated until the tape surface area was well loaded with thin graphite flakes. The purpose of this is to load the tape and maximise the graphite to substrate surface area, increasing the probability of larger and thinner flakes. These flakes could be thinned down further by using another piece of Nitto tape to cleave off the area of flakes currently on the original Nitto tape, and the folding-unfolding process was again repeated

for this second tape. If still thinner flakes are required, another tape can be used and the process repeated. Once a satisfactory thickness and concentration of flakes is attained, the Nitto tape was pressed down onto a carefully cleaned substrate (c.f. chapter 5.2) using the thumb, and held in place for one minute. The tape was then swiftly peeled off. Figure 44 shows an image of a monolayer obtained using this method and a schematic of the mechanical cleavage process to help gain a visual understanding of the process.

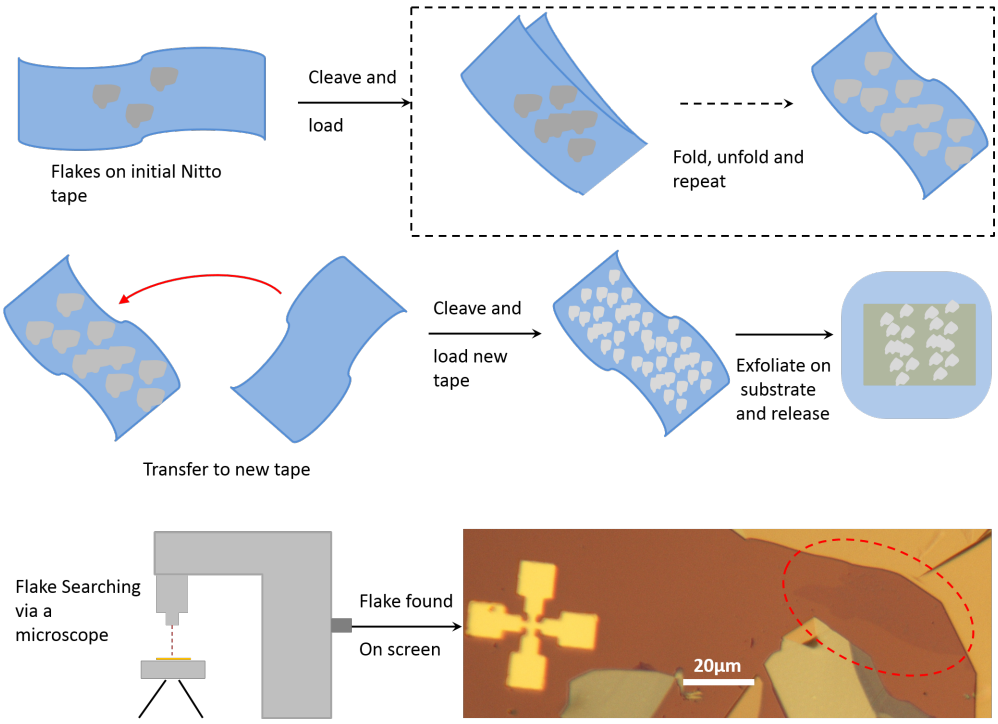

Figure 44: A schematic diagram of the exfoliation process using Nitto tape, including an optical microscope image of a monolayer (encircled in red) found on an Si/SiO_2 sample after exfoliation.

Flakes are usually searched for under an optical microscope. It is here that the advantage of using SiO_2 becomes apparent,as under a high enough optical magnification, monolayer flakes become readily identifiable. To make flake searching easier, the substrate to be exfoliated onto usually has pre-patterned Au registration marks in the shape of an inward tapering cross with a 200μm pitch (c.f. figure 44). The precise details of this process can differ depending on the flakes used and what one wants to do with them. For non-encapsulated devices this procedure is followed exactly. However, if searching for monolayer and few-layer flakes for encapsulation, the substrate should not be O_2 plasma cleaned beforehand, otherwise it becomes extremely challenging to pick up the flake due to the much larger adhesion force on an ultra-clean substrate. Thick flakes of hBN from HQ graphene were used for hBN-graphene-hBN encapsulation. Since we do not need few-layer hBN flakes and hBN is in much less supply than graphite, we use hBN flakes sparingly and only lightly load one tape using the method described above. The mechanical exfoliation

process is repeated until a few flakes of moderate thickness and reasonable size are found. The tape is then viewed under an optical microscope to find a region where there are reasonable thickness flakes of the right size which can then be exfoliated onto a 'pickup stamp'. This leads us onto the next section describing how 2D materials can be transferred to create more intricate devices and encapsulated stacks.

5.3.2 2D material transfer processes

To make 2D material heterostructures or 2D materials on top of other premade device structures, one must cleanly transfer them. There are generally two families of transfer methods, a dry and wet. Wet transfers in this work involve transferring CVD grown graphene on top of another 2D material flake supported on a substrate. This can be achieved starting from CVD graphene grown on copper by first spinning a support polymer layer on top of the graphene and etching away the copper using a copper etchant such as ammonium persulfate [148]. The graphene and polymer then end up floating in etchant, and can subsequently be 'fished' out using the target substrate and gently washed in deionised water. There is now a vast catalogue of different wet transfer methods [148]. Since the focus of this project is not the transfer process, we will not go into detail and confine our discussion to a simple transfer method using commercially supplied materials. In this case a PMMA/graphene/support-polymer stack is provided by commercial suppliers, Graphenea. Following similar steps as with graphene on copper, the stack is dipped into deionised water at an angle until the support polymer is detached and sinks to the bottom of the beaker. The PMMA/graphene should then be floating at the top of the water, and can be readily fished out using the target substrate. The substrate with graphene is then be removed and left to dry for 30 minutes before being held in a vacuum for 24 hours to improve graphene-substrate adhesion. The substrate is then be placed in acetone for one hour to remove the supporting polymer, followed by a soak in IPA for another hour. Finally, the graphene/substrate is annealed at 400◦C in an inert atmosphere for two to four hours. The process is summarised in figure 45.

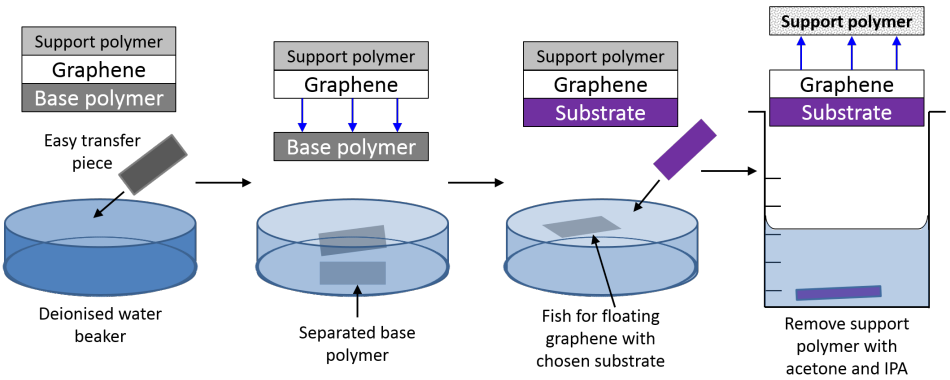

Figure 45: step-by-step sketch of the 'easy-transfer' process developed by Graphenea.

As with wet transfers, there are numerous methods for dry transfer. Again we will just

describe the one employed in this project. In our case we use a dry, polymer-free transfer method, whereby the graphene layer never touches a polymer layer and remains largely contaminant free. Graphene or hBN can be picked up with, or placed onto, a polydimethylpolysiloxane (PDMS)/polycarbonate (PC) stamp. The stamp is made by cutting a small window in a large piece of Nitto tape which is stuck onto a glass slide; a piece of PDMS is cut to fit in this window and PC is spin-coated over the PDMS. The Nitto tape can then be peeled away leaving behind the polymer stamp where the window was. After loading the stamp with the first flake, the glass slide with the stamp is loaded face down into a clamp on a 3-axis manual stage as shown in figure 46. The target substrate and the stamp each have their own x-y-z stage so the hBN or graphene flakes can be put down at whatever location the user wants by coordinating the motion of the two stages under a microscope (c.f. figure 46). The flake is slowly approached to the desired position while looking through the microscope. Contact is made once the contrast changes on one side of the field-of-view due to the stamp touching the surface. Once this happens, the flake is slowly further approached until the stamp sticks to all of the substrate in the field-of-view. At this point the flake is either picked up, or dropped down. Whether it is picked up or dropped down depends on the adhesion force between the flakes and the substrate. If the adhesion between the flake and the substrate is greater than the adhesion between the two different flakes, the sample on the substrate cannot be picked up. By heating to approximately 90°C using a substrate heater on the same stage, one can bias the interactions in favour of a stronger flake-flake adhesion. Thus, a flake can be picked up. This process can be repeated to form a stack, which can then be dropped down into another desired location. However, the stamp must now be removed by dissolving the PC layer with chloroform. This separates the stamp from the stack, leaving behind just the substrate holding the desired stack or single flake (such as hBN/graphene/hBN).

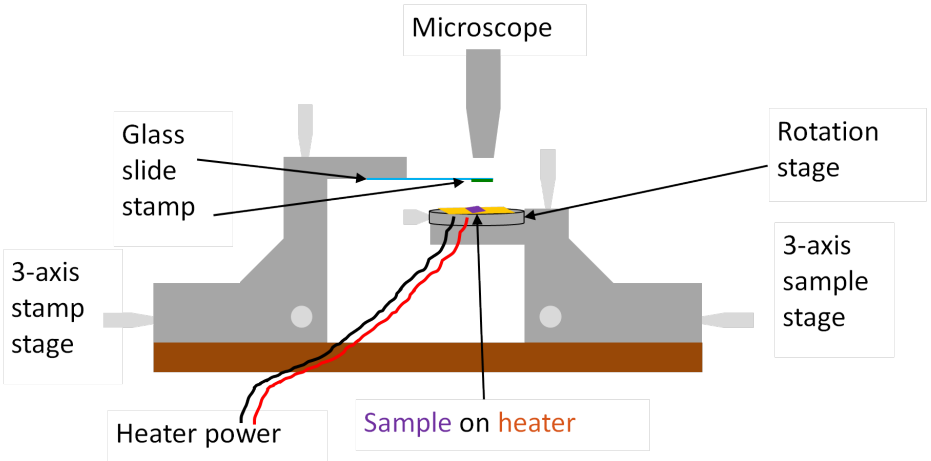

Figure 46: A side-view sketch of the dry transfer set-up.

5.3.3 Device design

The goal of most nanofabrication processes is to produce a device with some form of shape or artificial design. Lithography is the main tool used to do this for designs with features on the micrometer and nanometer scale. The two main types of lithographic processes used to make devices are photolithography and electron beam lithography, both of which will be described later in this chapter. These both involve reading from a data file which contains the design one wants to create and then writing this pattern directly on the sample. These digital patterns are created in a lithographic design software such as K-layout or Elphyplus.

In these software packages, polygons can be drawn to form the desired device structure. When designing it is important to consider where the centre of the design is with respect to the position on the substrate where we want to write it. Alignment marks can be added so that the center of these marks is easily identifiable, such as the centre of a cross or a sharp corner. Often these positions may already have been deposited or etched away on the chip prior to patterning. To carefully align to these features, one can import an optical image into a software package like K-layout and then design the structures in known alignment to the registration marks. An example of this is shown in figure 47.

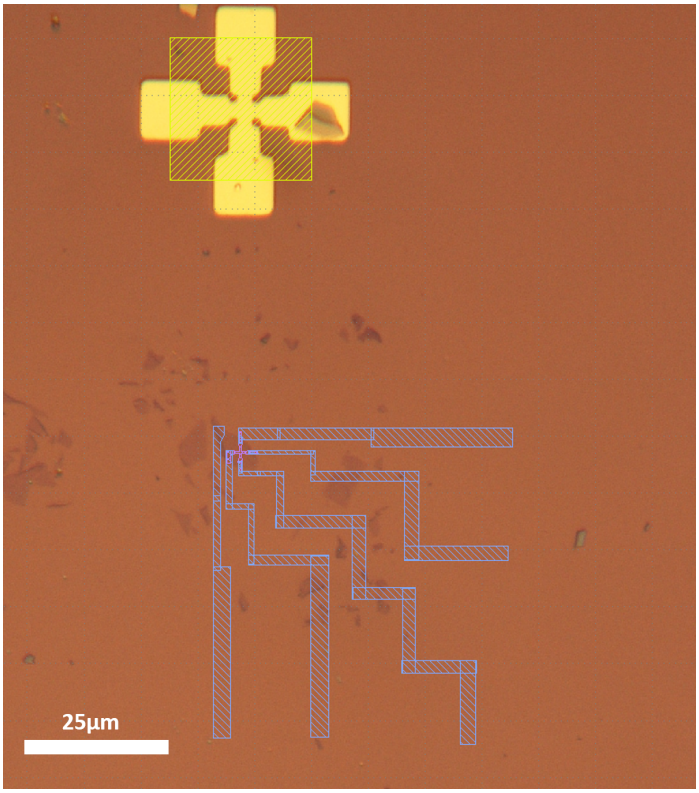

Figure 47: An example design in K-layout superimposed on an optical image of bilayer graphene flakes that are to be made contact to. The gold squares are windows which open up around the gold cross alignment marks designed for layer-to-layer electron beam lithography.

When designing patterns for electron beam lithography, it is important to consider the order and potential drift-related shifts between polygons being written. To minimise the impact of any slight shifts, small overlaps are added between adjacent polygons to ensure there are no discontinuous leads or etch windows. The polygons are also written in a well-controlled order, usually spiralling out from the smallest feature to the larger lead sections at the perimeter. Once the design is finished, it can now be used in the lithography process.

5.3.4 Photolithography

Photolithography can be performed using a direct laser writer (DLW) which uses a 375nm wavelength semiconductor laser to 'draw' out any desired structures with a spatial resolution in the range 06 – 1.0 micrometer. Shipley S1813 is a positive tone photoresist, meaning that the exposed (or written on) areas become soluble in alkaline developer due to polymer chain scission. A negative tone resist on the other becomes hardened upon exposure, usually by polymer cross-linking. For metal deposition, a positive tone resist should ideally be at least 3 times thicker than the thickness of the metal deposited to ensure clean lift-off when dissolved in acetone. In this case the DLW exposes windows in the photoresist on the substrate or material where metal contacts will be deposited or trenches will be etched. To achieve this, a layer of S1813 photoresist is spin coated on the substrate. This involves dropping resist onto a substrate from a syringe or pipette until covered. The sample is then held in place by a vacuum chuck integrated into the puck of the spinner and spun at a selected spin speeds to uniformly coat the substrate. A bake is subsequently performed to remove solvents. For S1813 resist, it is spun at 500rpm for 5s to uniformly spread the resist followed by 5000rpm for 30s to obtain a uniform film with thickness of approximately 1.25 micrometers and then baked for 30 minutes at 90°C.

In this project a Heidelberg Instruments μPG100 was used as the DLW. A schematic of the DLW is shown in figure 49. The sample is placed on a stage and secured via a vacuum chuck just as with the spinner. A motorised stage then moves the chip under the laser which approaches the sample using an automated focusing routine. The μPG100 can use two different methods of auto focusing, pneumatic and optical. In the case of pneumatic focusing, the laser head blows air and 'feels' the pressure built up inside the head. A pressure sensor reads this change in pressure and halts the approach at a certain pressure threshold. The optical approach is preferred as it can be used on smaller-sized samples (¡ 25mm) and achieves a more accurate focus. The optical focus operates by reflecting a laser beam from the substrate, with the shape of the reflection measured and converted into a signal. This controls the movement of the piezos adjusting the fine head height, until the ideal shape is attained. The pattern can be aligned to features on the substrate, either previously deposited metal structures or substrate corners, by entering x, y and θ (the angle shift between features).. Once aligned, the laser is manually focused onto the resist layer using the manual z axis piezo control and then the appropriate laser power (dose, usually determined via a dose test) selected to draw the pattern. Finally, the digital pattern to be written is loaded into the DLW) and the write routine is executed.

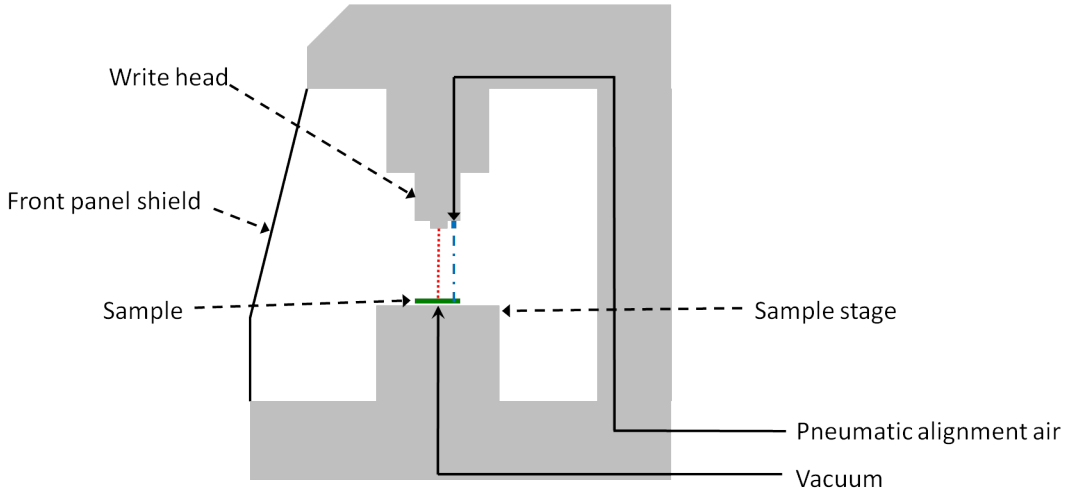

Figure 48: A schematic diagram of the Heidelberg μPG100 DLW system.

After having written the pattern, the stage releases the sample ready for development. For the case of S1813, a 2:7 ratio Microposit 351:deionised (DI) water mixture is used as developer. The sample is developed for 30 seconds and then taken out of the mixture to be rinsed in DI water. It is important to confirm complete development under a low magnification microscope before continuing, as any resist residues can compromise the metal lift-off process. After this, the sample is ready for etching or thin film deposition, depending on the next process step. An example of an exposed and developed pattern is seen in figure 49. The alternative approach for photolithography is to use a commercial mask aligner. However mask aligners have disadvantages compared to using the DLW. The mask aligner needs a dedicated mask for each pattern to be exposed, which can prove costly, especially in the case of fabricating devices from random shape and size flakes which all need their own unique pattern. This also allows greater flexibility when encountering unanticipated issues during device fabrication. However for large area structures such as large wafers of registration marks for exfoliated flake searching, it is faster to simultaneously expose many structures in a mask aligner compared to a DLW which takes time to write each feature sequentially.

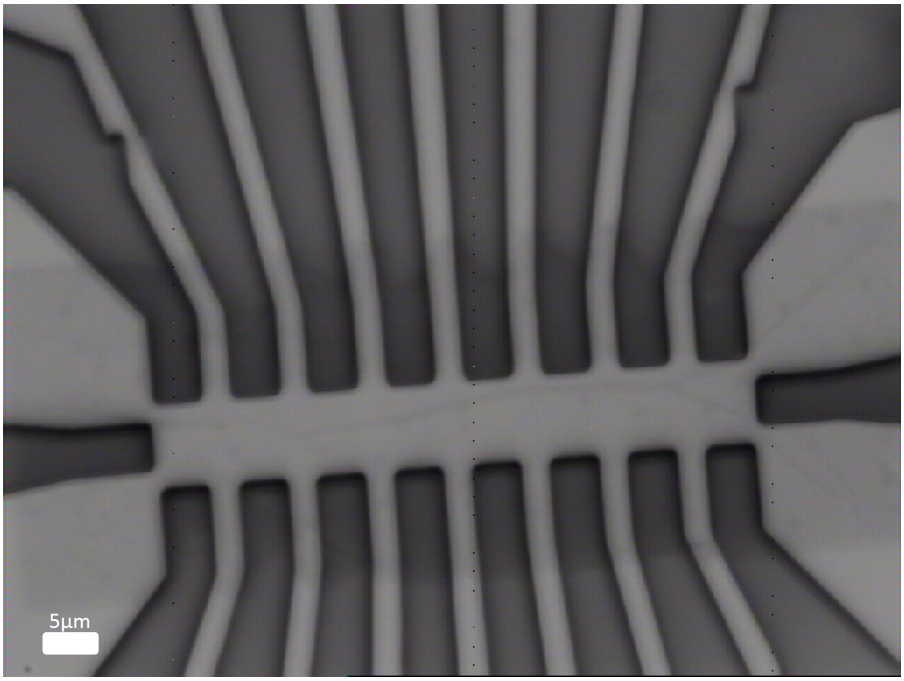

Figure 49: Optical image of an exposed and developed pattern written in S1813 photoresist with the DLW. The darker regions are exposed regions where thin metal films are to be deposited. A slightly darker rectangular-shaped region near the middle indicates the location of a CVD graphene film which is to be contacted in order to fabricate a Hall cross array.

5.3.5 Electron beam lithography

Electron beam lithography (EBL) is used instead of DLW in cases where high resolution (typically sub-micron) features or very precise alignment is needed The much higher resolution is achieved due to the very much shorter wavelength of high energy electrons. A beam of electrons accelerated to 10-30keV is produced from a field emission electron gun in a high vacuum chamber. The electron gun is followed by an aligner to collimate the beam, which then is focused by a condenser and objective lenses to bring the maximum number of electrons to a point on the resist surface. The electron beam position is controlled by deflection coils situated above the objective lens. An electrostatic beam blanker acts to turn (deflect) the beam on/off while writing. A stigmator and zoom lens help minimise aberrations and aid focusing of the beam. Forward- and backscattered primary electrons as well as secondary electrons broaden the beam in the resist, thus resist outside of the desired pattern area receives a non-zero dose [149]. This can affect the size and shape of the features being written and this so-called proximity effect can be minimised by carefully designed dose corrections and/or modifications to the pattern design. A schematic of an electron beam lithography system is shown in figure 50.

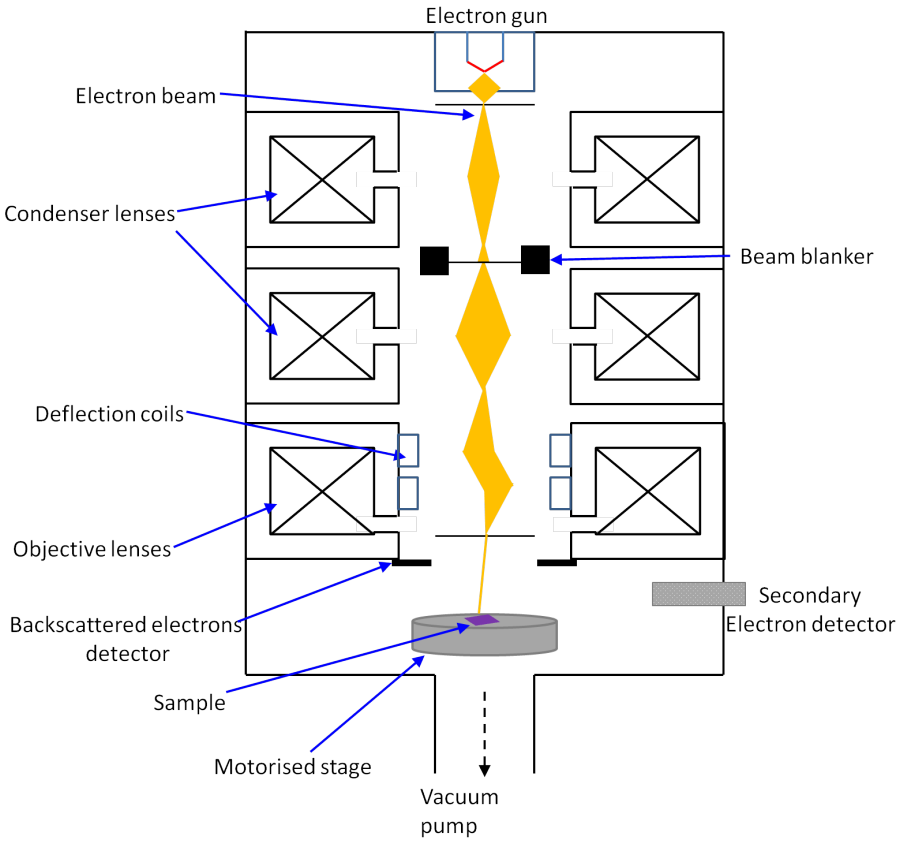

Figure 50: A schematic diagram of an EBL system.

Within this project the EBL system has been used to define the Hall crosses through use of a negative tone resist, Hydrogen silsesquioxane (HSQ), which acts as a robust etch mask. The HSQ slowly cross-links in air, however, so care must be taken that it is spun on and baked and immediately prior to exposure. In order to facilitate resist removal a thin layer (150nm) of PMMA is spun at 3000rpm on the graphene and baked on a hot plate for 15 minutes at 150°C prior to spin-coating with HSQ, The allows the exposed HSQ layer to be lifted off in acetone once device etching is complete. The thinner the HSQ layer the smaller the features one can pattern. Therefore, in order to pattern deep sub-micron Hall crosses a 2% solution of HSQ is spin-coated at high speeds (5000rpm) to obtain a very thin layer of 25-35nm. The sample is then baked on a hot plate at 150°C for 5 minutes. The HSQ is subsequently exposed at a typical dose of approximately $500\mu Ccm^{-2}$. The sample is then developed in 25% tetramethyl ammonium hydroxide (TMAH) alkaline developer at room temperature for up to 1 minute, until all the unexposed HSQ is removed.

5.3.6 Thin film physical vapour deposition and lift-off

Ohmic contacts for all devices made during this project consist of bilayers of chrome and gold. Additionally, samples and substrates requiring an electrically conductive coating (e.g.,

for SHPM) are usually coated with gold. These metals are deposited by electron beam (e-beam) evaporation using an electron beam from a charged tungsten tip to heat a target metal in a crucible. The chamber needs to be under high vacuum ($\leq \times 10^{-7}$mbar) to allow the electrons to pass to the evaporation source and to reduce ambient contaminants. The heated source metal in a crucible then sublimes, flying ballistically towards the sample, where it precipitates into solid form. The crucible is loaded in a water-cooled copper hearth to prevent it from heating up to the point where it also starts to evaporate material towards the sample. To avoid any chemical interactions with the electron beam filament it is kept well isolated from the source, and a magnetic field is used to bend the electron beam into the crucible. Multiple metal sources can be loaded into the e-beam evaporator and one can manually switch between them without having to vent the system. In practice a layer of chrome is needed as an adhesion layer between substrate/graphene and the gold for both inner contacts (5nm Cr) and outer contacts (20nm Cr). 70nm is then typically deposited for inner contacts and 250nm for outer contacts. The correct deposition rate is important to achieve good adhesion between layers, and is typically set at 0.25 to 0.75nm/s. Electromagnetic coils allow one to align and scan the electron beam across the surface of the source material in the crucible in order to optimise the stability and uniformity of the deposition. In addition, the sample holder rotates slowly to obtain a more uniform film thickness across large samples. After removal from the evaporator the sample is placed in acetone to lift-off the unwanted metal. Sonication is sometimes needed to remove metal in tight spaces between design features. Sonication should be limited to low powers and short times to avoid unwanted loss of graphene or occasionally even the contacts themselves.

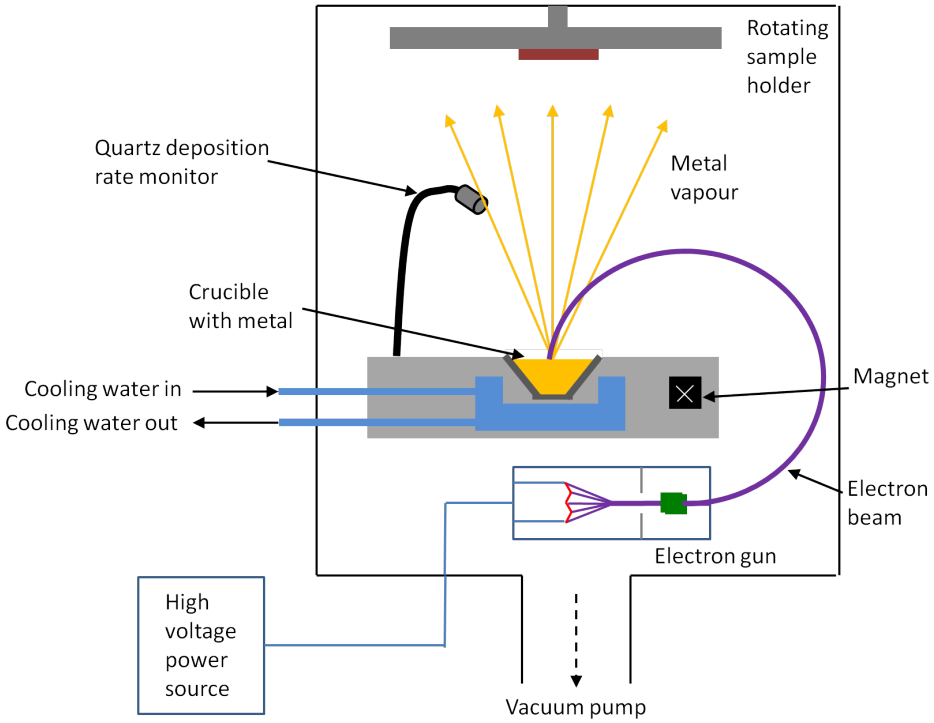

Figure 51: A schematic diagram of an E-beam evaporation system.

5.3.7 Dry plasma etching

Using a reactive ion etcher (RIE) or inductively coupled plasma (ICP) etcher, one can controllably remove PMMA, graphene, silicon and SiO_2 in a gas plasma. A plasma etching machine works by generating a low pressure plasma whereby the high energy ions attack the sample surface. Gas enters the chamber through the top and exits through the bottom, and the plasma is initiated by applying a strong radio frequency (RF) electromagnetic field to the wafer platter. The gas molecules are ionised by the oscillating electric field, creating a plasma, and in each cycle ions are accelerated up and down in the chamber, striking the wafer platter [150]. Electrons deposited on the wafer platter cause a build-up of charge which develops a negative voltage of a few hundred volts. The large voltage difference then causes positive ions to collide with the samples to be etched [150].

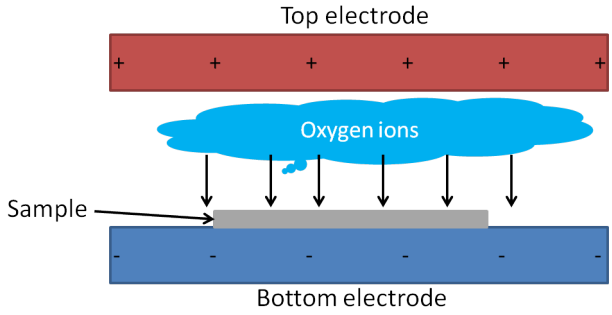

Figure 52: Sketch of the operation of an RIE chamber. This includes the two electrodes, creating the electric field (denoted by arrows) that accelerates the ions towards the sample wafer (gray).

Parameters to optimise during etching include: pressure, etching time, gas flow rate and power. Generally, increasing the power and pressure will decrease the time needed to etch to a given depth. The flow rate and pressure influence the sidewall angle of the unetched material. By deliberately over-etching masks used to define Hall devices, one can further reduce the width of the crosses by a few nm as the graphene beneath the PMMA/HSQ layer is gradually underetched (c.f. figure 53). The gases and process conditions depend strongly on what materials the user wants to etch. For silicon and silicon dioxide, a modified Bosch etching process involving SF_6 and C_4F_8, at quite high powers is typically used [151]. Graphene and PMMA can simply be etched in oxygen gas at low power and pressure, while hBN can be etched in a CHF_3 and O_2 gas mixture. Gas etching recipes are detailed in the relevant results chapters in which they were used.

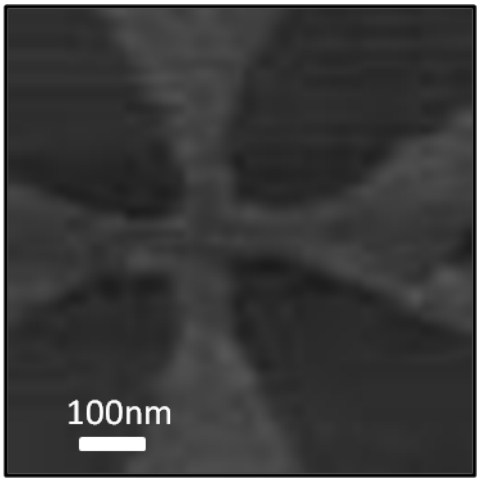

Figure 53: An atomic force micrograph of a nanoscale Hall cross after etching.

5.3.8 Annealing of devices

To remove or great reduce the density of polymer residues adsorbed on the graphene and/or hBN surfaces, one can employ a high temperature annealing step in inert gases such as Argon or Nitrogen. An inert gas is used because at high temperatures above 200 degrees graphene begins to etch in the presence of oxygen, thus destroying the device. We have utilised a quartz tube furnace which was sealed from ambient atmosphere at both ends. One end was connected to an Argon gas cylinder and the other end passed through an oil bubbler to allow gases to escape but denying atmospheric gases entry. Once the sample is inside and the tube is sealed, it is purged in Argon gas for 30 minutes to remove atmospheric gases. The temperature is then set and ramped up to its target at 2 K/min. When working with commercial CVD graphene, a pre-fabrication anneal is performed to minimise residues from the wet transfer process and increase the surface adhesion of the graphene on the substrate. This is made at 400°C for 2 hours. A post-fabrication and bonding anneal has also been performed to minimise residues from the fabrication process. As will be shown in chapter 6, this can also reduce extrinsic doping levels, bringing the graphene Dirac point closer to a zero back gate voltage. In this case the temperature is reduced to 200°C for 6 hours to avoid damage to the gold pads and leads which harden and become difficult to bond if higher temperatures are used.

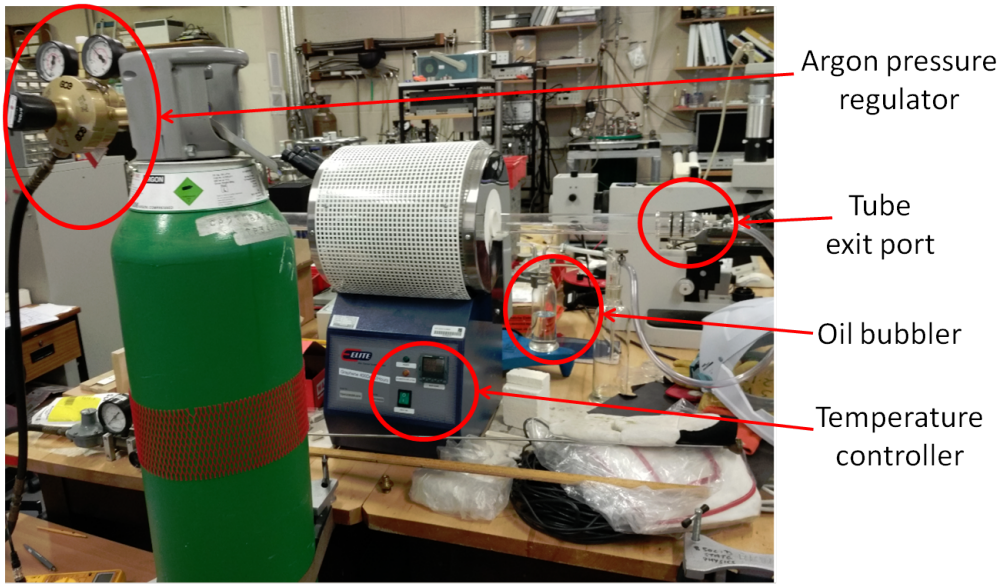

Figure 54: Labelled image of the furnace system used for the annealing of graphene devices. The valve on the pressure regulator of the Argon cylinder is connected to the inlet side of the tube furnace.

5.3.9 Characterisation of materials

Once device fabrication is completed it is important to check whether the process steps have degraded the material quality or whether specific steps, e.g., Ohmic contact formation, have failed. This section of the experimental methods chapter describes the various tools used to characterise the materials and devices throughout the project, focusing separately on their topography, composition, location and scale (i.e., lateral dimensions of of materials/devices). The most basic and most widely used of these tools is optical microscopy. This is employed to search for graphene and hBN flakes on pick-up stamps and Si/SiO_2 substrates, to confirm the success of each nanofabrication step such as etching, lift-off and development, to align components to registration marks and to check the general condition of materials and devices as they are used. However, optical microscopy has limited spatial resolution, and cannot yield accurate information about material composition or topography. Hence we need additional tools to be able to probe these.

5.3.10 Raman spectroscopy

Raman microscopy is one of the tools that can be used to characterise the thickness and quality of 2D materials (particularly in our case graphene). For example, it can indicate how many layers of graphene there are in a flake and give a measure of its quality [152]. It can also be used as a probe of the performance of materials that are integrated into devices, for example it can monitor how the quality of a material changes as it goes through fabrication process [153].

Raman microscopy works by measuring the inelastically scattered light that has interacted with phonon-excited matter. When light interacts with matter there is an energy exchange between the incident photons and the sample which results in the emission of red-shifted light at energies lower than that of the incident light. This is known as Stokes scattering, with the opposite (blue-shifted light) known as anti-Stokes scattering. In practice the Raman scattered intensity scales inversely with the fourth power of the excitation wavelength. This is in contrast to elastic scattering whereby molecules emit light with the same wavelength as it was excited by. This elastically scattered light is usually filtered out in a Raman spectroscopy experiment [154]. Ideally the incident light is monochromatic and high intensity, and generally comes from a laser source. The Raman shift is described as the energy lost (or gained) by a photon in this inelastic scattering event. This is given in wavenumbers with the conversion factor of $1cm^{-1} = 0.124meV$. A Raman spectrum is then built by measuring the intensity of these scattered photons as a function of the Raman shift. These intensities and shifts are directly related to the molecular structure of the sample, and this is what makes it such a powerful and simple tool for characterising materials. An example of a Raman spectrum of bilayer graphene is seen in figure 55.

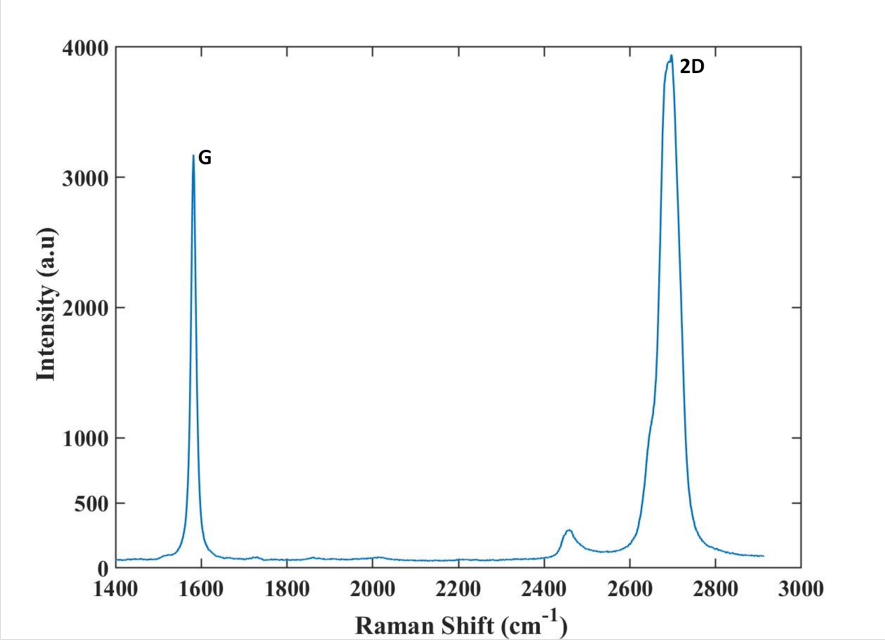

Figure 55: A Raman spectrum of a bilayer graphene flake on Si/SiO_2.

Figure 55 highlights one of the key uses of Raman spectroscopy, the identification of the number of layers of graphene in a flake. In this case there are three key features of the graphene Raman spectrum: the G peak, usually at $1580cm^{-1}$, the 2D peak, usually at $2700cm^{-1}$, and the so-called disorder (or sometimes defect) D peak, usually at $1350cm^{-1}$ [152]. The G peak represents first order Raman scattering from the in-plane transverse and longitudinal optical phonon modes at the Brillouin zone center. The 2D peak represents second order Raman scattering process from two in-plane transverse mode phonons near the

K point. The 2D peak is what allows the identification of the number of graphene layers. It gradually broadens as the flake thickness increases above a few layers, in comparison to monolayer, bilayer and trilayer graphene in which the 2D peak is much sharper. Monolayer, bilayer and trilayer graphene can best be determined from the intensity ratio between the 2D and G peaks ($I(2D)/I(G)$). These changes are also mixed with gradual shifts in the 2D peak, albeit not as straight forward as the peak shape and intensity. The D peak is as a result of the defect-mediated zone-edge phonons and indicates the defection level in graphene. These changes are also combined with gradual shifts in the 2D peak position, although this is not as straight forward to analyse the peak shape and intensity. The D peak is a result of defect-mediated scattering from zone-edge phonons and is a measure of the density of defects in the graphene. This peak is a very good probe of how graphene quality is affected as a result of CVD growth, as well as subsequent transfers and device processing. A clear example of the use of this peak in thickness identification is given by G. Liu *et al.*, and is reproduced in figure 56 [68].

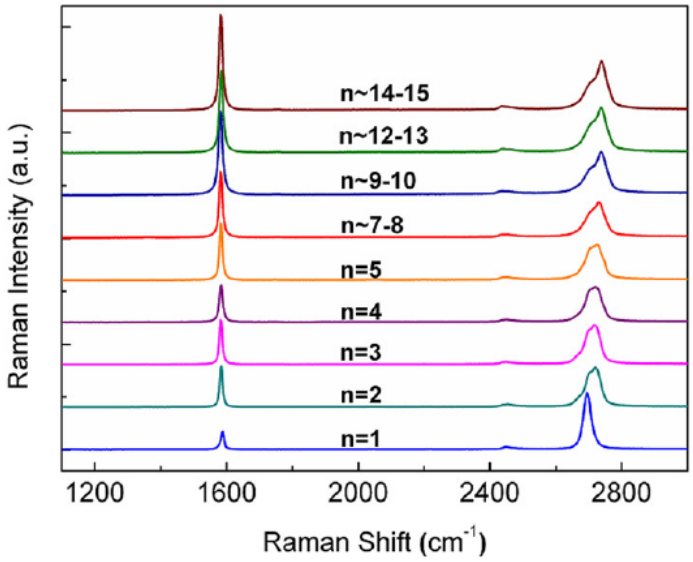

Figure 56: Raman spectra of different thickness few-layer graphene flakes on Si/SiO_2, where n is the number of layers, showing a clear evolution of the 2D peak as the thickness increases [68].

5.3.11 Atomic force microscopy

Atomic force microscopy (AFM) was used as an important characterisation tool throughout this project. Given the ability for AFM to operate in ambient conditions this makes it a frequently used characterisation tool in many research fields, becoming almost as widely used as optical microscopy. AFM was principally employed to obtain nanoscale resolution topographic images of graphene-based devices as well as being used to confirm the thickness and roughness of hBN and graphene flakes. Furthermore, an AFM can also be used as a magnetic force microscope (MFM) with the appropriate ferromagnetic tip, as described in

chapter 2.1.4.

AFM records the deflection of a microscopic cantilever as it raster scans over the sample. The deflection is a result of the force between the apex of the tip on the cantilever and the atoms/molecules on the surface of the sample. Just as with STM, a feedback loop is used to measure the deflection of the tip while keeping the height (or sometimes force) constant [155]. There are three main operation modes for an AFM: contact, tapping and non-contact modes. Since tapping mode AFM was the only mode used to image in this project, the discussion in this section will be limited to describing this. A nanometer sharp tip is brought to oscillation close to its resonant frequency using a piezoelectric element. In tapping mode, the frequency and amplitude of the driving signal is kept constant. As the tip approaches the sample surface it experiences either an attractive or a repulsive force, which causes the amplitude to change. A feedback circuit controls the piezoelectric scanner to keep the frequency and amplitude constant by adjusting the height. This height change can then be used to form a topographic map. Tapping mode is preferred to avoid damage to the sample as there is only ever intermittent contact between the tip and sample.. A schematic diagram of an AFM is shown in figure 57. This example uses a laser and a 4-quadrant photodetector to measure the deflection of the cantilever via the light reflecting off the metal-coated (usually Al) back side of the cantilever.. The sample stage motion is provided by nanometer-resolution piezoelectric positioners, enabling accurate images of devices with wire widths and pitches in the tens of nanometers. It is important to note that the ultimate resolution of a commercial, ambient AFM (e.g., the Asylum Research MFP-3D used here) does have limitations. Electrostatic forces on the tip, the finite tip apex radius apex and the finite angle tip sides are can all contribute to this. Other factors such as hydration layers on top of and between flakes and substrates distort the true measured thickness. In practice the accurate determination of the precise number of graphene layers in the range 1 - 10 is difficult with AFM alone, and one should ideally combine this with Raman microscopy to get an accurate confirmation.

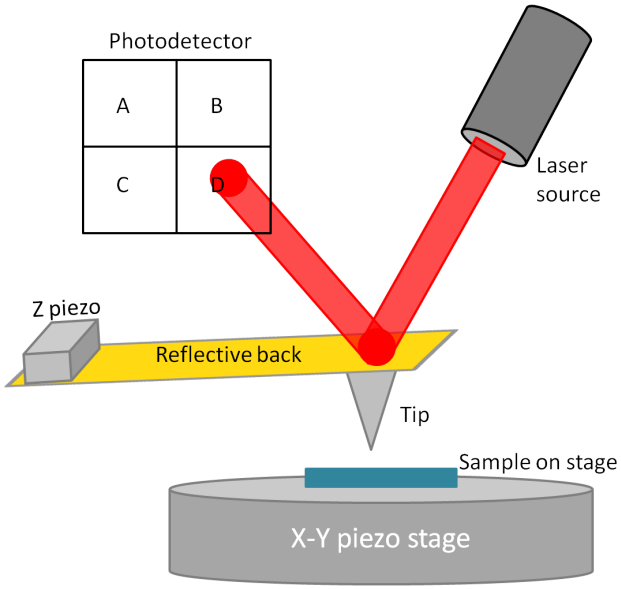

Figure 57: A diagram of an AFM cantilever deflected from the surface of sample. In this case, the deflection is monitored via a laser beam reflected from the metal-coated upper surface of a Si cantilever.

The laser light source can be positioned so that it reflects off the end of the cantilever. The closer to the end of the cantilever, the greater the sensitivity, but this can also add noise. Hence the user needs to find an appropriate balance when position the laser on the cantilever. Each cantilever has a slightly different resonant frequency which needs to be set in the control software by performing an auto tune process that oscillates the probe across a range of frequencies and locks into the resonant peak. The actuator then 'dithers' the cantilever near or below its fundamental oscillation frequency. Various parameters can be adjusted while scanning to optimise the quality of the image. The scan size and offsets can be altered, as well as the scan speed, for example in order to be able to scan smaller areas with higher resolution. A final, and important parameter, is the set-point which is the value that the height feedback loop will maintain during the scans. This usually should be about 80% of the free amplitude (amplitude when not touching the sample surface). Since the tip moves back and forth over the same line, two traces are obtained, these should ideally closely match each other, if not, then the set-point needs to be tuned until they approximately agree.

5.3.12 Scanning Electron Microscopy

The operation of an SEM in the context of electron beam lithography was described in chapter 5.3.5. An SEM can be used for high spatial resolution imaging of materials or devices. It uses a focused high energy (1-100keV) electron beam and raster scans it over a sample. At each spot where the sample is hit by the electron beam, the electrons lose energy by multiple random scattering events and electron absorption within a teardrop shaped volume, as shown in figure 58. The size of this teardrop depends on the electron's impact

energy and the material it is incident on. Low energy secondary electrons are emitted from inelastic scattering. The high-energy electrons from the electron beam, can be reflected or back-scattered from the sample by elastically scattering with the sample's atoms. Electrons backscatter stronger with heavy elements than light ones, therefore detecting backscattered electrons can be used to differentiate between regions with different chemical compositions in a sample. The intensity of the secondary electrons is directly related to the atomic composition and geometry of the features in the sample. In the light of this it is clear that the SEM is still a surface analysis method, similar to AFM, but with a much higher spatial resolution down to a couple of nanometers. It is also capable taking images from different angles and exploring the 3D structure of samples. As for EBL, the SEM chamber must be at a high vacuum in order to be able to operate the field emission gun.

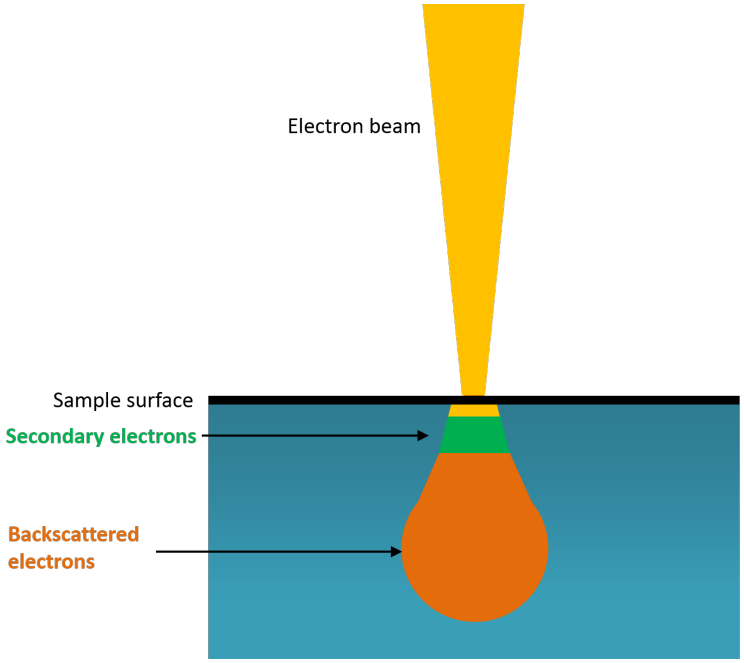

Figure 58: A sketch of the electron beam-sample interaction as the main electron beam hits a spot on the sample.

An extension to the SEM technique is energy dispersive x-ray analysis (EDX or sometimes EDS). EDX takes advantage of the fact that an inner shell electron can get excited when the electron beam hits the sample.. This creates a hole that is filled by an electron from a higher energy shell, with the emission of an X-ray whose wavelength is characteristic for the atomic structure of the emitting element [156]. When an SEM is fitted with an appropriate solid state energy dispersive X-ray detector, it can analyse the energy and intensity of these collected X-rays. Results from an EDX measurement are typically plotted as a graph of counts versus energy and, using a catalogue of known spectra, one can deduce the elemental composition of a sample.

5.4 Electronic measurement methods

The interest of this project has been primarily focused on the electronic properties of graphene, as outlined in the chapter 3. In addition, resistance-temperature measurements have been employed to accurately determine the Tc of a superconductor. This section describes the electronic measurement techniques used, included a discussion of how the sample and appropriate apparatus was prepared and how the measurement equipment was used and controlled.

5.4.1 Packaging and wire bonding

The multiple-device substrates fabricated using the methods described in chapter 5.3 scribed with a diamond scriber and manually cleaved into individual devices. Two types of packages were routinely used. The first of these is a 20 pin 'leadless' package which makes contact to the rest of the sample probe via a socket, whose spring-loaded pins make contact to gold pads on the leadless package. The latter has a gold base which can be bonded to one of the pins to provide a back gate voltage to the device. The second package is similar, but is not leadless, and has 20 pins in a dual in-line configuration which fit into a matching socket. These sockets connect the device to the sample holder and from there to a connection box and the measurement apparatus. Schematics of both of these carriers are shown in in figure 59.

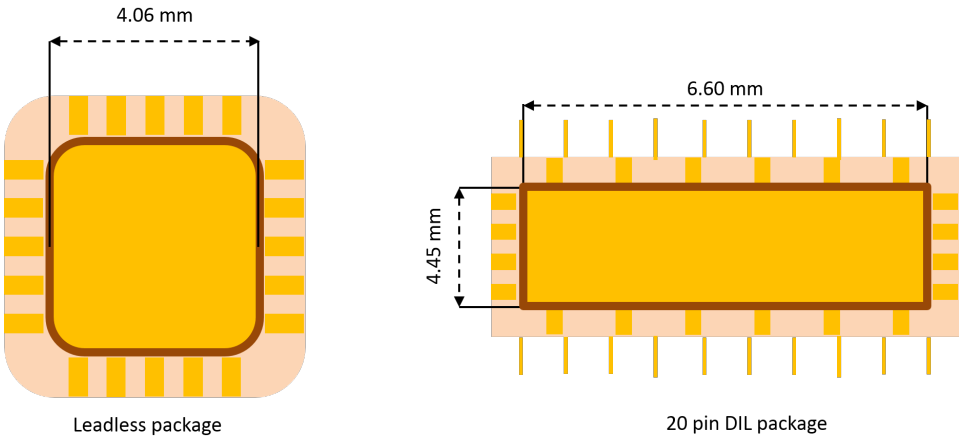

Figure 59: Schematics of the two different types of chip packages most frequently used during the project.

For graphene based devices where the carrier density needed to be tuned, a small part of the oxide layer on the bottom of the chip was scratched off to make electrical contact to the ground plane of the package for a back gate voltage. Insulating GE varnish was painted around the edges of the chip to avoid shorts between bond wires and any exposed silicon. The device was then stuck into a 20 pin package with conducting silver paint and wire bonded with 25μm gold wires to the package pins. Slabs of insulating ceramic were sometimes used to elevate the device above the highest point of the package in the

event that any surface mapping needed to be performed, e.g. AFM/MFM. If the sample was to be cooled to lower temperatures, a conducting epoxy adhesive was generally used as it is more robust under thermal cycling. The wire bonder uses a combination of heat, pressure and an ultrasonic pulse to bond wires without the need for more traditionally used solders, allowing for much better micrometer-level precision. The two most commonly used methods are 'wedge' and 'ball' bonding. In our case 'wedge' bonding is used whereby the bond wire is pressed between the foot of a wedge tool and the gold bond pad, a ultrasonic pulse and heating is then applied to then weld the wire to the pad. The free end of the wire can then be moved in a straight line to the next bond position and the process repeated. At this point a clamp closes on the wire and it breaks at the bond tail. The completed package is then pushed into the package holder on the end of the sample insert which is then loaded into the cryostat where all measurements are performed.

5.4.2 Sample holder and cryostat

The end of the sample holder consists of the package socket, which is either a spring loaded leadless package socket, or a 20 pin dual-in-line package socket. Wires then run through the interior of the insert in twisted pairs and link via a connector to a 20 core cable with grounded shielding. This is terminated at a box with BNC connectors, from where individual BNC cables lead to the measurement equipment (as shown in figure 60) to perform electronic data collection.

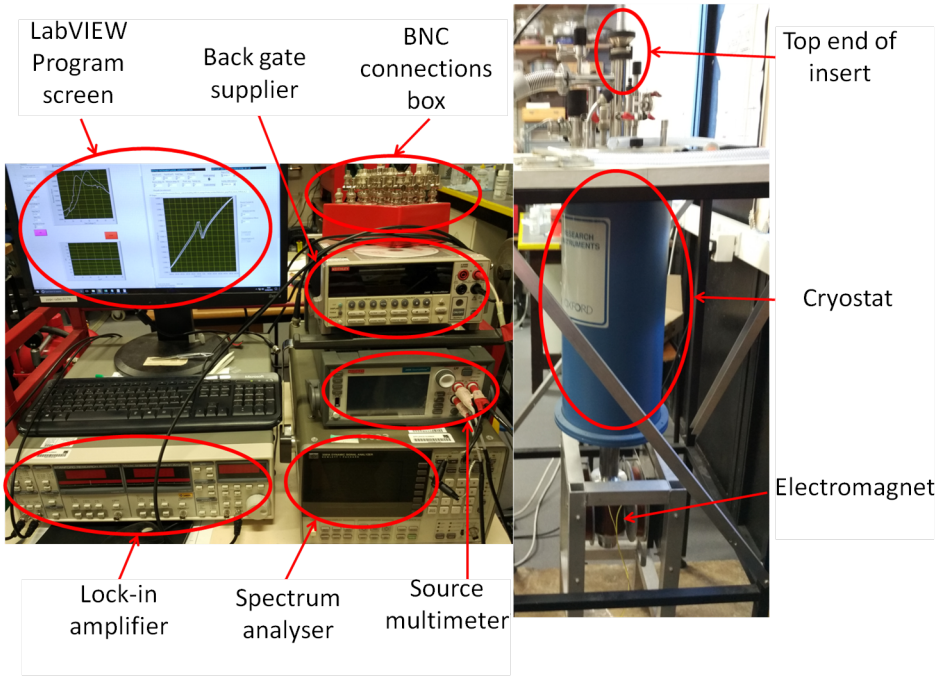

Figure 60: Image of the electronic characterisation setup. The top of the insert has a female Lemo connector which allows a 20 pin shielded cable to be plugged in via a male Lemo connector, linking the sample to a home-built connection box with 20 BNC terminals.

The insert lowers the sample into the cryostat so that it is positioned in the centre of a 35mT electromagnet. The insert is then joined to a connection box with multiple BNC sockets for cabling to source-measurement units, a low noise amplifier and lock-in amplifiers. An Oxford instruments low temperature cryostat is used to evacuate the sample space and isolate devices from the ambient atmosphere, and allow us to cool to 77K (following the same process as described in chapter 5.1.1) and bring to a vacuum the sample space. A rotary pump is used to pump this space down to approximately 10^{-2}mbar, followed by a turbo pump down overnight to approximately 10^{-6}mbar. We find that this is sufficient time to desorb e.g. water molecules from the surface of devices.

Low temperature R-T measurements were performed using a LabVIEW program which controls a Lakeshore temperature controller and a Stanford Research SR380 digital lock-in amplifier. A heater coil located around the sample space enabled a controlled 2K per minute cool down with liquid nitrogen from 300K down to 77K, while the SR380 measured the sample voltage with a known fixed current to calculate the resistance.

5.4.3 Hall measurements

A LabVIEW program was designed to automatically perform Hall measurements using a programmable bipolar power supply for the electromagnet, and source-measurement unit (SMU) to supply a fixed dc current drive to the Hall sensor and measure the Hall voltage in a conventional 4-lead configuration (c.f. figure 11). The flowchart in figure 61 describes the automated measurement process for collecting Hall data. The back gate voltage is set manually with a second Keithley SMU and systematically changed while the Hall voltage sweep is repeated at each value.

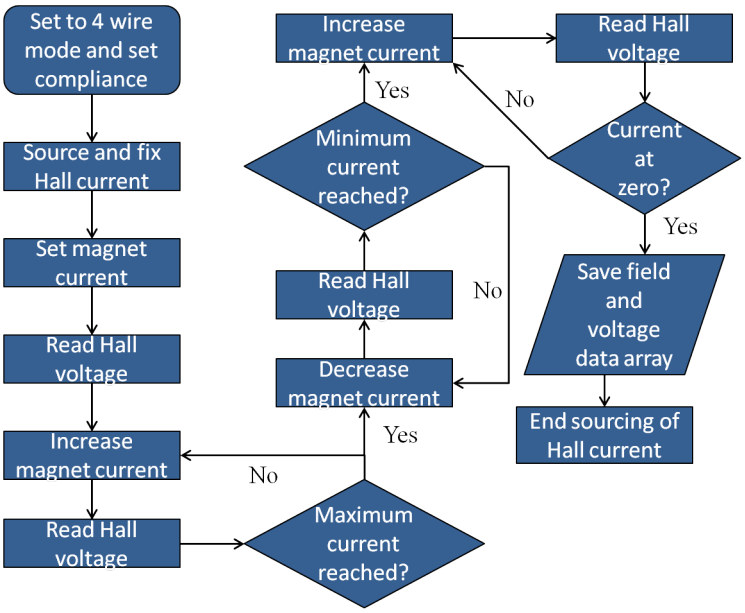

Figure 61: Flow chart of the labVIEW program to obtain Hall voltage data.

5.4.4 Back gate measurements

To locate the DP of graphene devices, the resistance was measured for each value of back gate voltage applied. In this case an ac current source was created from the signal output of the lock-in amplifier by connecting large resistor in series with the device. A 0.5MΩ resistor was chosen so that an output voltage of 5V produces the desired 10μA source current. This value of resistor was chosen were used because the maximum output voltage of the lock-in amplifier is 5V, so to ensure that a reasonable current range from 10μA down to 100nA was used we selected a 0.5MΩ resistor. The Hall voltage leads were then connected to the differential input of the same lock-in. A LabVIEW code reads the voltage from the lock-in amplifier automatically at each programmed back gate voltage which is slowly ramped up and down at a user-defined rate. The resistance is calculated from the entered (but manually set) ac drive current, and plotted on monitor. For two wire-measurements (i.e., ones including contact resistances) the just the single 'A' input of the SR380 was used, whereas for four-wire measurements (e.g., when measuring Hall voltages), the two 'A' and 'B' inputs were used in differential mode.

5.4.5 Low frequency noise measurements

For low frequency noise measurements, the Hall cross was driven by a low noise current source (powered by two 9V batteries to reduce 50Hz mains pick-up), and the voltage was amplified by 10001x with an ultra-low noise amplifier. This amplifier was based on an Analog Devices AD625 programmable gain instrumentation amplifier, which has a very low voltage noise of $4nV/\sqrt{Hz}$ at 1kHz. The drive current was altered by a potentiometer which, for the given choice of resistors allowed currents from 1.34μA to a maximum of 308μA. The output of the amplifier (the amplified Hall voltage) is then fed into the HP3561A dynamic signal analyser. This provided a plot of the spectral frequency content of the signal in the range 1Hz to 100kHz,ultimately being limited by the frequency-dependence of the AD625 amplifier gain Typically about 100 spectrum analyser traces were averaged to suppress the scatter in the data as shown in figure 12. A disadvantage is that the analyser only provides 401 points. In combination with the measurement bandwidth, this makes it better for us to make the frequency range 1kHz as this is the region of interest for our SHPM. Using a labVIEW code, the data from the spectrum analyser can be dumped to a text file, which can be read and re-plotted using a graphical software package. As with Hall measurements, the back gate is set manually and gradually altered by a separate Keithley SMU, after which the program is repeated. A basic schematic of the set-up is shown in figure 62.

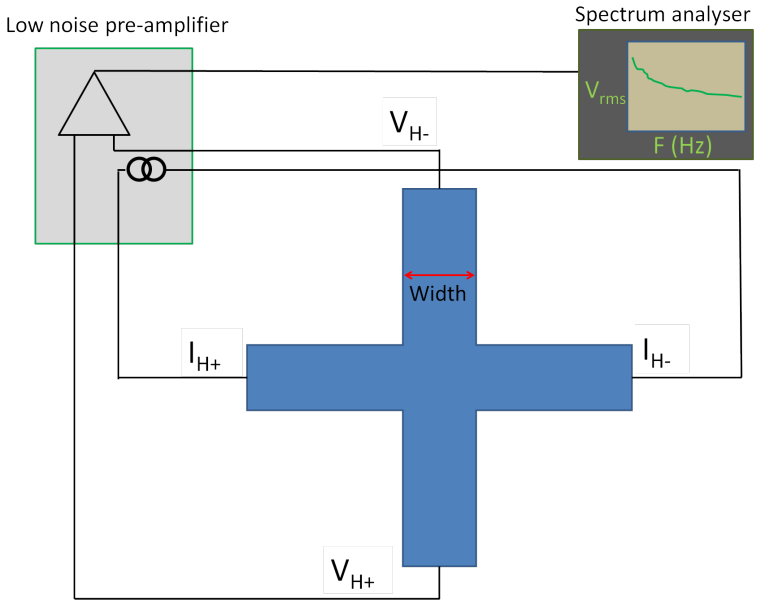

Figure 62: A sketch of the noise measurement set-up, showing the connections made to the Hall cross.

6 Development and characterisation of Nanoscale CVD graphene Hall probes

It is clear from the electronic performances described in chapter 3 that graphene has what it takes to become the Hall sensor material of the next generation of SHPMs. Graphene so far has shown promising nanofabrication versatility and protection layers can be incorporated above the graphene layer for devices operating in ambient or potentially harmful conditions. This chapter explores graphene's potential as a material for nanoscale magnetic imaging and investigates the suitability of hydrogen silsesquioxane (HSQ) as a protective and potentially performance-enhancing layer for graphene Hall devices.

6.1 Development of nanoscale graphene Hall probes

6.1.1 Preamble on nanoscale Hall probes

The guarantee that graphene would be an ideal candidate for the Hall probe component of a nanoscale SHPM is not assured, however, especially since graphene Hall devices with potential nanoscale spatial resolution have not been extensively tested or optimised. The first step should therefore be to characterise the performance of graphene Hall probes with respect to the desired spatial resolution and benchmark the key figures of merit for an SHPM against previous materials. The following section presents a published paper describing the performance of CVD graphene Hall probes with wire widths ranging from 50nm wire to 1500nm.

This declaration concerns the article entitled: **Nanoscale graphene Hall sensors for high-resolution ambient magnetic imaging**				
Publication status				
Draft	Submitted	In review	Accepted	Published ✓
Reference	D. Collomb, P. Li, S. J. Bending. Nanoscale graphene Hall sensors for high-resolution ambient magnetic imaging. Scientific Reports **1** 023029 (2019)			
Candidate's contribution to the paper	The candidate performed most of the fabrication of the devices as well as the majority of the data collection. The candidate was involved significantly in the interpretation of results, and performed most of the data analysis. Figures for the manuscript were produced by the candidate. The candidate wrote the manuscript with assistance and feedback from S.J.B. and P.Li. • Formulation of ideas: 75% • Design of methodology: 85% • Experimental work: 95% • Computational work: N/A • Presentation of data in journal format: 90%			
Statement from candidate	This paper reports on original research I conducted during the period of my Higher Degree by Research candidature.			
Signature	[redacted]		Date	01/09/2020

6.1.2 Nanoscale graphene Hall sensors for high-resolution ambient magnetic imaging

This page is available in the following languages:

Creative Commons License Deed

Attribution 4.0 International (CC BY 4.0)

This is a human-readable summary of (and not a substitute for) the license.

You are free to:

Share — copy and redistribute the material in any medium or format

Adapt — remix, transform, and build upon the material

for any purpose, even commercially.

The licensor cannot revoke these freedoms as long as you follow the license terms.

Under the following terms:

Attribution — You must give appropriate credit, provide a link to the license, and indicate if changes were made. You may do so in any reasonable manner, but not in any way that suggests the licensor endorses you or your use.

No additional restrictions — You may not apply legal terms or technological measures that legally restrict others from doing anything the license permits.

Notices:

You do not have to comply with the license for elements of the material in the public domain or where your use is permitted by an applicable exception or limitation.

No warranties are given. The license may not give you all of the permissions necessary for your intended use. For example, other rights such as publicity, privacy, or moral rights may limit how you use the material.

SPRINGER NATURE

Title:	Nanoscale graphene Hall sensors for high-resolution ambient magnetic imaging
Author:	David Collomb et al
Publication:	Scientific Reports
Publisher:	Springer Nature
Date:	Oct 8, 2019

Creative Commons

SCIENTIFIC REPORTS
nature research

OPEN

Nanoscale graphene Hall sensors for high-resolution ambient magnetic imaging

Received: 19 June 2019
Accepted: 19 September 2019
Published online: 08 October 2019

David Collomb, Penglei Li & Simon J. Bending

A major challenge to routine non-invasive, nanoscale magnetic imaging is the development of Hall sensors that are stable under ambient conditions and retain low minimum detectable fields down to nanoscale dimensions. To address these issues we have fabricated and characterised chemical vapour deposition (CVD) graphene Hall sensors with wire widths between 50 nm and 1500 nm, in order to exploit the high carrier mobility and tuneability of this material. The measured Hall voltage noise is in good agreement with theoretical models and we demonstrate that minimum detectable fields at fixed drive current are lowest in the vicinity of the charge neutrality point. Our best performing deep sub-micron sensors, based on a wire width of 85 nm, display the excellent room temperature resolution of 59 μT/√Hz at a dc drive current of 12 μA and measurement frequency of 531 Hz. We observe a weak increase in minimum detectable field as the active sensor area is reduced while the Hall offset field is largely independent of size. These figures-of-merit significantly surpass prior results on larger probes in competing materials systems, with considerable scope for further optimisation. Our results clearly demonstrate the feasibility of using CVD graphene to realise very high spatial resolution nanosensors for quantitative room temperature magnetic imaging.

Magnetic field sensors are used for a very wide variety of purposes, including but not limited to; biosensing, instrumentation and process calibration as well as high precision magnetic field mapping such as Scanning Hall Probe Microscopy (SHPM) and magnetic susceptometry[1–5]. Although there are many different approaches to magnetic sensing, Hall-effect sensors have frequently been employed due to their high magnetic field sensitivities, quantitative linear response, non-invasive performance and fabrication versatility. This allows them to be used in a range of applications where other semi-quantitative and potentially invasive sensor types, such as magnetic force microscopy (MFM) cantilevers, may not meet requirements[6]. They are also much more compact and simple to use than the recently developed diamond Nitrogen vacancy (NV) centre magnetic microscope, which requires precisely fabricating a single crystal diamond with an NV center at the apex of an AFM tip as well as additional lasers and microwave excitation[7]. The fabrication of Hall probes based on nanoscale wire widths allows high spatial resolution mapping applications to be realised. This requirement is increasingly in demand due to the rapid miniaturisation of modern technologies, for example ultra-high density magnetic storage media or magnetic domain-wall racetrack memory. However, such probes have a much broader range of potential imaging applications including combined high-resolution topographic and magnetic imaging of vortices in superconductors and domains/domain walls in ferromagnetic films based on SHPM with scanning tunnelling microscopy (STM) or atomic force microscopy (AFM) surface tracking. Through the addition of field excitation coils they can also be used to perform highly local magnetic susceptometry.

To attain higher spatial resolution for these smaller scale applications, the active area of the Hall probe must be reduced while retaining sufficiently low minimum detectable fields. In Table 1 we summarise the performance of previously reported Hall probes, including the estimated spatial resolution the sensor would have in magnetic imaging applications.

Probes based on GaAs heterostructures are the material of choice for low temperature imaging but, as reflected in Table 1, their electronic properties deteriorate undesirably at room temperature[8]. In addition, edge depletion effects make it very challenging to achieve suitably high spatial resolution devices on the order of hundreds of nanometres or below, with no Hall crosses yet demonstrated below 100 nm[8]. High quality epitaxial growth of InSb-based probes is challenging and active layers are typically buried ≥50 nm below the epilayer surface[1]. The

University of Bath, Claverton Down, Bath, BA2 7AY, United Kingdom. Correspondence and requests for materials should be addressed to D.C. (email: d.collomb@bath.ac.uk)

Hall material	R_H (Ω/T)	I_H (μA)	f (Hz)	B_{min} (μT/√Hz)	X_{min} (μm)
GaAs quantum well[8]	1100	100	277	1000	0.8
InSb thin film[1]	370	100	200	0.72	0.5
InSb thin film[9]	300	300	N/A	0.08	1.25
Bi thin film[10]	1.81	73	30	900	0.1
Bi thin film[11]	4	40	1000	80	0.05
Epitaxial graphene[36]	640	10	3300	49.3	0.5
CVD graphene[18]	800	100	3000	0.5	15
CVD graphene[19]	2093	200	3000	0.1	50
CVD graphene (this work)	140	12	531	59	0.085

Table 1. A comparison of previous Hall probe architectures at room temperature and low measurement frequencies. The figures of merit include, when applicable, the Hall coefficient, R_H, the drive current, I_H, the measurement frequency, f, the minimum detectable field, B_{mim}, and the estimated spatial resolution based on the wire width, X_{min}.

device reported in ref.[1] was also fabricated in a 320 nm thick InSb film leaving little scope for further reduction in size[1,9]. This is detrimental for applications such as SHPM, where the active layer must be as close to the sample surface as possible to achieve the highest spatial resolution. Bismuth probes have demonstrated reasonable 300 K resolutions, yet these suffer from poor chemical and mechanical stability and the reproducible growth of Bi films is challenging[10,11], making them unsuitable for extended operation under ambient conditions.

In contrast, graphene's low carrier density, tolerance to nanoscale pattering, mechanical and chemical stability and its unique band structure, whereby massless Dirac Fermions exhibit extremely high room temperature mobilities, make it an ideal contender for high-resolution nanoscale Hall probes[12]. Being atomically thin it also allows the active probe to get extremely close to samples under study, enabling very high spatial resolution mapping. Looking towards the more routine fabrication of graphene-based Hall devices, chemical vapour deposition (CVD) holds promise as a facile growth technique for the scalable fabrication of large arrays of sensors[13,14]. In addition, once transferred to an appropriate insulating substrate, graphene is a much easier material to pattern at the nanoscale than alternative Hall probe materials; a lithography mask can readily be used to transfer a Hall cross pattern by etching in a simple O_2 plasma. Monolayer CVD graphene is now readily available and is the obvious choice for the scaleable production of graphene-based Hall effect sensors[15]. Combined with a back gate dielectric such as SiO_2, the carrier density and type can also be tuned, allowing an additional 'tool' for optimising minimum detectable fields that has not previously been available.

Micrometer-sized graphene Hall probes have been extensively studied in recent years, showing impressive figures-of-merit, with some of the best reported probes shown in Table 1. However, investigations of Hall sensors with nanoscale active areas, i.e., <1 μm wire widths as required for high spatial resolution magnetic imaging, have not been reported[16–19]. Studies of the mobility of graphene devices with nanoscale dimensions have shown a decrease from ~3000 cm^2/Vs for probes greater than 100 nm to <200 cm^2/Vs for probes smaller than 20 nm. A rapid decrease in mobility due to edge scattering tends to set in below 60 nm[20].

However, we demonstrate that the figures-of-merit of CVD graphene nanosensors significantly surpass those based on competing materials with much larger dimensions. We have studied the influence of wire width, w, on the minimum detectable field, B_{min}, and systematically investigated the impact of increasing drive currents and varying carrier density and carrier type. These critical variables have previously either been overlooked or studies have produced inconclusive results[16–19]. We establish the practical limitations for nanoscale CVD Hall sensors and ascertain the optimal measurement conditions for real-world high spatial resolution imaging applications.

Estimation of the minimum detectable field. The Hall voltage from our sensors contains several intrinsic sources of noise with different characteristic frequency dependencies. At low frequencies this is dominated by "1/f noise" whose power density is inversely proportional to the measurement frequency. The origin of 1/f noise in graphene Hall devices has been the subject of several experimental studies[21–23], and it is widely accepted that it arises from 'exchange noise' due, for example, to carrier capture and release at traps in the SiO_2 gate dielectric leading to fluctuations in the carrier density, n[24]. A second contribution arises from 'configuration noise' due to rearrangement of adjacent trapped charges which modify the disorder potential landscape, leading to fluctuations in the carrier mobility, μ[24,25]. However, as the measurement frequency is increased the 1/f noise power drops below the frequency-independent Johnson noise power at a characteristic noise corner as plotted schematically in Fig. 1. The latter arises due to the thermally excited motion of charge carriers within the sensor, and its magnitude depends on the resistance of the Hall voltage leads.

The low frequency (below the 1/f noise corner) transverse voltage noise power limit for our 2D Hall sensors can be described using the conductivity fluctuation model proposed by L. K. J. Vandamme *et al.*[26]

$$S_Q^{1/f} = \frac{I_H^2 \rho_{xx}^2 \alpha}{AFfn}, \tag{1}$$

where I_H is the drive current, ρ_{xx} the longitudinal resistivity, α a dimensionless constant (expected to be on the order of 10^{-3}), A is the contact-free surface area, F is a geometric factor (~1 for a cross with the aspect ratio of 5:1 used here) and f is the measurement frequency.

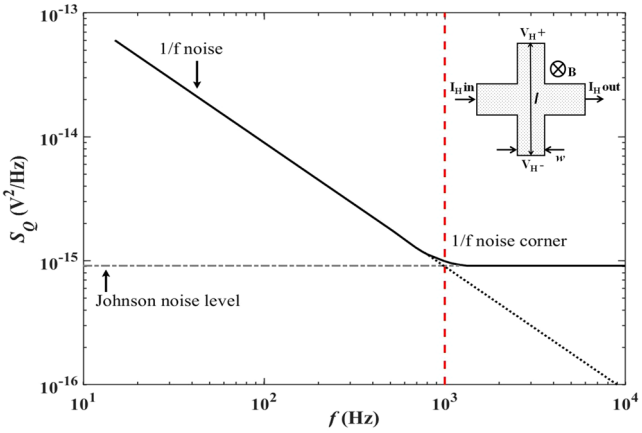

Figure 1. Schematic frequency dependence of the noise power in Hall devices with extrapolated lines indicating the behaviour of Johnson noise and 1/f noise below and above the 1/f noise corner. The inset shows a sketch of a typical Hall cross indicating the current leads, Hall voltage leads and their dimensions.

Well above the 1/f noise corner the Johnson noise power per unit bandwidth is given by

$$S_Q^J = 4R_{vv}k_BT, \tag{2}$$

where R_{vv} is the resistance between the Hall voltage contacts and T is the temperature. Comparing Eqs (1) and (2) we see that 1/f noise depends strongly on the Hall probe current, I_H, while the Johnson noise is independent of it. Hence the position of the 1/f corner (and the dominant noise mechanism) varies with the sample current, moving to higher frequencies as the current is increased. As a consequence the minimum detectable field at a fixed measurement frequency will depend strongly on the current density and can be defined by

$$B_{min} = \frac{\sqrt{S_Q\Delta f}}{R_H I_H}, \tag{3}$$

where Δf is the measurement bandwidth and R_H is the Hall coefficient given by

$$R_H = \frac{1}{nq} = \frac{1}{I_H}\frac{\delta V_H}{\delta B}. \tag{4}$$

Here V_H is the measured Hall voltage and B is the applied magnetic field. Using the standard expression for the resistivity, $\rho_{xx} = 1/ne\mu$, in the low frequency limit described by Eq. (1) this yields

$$B_{min}^{1/f} = \frac{1}{\sqrt{n}\,e\mu}\sqrt{\frac{\alpha\Delta f}{AFf}}, \tag{5}$$

while in the high frequency limit defined by Eq. (2) we find

$$B_{min}^{J} = \frac{1}{I_H}\sqrt{\frac{n}{\mu}}\sqrt{\frac{4lek_BT\Delta f}{w}}, \tag{6}$$

where l is the length and w the width of the Hall voltage contacts as illustrated in the inset of Fig. 1.

In practice it is well established that the carrier mobility in CVD graphene implicitly depends on the carrier density, n[27]. Assuming $\mu \sim 1/n^{\eta}$ we find the following limiting dependencies on carrier density, current and frequency in both limits.

$$B_{min}^{1/f} \propto \frac{n^{(\eta-0.5)}}{\sqrt{f}}, \tag{7}$$

and

$$B_{min}^{J} \propto \frac{n^{(\eta/2+0.5)}}{I_H}. \tag{8}$$

In practice, upon fitting transconductance curves for all our devices we find $\eta \sim 0.6$, suggesting that scattering by neutral impurities is dominant in our structures[28]. Hence we expect the coefficient of carrier density to lie somewhere between the limiting values of ~0.1 and ~0.8, while the coefficient of Hall current will lie between 0 and −1.

Results and Discussion

Hall sensor transfer characteristics. Transfer characteristics ($R_{DS}(V_{GS})$) of the graphene Hall crosses were measured in 2-lead configuration across pairs of Hall voltage leads. A typical curve is shown in Fig. 2 for a CVD graphene Hall cross based on a 1000 nm wire width immediately after fabrication. All of our devices were found to be quite heavily hole doped ($n_h \sim 1.7 \times 10^{16}$–$5.0 \times 10^{16}\,m^{-2}$), with the charge neutrality point (CNP) up to and sometimes beyond $V_{GS} = +100$ V before post-fabrication annealing.

We estimate a field-effect mobility for our Hall cross devices from $\mu_{FE} = \frac{t}{\epsilon_r \epsilon_0} \frac{d\sigma_{DS}}{dV_{GS}}$, where σ_{DS} is the conductivity determined from transfer curves for the known geometry of the graphene segment, t is the gate oxide thickness and ε_r the relative permittivity of the SiO_2 gate oxide. The extracted mobilities range from 5100 cm^2/Vs for a 1000 nm wire width cross down to 840 cm^2/Vs for a 50 nm cross measured after annealing in the hole-doped regime at $V_g - V_{DP} = +7$ V. The lower mobility of nanoscale devices is a consequence of the increasing role of edge disorder as the perimeter: surface area ratio increases, and is also seen in graphene nanoribbons[20]. An asymmetry between hole-doped and electron-doped regimes was observed in many devices and ascribed to the different scattering mechanisms affecting the charge carriers in graphene, such as the presence of charged-defects from transfer and fabrication processes which lead to the preferential scattering of one carrier type[29]. Another potential source of the carrier-type asymmetry arises from the metal contacts; charge transfer from the metal to graphene can lead to p-p or p-n junctions[30].

Hall coefficient and Hall voltage noise characterisation. It has been shown in previous studies that the maximum magnetic sensitivity is found just either side of the CNP[31]. The carrier density is calculated from Eq. (4) using the Hall coefficient obtained from traces of the Hall voltage measured as a function of magnetic field, such as in Fig. 3(a).

Treating graphene and the doped Si substrate as the plates of a capacitor the surface charge density induced by a back gate voltage can be described by the parallel plate capacitor equation. For the general case of graphene with extrinsic doping this yields

$$n = \frac{\epsilon_r \epsilon_0}{te}(V_{GS} - V_D), \tag{9}$$

where t is the thickness of the gate oxide with relative permittivity ϵ_r and V_D is the gate voltage at the CNP. The effect of the graphene quantum capacitance can be ignored at room temperature since it is several orders of magnitude larger than the classical gate oxide capacitance in series with it. Figure 3(b) confirms that the net carrier concentration depends linearly on the back gate voltage, as expected.

Figure 4(a) shows Hall voltage noise power as a function of frequency in the range 1 Hz to 1 kHz for a 1500 nm Hall cross at several different fixed drive currents. For all currents the spectrum is dominated by 1/f noise at low frequencies, with a 1/f noise corner of about 300 Hz at the lowest 2 μA drive current. The 1/f noise level increases substantially as the drive current is increased and the corner frequency rapidly moves above our maximum measurement frequency. For comparison Fig. 4(b) plots the noise power per unit bandwidth for a much smaller 85 nm Hall sensor at several drive currents, when in all cases we observe a 1/f noise spectrum across our entire measurement window. Comparing the noise spectra of smaller and larger devices, we note that larger probes generally have lower corner frequencies than smaller ones as expected.

Despite being the subject of several experimental studies, there does not appear to be a consensus on how the low-frequency noise depends on carrier density in graphene, and several different relationships have been reported[21–23]. For devices which are fully in the $1/f$ limit, using known ρ_{xx} values, we calculate the value of α in Eq. (1) to be on the order of $\sim 10^{-3}$ as expected.

Figure 5(a) shows that the measured Hall voltage noise of our devices as a function of carrier concentration tends to diverge as the CNP is approached from above or below, and both pre- and post-annealed datasets appear to sit on a single universal curve. Figure 5(b) is a plot of the carrier density dependence of B_{min} for the same 400 nm Hall cross with a fixed current of 2 μA, showing that away from the CNP the data are well described by the $n^{0.1}$ dependence predicted by Eq. (7) in the 1/f noise-dominated limit. Empirically we find that the lowest minimum detectable fields at a constant drive current are located at about $\pm 2.5 \times 10^{15}\,m^{-2}$ either side of the CNP.

Optimisation of B_{min} via the drive current. In previous Hall probe architectures, it has been shown that B_{min} could be optimised by increasing the drive current (or current density, J_H). For large sensors, that are initially closer to the thermal noise limit, B_{min} starts to increase again if the current is raised beyond this optimum point[1,6]. Figure 6 plots B_{min} at 531 Hz as a function of J_H for two different sized probes after scaling by a fractional power of n in order to collapse the data onto a single universal curve. For the 100 nm probe the same $n^{0.1}$ density noise scaling is found as for the 400 nm probe in Fig. 5. However the larger 800 nm probe is much closer to being in the Johnson noise limit and, as expected, we find a stronger $n^{0.4}$ scaling in this case. Both data sets show a decrease in B_{min} as J_H increases from zero, with a noticeably weaker dependence in the smallest sensor. We have quantified this by making fits to the data of the form $1/J_H^{\beta}$ (dashed lines), and find $\beta = 0.11$ for the 100 nm probe and $\beta = 0.41$ for the 800 nm probe. In practice the Hall voltage offset saturated our low noise preamplifier at higher current densities before the regime of increasing noise levels could be accessed in the larger probe.

B_{min} in all our CVD graphene devices appears to be well-described by $1/J_H^{\beta}$, with values of β ranging from 0.87 for the largest Hall crosses to 0.08 for the smallest sensors studied. This is broadly consistent with our expectations that it will depend as $1/I_H$ in very large sensors in the thermal noise limit (Eq. (8)) and be independent of I_H in very small sensors dominated by 1/f noise (Eq. (7)). In practice the trapping of carriers in the gate dielectric is a thermally activated process which is strongly influenced by the temperature of the carrier population. At high current densities carriers can be heated well above the lattice temperature leading to much higher trapping

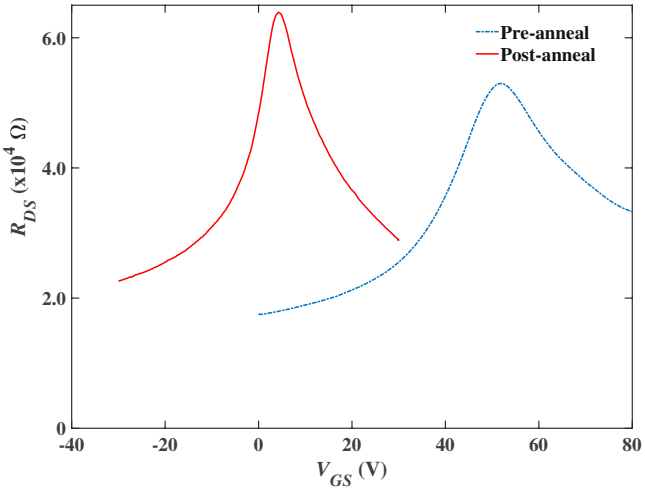

Figure 2. Resistance (R_{DS}) versus back gate voltage (V_{GS}) for a 1000 nm cross before and after the post-fabrication anneal, showing a pronounced downwards shift of the CNP.

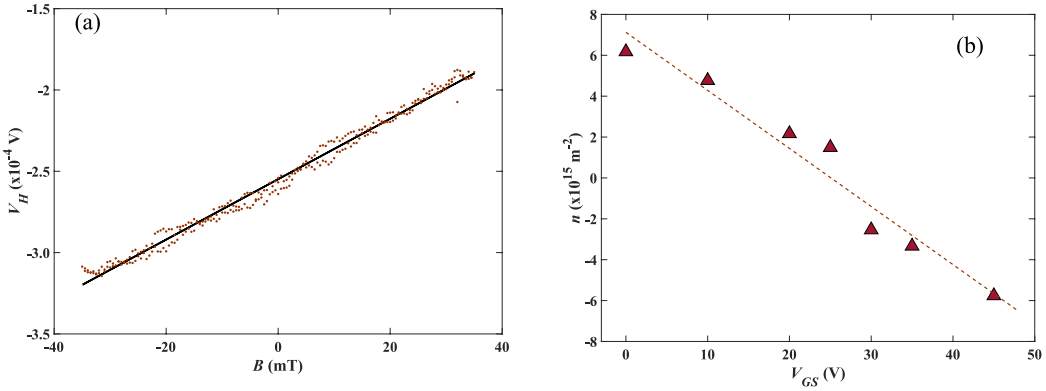

Figure 3. (**a**) A typical Hall voltage versus magnetic field trace at $I_H = 10\,\mu A$ for a 700 nm cross. (**b**) The carrier density, n, calculated from measurements of R_H as a function of V_{GS} for a 700 nm Hall cross with the CNP located at $V_D = 27$ V. The dotted line represents a linear fit to Eq. (9).

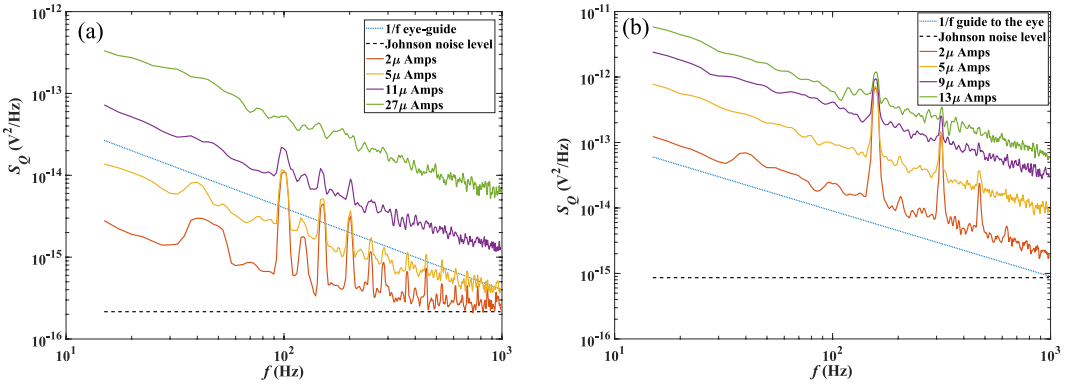

Figure 4. Hall voltage noise power, S_Q, in the range 1 Hz to 1 kHz at various dc drive currents for a 1500 nm (**a**) Hall cross and for a 85 nm (**b**) Hall cross with no applied back gate voltage. The dashed lines indicate the calculated Johnson noise level for the devices. Both structures were measured at similar carrier densities of $n_h \sim 2.5 \times 10^{16} m^{-2}$. Peaks in the very low current spectra arise from 50 Hz (and higher harmonic) pick-up from the 230 V ac mains supply, but since these occur at discrete frequencies they do not influence the underlying 1/f noise dependence.

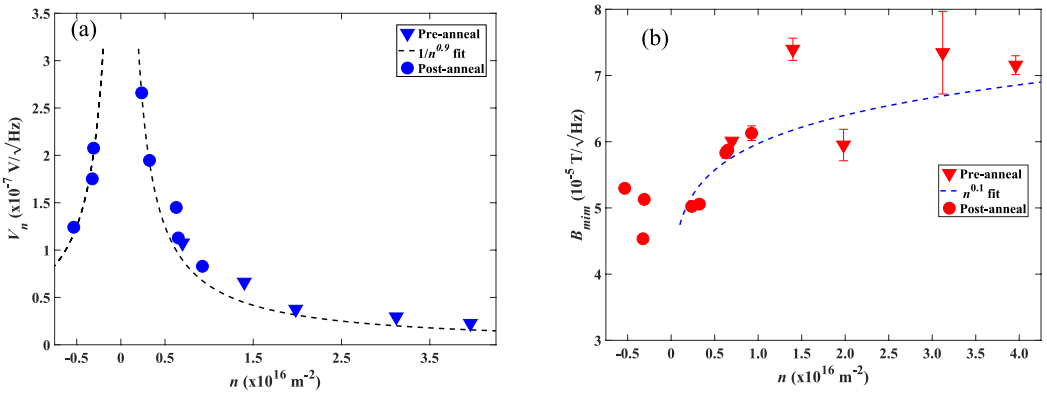

Figure 5. (**a**) The measured Hall voltage noise at 531 Hz with a 2 μA drive current for a 400 nm wire width cross at various carrier concentrations in both the electron- and hole-doped regimes. (**b**) The minimum detectable field for the same cross estimated by inputting the measured Hall-coefficient (from Hall voltage traces such as that in Fig. 3(a)) and the measured Hall voltage noise into Eq. (3). The results are compared with the expected $n^{0.1}$ dependence in the "1/f noise-dominated limit" (dashed line, see text) for the data in the hole-doped regime.

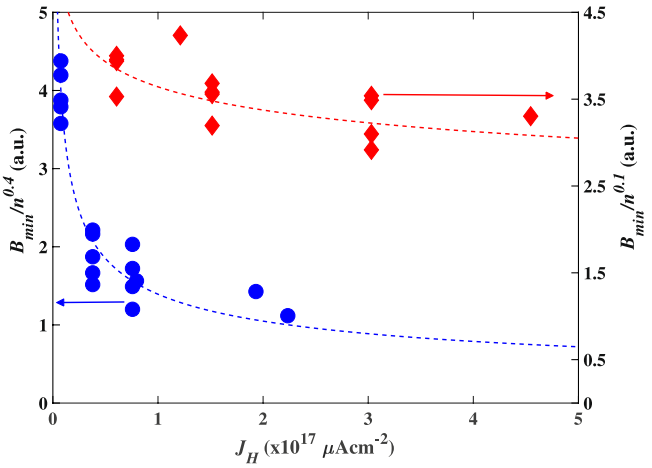

Figure 6. Estimated minimum detectable fields scaled by $n^{0.4}$ for an 800 nm (left axis) and $n^{0.1}$ for a 100 nm (right axis) wire width probe at 531 Hz as a function of drive current density. The dotted lines show a $1/J_H^{0.41}$ fit for the 800 nm probe and a $1/J_H^{0.11}$ fit for the 100 nm probe.

rates, increasing the noise power at a given frequency and shifting the 1/*f* noise corner up to higher frequencies[32]. Hence, even very large sensors should be shifted towards the 1/f noise-dominated regime as the current density is increased.

Upon increasing the drive current, we have obtained our lowest minimum detectable field of 6 μT/√Hz at 30 μA and 531 Hz for a 1000 nm wire width cross, significantly surpassing values achieved in prior works on similar-sized devices[33]. Since B_{min} does not exhibit saturation at the highest current densities used there is evidently still scope for reducing the minimum detectable field still further if the offset voltage could be reduced.

Wire width-dependence of minimum detectable field. Figure 7 indicates that minimum detectable fields for a fixed drive current show a gradual increase as the Hall probe size decreases down to about 85 nm. Results for two different CVD graphene wafers have been compared to indicate the variability that can exist for different CVD growth runs and wet transfers. Otherwise identical devices fabricated from wafer 2 had higher lead-to-lead resistances than wafer 1 for similar carrier densities, leading to higher noise levels and minimum detectable fields. In addition to different concentrations of contaminants that become adsorbed on the graphene during transfer we attribute this to different densities of grain boundaries, other defects and localised impurities formed during CVD growth. The rapid increase in B_{min} observed in the 50 nm Hall cross may indicate that edge scattering is starting to dominate the noise in such small sensors, and would be consistent with the conclusions of previous studies showing that the mobility of graphene nanoribbons begins to drop more rapidly below ~60 nm wire widths[20].

Despite the gradual reduction in performance as the Hall cross size is reduced, our best performing deep sub-micron cross with an 85 nm wire width, exhibits a minimum detectable field of 59 μT/√Hz at a drive current

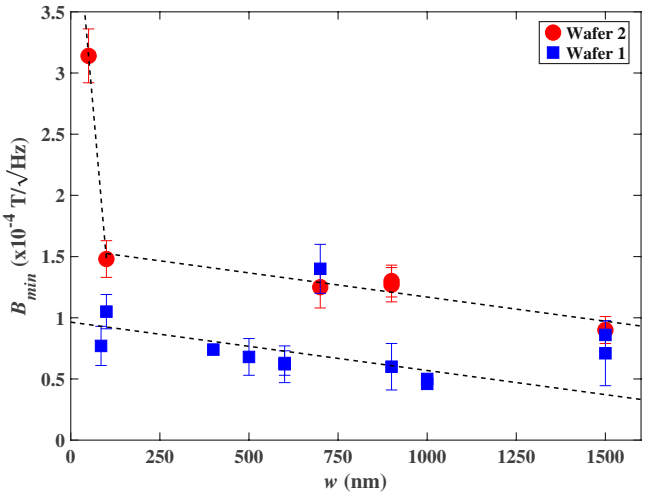

Figure 7. Estimated minimum detectable field as a function of wire width for a fixed drive current of 2 μA at 531 Hz and similar values of R_H in the range 140–180Ω/T. Solid circles and squares indicate samples fabricated from different CVD graphene wafers. Dashed lines are given as a guide to the eye.

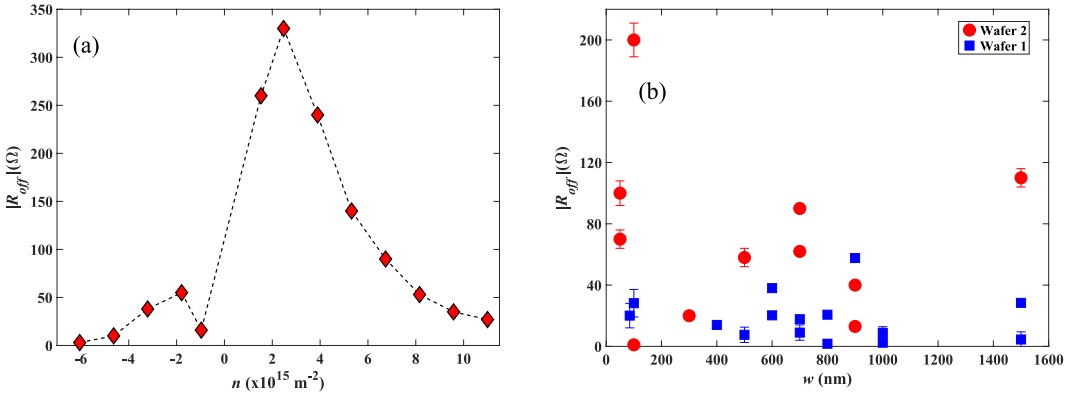

Figure 8. (**a**) Hall offset as a function of n for a 700 nm cross. The dashed line is a guide to the eye. (**b**) Hall offset as a function of device size at similar values of R_H in the range 140–180Ω/T and fixed drive currents of 10 μA for two different graphene wafers.

of 12 μA at 531 Hz, with significant room remaining for improvement by increasing the drive current. This surpasses the optimum figure-of-merit for prior Bismuth Hall probes (~900 μT/√Hz for a 100 nm probe) by more than an order of magnitude[10], paving the way for graphene-based Hall probes to become the state-of-the-art in high spatial resolution room temperature magnetic imaging applications.

Hall offset resistance in graphene devices. An aspect that is frequently overlooked in investigations of Hall sensors is the offset resistance, R_{off}. This is the Hall voltage output when no magnetic field is present, arising due to misalignment of the Hall voltage contacts and inhomogeneous current flow in the active sensor area[34]. In practice it is highly desirable to minimise this to avoid saturating low noise preamplifier stages. In addition, by mixing the longitudinal resistance into the Hall voltage, the offset resistance contributes substantial new sources of noise that ultimately limit the best achievable minimum detectable fields.

Figure 8(a) shows offset voltages were broadly observed to increase in inverse proportion to the carrier density, while around the CNP we frequently observe an abrupt discontinuous change with a rather different behaviour for electron and hole carrier types. In our CVD graphene sensors the offset resistance appears to predominantly arise from spatially inhomogeneous current flows linked to the presence of grain boundaries, wrinkles introduced during transfer, multilayer regions or other defects. The fact that the offset resistance roughly scales with the Hall coefficient suggests that the degree of inhomogenity is approximately preserved as the carrier concentration is changed with a back gate. The different behaviour for the two carrier types is in part to be expected since potential minima for holes become potential maxima for electrons upon crossing the CNP. Certainly, it indicates that the level of current inhomogeneity for holes can be appreciably different to that for electrons.

The potential invasiveness of our Hall probes can be characterised by estimating the self-field using Ampere's law. For a 85 nm probe carrying a 12 μA current, the self-field is estimated to be ~0.5 G at a distance of 50 nm, which is comparable to the earth's magnetic field and hence relatively non-invasive. If the dominant cause of the offset

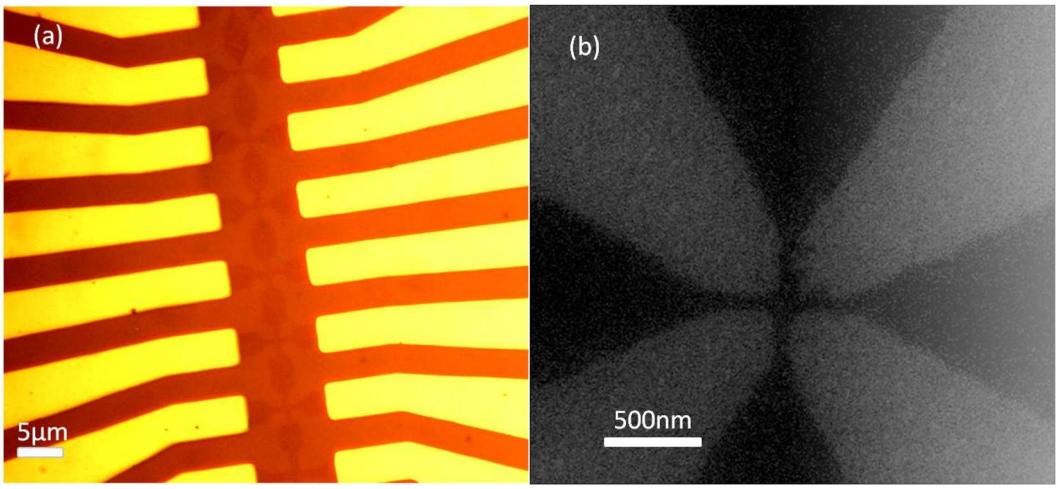

Figure 9. (**a**) Optical micrograph showing part of a fabricated Hall cross array (darker brown) and the inner Cr/Au contact leads (gold). (**b**) An SEM image of an 85 nm CVD graphene Hall cross.

resistance in our devices was linked to grain boundaries, one would expect a substantial reduction in sensors that are very much smaller than a characteristic grain size in CVD graphene (~10 µm). However, this is not supported by the data for R_{off} as a function of wire width in Fig. 8(b), which shows no strong evidence for a systematic size dependence. This suggests that the current inhomogeneity still occurs on a length scale much finer than the smallest sensors fabricated here, possibly as a result of disorder introduced via graphene transfer to the SiO_2 substrate.

Conclusion

We have demonstrated that CVD graphene can be used to fabricate nanoscale Hall sensors for state-of-the-art high spatial resolution magnetic imaging. Their minimum detectable fields can be optimised by tuning the carrier concentration with a back gate to values of about $\pm 2.5 \times 10^{15}\,m^{-2}$, just either side of the charge neutrality point. Hall probe performance can be still further improved by increasing the drive current, leading to figures-of-merit that significantly surpass those of competing Hall sensor structures, e.g., a minimum detectable field of $59\,\mu T/\sqrt{Hz}$ for an 85 nm wire width sensor at 531 Hz at a 12 µA drive current. Advances in highly quality CVD graphene growth and transfer methodologies, combined with the rather simple fabrication processes for deep sub-micron probes, makes them extremely attractive for high-resolution magnetic imaging applications such as SHPM and magnetic susceptometry. A dramatic improvement in the performance of exfoliated graphene devices after encapsulation is well documented and we expect to be able to achieve much better figures-of-merit in sensors encapsulated with hBN[19], although achieving this with CVD graphene remains a major challenge. The introduction of these improvements should make nanoscale graphene Hall sensors the quantitative tools of choice for high resolution magnetic imaging under ambient conditions.

Experimental Section

Hall cross array fabrication. Hall probe arrays were fabricated from CVD graphene purchased from Graphene Supermarket, which had been grown on a copper foil and wet-transferred onto a highly-doped Si substrate with a 285 nm thick SiO_2 surface gate oxide. An optical micrograph of a CVD graphene Hall cross array and the Cr/Au inner contact leads is shown in Figure. 9(a), while an SEM micrograph of a deep sub-micron Hall cross based on an 85 nm wire width is shown in Figure. 9(b). Hall crosses based on the intersection of wires of widths in the range 50–1500 nm, with length-to-width aspect ratios of five, have been systematically investigated.

Contact pads were defined by direct-write laser lithography in Shipley S1813 optical photoresist. The exposed CVD graphene in the developed window was then ICP-etched in an Oxygen plasma, followed by the deposition of 20 nm of Cr and 250 nm of Au by electron beam evaporation and lift-off. Inner contact leads were then defined by laser lithography, followed by the deposition of 5 nm of Cr, 70 nm of Au and lift-off.

To achieve the best lateral resolution, the fabrication of nanoscale Hall probes made use of a bilayer Poly(methyl methacrylate) (PMMA)/Hydrogen Silsesquioxane (HSQ) electron beam resist as an etch mask. PMMA was first spin coated at a thickness of 100 nm, and baked at 150 °C for 15 minutes. A 2% solution of negative tone HSQ from Dow corning was then spin coated to form a 30 nm thick layer and baked for 5 minutes at 150 °C. A 30 kV field emission Hitachi S-4300 scanning electron microscope (SEM) integrated with the Raith ELPHY Plus electron beam lithography system was used to pattern the Hall cross arrays in HSQ with an exposure dose of $500\,\mu Ccm^{-2}$. After development in Tetramethylammonium hydroxide (TMAH) the unprotected PMMA and graphene were ICP-etched away in an O_2 plasma. The HSQ mask was subsequently lifted-off by dissolving the PMMA layer in acetone under light sonication.

Post anneal treatment. We utilise a post-fabrication anneal in inert Argon gas at 200 °C for 6 hours to reduce extrinsic doping due to any low molecular weight contaminants adsorbed on the graphene during the

fabrication process. Annealing temperatures up to 400 °C have been widely report in the literature[35], but we find that such high temperatures lead to hardening of the gold contact pads making them very difficult to wire bond. This post-fabrication annealing step successfully reduces the extrinsic (hole) doping level, shifting the graphene CNP by up to −60V.

Device characterisation. A portion of the oxide layer on the bottom of each chip was scratched away to allow a contact to be made for the application of a back gate voltage. Each chip was glued into a 20-pin leadless ceramic package using conducting silver paint. Contact pads were bonded to the package pins with 25 µm diameter gold wires using an ultrasonic wedge bonder. The sample package was then inserted in to a spring-loaded holder at the end of a sample rod which fitted inside a commercial Oxford Instruments cryostat. A Cu-wound solenoid mounted on the tail of the cryostat was driven by a programmable bipolar Kepco power supply, generating a maximum magnetic field of 37.5 mT perpendicular to the plane of the Hall cross. A turbo pump was used to evacuate the sample space to ~10^{-6} mbar to remove adsorbed water molecules and other volatile surface contaminants and all measurements were made at ambient temperature.

Two-lead Resistance (R_{DS}) - back gate voltage (V_{GS}) measurements were performed using a Stanford Research Systems SR830 digital lock-in amplifier to provide a 10 µA, 32 Hz AC current and detect the resulting AC voltage, and a Source Measure Unit (SMU) provided the back gate voltage. A Keithley 2450 (SMU) in 4-wire configuration was employed to characterise the Hall coefficient and Hall offset of devices using a 10 µA DC current. The Hall voltage noise was characterised using a battery-driven DC current source and an ultra-low-noise preamplifier with 10^4 gain, whose output was recorded at set Hall currents using a HP3561A dynamic signal analyser (DSA). Noise spectra were measured in the range 1 Hz – 1 kHz with a bandwidth of 1 Hz and averaged 100 times to reduce scatter.

Data Availability

All data captured in the course of this research work are openly available from the University of Bath Research Data Archive at https://doi.org/10.15125/BATH-00587.

References

1. Sandhu, A., Sanbonsugi, H., Shibasaki, I., Abe, M. & Handa., H. High sensitivity InSb ultra-thin film micro-hall sensors for bioscreening applications. *Jpn. J. Appl. Phys.* **43**, 868 (2004).
2. Thiaville, A., Belliard, L., Majer, D., Zeldov, E. & Miltat, J. Measurement of the stray field emanating from magnetic force microscope tips by Hall effect microsensors. *J. Appl. Phys.* **82**, 3182–3191 (1997).
3. Oral, A., Bending, S. J. & Henini, M. Real-time scanning Hall probe microscopy. *Appl. Phys. Lett.* **69**, 1324–1326 (1996).
4. Ketchen, M. B., Kopley, T. & Ling, H. Miniature SQUID susceptometer. *Appl. Phys. Lett.* **44**, 1008–1010 (1984).
5. Sandhu, A., Iida, N., Masuda, H., Oral, A. & Bending, S. J. Room temperature scanning Hall probe microscopy of localized magnetic field fluctuations on the surfaces of magnetic recording media, permanent magnets and crystalline garnet films in external bias fields. *J. Magn. Magn. Mater.* **242**, 1249–1252 (2002).
6. Oral, A. Scanning Hall Probe Microscopy: Quantitative & Non-Invasive Imaging and Magnetometry of Magnetic Materials at 50 nm Scale. In *Magn. Nanostruct*. Springer, 7–14 (Berlin, Heidelberg, 2007).
7. Pelliccione, M. *et al*. Scanned probe imaging of nanoscale magnetism at cryogenic temperatures with a single-spin quantum sensor. *Nat. Nanotechnol.* **11**, 700 (2016).
8. Vervaeke, K., Simoen, E., Borghs, H. & Moshchalkov, V. V. Size dependence of microscopic Hall sensor detection limits. *Rev. Sci. Instrum.* **80**, 074701 (2009).
9. Gregory, J. K., Bending, S. J. & Sandhu, A. A scanning Hall probe microscope for large area magnetic imaging down to cryogenic temperatures. *Rev. Sci. Instrum.* **73**, 3515–3519 (2002).
10. Mohammed, H. A. & Bending, S. J. Fabrication of nanoscale Bi Hall sensors by lift-off techniques for applications in scanning probe microscopy. *Semicond. Sci. Technol.* **29**, 085007 (2014).
11. Sandhu, A., Kurosawa, K., Dede, M. & Oral, A. 50 nm Hall sensors for room temperature scanning Hall probe microscopy. *Jpn. J. Appl. Phys.* **43**, 777 (2004).
12. Geim, A. K. Graphene: status and prospects. *Science* **324**, 1530–1534 (2009).
13. Li, X. *et al*. *Science* **324**, 1312–1314 (2009).
14. Xu, H. *et al*. Batch-fabricated high-performance graphene Hall elements. *Scientific Reports* **3**, 1207 (2013).
15. Wu, X. *et al*. Growth of continuous monolayer graphene with millimeter-sized domains using industrially safe conditions. *Scientific Reports* **6**, 21152 (2016).
16. Tang, C. C., Li, M. Y., Li, L. J., Chi, C. C. & Chen, J. C. Characteristics of a sensitive micro-Hall probe fabricated on chemical vapor deposited graphene over the temperature range from liquid-helium to room temperature. *Appl. Phys. Lett.* **99**, 112107 (2011).
17. Xu, H. *et al*. Flicker noise and magnetic resolution of graphene hall sensors at low frequency. *Appl. Phys. Lett.* **103**, 112405 (2013).
18. Huang, L. *et al*. Ultra-sensitive graphene Hall elements. *Appl. Phys. Lett.* **104**, 183106 (2014).
19. Dauber, J. *et al*. Ultra-sensitive Hall sensors based on graphene encapsulated in hexagonal boron nitride. *Appl. Phys. Lett.* **106**, 193501 (2015).
20. Yang, Y. & Murali, R. Impact of size effect on graphene nanoribbon transport. *IEEE Electron Device Lett.* **31**, 237–239 (2010).
21. Zhang, Y., Mendez, E. E. & Du, X. Mobility-dependent low-frequency noise in graphene field-effect transistors. *ACS Nano* **5**, 8124–8130 (2011).
22. Pal, A. N. & Ghosh, A. Ultralow noise field-effect transistor from multilayer graphene. *Appl. Phys. Lett.* **95**, 082105 (2009).
23. Kaverzin, A. A., Mayorov, A. S., Shytov, A. & Horsell, D. W. Impurities as a source of 1/f noise in graphene. *Phys. Rev. B* **85**, 075435 (2012).
24. Pal, A. N. *et al*. Microscopic mechanism of 1/f noise in graphene: Role of energy band dispersion. *ACS Nano* **5**, 2075–2081 (2011).
25. Jindal, R. P. & der Ziel, V. A. Model for mobility fluctuation 1/f noise. *Appl. Phys. Lett.* **38**, 290–291 (1981).
26. Vandamme, L. K. J. & De Kuijper, A. H. Conductance noise investigations on symmetrical planar resistors with finite contacts. *Solid-State Electron.* **22**, 981–986 (1979).
27. Zion, E., Butenko, A., Sharoni, A., Kaveh, M. & Shlimak, I. Charge carrier transport asymmetry in monolayer graphene. *Phys. Rev. B* **96**, 245143 (2017).
28. Das Sarma, S., Adam, S., Hwang, E. H. & Rossi, E. Electronic transport in two-dimensional graphene. *Rev. Mod. Phys.* **83**, 407 (2011).
29. Bai, K. K. *et al*. Detecting giant electron-hole asymmetry in a graphene monolayer generated by strain and charged-defect scattering via Landau level spectroscopy. *Phys. Rev. B* **92**, 121405 (2015).

30. Huard, B., Stander, N., Sulpizio, J. A. & Goldhaber-Gordon, D. Evidence of the role of contacts on the observed electron-hole asymmetry in graphene. *Phys. Rev. B* **78**, 035101 (2008).
31. Chen, B. *et al*. Exploration of sensitivity limit for graphene magnetic sensors. *Carbon* **94**, 585–589 (2015).
32. Balandin, A. A. Low-frequency 1/f noise in graphene devices. *Nat. Nanotechnol.* **8**, 549 (2013).
33. Sonusen, S., Karci, O., Dede, M., Aksoy, S. & Oral, A. Single layer graphene Hall sensors for scanning Hall probe microscopy (SHPM) in 3–300 K temperature range. *Appl. Surf. Sci.* **308**, 414–418 (2014).
34. Popović, R. S. Hall-effect devices. *Sens. Actuators* **17**, 39–53 (1989).
35. Hong, J. *et al*. Origin of new broad Raman D and G peaks in annealed graphene. *Scientific Reports* **3**, 2700 (2013).
36. Panchal, V. *et al*. Small epitaxial graphene devices for magnetosensing applications. *J. Appl. Phys.* **111**, 07E509 (2012).

Acknowledgements

We acknowledge financial support from EPSRC in the UK under grant nos. EP/R007160/1 and the Nanocohybri COST Action CA-16218. DC is supported by a PhD studentship from Lloyds Register Foundation ICON (award nos. G0086). We acknowledge access to the University of Bath Nanofabrication Facility where device fabrication has been performed as well as training and process support from Dr. Stephen Wedge and Dr. Siva Sivaraya.

Author Contributions

S.B. conceived the study. D.C. designed the devices. D.C. fabricated the Hall probe devices. D.C. performed electrical characterisation. D.C. interpreted the data with assistance from P.L. and S.B. D.C. wrote the manuscript and prepared all figures. All authors reviewed the manuscript and provided feedback.

Additional Information

Competing Interests: The authors declare no competing interests.

Publisher's note Springer Nature remains neutral with regard to jurisdictional claims in published maps and institutional affiliations.

6.1.3 Discussion of nanoscale Hall probes

The research in this paper shows that graphene is a very suitable candidate for deep submicron and nanoscale Hall probes. We show that CVD graphene remains competitive down to 50nm despite the possible reduction in performance when dropping below 85nm in size due to the increasing importance of 'edge' noise sources. The onset of the electron-hole puddles defining boundary of the optimum magnetic sensitivity is found around $\pm$3V from the Dirac point. These results show that graphene is an ideal candidate for the active Hall probe material for the next generation of SHPMs. However, the probes could still be further improved for possible SHPM applications by protecting or encapsulating them for use under ambient conditions. This leads us into the following section of the chapter.

6.2 Development of hydrogen silsesquioxane capped graphene Hall devices

6.2.1 Preamble on hydrogen silsesquioxane capped graphene Hall devices

While the results from chapter 6.1.2 demonstrate that graphene has the ideal figures of merit to be the active component of an SHPM, there are further enhancements that can be made. Looking towards combining the scanning Hall technique with AFM techniques under ambient conditions, the graphene layer will need to be protected from possible environmental damage or degredation. Recalling previous experiments outlined in chapter 2 one may see hBN as an ideal candidate to act as the protection layer for the graphene. On the other hand, the methods used in chapter 6.1.2 to fabricate nanoscale Hall probes using HSQ etch masks suggest an opportunity to make protected graphene devices which are more scalable (through the use of CVD graphene and spinning large areas of HSQ) and can be readily integrated with reliable fabrication techniques. By removing the PMMA layer beneath the HSQ, the HSQ layer can become a permanent cap above the CVD graphene layer. The HSQ can be patterned in the usual way with EBL and any unwanted graphene etched away in an O_2 plasma. Although HSQ was expected to provide some form of protection, it was unclear if the performance of graphene Hall devices encapsulated with it would improve or deteriorate [153]. Furthermore, with HSQ as a capping layer the method of making contact to the graphene device should be revisited. Standard top contacts to the graphene layer can still be made, but the possibility of realising one dimensional edge contacts is an interesting alternative and the performance of the two approaches may vary considerably. It is hence important to first compare the performance of HSQ capped graphene devices using different contact methods. By investigating the performance of capped graphene devices with different thicknesses of HSQ it is also possible to probe the reasons for any performance changes.

This second section presents a paper describing the results of investigations into the effect of using HSQ as a capping layer for CVD graphene Hall devices as well as different methods to make Ohmic contacts. The primary figure of merit used to compare devices with and without graphene is the Hall mobility and results are corroborated with supporting Raman measurements. The candidate made conceptual inputs to this study and contributed to the research work by setting up the Hall mobility measurement apparatus and control systems. The candidate also performed a small number of Hall measurements on HSQ capped devices

to corroborate previously taken measurements and confirm the correct operations of the measurement apparatus.

<table>
<tr><td colspan="5">This declaration concerns the article entitled:
High quality hydrogen silsesquioxane encapsulated graphene devices with edge contacts</td></tr>
<tr><td colspan="5">Publication status</td></tr>
<tr><td>Draft</td><td>Submitted</td><td>In review</td><td>Accepted</td><td>Published ✓</td></tr>
<tr><td>Reference</td><td colspan="4">P. Li, D. Collomb, S. J. Bending. High quality hydrogen silsesquioxane encapsulated graphene devices with edge contacts. Materials Letters 1 023029 (2019)</td></tr>
<tr><td>Candidate's contribution to the paper</td><td colspan="4">The candidate made minor contributions to the conception of the study. The candidate contributed by taking part in setting up the Hall mobility measurement apparatus and systems. The candidate made a small amount of Hall measurements on HSQ capped devices to corroborate previously taken measurements and the working of the measurement apparatus. The candidate provided feedback on the results and the completed manuscript.
Formulation of ideas: 5%
Design of methodology: 10%
Experimental work: 5%
Computational work: N/A
Presentation of data in journal format: 0%</td></tr>
<tr><td>Statement from candidate</td><td colspan="4">This paper reports on original research I conducted during the period of my Higher Degree by Research candidature.</td></tr>
<tr><td>Signature</td><td colspan="2">[redacted]</td><td>Date</td><td>01/09/2020</td></tr>
</table>

6.2.2 High quality hydrogen silsesquioxane encapsulated graphene devices with edge contacts

Title: High quality hydrogen silsesquioxane encapsulated graphene devices with edge contacts

Author: Penglei Li,David Collomb,Simon Bending

Publication: Materials Letters

Publisher: Elsevier

Date: Available online 3 October 2019

Materials Letters 257 (2019) 126765

Contents lists available at ScienceDirect

Materials Letters

journal homepage: www.elsevier.com/locate/mlblue

High quality hydrogen silsesquioxane encapsulated graphene devices with edge contacts

Penglei Li *, David Collomb, Simon Bending

Department of Physics, University of Bath, Claverton Down, Bath BA2 7AY, UK

ARTICLE INFO

Article history:
Received 3 August 2019
Received in revised form 3 September 2019
Accepted 1 October 2019
Available online 3 October 2019

Keywords:
Carbon materials
Chemical vapour deposition
Edge contact
Graphene
Hydrogen silsesquioxane
Mobility

ABSTRACT

A simple process has been developed to fabricate chemical vapor deposition (CVD) graphene devices that are encapsulated by hydrogen silsesquioxane (HSQ) and addressed via edge contacts. Ohmic contacts are achieved with a contact resistance of approximately 540 Ω·μm. The upper graphene surface is protected by HSQ from the very first processing step allowing device fabrication to be performed without any impairment of carrier mobility. On the contrary, mobility enhancements have been observed after HSQ encapsulation. This approach not only effectively protects devices from the ambient environment but could also be important for enabling HSQ-assisted transfer of graphene and other 2D materials.

1. Introduction

Chemical vapor deposition (CVD) graphene has immense potential in large-scale applications, including electronics, optoelectronics and sensing [1–4]. However, graphene sheets can easily be damaged during multiple fabrication steps, especially when there are already defects, holes, cracks and wrinkles present [5], which is often the case for CVD graphene. As a result, the fabrication yield starting with CVD graphene can be low, and the device performance compromised if the layer has been damaged. One strategy [6,7] is to create a sandwich structure with CVD graphene contained within two layers of hexagonal boron nitride (hBN). However, the required step-by-step transfer is challenging and the final device size limited by the overlap of the CVD graphene and the top and bottom layers of (CVD) hBN. In this letter, we describe a simple fabrication process for CVD graphene devices which are encapsulated by hydrogen silsesquioxane (HSQ) and addressed via edge contacts [6,8,9]. HSQ is widely used as a negative tone electron beam resist due to its sub-5 nm resolution capability [10] and has, for example, been used to pattern graphene nanoribbons [11,12]. It is standard practice to remove HSQ after device pattering using highly toxic hydrofluoric acid (HF) solution in order to expose the graphene for contact deposition. We demonstrate here that the removal of HSQ is not necessary if edge contacts are implemented. This effectively makes the fabrication process much simpler and safer and, importantly, actually leads to an enhancement of the carrier mobility in graphene after HSQ encapsulation.

2. Experimental

Fig. 1 illustrates the process of edge contact formation in HSQ/Graphene devices. Pre-transferred CVD graphene on n-Si/SiO2 (300 nm) wafers was used as received from Graphenea (Fig. 1(a)). 2% and 6% HSQ (Dow Corning XR-1541) were spin coated on CVD graphene and then baked at 150 °C for 5 mins to form 30 and 80 nm thick films, respectively. Samples were then immediately patterned using electron beam lithography (EBL) with an acceleration voltage of 30 kV. After EBL, samples were developed in 25% Tetramethylammonium hydroxide (TMAH) for 10 s with a subsequent rinse in DI water and IPA, for 1 min each (Fig. 1(b)). To make edge contacts a Heidelberg uPG101 direct laser writer (DLW) with 25 mW laser power was used to expose a window in Shipley S1813 photoresist, which was then developed for 35 s in Microposit 351 developer and rinsed in DI water (Fig. 1(c)). An inductively coupled plasma (ICP) etch recipe has been developed to remove unwanted graphene and form edge contacts. A CHF_3/O_2 (40:4 sccm) process gas flow at a pressure of 40 mTorr and a RF power of 60 W was introduced into an Oxford ICP 100, and devices etched for 30 s (Fig. 1(d)). Without further treatment, 5 nm Cr and 250 nm Au were deposited in an electron beam

* Corresponding author.
E-mail address: p.li@bath.ac.uk (P. Li).

https://doi.org/10.1016/j.matlet.2019.126765

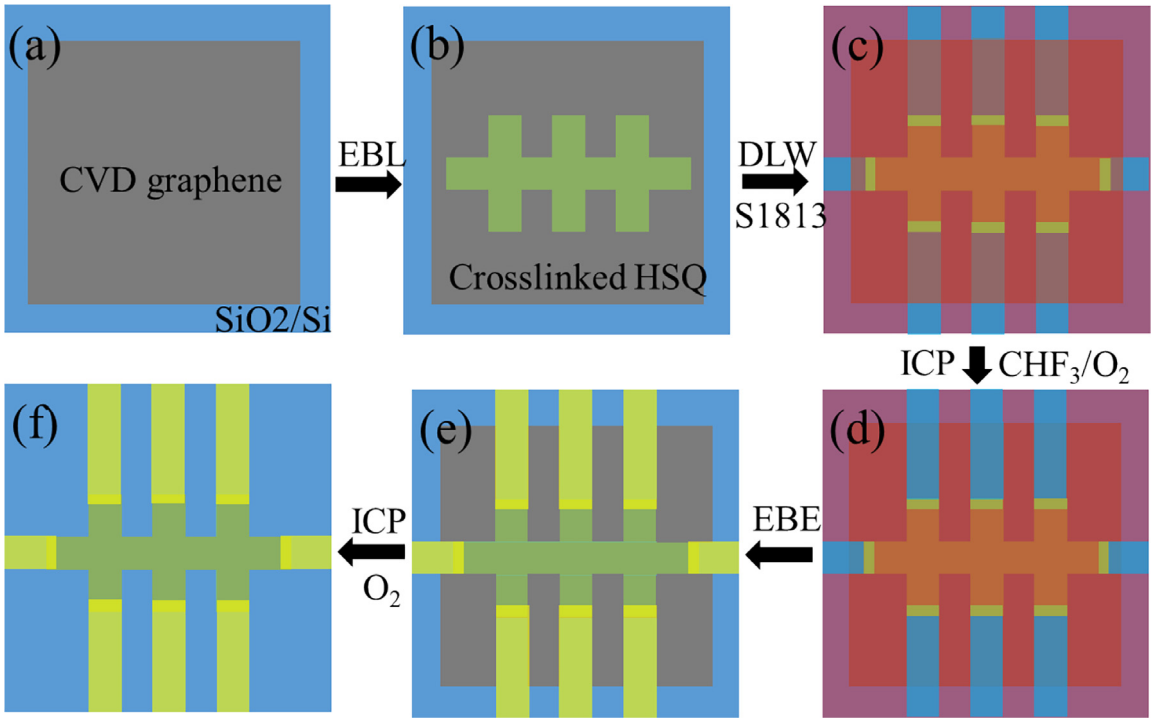

Fig. 1. Schematic plan of fabrication steps for edge contacts to an HSQ-encapsulated graphene device. (a) CVD graphene as received. (b) EBL crosslinked HSQ pattern. (c) DLW pattern in S1813 photoresist to open windows for etching. (d) ICP etching of unprotected graphene to expose edge contacts. (e) E-beam evaporation (EBE) of Cr/Au and lift-off. (f) Second ICP etch to remove remaining graphene, between the metal leads.

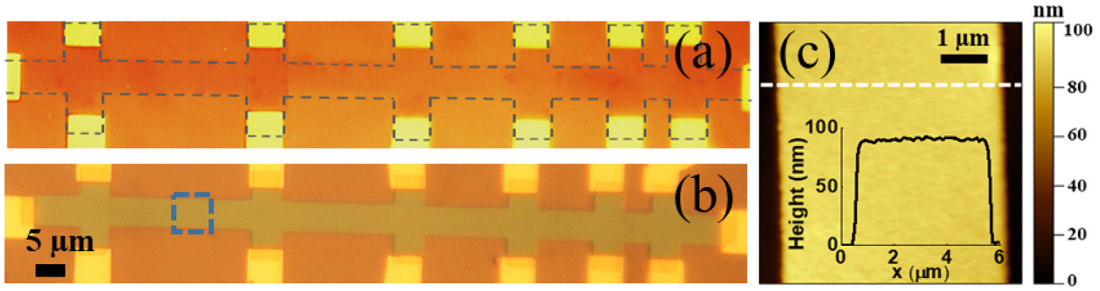

Fig. 2. Optical images of devices (a) without and (b) with HSQ (6%). Dotted lines in (a) indicate the location of graphene. (c) AFM image of region of graphene channel indicated in (b). Inset is a topographic profile across the channel along the dashed line shown.

evaporator (EBE) at a pressure of $\sim 7 \times 10^{-6}$ mbar and lift-off performed in acetone (Fig. 1(e)). Finally, a second ICP etch with only O_2 was performed for 15 s to remove the remaining graphene between the contact electrodes (Fig. 1(f)).

For comparison, conventional surface-contacted devices without HSQ encapsulation (noHSQ) were also fabricated by EBL using a bilayer poly(methyl methacrylate) (PMMA)/HSQ ICP etch mask.

Raman measurements (Fig. S1 in Supporting Information) were performed using a Renishaw inVia confocal Raman microscope with a 532 nm illumination wavelength. Topographic imaging of devices was carried out with an Asylum Research MFP-3D atomic force microscope (AFM) in tapping mode.

Four-wire AC transconductance measurements were performed using a Stanford Research Systems SR830 lock-in amplifier with a 100 nA drive current. Transmission line measurements (TLM) were applied to characterize edge contacts using a Keithley 2450 to measure DC current-voltage characteristics. Hall effect measurements were performed with a 10 μA DC drive current. A perpendicular magnetic field up to 35 mT was generated using a normal electromagnet. All measurements were performed at room temperature under ambient conditions.

3. Results and discussion

Fig. 2(a) and (b) show optical images of Hall bar devices with and without HSQ encapsulation, respectively. Owing to the relatively long channel length (125 μm), the yield of noHSQ device was less than 60% (4 out of 7 devices) due to fragmentation and delamination of the graphene during processing, while it approached 100% (33 out of 35 devices) for HSQ-encapsulated ones. The Graphene/HSQ devices also survived vigorous agitation in an ultrasonic bath during lift-off, if required. This robust protection during device fabrication would be extremely important for making large area devices. Fig. 2(c) shows AFM measurements of the topography of the 6% HSQ device, from which we estimate that the edges exhibit a slope ranging from 25 to 30° to the horizontal, somewhat shallower than the 45° angle typical for hBN-encapsulated devices [6], facilitating the formation of edge contacts during metallization. The etching slope is mainly determined by the material itself, as well as the gases, ICP power and pressure.

Linear I-V characteristics in TLM structures have been observed at all back gate voltages, as shown in Fig. 3(a), confirming Ohmic

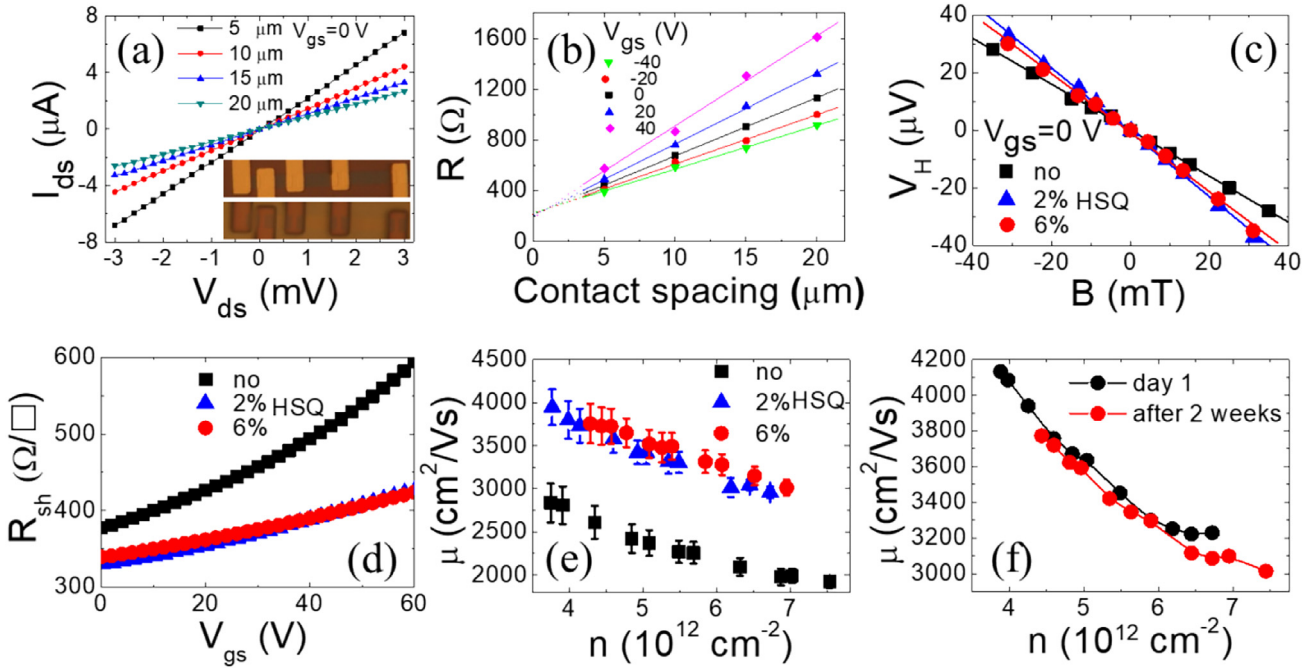

Fig. 3. (a) I_{ds}-V_{ds} for a device with 2% HSQ. Inset are optical images of a TLM structure with edge-contacts: before (upper) and after (lower) metal deposition. (b) Two-terminal resistance measured as a function of contact spacing at different gate voltages. (c) Typical Hall voltage data as a function of magnetic field at V_{gs} = 0 V and (d) sheet resistance as a function of V_{gs}. (e) Hall mobility versus carrier density. Error bars represent mobility variation observed in several different devices. (f) Electrical stability of a typical device in air after 6% HSQ encapsulation.

contact behaviour. The resistances show a good linear dependence on contact spacing (Fig. 3(b)), allowing a contact resistance of 540 Ω·μm to be inferred at V_{gs} = 0 V, which is ~ 1.5 time lower than typical top contacts in our CVD graphene devices.

Fig. 3(c) shows typical plots of Hall voltage (V_{Hall}) versus applied magnetic field (B). The linear behaviour confirms the expected relationship, V_{Hall} = IB/ne, where I is the channel current, e is the electronic charge and n is the 2D carrier density. The Hall mobility, μ, is extracted from the expression σ = neμ, where σ is the conductivity of the graphene channel obtained from transconductance measurements as shown in Fig. 3(d). As calculated in Fig. 3(e), measured Hall mobilities increased from 2840 ± 230 $cm^2 \cdot V^{-1} \cdot s^{-1}$ for noHSQ devices, to 3950 ± 210 $cm^2 \cdot V^{-1} \cdot s^{-1}$ for devices with 2% and 6% HSQ at carrier densities close to 3.7 × 10^{12} cm^{-2}. We attribute the mobility enhancements to the following factors: 1) Since HSQ encapsulation is performed as the first step it protects the graphene from contact with resists and solvents throughout the entire process of device fabrication. Currently the ultimate CVD graphene mobility in our structures is limited by the PMMA-assisted transfer from copper, which introduces defects, cracks, holes and wrinkles [13]. This common PMMA-based method could be replaced by a recently reported paraffin-enabled graphene transfer [14] which has demonstrated significant advantages due to reduced wrinkles and polymer contamination. HSQ-assisted transfer could work in a similar manner but with additional benefits as there is no need to remove HSQ, thus physical protection is achieved at the same time. 2) It is suggested that Coulomb scattering centers are the main cause of the relatively low mobility in CVD graphene devices. Thus HSQ, with a higher dielectric constant of 3 [15] as compared to air in the case of noHSQ, more effectively screens charged impurities in the SiO_2 beneath the graphene [16,17]. Apart from mobility enhancement, HSQ encapsulation lends chemical stability to the graphene devices, leaving them unaffected by severe environmental conditions, and their performance remains unchanged after two weeks, as evidenced in Fig. 3(f).

4. Conclusion

In summary, we have demonstrated that low resistance edge contacts can be fabricated on HSQ-encapsulated CVD graphene devices using a simple process. This approach retains the good pre-processing electronic quality of the graphene and even leads to mobility enhancements over otherwise identical devices without an HSQ overlayer. Since the HSQ does not need to be removed after device fabrication, e.g., using toxic HF, this step can be eliminated making device processing simpler and safer. In addition, our technique can be readily extended to other 2D materials, e.g., environmentally-sensitive ones such as black phosphorus, FeSe and Silicene. It can also be applied to other dielectric materials such as Al_2O_3, HfO_2 and Si_3N_4 where dry etching is possible. Finally, this approach is fully compatible with HSQ-assisted transfer of CVD graphene and other 2D materials, and could hence lead to further significant technological advantages.

Conflicts of interest

None declared.

Declaration of Competing Interest

The authors declare that they have no known competing financial interests or personal relationships that could have appeared to influence the work reported in this paper.

Acknowledgment

This work was supported by the Engineering and Physical Sciences Research Council (EPSRC), UK (Grant No. EP/R007160/1).

Appendix A. Supplementary data

Supplementary data to this article can be found online at https://doi.org/10.1016/j.matlet.2019.126765.

References

[1] X. Li, W. Cai, J. An, S. Kim, J. Nah, D. Yang, et al., Science 324 (5932) (2009) 1312–1314.
[2] A. Reina, X. Jia, J. Ho, D. Nezich, H. Son, V. Bulovic, et al., Nano Lett. 9 (1) (2009) 30–35.
[3] S. Hofmann, P. Braeuninger-Weimer, R.S. Weatherup, Acc. Chem. Res. 6 (14) (2015) 2714–2721.
[4] P. Shen, Y. Lin, H. Wang, J. Park, W.S. Leong, A. Lu, et al., IEEE Trans. Electron Devices 65 (10) (2018) 4040–4052.
[5] S. Deng, V. Berry, Mater. Today 19 (4) (2016) 197–212.
[6] L. Wang, I. Meric, P.Y. Huang, Q. Gao, Y. Gao, H. Tran, et al., Science 342 (6158) (2013) 614–617.
[7] L. Banszerus, M. Schmitz, S. Engels, J. Dauber, M. Oellers, F. Haupt, et al., Sci. Adv. 1 (6) (2015) e1500222.
[8] S.M. Song, T.Y. Kim, O.J. Sul, W.C. Shin, B.J. Cho, Appl. Phys. Lett. 104 (18) (2014) 183506.
[9] D.W. Yue, C.H. Ra, X.C. Liu, D.Y. Lee, W.J. Yoo, Nanoscale 7 (2) (2015) 825–831.
[10] V.R. Manfrinato, L. Zhang, D. Su, H. Duan, R.G. Hobbs, E.A. Stach, et al., Nano Lett. 13 (4) (2013) 1555–1558.
[11] Z.H. Chen, Y.M. Lin, M.J. Rooks, P. Avouris, Physica E 40 (2) (2007) 228–232.
[12] M.Y. Han, B. Özyilmaz, Y. Zhang, P. Kim, Phys. Rev. Lett. 98 (20) (2007) 206805.
[13] A. Hsu, H. Wang, K.K. Kim, J. Kong, T. Palacios, IEEE Electron Device Lett. 32 (8) (2011) 1008–1010.
[14] W.S. Leong, H. Wang, J. Yeo, F.J. Martin-Martinez, A. Zubair, P.-C. Shen, et al., Nat. Commun. 10 (1) (2019) 867.
[15] https://consumer.dow.com/en-us/document-viewer.html?ramdomVar=2752427074889913267&docPath=/documents/en-us/productdatasheet/10/10-713-dow-corning-flowable-oxide-product-info.pdf.
[16] R. Nashed, C. Pan, K. Brenner, A. Naeemi, J. Electron Devices Soc. 4 (6) (2016) 466–472.
[17] L.A. Ponomarenko, R. Yang, T.M. Mohiuddin, M.I. Katsnelson, K.S. Novoselov, S. V. Morozov, et al., Phys. Rev. Lett. 102 (20) (2009) 206603.

6.2.3 Discussion of hydrogen silsesquioxane capped graphene Hall devices

The work described in the paper has demonstrated a significant increase in mobility of HSQ-capped devices. Although there was also a parallel increase in the extrinsic doping level, this should not negatively impact the overall effectiveness of future Hall probe scanners based on HSQ-capped CVD graphene. Results presented in chapter 6 show that the change in the minimum detectable field as carrier concentration changes is negligible. Only applications requiring a large Hall coefficient (magnetic sensitivity) would be significantly impacted. However, for the purposes using this type of sensor for SHPM, the increased mobility would result in lower noise while a lower Hall coefficient can be mitigated via increased amplification of the Hall voltage signal. This not only shows that graphene can be reliably capped with HSQ for scanner operating under ambient conditions in the future but this approach can be used to increase the device yield of sensors designed for any type of operation environment, e.g., UHV and low temperatures.

6.3 Innovating graphene Hall probes

Based on the results of chapter 6.1,SHPMs based on commercial graphene seem to be the clear path forward. However, after fabricating Hall crosses with Ohmic contacts before any mesa etching, it is found that the yield is low with roughly only half of the leads of the set of fabricated SHPMs being conducting. This would defeat one of the main advantages of using CVD graphene over exfoliated graphene. Furthermore, a significant fraction of the leads showing finite conductance have resistances that are too high, leading to unsatisfactory noise levels whereby not even a change of a few mT could be satisfactorily detected. In other cases, where there are enough leads for a Hall configuration, the Hall offset voltage was often found to be too large, such that any compensation voltage applied to the detection electronics to counter the intrinsic offset voltage would not be enough to keep the SHPM Hall voltage signal amplifier from saturating. The reason for these problems cannot be ascribed to one single cause. Contact resistances could play a major role in driving the noise and offset up, but an inability to perform 2-point and 4-point measurements in the Hall configuration means that contact resistances cannot be precisely determined. The quality of the graphene after a significant amount of processing could also be significantly degraded. A completed SHPM probe prior to HSQ removal and mesa patterning is shown figure 63.

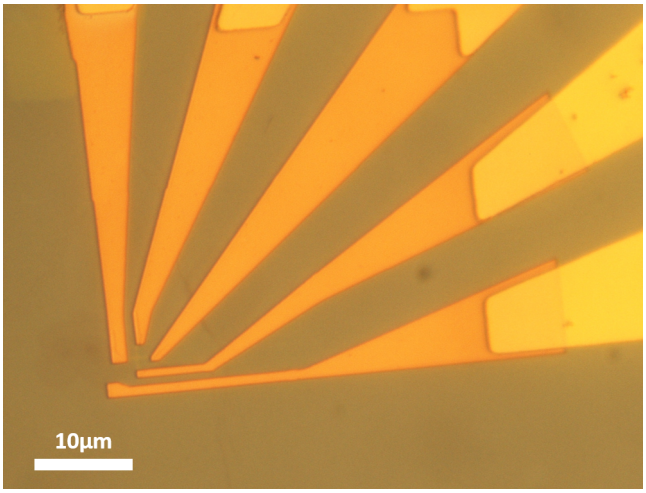

Figure 63: A completed SHPM device with a 0.5μm Hall cross prior to mesa patterning, capped with a HSQ mask layer.

As an attempt to remedy the above issues, SHPMs were fabricated by encapsulating the graphene crosses with HSQ, as described in chapter 6.2. The differences in sizes and exposure doses between the work carried out in chapter 6.2 and for the development of CVD-based SHPMs has resulted in major differences during fabrication. Because the Hall crosses are smaller, the graphene is much less well anchored down onto the substrate. This has resulted in graphene delamination during development which also takes the written resist mask with it. Even with development times as low as a 5s (much lower than the recommended 1 minute) the resist mask is either not well developed, leaving behind HSQ islands, or delaminated graphene ends up covering part of the mask structure, making the fabrication of edge contacts challenging.

These results represent challenges for using CVD graphene as the active material in SHPMs. There are two possible avenues that can be followed to overcome them: encapsulation in hBN or, avoiding etching the CVD graphene and relying on closely patterned gold leads to simulate a similar current flow pattern as one would find in a Hall cross. In this chapter, better graphene SHPM fabrication methods are explored, and encapsulated CVD graphene Hall probes are compared to show how the figures-of-merit can improved by replacing the SiO_2 substrate with hBN.

6.3.1 Encapsulated CVD graphene sensor performance

Since the processes to create 2D material heterostructures were first developed, hBN has emerged as an ideal substrate for many other 2D materials [81], and graphene is now routinely encapsulated with it [77, 6, 43]. The reasons for this in the case of the development of encapsulated Hall probes were outlined in chapter 3.1.3, whereby the higher mobility could lead to a lower low frequency noise contribution to the Hall probe signal-to-noise ratio. Here we briefly explore the performance of a micron sized encapsulated CVD graphene Hall device. We find that encapsulation can greatly improve the Hall probe performance, clearly

indicating that the future of graphene Hall probes lies in encapsulated sensors.

We fabricate the device via a combination of dry stamping of hBN flakes, and the easy wet transfer of CVD graphene provided by the commercial supplier, Graphenea. Pre-pattered outer contacts were first created by standard photolithography, metal deposition and lift-off steps. This included two sets of electron beam lithography alignment marks in the center of each set of outer contacts on the chip. One set of alignment marks is used for a 400 x 400μm write field used to fabricate the inner contacts to the heterostructure. The other set is used for a 100 x 100μm writefield to pattern sub-micron Hall bars in a high resolution negative photoresist. The heterostructure is formed by first transferring a 10-100nm thick flake of hBN close to the center of the 100 x 100μm field. The flake ideally needs to be large enough in its lateral dimensions to pattern a Hall bar with a minimum 4 leads. Using with thicker flakes, this is readily achievable. Normally, when micromechanically exfoliating graphene, achieving large monolayer graphene flakes is challenging and rather time consuming. Keeping the aim of scaleable Hall probe devices in mind, we have used CVD graphene as the source of graphene. Here we have used an 'easy transfer' graphene sheet provided by commercial growers, Graphenea. The process of transferring these sheets is described in chapter 5.3.2. Once transferred, and the protective polymer layer removed, the top hBN flake is dry transferred on top of the hBN and CVD graphene stack to complete the heterostructure. To pattern the Hall bar, the chip holding the heterostructure was first coated with a 100nm PMMA resist layer and baked at 150 degrees for 15 minutes. Next, a thin 30nm layer of HSQ resist was then spun onto the device, and baked at 150 degrees for 5 minutes. The HSQ layer is a negative electron beam resist which acts as an effective hard, dry etching mask to pattern the Hall bar. The PMMA layer's role is to enable lift-off removal of the HSQ mask after etching. The heterostructure stack was etched with a CHF_3 and O_2 RIE plasma, with the etch time dependent on the thickness of the hBN flakes, a typical hBN etch rate being 2-3nm/s. Once etched, electron beam lithography was used again to pattern inner contacts to the Hall bar from the outer contacts, where edge contacts (c.f. chapter 3.1.3) are formed to the micron sized Hall bar. A finished device is shown in the inset of figure 64.

The resistance was first measured as a function of applied back gate voltage. It was found that the Dirac point fell close to zero applied back gate voltage (c.f. figure 64), a large shift down from higher positive biases as compared to the results in chapter 6.1.2 using CVD graphene from the same source. Assuming that the minimum detectable field as a function of carrier density follows the same trend as in chapter 6.1.2, this could be extremely advantageous as the Hall probe will not need a back gate applied to optimise the value of B_{min}. To confirm this, we have performed noise and Hall measurements as a function of carrier density on both sides of the Dirac point (electron- and hole-doped regimes).

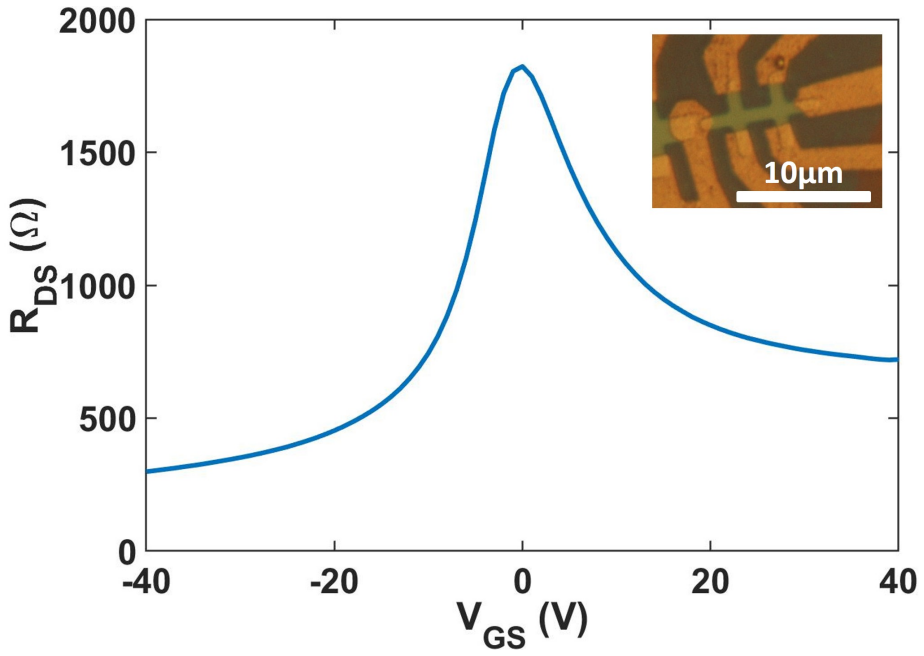

Figure 64: Resistance (R_{DS}) as a function of applied back gate voltage (V_{GS}) for a 1μm wide channel. The inset shows a completed micron-size encapsulated CVD graphene Hall bar device. The longitudinal spacing between voltage contacts is 4μm and the wire width is 1μm.

The highest observed Hall coefficient in encapsulated exfoliated graphene Hall probes varies from over 5000Ω/T in room temperature devices, to 240kΩ/T (-340kΩ/T) in electron (hole) doping regimes at 4.2K [77, 157]. For our device, we measure a maximum of $\sim$-4300Ω/T in the hole regime, and a maximum of $\sim$3300Ω/T in the electron regime. This is not much larger than values obtained for the unencapsulated devices in chapter 6.1.2, suggesting that although the extrinsic doping has been substantially reduced by hBN encapsulation there is much less impact on the charge puddles around the CNP. The asymmetry between hole-doped and electron-doped regimes is still observed in the encapsulated devices, just as in the non-encapsulated devices. This is ascribed to the different scattering mechanisms affecting the charge carriers in graphene, probably due to the presence of charged-defects created in the wet transfer process. This shows that it is the transfer process rather than the fabrication processes that leads to the preferential scattering of one carrier type. This could be serendipitous for optimising Hall probe devices since, according to recent studies on limits of the Hall coefficient in graphene, the value of R_H can be increased in one particular doping regime by increasing the asymmetry [158].

Low frequency Hall voltage noise spectra reveal that up to approximately 1kHz the noise is dominated by 1/f noise when operated near the charge neutrality point. As the device is intrinsically close to the CNP, the Hall coefficient is intrinsically large as it scales with 1/n. Likewise, recalling equation 16, low frequency noise is expected to also scale with 1/n. Thus low frequency noise should also reach its maximum close to the CNP. However,

equation 17 also harbours a dependence on the carrier mobility through the longitudinal resistivity, which in turn is expected to depend inversely on the carrier density with some power of η (assuming $\eta \sim 1/n\eta$). This means that although the overall relationship of noise on n is still inversely dependent, the exponent of this inverse dependent will not be equal to 1, unlike that of the Hall coefficient. As we explore later, this results in a dependence of the minimum detectable field on n, as opposed to an independence if both noise and Hall coefficient had the same inverse dependence on n. Increasing the current also increases the noise level, as expected from equation 16. An example of the low frequency noise spectra at zero applied back gate voltage is shown in figure 65.

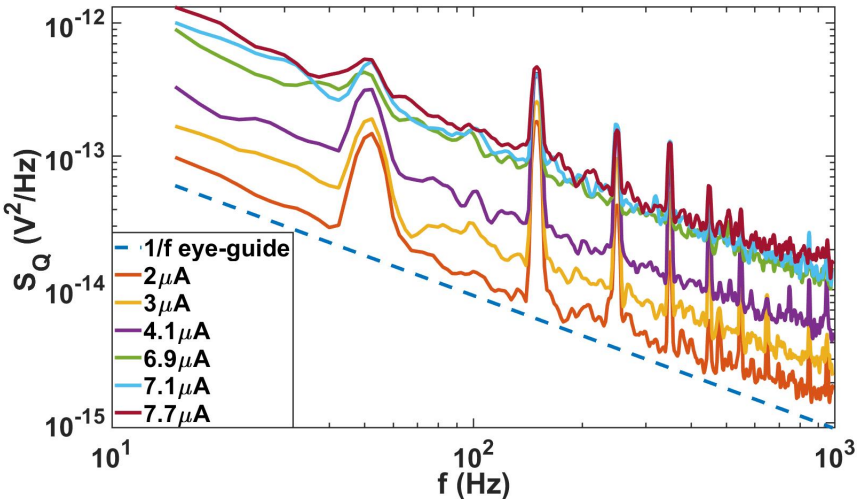

Figure 65: Hall voltage noise power, S_Q, in the range 1Hz to 1 kHz at various dc drive currents for a 1000nm wire width Hall bar at zero back gate voltage.

Plotting the noise as a function of back gate voltage in figure 66, we see a similar trend to that seen in chapter 6.1.2 where the noise peaks at the Dirac point. Upon comparison, one can immediately notice a benefit of encapsulation which causes an order of magnitude reduction in the noise voltage compared to the non-encapsulated devices in chapter 6.1.2. This is expected for the various reasons described in chapter 3.1.3, the biggest impact probably arising from a reduction in charge traps, strain and corrugations as a result of the change in substrate.

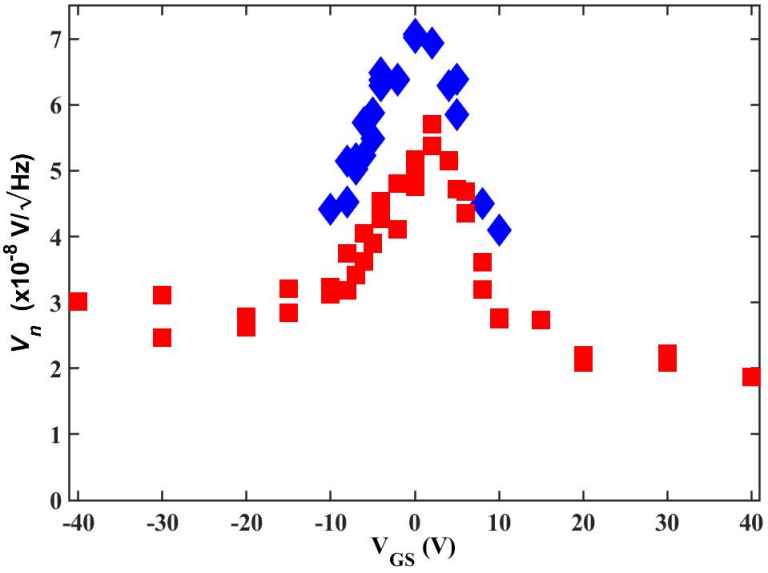

Figure 66: Low frequency noise at 531Hz as a function of back gate voltage for two different currents, 2μA (filled squares) and 3μA (filled diamonds) for a 1000nm wire width Hall bar at zero back gate voltage.

To determine the minimum detectable field as a function of carrier density, the Hall coefficient and noise at a measured drive current was entered into equation 5. From the measured R_H, we can also estimate the carrier density as a function of back gate voltage. We plot the calculated minimum detectable field as a function of the carrier density in figure 67. A clear trend revealing a minimum in B_{min} close to the CNP, can be seen which is much stronger than that observed in the unencapsulated devices in chapter 6.1.2. Here an order of magnitude of improvement can be achieved by fixing the carrier density close to zero. As previously mentioned, the ability for encapsulated devices to lie intrinsically very close to the charge neutrality point is a significant advantage, especially for use in an SHPM where the application of a back gate may not always be possible or desirable. We explore the trend of B_{min} as a function of n in greater detail by performing the same analysis as performed in chapter 6.1.2. To achieve this, we first need to calculate the mobility as a function of carrier density to determine the value of the exponent, η, assuming $\mu \sim 1/n^{\eta}$. Since the device geometry is that of a Hall bar device with multiple voltage taps, we can perform accurate Hall mobility measurements, using equations described in 3.1.1. We obtain values in excess of 1x10^{5}cm^2/Vs for hole and electron densities less than 5x10^{-16}cm^{-2}. Upon comparing once again with the values attained in chapter 6.1.2, this demonstrates the role played by the hBN substrate to reduce phonon scattering from the substrate as well as remote charged impurity scattering (e.g., from SiO_2). This mobility is still below other reported values for encapsulated exfoliated devices in a similar parameter range [159], suggesting that growth defects in CVD graphene and charge impurities from the transfer process still limit the full potential of our device. Values of η ~0.6 are obtained for the electron- and hole-doped regimes respectively. Incorporating this into the Vandamme transverse noise

equations described in chapter 6.1.2, we expect the coefficient of carrier density to lie somewhere between the limiting values of ∼0.1 and ∼0.8. Upon fitting our data, we find that the coefficient of carrier density lies towards the Johnson noise limit (∼0.8) in both regimes. This suggests that our devices operate closer to a Johnson noise limit than a full 1/f noise limit, indicating that encapsulated devices have a lower and more mobile (i.e., it falls faster as the carrier density is reduced) noise corner frequency than non-encapsulated devices.

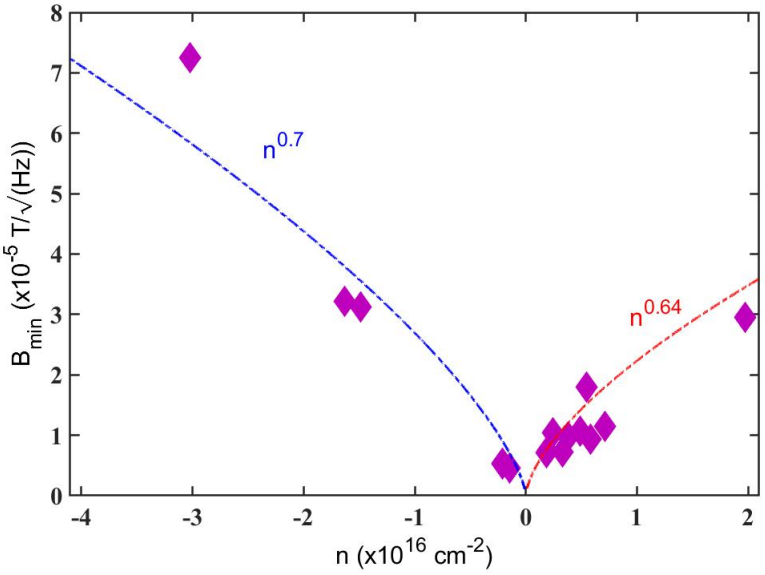

Figure 67: Minimum detectable field at 531Hz as a function of carrier density for a 2μA Hall current.

These first results clearly show the feasibility of realising scaleable encapsulated devices. Comparing the minimum detectable field between encapsulated and non-encapsulated devices from the previous chapter, we see that the performance can be at least a factor of ten better. It is also expected that the minimum detectable field of these devices can be further improved with an increase in drive current, as demonstrated in chapter 6.1.2. Efforts are now being made to study the performance of deep sub-micron devices and to pattern these in heterostructures on top of an SHPM-ready mesa with an integrated scanning tunnelling tip. If successful, further optimisation of the key figures-of-merit will be explored through modifications of the fabrication process.

7 Imaging of vortex matter in the ferromagnetic pnictide superconductor; $RbEuFe_4As_4$

One of the numerous powers of SHPM is its ability to make quantitative images of magnetic and superconducting materials. This allows SHPM to be able to be used to perform a direct measure of the superconductivity of a material, specifically, important quantities

such as the superconducting penetration depth, λ_L, superconducting transition temperature, T_c, via local magnetometry and the critical current density of a superconductor, J_c. This chapter puts SHPM into action by studying the effect of the in-plane magnetism in a unique ferromagnetic-superconductor, $RbEuFe_4As_4$, on the material's superconductivity. One of the key strengths of SHPM is its ability to make quantitative images of magnetic and superconducting materials. This allows SHPM to be used to obtain a direct measure of important superconducting properties of a material such as the superconducting penetration depth, λ_L, and, via local magnetometry, the superconducting transition temperature, T_c, and the critical current density, J_c. This chapter describes the use of SHPM to study the effect of the in-plane magnetic order in a unique ferromagnetic-superconductor, $RbEuFe_4As_4$, on its superconducting properties.

7.1 Preamble on vortex imaging of a ferromagnetic superconductor: $RbEuFe_4As_4$

As explained in chapter 4, magnetism and superconductivity should not normally co-exist due to the strong exchange fieldof a ferromagnet that suppresses singlet superconductivity via the paramagnetic effect [160]. One recently-synthesised material that seems able to overcome this limitation is $RbEuFe_4As_4$. Large single crystals of $RbEuFe_4As_4$ have been grown using a RbAs flux and typical superconducting transition temperatures of 36.8K [161]. Their crystal structure can be seen in the inset of the first figure of the paper. Previous temperature-dependent magnetic susceptibility and specific heat measurements revealed a magnetic transition at 15K, corresponding to the ordering of the Eu^{2+} magnetic sub-lattice [161]. Although transport measurements have shown that the ferromagnetic ordering does not lead to a finite resistivity at the magnetic transition temperature, the influence of the in-plane magnetism on the superconducting parameters (e.g., the penetration depth and superfluid density) as a function of temperature has only previously been explored in a qualitative MFM imaging study [162, 163].

There is therefore a unique opportunity for SHPM to shine light on the elusive effect of magnetic order on the superconductivity in such materials via quantitative estimations of the superfluid density. Understanding how the superconductivity is impacted could open up possible applications for such materials in advanced superconducting hybrid devices. The following paper demonstrates the use of fits to vortex line profiles obtained from SHPM images to calculate the superfluid density at various temperatures. This, in turn, allows a direct comparison between our results and a recently-proposed model for the penetration depth enhancement due to correlated quasi-two-dimensional magnetic fluctuations [164].

<table>
<tr><td colspan="5">This declaration concerns the article entitled:</td></tr>
<tr><td colspan="5">Publication status</td></tr>
<tr><td>Draft</td><td>Submitted</td><td>In review ✓</td><td>Accepted</td><td>Published</td></tr>
<tr><td>Reference</td><td colspan="4">D. Collomb, S. J. Bending, A. E. Koshelev, M. P. Smylie, L. Farrar, J. Bao, D. Y. Chung, M. G. Kanatzidis, W.-K. Kwok, D. Y. Chung, U. Welp. (2020)</td></tr>
<tr><td>Candidate's contribution to the paper</td><td colspan="4">The candidate performed most of the imaging. Crystals were grown by J.B. and M.G K. U.W. and M.P.S. performed the magnetisation measurements for figure 1. L.F. performed the R-T measurements in figure 1. The candidate was involved significantly in the interpretation of results, and performed data analysis with S.J.B alongside guidance from A.E.K. Computational work was carried out by the candidate and S.J.B., with the formulation of most theoretical ideas performed by A.E.K. Figures for the manuscript were produced by the candidate. The candidate wrote the manuscript with assistance and feedback from all other authors. A.E.K. wrote most of the supplementary information and provided contributions to the analysis section of the manuscript. The methodology used is not novel and has been determined before by S.J.B. and U.W., although some new analysis directions were developed by S.J.B. and the candidate. All author contributed towards feedback of the finalised manuscript.
• Formulation of ideas: 20%
• Design of methodology: 20%
• Experimental work: 70%
• Computational work: 45%
• Presentation of data in journal format: 85%</td></tr>
<tr><td>Statement from candidate</td><td colspan="4">This paper reports on original research I conducted during the period of my Higher Degree by Research candidature.</td></tr>
<tr><td>Signature</td><td colspan="2">  </td><td>Date</td><td>01/09/2020</td></tr>
</table>

7.1.1 Vortex imaging of a ferromagnetic superconductor: RbEuFe$_4$As$_4$

Observing the suppression of superconductivity in $RbEuFe_4As_4$ by correlated magnetic fluctuations

D. Collomb,[1,*] S. J. Bending,[1] A. E. Koshelev,[2] M. P. Smylie,[2,3] L. Farrar,[1]
J.-K. Bao,[2] D. Y. Chung,[2] M. G. Kanatzidis,[2,4] W.-K. Kwok,[2] and U. Welp[2]

[1] *University of Bath, Claverton Down, Bath, BA2 7AY, United Kingdom*
[2] *Materials Science Division, Argonne National Laboratory, 9700 S. Cass Ave., Lemont, Illinois 60439, USA*
[3] *Department of Physics and Astronomy, Hofstra University, Hempstead, New York, 11549, USA*
[4] *Department of Chemistry, Northwestern University, Evanston, Illinois, 60208, USA*

(Dated: October 10, 2020)

In this letter, we describe quantitative magnetic imaging of superconducting vortices in $RbEuFe_4As_4$ in order to investigate the unique interplay between the magnetic and superconducting sublattices. Our scanning Hall microscopy data reveal a pronounced suppression of the superfluid density near the magnetic ordering temperature in good qualitative agreement with a recently-developed model describing the suppression of superconductivity by correlated magnetic fluctuations. These results indicate a pronounced exchange interaction between the superconducting and magnetic subsystems in $RbEuFe_4As_4$ with important implications for future investigations of physical phenomena arising from the interplay between them.

The interplay between magnetism and superconductivity has intrigued scientists for decades [1–3]. Unlike the coexistence of ferromagnetism and superconductivity in unconventional spin-triplet uranium compounds [4, 5], their coexistence in spin-singlet superconductors is generally unfavourable because the magnetic exchange field destroys opposite spin Cooper pairs [1–3]. Nevertheless, a growing number of rare spin-singlet superconductors with a magnetic transition temperature, T_m, *below* the superconducting transition temperature, T_c, has been discovered. This includes the rare-earth (R) based materials RRh_4B_4 [6], RMo_8S_8 [7], in which magnetic ordering eventually destroys superconductivity, and also the nickel borocarbides with full co-existence of superconductivity and magnetism [8, 9]. The magnetic moments in these compounds reside in sublattices that are spatially separated from the superconducting electrons, thus the magnetic exchange interaction is weak enough to allow for the coexistence of superconductivity and magnetism below their respective transition temperatures [10].

One family with growing prominence in this field is the europium-containing iron pnictides [11, 12]. These typically exhibit high T_cs in excess of 30K, and somewhat lower magnetic ordering temperatures (15K-20K). Hence the strong superconducting pairing, relatively large magnetic exchange interaction and wide temperature window makes them ideal materials to investigate emerging new physical phenomena. Unlike the Eu-122 compounds, which require doping [13–17], or the application of pressure to obtain superconducting and magnetic transitions [18, 19], the stoichiometric 1144 compounds (e.g. $RbEuFe_4As_4$ and $CsEuFe_4As_4$) yield both under ambient conditions [20–23]. The Eu atoms in $RbEuFe_4As_4$ carry large, spin-only moments that undergo long-range ordering at 15K. Below the magnetic transition temperature these moments exhibit in-plane alignment, and there is a large anisotropy of the in-plane and out-of-plane exchange constants [24]. This makes it distinct from materials where the moments order along the c-axis, which can create their own unique states of vortex matter linked to ferromagnetic stripe domain structures such as in $EuFe_2(As_{0.79}P_{0.21})_2$ [25]. Neutron scattering experiments have revealed helical ordering of successive layers with a period of 4 unit cells along the c-axis due to a weak antiferromagnetic exchange interaction in this direction [26].

Although the magnetic structure in $RbEuFe_4As_4$ is now quite well understood, its impact on the coexisting superconductivity is still unclear. Above the magnetic ordering temperature fluctuating magnetic moments are thought to suppress superconductivity via magnetic scattering[27–29], while in the vicinity of T_m these moments become strongly correlated, further enhancing this suppression[30–32]. Optical conductivity measurements probing the $RbEuFe_4As_4$ superconducting gap revealed a small drop in $\Delta(T)$ as T_m is approached from above, followed by a recovery at lower temperatures [33]. Additionally, magnetic force microscopy (MFM) imaging of vortices revealed a gradual reduction in vortex density below ∼18K, which drops to a weak minimum at ∼12K and recovers again at lower temperatures, further hinting at a weak interaction between the superconducting and magnetic subsystems [33]. The analysis of the MFM measurements was, however, limited to counting vortex numbers as a function of temperature, rather than a direct investigation of the vortex structures themselves. On the other hand, recent angle resolved photoemission spectroscopy (ARPES) reveals no significant suppression of the superconducting gaps around the magnetic ordering temperature and DFT calculations show that the topology and orbital character of the Fe3d band

* d.collomb@bath.ac.uk

do not strongly depend on the magnetic order, although the band structure evidently exhibits a degree of sensitivity to it [34]. However, these measurements would not capture the full impact of the effect of magnetic fluctuations on superconductivity as the relative exchange correction to the gap is predicted to be significantly smaller than the correction to the superfluid density [32]. Here we use high-resolution scanning Hall microscopy (SHM) to investigate the influence of magnetism on individual superconducting vortices and directly extract the temperature dependence of the penetration depth, $\lambda(T)$, and the superfluid density, $\rho_s(T)$. This approach has the advantage that it is not influenced by the statistical nature of vortex patterns or by internal flux pumping effects by the magnetic sublattice [35].

The exchange interaction between the localized moments and Cooper pairs is expected to suppress the superfluid density. In the paramagnetic phase, in the regime when the exchange-field correlation length ξ_h is much smaller than the in-plane coherence length ξ_s, this suppression is caused by magnetic scattering and very similar to the case of magnetic impurities [28, 29]. However, as the correlation length diverges for $T \to T_m$, it always exceeds ξ_s in the vicinity of T_m leading to a different 'smooth' regime of interaction between the magnetic and superconducting subsystems. In the case of $RbEuFe_4As_4$, ξ_s is very small [24, 36], resulting in a 'smooth' regime across a significant temperature range. The crossover between these 'scattering' and 'smooth' regimes has been quantitatively described in Ref. [32] and results are summarized in the Supplementary materials [37]. The correction to ρ_s has two main temperature dependencies: via the ratio $T/\Delta_0(T)$, and via the correlation length $\xi_h(T)$. In the vicinity of T_m the second of these dependencies is expected to dominate, whereas across a wider temperature range both are expected to contribute.

We have used SHM to image discrete vortices in high-quality $RbEuFe_4As_4$ crystals, and studied the influence of the emerging magnetic order on the penetration depth, $\lambda(T)$, and the superfluid density, $\rho_s(T)$ [38]. SHM has the advantage of being a quantitative, and non-invasive magnetic imaging technique that allows the magnetic penetration depth to be directly obtained from model fits. The temperature-dependent superfluid density has then been calculated assuming $\rho_s(T) \propto \lambda(T)^{-2}$, and exhibits a very substantial drop in the vicinity of T_m. A direct comparison between our data and the model suggests that there must be a noticeable exchange interaction between the Eu^{2+} moments and Cooper pairs that substantially suppresses superconductivity near T_m. A recovery of the superfluid density at lower temperatures reflects a reduction of the magnetic correlation length and resulting weakening of the magnetic scattering. The good qualitative agreement with our model represents an important step forward in our understanding of the subtle physics at play in magnetic superconductors.

High-quality single crystals of $RbEuFe_4As_4$ were grown using a RbAs flux, yielding flat, rectangular platelet-like crystals with lateral dimensions of ∼1 mm in the a-b plane and thickness ∼60μm parallel to the c axis [22]. X-ray diffraction and specific heat measurements have previously confirmed that the crystals are single-phase material without $EuFe_2As_2$ inclusions [22]. $RbEuFe_4As_4$ has a simple tetragonal structure and a P4/mmm space group, with one formula per unit cell and lattice constants $a = b = 3.88$Å and $c = 13.27$Å [22]. A single unit cell of the crystal structure and atom-to-atom bonding is shown in the inset of Fig. 1. The high quality of the crystals was confirmed via electronic transport and magnetization measurements. These were performed by attaching gold wires with silver paint in a standard 4-lead Hall bar configuration, and the in-plane resistivity then measured as a function of temperature. This is shown in Fig. 1, revealing a superconducting transition of ∼37K. The magnetic susceptibility as a function of temperature was measured with a commercial magnetic property measurement system (MPMS3, Quantum Design) with magnetic fields applied along the c-axis revealing a magnetic transition at ∼15K.

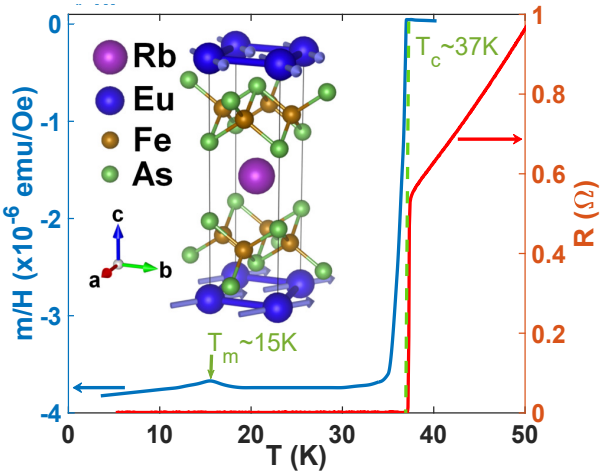

FIG. 1. Temperature dependence of the in-plane resistivity of $RbEuFe_4As_4$ near the superconducting transition, and the magnetic susceptibility of a zero-field-cooled $RbEuFe_4As_4$ single-crystal with a 10Oe magnetic field applied along the c-axis. The inset shows one unit cell of $RbEuFe_4As_4$, where the magnetic structure of the Eu sublattice is indicated.

To prepare samples for SHM a crystal of $RbEuFe_4As_4$ was glued flat on a gold-coated Si substrate and mechanically cleaved immediately prior to coating with a Cr(5nm)/Au(40nm) film (c.f., Fig. 2 (a)). This ensured good electrical contact between the scanning tunnelling microscopy (STM) tunnelling tip on the SHM sensor and the sample surface. The Hall probe used was based on a GaAs/AlGaAs heterostructure two-dimensional electron gas defined by the intersection of two 700nm wide wires. This was located ∼5μm from the gold-coated corner of a deep mesa etch acting as the STM tip [38]. The Hall probe was mounted at an angle of approximately 1° with respect to the sample plane, ensuring that the STM tip is

always the closest point to the sample surface. The Hall probe was approached to the sample until a threshold tunnel current was reached at which point the probe was manually lifted out of tunnelling by ∼50nm for rapid 'flying mode' scanning. From this a two-dimensional map of the magnetic induction across the surface of the sample was obtained [38], and several images were then averaged frame-by-frame to suppress low-frequency noise from the Hall probe.

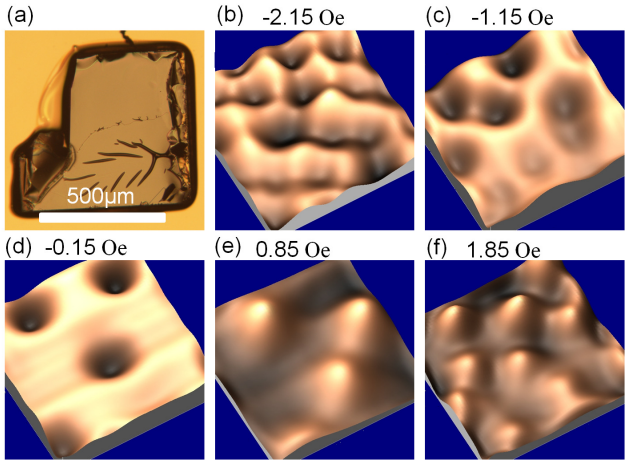

FIG. 2. (a) Optical micrograph of a $RbEuFe_4As_4$ single crystal after cleaving and deposition of a conductive coating. (b) - (f): Three dimensional SHM images of vortices in a $RbEuFe_4As_4$ single crystal after field-cooling to 30K in applied perpendicular fields between -2.15Oe and 1.85Oe [39]. The scan size is 12.6μm × 12.6μm. Vertical scales span 0.4G (-2.15Oe), 0.5G (-1.15Oe), 0.8G (-0.15Oe), 0.7G (0.85Oe), 0.5G (1.85Oe).

Figure 2 (b) - (f) displays vortex-resolved SHM images for a $RbEuFe_4As_4$ crystal after field-cooling to 30K from above T_c at various small, perpendicular applied magnetic fields between -2.15Oe and 1.85Oe. Note that these are nominal applied fields and in practice the sample also sees contributions from the earth's field as well as nearby ferrous materials. The scan range of the piezoelectric scanner is strongly temperature dependent and varies from 8.5μm × 8.5μm to 13.5μm × 13.5μm between 10K and 35K. Even below T_m, we can attribute all the magnetic contrast in the images to vortices and see no sign of c-axis fields associated with domain walls between magnetic domains. This differs from the MFM images in Ref. [33] which showed the presence of such stray magnetic fields at temperatures below T_m. It is possible that these domain-wall fields are also present in our sample on much larger length scales than we probe in our measurements.

A sample was then field-cooled at $H_z = -1.35$Oe from the normal state and images captured at several fixed temperatures down to 10K. Profiles of one particular vortex at a few selected temperatures are presented in Fig. 3. The influence of the long-range magnetic ordering is clearly reflected in the peak amplitude of the vortex which weakens (and broadens) as we approach 15K from above. The amplitude then starts to grow again at lower temperatures. The same behaviour is observed in our detailed analysis of the temperature-dependence of four distinct vortices in two different crystals. We also observe an unexpected increase in low-frequency noise in our images between 20K and 15K in a regime where the intrinsic Hall sensor noise would normally fall as the temperature is lowered, see Supplementary Materials [37] for more details. We tentatively associate this additional noise with magnetic fluctuations near the sample surface that have not been screened out by superconductivity. We also checked that there was no detectable hysteresis in the influence of the long-range magnetic order on the vortices by capturing images at both increasing and decreasing temperatures.

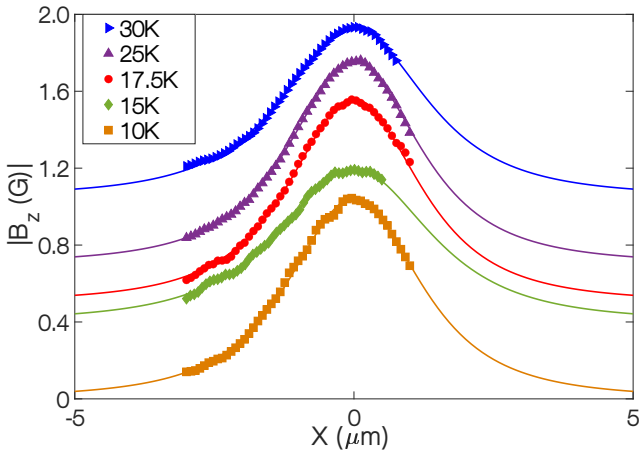

FIG. 3. Vortex profiles extracted from SHM images captured after field-cooling in $H_z = -1.35$Oe to various fixed temperatures with superimposed fits to a modified Clem model, Eq. (1).

To investigate this behavior further, we have performed a quantitative analysis of the temperature-dependent vortex profiles $B_z(x_0, z, \lambda)$ by fitting them to a modified Clem model [40, 41] to extract the magnetic penetration depth, $\lambda(T)$,

$$B_z(x_0,z,\lambda) = \frac{\Phi_0}{2\pi w^2 \lambda K_1\left(\frac{\xi_s}{\lambda}\right)} \int_{-w/2}^{w/2} dy \int_{x_0-w/2}^{x_0+w/2} dx \int_0^\infty q dq \frac{K_1\left(\sqrt{q^2+\lambda^{-2}}\xi_s\right)\exp(-qz)J_0\left(q\sqrt{x^2+y^2}\right)}{\sqrt{q^2+\lambda^{-2}}+q}, \quad (1)$$

where z is the sensor scan height measured from the sample surface, $w = 0.5\mu$m is the electronic width of the Hall probe, K_1 and J_0 are Bessel functions, ξ_s is the coherence length for which we assume $\xi_s = 1.46\text{nm}/\sqrt{1-T/T_c}$, and Φ_0 is the flux quantum. Fits to Eq. (1) have been superimposed on the measured profiles in Figure 3 showing excellent agreement. The value of z=1.45±0.01μm extracted from fits is consistent with the sensor tilt angle used. The same scan height was maintained at all other temperatures and, although it is large compared to the penetration depth we are trying to measure, we are nevertheless able to extract values of $\lambda(T)$ from fits with good accuracy (c.f., inset to Fig. 4).

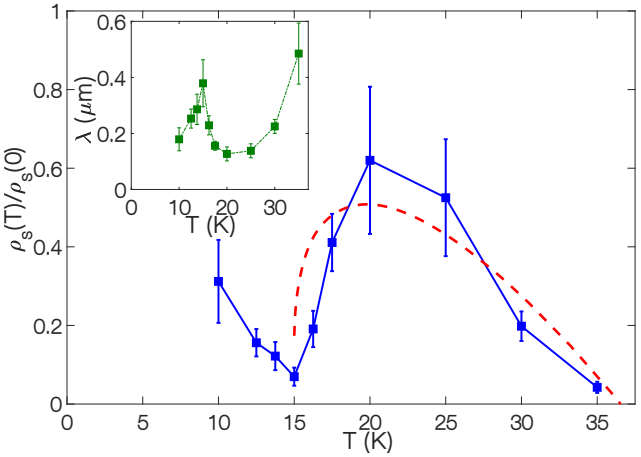

FIG. 4. Temperature dependence of the normalised superfluid density, $\rho_s(T)/\rho_s(0)$ (solid symbols), and a fit to the model described in the text (dashed line). The inset shows a plot of the normalised penetration depth as a function of temperature extracted for one vortex from fits to a modified Clem model, Eq. (1).

The normalised superfluid density, $\rho_s(T)/\rho_s(0) = \lambda(0)^2/\lambda(T)^2$, is plotted as a function of temperature in the main panel of Fig. 4. The zero temperature penetration depth, $\lambda(0) = 100 \pm 18$nm, has been estimated from the specific heat jump and a temperature dependence, $\lambda(T) = \lambda(0)/\sqrt{1-(T/T_c)^2}$, assumed between 20K and 35K. [42]. The large vertical error bars arise from the impact of the sensor noise level on the vortex profile fitting process combined with uncertainties in the estimated scan height, z.

The bare penetration depth is modified by the exchange interaction with the localized Eu^{2+} moments. This effect becomes especially pronounced in the vicinity of the magnetic transition, where the moments become strongly correlated. The quantitative description of the suppression of superconducting parameters by correlated magnetic fluctuations has been elaborated in Ref. [32]. In the Supplementary materials [37], we summarize the results for the correction to the superfluid density which we use for the modeling of the data. The relative correction is proportional to the square of the amplitude of the exchange field, h_0, and depends on two ratios, $T/\Delta_0(T)$ and $\xi_s(T)/\xi_h(T)$. We also account for renormalization of parameters due to the nonlocality of the exchange interaction described by the range a_J, $\xi_h^2 = \xi_S^2 + 2a_J^2$ and $\tilde{h}_0^2 = h_0^2\xi_S^2/\xi_h^2$, where ξ_S is the spin correlation length. We assume the Berezinskii-Kosterlitz-Thouless (BKT) shape for the latter, $\xi_S(T) = a\exp[b\sqrt{T_m/(T-T_m)}]$, where $a = 0.39$nm is the in-plane Eu atom spacing, and we use the numerical factor b as a fit parameter.

We plot the results of our model as a dashed line alongside our data using the amplitude of the exchange field, $h_0 = 15$K, a zero temperature superconducting gap, $\Delta(0) = 2$meV, a BKT constant $b = 1$, and the nonlocality range $a_J = 3$a. We use the BCS temperature dependence to describe Δ(T), which is corrected in the model for the magnetic exchange interaction. The Ginzburg-Landau coherence length is estimated to be $\xi^{GL} = 1.46$nm, deduced from the linear slope of the c-axis upper critical field near T_c [24, 36].

The strong suppression of superfluid density in the vicinity of T_m is remarkable and was not previously observed in $RbEuFe_4As_4$ or indeed any other ferromagnetic-superconductor, although this possibility was recently suggested by Willa et al. [36]. This is also in apparent conflict with the analysis of recent ARPES measurements which concluded that the two sublattices are almost fully decoupled [34]. To understand the temperature-dependent trend of the suppression seen in our data in Fig. 4, we turn to our model. Comparing the measured normalised ρ_s with predictions of the model, we find good qualitative agreement with our 2D BKT description of the magnetic correlations above the magnetic transition temperature, $T_m = 15$K, confirming the nature of the ordering and its impact through $\xi_h(T)$ on superconductivity in the vicinity of T_m. The temperature-dependent magnetic correlation length, $\xi_h(T)$, which is governed by the constant, b, is responsible for the wide temperature range over which the magnetic ordering influences the superconducting parameters. Above T_m, the suppression decreases rapidly as temperature increases, while the shift in T_c is $\sim$ 1K. Although the suppression of superfluid density is quite large, the fitted magnetic exchange constant remains moderate at $h_0 \approx 0.4T_c$. This is still significantly smaller than exchange constants estimated for the ternary compounds, which are several orders of magnitude larger than T_c [3]. This suggests a weak enough coupling between Eu moments and Cooper pairs in our material that superconductivity is never destroyed, yet one that is strong enough to have a substantial impact on the superconducting parameters near T_m. We emphasize that our model is a qualitative one and at best only qualitative agreement with our data is expected. In particular, the model assumes two-dimensional scattering behavior across the whole temperature range, $T > T_m$, while this assumption must break down in the vicinity of the magnetic transition where a crossover to a three-dimensional regime takes place. In addition, the BCS expressions we have used for the temperature dependence of the gap and

penetration depth were derived for single-band materials, whereas $RbEuFe_4As_4$ has a more complicated multiband structure. Nevertheless, the qualitative agreement between the model and data validates our simple assumptions in this fascinating magnetic superconducting material.

In conclusion, we have directly quantified the temperature-dependent superfluid density in $RbEuFe_4As_4$ crystals to reveal a significant suppression of superconductivity due to correlated quasi-two-dimensional magnetic fluctuations, despite the apparent spatial separation of the two sublattices. Although insufficient to completely destroy superconductivity, this suggests a significant influence of the exchange interaction on the superconducting subsystem. Our results will stimulate additional investigations into the properties of $RbEuFe_4As_4$, and other magnetic-superconductors, building on the existing analytical model.

We acknowledge support from the U.S. Department of Energy, Office of Science, Basic Energy Sciences, Materials Sciences and Engineering Division for the crystal growth, theoretical modelling and magnetotransport measurements. Financial support was also provided by the Engineering and Physical Sciences Research Council (EPSRC) in the UK under grant nos. EP/R007160/1, and the Nanocohybri COST Action CA-16218. D.C. acknowledges financial support from the Lloyds Register Foundation ICON (award nos. G0086) and L.F. from the EPSRC Centre for Doctoral Training in Condensed Matter Physics, Grant No. EP/L015544/1.

[1] P. Fulde and J. Keller, Theory of magnetic superconductors, in *Superconductivity in Ternary Compounds II*, edited by M. B. Maple and Ø. Fischer (Springer, 1982) pp. 249–294.

[2] L. Bulaevskii, A. Buzdin, M. Kulić, and S. Panjukov, Coexistence of superconductivity and magnetism theoretical predictions and experimental results, Adv. Phys. **34**, 175 (1985).

[3] M. L. Kulić and A. I. Buzdin, Coexistence of singlet superconductivity and magnetic order in bulk magnetic superconductors and sf heterostructures, in *Superconductivity: Conventional and Unconventional Superconductors*, edited by K. H. Bennemann and J. B. Ketterson (Springer, Berlin, Heidelberg, 2008) p. 163.

[4] S. Saxena, P. Agarwal, K. Ahilan, F. Grosche, R. Haselwimmer, M. Steiner, E. Pugh, I. Walker, S. Julian, P. Monthoux, *et al.*, Superconductivity on the border of itinerant-electron ferromagnetism in uge 2, Nature **406**, 587 (2000).

[5] D. Aoki, K. Ishida, and J. Flouquet, Review of u-based ferromagnetic superconductors: Comparison between UGe_2, URhGe, and UCoGe, J. Phys. Soc. Jpn. **88**, 022001 (2019).

[6] M. B. Maple, H. C. Hamaker, and L. D. Woolf, in *Superconductivity in Ternary Compounds II*, edited by M. B. Maple and Ø. Fischer (Springer, 1982) pp. 99–141.

[7] M. B. Maple and Ø. Fischer, in *Superconductivity in Ternary Compounds II*, edited by M. B. Maple and Ø. Fischer (Springer, 1982) pp. 1–10.

[8] K. H. Müller and V. N. Narozhnyi, Interaction of superconductivity and magnetism in borocarbide superconductors, Rep. Prog. Phys. **64**, 943 (2001).

[9] D. Wulferding, I. Yang, J. Yang, M. Lee, H. C. Choi, S. L. Bud'ko, P. C. Canfield, H. W. Yeom, and J. Kim, Spatially resolved penetration depth measurements and vortex manipulation in the ferromagnetic superconductor erni 2 b 2 c, Physical Review B **92**, 014517 (2015).

[10] H. Eisaki, H. Takagi, R. J. Cava, B. Batlogg, J. J. Krajewski, W. F. Peck, K. Mizuhashi, J. O. Lee, and S. Uchida, Competition between magnetism and superconductivity in rare-earth nickel boride carbides, Phys. Rev. B **50**, 647 (1994).

[11] G.-H. Cao, W.-H. Jiao, Y.-K. Luo, Z. Ren, S. Jiang, and Z.-A. Xu, Coexistence of superconductivity and ferromagnetism in iron pnictides, in *J. Phys. Conf. Ser.*, Vol. 391 (2012) p. 012123.

[12] S. Zapf and M. Dressel, Europium-based iron pnictides: a unique laboratory for magnetism, superconductivity and structural effects, Rep. Prog. Phys. **80**, 016501 (2017).

[13] Z. Ren, Q. Tao, S. Jiang, C. Feng, C. Wang, J. Dai, G. Cao, and Z. Xu, Superconductivity induced by phosphorus doping and its coexistence with ferromagnetism in $EuFe_2(As_{0.7}P_{0.3})_2$, Phys. Rev. Lett. **102**, 137002 (2009).

[14] H. Jeevan, Z. Hossain, D. Kasinathan, H. Rosner, C. Geibel, and P. Gegenwart, High-temperature superconductivity in $Eu_{0.5}K_{0.5}Fe_2As_2$, Phys. Rev. B **78**, 092406 (2008).

[15] J. Maiwald, H. Jeevan, and P. Gegenwart, Signatures of quantum criticality in hole-doped and chemically pressurized $EuFe_2As_2$ single crystals, Phys. Rev. B **85**, 024511 (2012).

[16] Anupam, P. L. Paulose, S. Ramakrishnan, and Z. Hossain, Doping dependent evolution of magnetism and superconductivity in $Eu_{1-x}K_xFe_2As_2$(x= 0-1) and temperature dependence of the lower critical field H_{c1}, J. Phys.: Condens. Matter **23**, 455702 (2011).

[17] Y. Qi, L. Wang, Z. Gao, X. Zhang, D. Wang, C. Yao, C. Wang, C. Wang, and Y. Ma, Superconductivity at 34.7K in the iron arsenide $Eu_{0.7}Na_{0.3}Fe_2As_2$, New J. Phys. **14**, 033011 (2012).

[18] C. Miclea, M. Nicklas, H. Jeevan, D. Kasinathan, Z. Hossain, H. Rosner, P. Gegenwart, C. Geibel, and F. Steglich, Evidence for a reentrant superconducting state in $EuFe_2As_2$ under pressure, Phys. Rev. B **79**, 212509 (2009).

[19] K. Matsubayashi, K. Munakata, M. Isobe, N. Katayama, K. Ohgushi, Y. Ueda, N. Kawamura, M. Mizumaki, N. Ishimatsu, M. Hedo, I. Umehara, and Y. Uwatoko, Pressure-induced changes in the magnetic and valence state of $EuFe_2As_2$, Phys. Rev. B **84**, 024502 (2011).

[20] Y. Liu, Y.-B. Liu, Z.-T. Tang, H. Jiang, Z.-C. Wang, A. Ablimit, W.-H. Jiao, Q. Tao, C.-M. Feng, Z.-A. Xu, and G.-H. Cao, Superconductivity and ferromagnetism in hole-doped $RbEuFe_4As_4$, Phys. Rev. B **93**, 214503 (2016).

[21] K. Kawashima, T. Kinjo, T. Nishio, S. Ishida, H. Fu-

jihisa, Y. Gotoh, K. Kihou, H. Eisaki, Y. Yoshida, and A. Iyo, Superconductivity in Fe-based compound $EuAFe_4As_4$ (A = Rb and Cs), J. Phys. Soc. Jpn. **85**, 064710 (2016).

[22] J.-K. Bao, K. Willa, M. P. Smylie, H. Chen, U. Welp, D. Y. Chung, and M. G. Kanatzidis, Single crystal growth and study of the ferromagnetic superconductor $RbEuFe_4As_4$, Crystal Growth & Design **18**, 3517 (2018).

[23] Y. Liu, Y.-B. Liu, Q. Chen, Z.-T. Tang, W.-H. Jiao, Q. Tao, Z.-A. Xu, and G.-H. Cao, A new ferromagnetic superconductor: $CsEuFe_4As_4$, Sci. Bull. **61**, 1213 (2016).

[24] M. Smylie, K. Willa, J.-K. Bao, K. Ryan, Z. Islam, H. Claus, Y. Simsek, Z. Diao, A. Rydh, A. Koshelev, W.-K. Kwok, D. Y. Chung, M. G. Kanatzidis, and U. Welp, Anisotropic superconductivity and magnetism in single-crystal $RbEuFe_4As_4$, Phys. Rev, B **98**, 104503 (2018).

[25] V. S. Stolyarov, I. S. Veshchunov, S. Y. Grebenchuk, D. S. Baranov, I. A. Golovchanskiy, A. G. Shishkin, N. Zhou, Z. Shi, X. Xu, S. Pyon, Y. Sun, W. Jiao, G.-H. Cao, L. Y. Vinnikov, A. A. Golubov, T. Tamegai, A. I. Buzdin, and D. Roditchev, Domain Meissner state and spontaneous vortex-antivortex generation in the ferromagnetic superconductor $EuFe_2(As_{0.79}P_{0.21})_2$, Sci. Adv. **4**, 1061 (2018).

[26] K. Iida, Y. Nagai, S. Ishida, M. Ishikado, N. Murai, A. D. Christianson, H. Yoshida, Y. Inamura, H. Nakamura, A. Nakao, K. Munakata, D. Kagerbauer, M. Eisterer, K. Kawashima, Y. Yoshida, H. Eisaki, and A. Iyo, Coexisting spin resonance and long-range magnetic order of Eu in $EuRbFe_4As_4$, Phys. Rev. B **100**, 014506 (2019).

[27] A. A. Abrikosov and L. P. Gor'kov, Contribution to the theory of superconducting alloys with paramagnetic impurities, [Zh. Eksp. Teor. Fiz. **39**, 1781 (1960)] Sov. Phys. JETP **12**, 1243 (1961).

[28] S. Skalski, O. Betbeder-Matibet, and P. R. Weiss, Properties of superconducting alloys containing paramagnetic impurities, Phys. Rev. **136**, A1500 (1964).

[29] V. G. Kogan, R. Prozorov, and V. Mishra, London penetration depth and pair breaking, Phys. Rev. B **88**, 224508 (2013).

[30] K. Machida and D. Youngner, Superconductivity of ternary rare-earth compounds, J. Low Temp. Phys. **35**, 449 (1979).

[31] D. Rainer, Influence of correlated spins on the superconducting transition temperature, Z. Phys. **252**, 174 (1972).

[32] A. E. Koshelev, Suppression of superconducting parameters by correlated quasi-two-dimensional magnetic fluctuations, Phys. Rev. B **102**, 054505 (2020).

[33] V. Stolyarov, A. Casano, M. Belyanchikov, A. Astrakhantseva, S. Y. Grebenchuk, D. Baranov, I. Golovchanskiy, I. Voloshenko, E. Zhukova, B. Gorshunov, A. V. Muratov, V. V. Dremov, L. Y. Vinnikov, D. Roditchev, Y. Liu, G.-H. Cao, M. Dressel, and E. Uykur, Unique interplay between superconducting and ferromagnetic orders in $EuRbFe_4As_4$, Phys. Rev. B **98**, 140506 (2018).

[34] T. K. Kim, K. Pervakov, D. Evtushinsky, S. W. Jung, G. Poelchen, K. Kummer, V. A. Vlasenko, V. M. Pudalov, D. Roditchev, V. S. Stolyarov, D. Vyalikh, V. Borisov, R. Valent1, A.Ernst, S. Eremeev, and E. V. Chulkov, When superconductivity does not fear magnetism: Insight into electronic structure of $EuRbFe_4As_4$, preprint arXiv:2008.00736 (2020).

[35] V. K. Vlasko-Vlasov, A. E. Koshelev, M. Smylie, J.-K. Bao, D. Y. Chung, M. G. Kanatzidis, U. Welp, and W.-K. Kwok, Self-induced magnetic flux structure in the magnetic superconductor $RbEuFe_4As_4$, Phys. Rev. B **99**, 134503 (2019).

[36] K. Willa, R. Willa, J.-K. Bao, A. E. Koshelev, D. Y. Chung, M. G. Kanatzidis, W.-K. Kwok, and U. Welp, Strongly fluctuating moments in the high-temperature magnetic superconductor $RbEuFe_4As_4$, Phys. Rev. B **99**, 180502 (2019).

[37] The supplementary materials include a description of the model and the details on how the magnetic noise measurements were performed, including its results.

[38] S. J. Bending, Local magnetic probes of superconductors, Adv. Phys. **48**, 449 (1999).

[39] I. Horcas, R. Fernández, J. Gomez-Rodriguez, J. Colchero, J. Gómez-Herrero, and A. Baro, Wsxm: a software for scanning probe microscopy and a tool for nanotechnology, Review of scientific instruments **78**, 013705 (2007).

[40] J. R. Clem, Simple model for the vortex core in a type ii superconductor, J. Low Temp. Phys. **18**, 427 (1975).

[41] J. R. Kirtley, C. Kallin, C. W. Hicks, E.-A. Kim, Y. Liu, K. A. Moler, Y. Maeno, and K. D. Nelson, Upper limit on spontaneous supercurrents in Sr_2RuO_4, Phys. Rev. B **76**, 014526 (2007).

[42] C. P. Poole, H. A. Farach, R. J. Creswick, and R. Prozorov, in *Superconductivity* (Elsevier, 2007) pp. 406–413.

Supplementary: Observing the suppression of superconductivity in $RbEuFe_4As_4$ by correlated magnetic fluctuations

D. Collomb,[1,*] S. J. Bending,[1] A. E. Koshelev,[2] M. P. Smylie,[2,3] L. Farrar,[1]
J.-K. Bao,[2] D. Y. Chung,[2] M. G. Kanatzidis,[2,4] W.-K. Kwok,[2] and U. Welp[2]

[1] *University of Bath, Claverton Down, Bath, BA2 7AY, United Kingdom*
[2] *Materials Science Division, Argonne National Laboratory, 9700 S. Cass Ave., Lemont, Illinois 60439, USA*
[3] *Department of Physics and Astronomy, Hofstra University, Hempstead, New York, 11549, USA*
[4] *Department of Chemistry, Northwestern University, Evanston, Illinois, 60208, USA*

(Dated: October 10, 2020)

I. THEORETICAL MODEL FOR SUPPRESSION OF SUPERFLUID DENSITY BY CORRELATED QUASI-TWO-DIMENSIONAL MAGNETIC FLUCTUATIONS

The suppression of the superconducting gap and superfluid density by correlated magnetic fluctuations in the vicinity of the magnetic transition has been evaluated recently in Ref.[1] and here we summarize the results for the superfluid density with small generalization accounting for the nonlocality of the exchange interactions. The models assumes a clean layered magnetic superconductor in which a continuous magnetic transition takes place inside superconducting state. Increase of the exchange-field correlation length ξ_h in the vicinity of the magnetic transition enhances suppression of superconductivity. The influence of nonuniform exchange field on superconducting parameters is very sensitive to the relation between ξ_h, and superconducting coherence length ξ_s defining the 'scattering' ($\xi_h < \xi_s$) and 'smooth' ($\xi_h > \xi_s$) regimes. The model in Ref.[1] provides a quantitative description of this 'scattering-to-smooth' crossover for the case of quasi-two-dimensional magnetic fluctuations.

For a material composed of magnetic and superconducting layers, the exchange field acting on the conduction electron spins has the form

$$\boldsymbol{h}_n(\boldsymbol{r}) = -\sum_{m,\boldsymbol{R}} J_{nm}(\boldsymbol{r}-\boldsymbol{R})\boldsymbol{S}_m(\boldsymbol{R}) \tag{1}$$

where the indices n and m correspond to conducting and magnetic layers, respectively, $\boldsymbol{S}_m(\boldsymbol{R})$ are localized spins, and $J_{nm}(\boldsymbol{r}-\boldsymbol{R})$ are the exchange constants. In the paramagnetic state the field $\boldsymbol{h}_n(\boldsymbol{r})$ is random and the Fourier transform of the exchange-field correlation function for an isolated layer is

$$\left\langle |\boldsymbol{h}_{\mathbf{q}}|^2 \right\rangle = \sum_m \left[J_{nm}(\boldsymbol{q})\right]^2 \left\langle |\boldsymbol{S}_{\mathbf{q}}|^2 \right\rangle. \tag{2}$$

We neglect magnetic correlation between different magnetic layers and assume the spin correlation function for an isolated layer in the standard form

$$\left\langle |\boldsymbol{S}_{\mathbf{q}}|^2 \right\rangle = \frac{2\pi S_0^2 \xi_S^2 / \ln\left(\xi_S/a\right)}{1+\xi_S^2 q^2}. \tag{3}$$

It is normalized by the condition $\int \frac{d^2\boldsymbol{q}}{(2\pi)^2} \left\langle |\boldsymbol{S}_{\mathbf{q}}|^2 \right\rangle = S_0^2$, where S_0 is the magnitude of spin (7/2 for Eu^{2+}). As in $RbEuFe_4As_4$ the magnetic and superconducting layers are separated, the exchange interaction is most likely is indirect and has significant nonlocality. We assume a simple shape for $J_{nm}(\boldsymbol{q})$,

$$J_{nm}(\boldsymbol{q}) = \frac{\mathcal{J}_{nm}}{1+a_J^2 q^2}, \tag{4}$$

where a_J is the nonlocality range, which is probably $2-3$ lattice spacings. Then we have

$$\left\langle |\boldsymbol{h}_{\mathbf{q}}|^2 \right\rangle = \sum_m \mathcal{J}_{nm}^2 \frac{2\pi S_0^2 \xi_S^2 / \ln\left(\xi_S/a\right)}{\left(1+a_J^2 q^2\right)^2 \left(1+\xi_S^2 q^2\right)}.$$

To capture the qualitative effect of crossover at $\xi_S \sim a_J$, we approximate this correlation function with

$$\left\langle |\boldsymbol{h}_{\mathbf{q}}|^2 \right\rangle \approx \frac{2\pi h_0^2 \xi_S^2 / \ln\left(\xi_S/a\right)}{1+\left(2a_J^2+\xi_S^2\right) q^2}$$

with $h_0^2 = \sum_m \mathcal{J}_{nm}^2 S_0^2$ is the maximum amplitude of the exchange field. The last result can be rewritten as

$$\left\langle |\boldsymbol{h}_{\mathbf{q}}|^2 \right\rangle = \frac{2\pi \tilde{h}_0^2 \xi_h^2 / \ln\left(\xi_S/a\right)}{1+\xi_h^2 q^2}, \tag{5}$$

where $\xi_h^2 = 2a_J^2 + \xi_S^2$ and $\tilde{h}_0^2 = h_0^2 \frac{\xi_S^2}{2a_J^2+\xi_S^2}$ are the correlation length and exchange-field amplitude renormalized by the nonlocality of the exchange interaction. Therefore nonlocality increases the effective correlation length and reduces the effective amplitude of the exchange field. This effect becomes noticeable when temperature is not too close the to magnetic transition when the spin correlation length becomes comparable with the nonlocality range.

The correction of the to λ^{-2} caused by a nonuniform exchange field with the correlation function in Eq. (5) evaluated in Ref.[1] is given by

$$\lambda_1^{-2}(T) = -\lambda_0^{-2}(T) \frac{\tilde{h}_0^2}{2\Delta_0^2(T) \ln\left(\xi_S(T)/a\right)} \mathcal{V}_Q\left(\frac{2\pi T}{\Delta_0(T)}, \frac{\xi_s(T)}{\xi_h(T)}\right), \tag{6}$$

where $\lambda_0(T)$ and $\Delta_0(T)$ are the unperturbed values of the London penetration depth and the gap, $\xi_s(T) = v_F/2\Delta_0(T)$ is the coherence length. The reduced function $\mathcal{V}_Q\left(\tilde{T}, \alpha_h\right)$ is defined by relations

$$\mathcal{V}_Q\left(\tilde{T}, \alpha_h\right) = \left[\mathcal{D}\left(\tilde{T}\right)\right]^{-1} \tilde{T} \sum_{n=0}^{\infty} \left\{ K_Q\left[\tilde{T}(n+\tfrac{1}{2})\right] \mathcal{V}_\Delta\left(\tilde{T}, \alpha_h\right) + R_Q\left[\tilde{T}(n+\tfrac{1}{2}), \alpha_h\right] \right\}, \tag{7}$$

$$\mathcal{D}\left(\tilde{T}\right) = \tilde{T} \sum_{n=0}^{\infty} \left(\left[\tilde{T}(n+\tfrac{1}{2})\right]^2 + 1 \right)^{-3/2}, \tag{8}$$

where we used the reduced variables $\tilde{T} = 2\pi T/\Delta_0(T)$ and $\alpha_h = \xi_s(T)/\xi_h(T)$. Here the first term in the curly brackets in Eq. (7) is due to the gap reduction by magnetic scattering and the functions $K_Q(z)$ and $\mathcal{V}_\Delta\left(\tilde{T}, \alpha_h\right)$ are defined as

$$K_Q(z) = -\frac{\partial}{\partial z} \frac{z}{\left(z^2+1\right)^{3/2}}, \tag{9}$$

$$\mathcal{V}_\Delta\left(\tilde{T}, \alpha_h\right) = \left[\mathcal{D}\left(\tilde{T}\right)\right]^{-1} \tilde{T} \sum_{n=0}^{\infty} R\left[\tilde{T}(n+\tfrac{1}{2}), \alpha_h\right], \tag{10}$$

with

$$R(z, \alpha_h) = \frac{1}{\left(z^2+1\right)^{3/2}\left(z^2+1-\alpha_h^2\right)} \left[1 + \left(2z^2 - 1 - \frac{2z^2\alpha_h^2}{z^2+1}\right) L(z, \alpha_h)\right], \tag{11}$$

$$L(z, \alpha_h) = \begin{cases} \frac{\sqrt{z^2+1}}{\sqrt{z^2+1-\alpha_h^2}} \ln\left(\frac{\sqrt{z^2+1}+\sqrt{z^2+1-\alpha_h^2}}{\alpha_h}\right), & z^2 > \alpha_h^2 - 1 \\ \frac{\sqrt{z^2+1}}{\sqrt{\alpha_h^2-z^2-1}} \arctan \frac{\sqrt{\alpha_h^2-z^2-1}}{\sqrt{z^2+1}}, & z^2 < \alpha_h^2 - 1 \end{cases}. \tag{12}$$

The function $R_Q(z, \alpha_h)$ in Eq. (7) describes the direct influence of the magnetic scattering on the superfluid density and is defined as

$$R_Q(z, \alpha_h) = \frac{\partial}{\partial z} \frac{z\left[1 - \left(3 - \frac{2\alpha_h^2}{z^2+1}\right) L(z, \alpha_h)\right]}{\left(z^2+1\right)^{3/2}\left(z^2+1-\alpha_h^2\right)}. \tag{13}$$

We use Eq. (6) to model the experimental behavior of $\lambda^{-2}(T)$. The necessary input model parameters are the temperature dependent gap $\Delta_0(T)$ which also determines the coherence length $\xi_s(T)$, spin correlation length $\xi_S(T)$, the bare strength of exchange field h_0, and the nonlocality range a_J. We assumed the Berezinskii-Kosterlitz-Thouless shape for the magnetic length, $\xi_S(T) = a \exp[b\sqrt{T_m/(T-T_m)}]$ and treated the nonuniversal numerical constant b as an additional fit parameter.

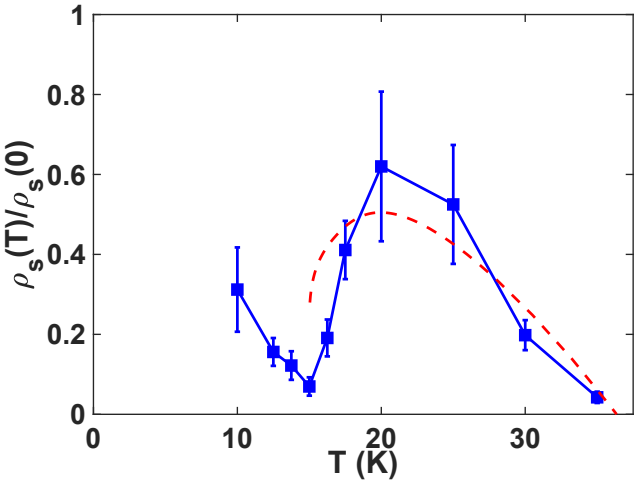

FIG. 1. Temperature dependence of the normalised superfluid density, $\rho_s(T)/\rho_s(0)$ (solid symbols), as in Fig. 4 of the main text, and a fit to the model with BCS value of the gap, $\Delta(0)=5$meV, exchange field $h_0=50$K, a BKT constant $b=1$, and the nonlocality range $a_J=4$a (dashed line).

II. SELECTION OF MODEL PARAMETERS

Since $RbEuFe_4As_4$, as other iron-pnictide superconductors, has multiple bands with different superconducting gaps, our model is only capable to provide qualitative description of the data. To reduce uncertainties of the model, we assume the BCS temperature dependence of the gap $\Delta_0(T)$ but leave the zero-temperature gap $\Delta_0(0)$ as a free parameter. Other three parameters of the model are the bare strength of the exchange field h_0, the constant b in the BKT temperature dependence of the spin correlation length, and the nonlocality range a_J. On general grounds, as we observe a substantial suppression of the superfluid density near T_m, the model requires h_0 comparable with $\Delta_0(0)$. The shape of the temperature dependence is sensitive to the parameters b and a_J.

If we assume that the zero-temperature gap $\Delta_0(0)$ has the BCS value ≈ 5meV, which also coincides with the value extracted from the optical data[2], then the model describes our data if we take $h_0=50$K, $b=1$, and $a_J=4$a, see Fig. 1. However, this value of h_0 looks unrealistically high as it exceeds the Eu to Eu moment interaction yielding the magnetic transition temperature, 15K. Also, the nonlocality range is somewhat higher than expected. This is why we assumed the smaller value of $\Delta_0(0) = 2$meV, for which the data can be modeled with more reasonable values of $h_0=15$K and $a_J=3$a. The value $b = 1$ does not change. The model curve with these parameter is shown in Fig. 4 of the main text and it provides a somewhat better description of our data in comparison with the first set.

III. MAGNETIC NOISE FLUCTUATIONS ABOVE THE FERROMAGNETIC TRANSITION TEMPERATURE

While performing magnetic imaging of $RbEuFe_4As_4$ we noticed an unexpected increase in very low frequency Hall sensor noise in images captured between 20K and 15K. Sensor noise would normally reduce at lower temperatures due to the lower thermal noise contribution to the Hall probe signal. We tentatively associate the observed increase with the detection of magnetic fluctuations near the sample surface. To investigate this further we have generated 2D FFT spectra of the images to estimate the 'spatial' noise amplitude (which can be directly related to temporal noise amplitude) at various frequencies and temperatures, as plotted in Fig. 2. To generate Fig. 2 we take a linescan across a 2D FFT parallel to the slow scan direction and fit this to a Lorentzian profile. Since all images take approximately 240 seconds to complete, this allows us to directly convert between spatial frequencies and temporal frequencies.

* d.collomb@bath.ac.uk

[1] A. E. Koshelev. Suppression of superconducting parameters by correlated quasi-two-dimensional magnetic fluctuations. *Phys. Rev. B*, 102:054505, Aug 2020.

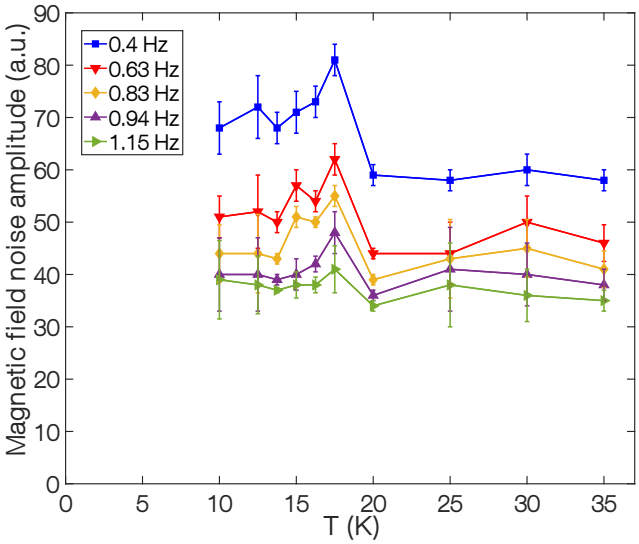

FIG. 2. Magnetic field noise amplitude extracted from 2D FFT linescans at various frequencies as a function of temperature. As the temperature is reduced the low frequency noise rises to a peak around 17.5K, before falling again as the temperature is lowered further down to 10K.

[2] V.S. Stolyarov, A Casano, M.A. Belyanchikov, A.S. Astrakhantseva, S Yu Grebenchuk, D.S. Baranov, IA Golovchanskiy, I Voloshenko, E.S. Zhukova, B.P. Gorshunov, A. V. Muratov, V. V. Dremov, L. Ya. Vinnikov, D. Roditchev, Y. Liu, G.-H. Cao, M. Dressel, and E. Uykur. Unique interplay between superconducting and ferromagnetic orders in $EuRbFe_4As_4$. *Phys. Rev. B*, 98(14):140506, 2018.

7.1.2 Discussion on vortex imaging of a ferromagnetic superconductor: $RbEuFe_4As_4$

The quantitative imaging capabilities of SHPM have allowed us to confirm that the superconductivity in a ferromagnetic-superconducting crystal is indeed affected by the onset of magnetic order. For the first time we have shown that the superfluid density is actually significantly suppressed by correlated magnetic fluctuations. According to our theoretical model, the exchange field acting upon the conduction electron spins must be fairly substantial to cause this level of suppression, however, the critical level of fluctuations leading to the destruction of superconductivity is never reached. This highlights the importance of the spatial separation between the magnetic and superconducting layers to achieve this unique coexistence within the same material, and also places a limit on the exchange coupling between the magnetic atom moments and the Cooper pairs. This should attract more attention to the families of magnetic-superconductors, hopefully driving the hunt for new materials with the aim of finding the ideal candidate system for fascinating applications such as superspintronics.

While the paper reports the clear observation of the effect of the local magnetism on 'bulk' superconductivity, it also makes a brief mention of the influence of magnetic fluctuations near the sample surface that have not been screened out by superconductivity. The importance of these was inferred from an unexpected increase in low-frequency noise in the scanning Hall probe signal between 20K and 15K [Fig. S2]. As mentioned in the text, one would normally expect the amplitude of the sensor noise at any frequency to drop as the temperature falls. This preliminary observation suggest a way to directly study magnetic fluctuations across the whole temperature spectrum in future studies on $RbEuFe_4As_4$, or indeed other magnetic-superconductors.

8 Vortex pinning in high temperature superconducting tapes

The cuprate family of superconductors are one of the most widely studied superconductor families since the discovery of high temperature superconductivity. These are well known for their high critical temperature, exceeding 77K, making them a much easier target material for fundamental studies and applications [165]. GBCO can be grown through various means, including; seed growth for large single domains [166], and deposition techniques such as via; pulsed laser deposition, inclined substrate deposition and reactive co-evaporation by deposition and reaction [167, 168, 8]. Looking towards industrial applications, the latter growth techniques are under intense study to attain the best performing superconducting tapes. Properties of the superconductor pinning and current carrying capacity can be obtained through electronic transport and magnetometry on bulk samples. On the other hand, we are in a unique position to be able to study the vortex pinning landscape and vortex micro structure directly by SHPM images, supported by additional scanning electron microscopy and local magnetometry measurements. This chapter continues to put SHPM into action by studying the vortex pinning behaviour of a high J_c and T_c superconducting tape made by SuNAM.

8.1 Preamble on vortex imaging of high temperature superconducting tapes

The most well known cuprate compounds are BSSCO and YBCO, however in the recent decade, a sister to YBCO, GdBaCuO (GBCO), has entered at the forefront of the field. GBCO boasts both a high critical current density and critical temperature [124], turning it into one of the most attractive cuprates for potential applications in the energy sector through energy transportation and superconducting magnetic energy storage [169, 170]. To realise these applications, manufacturers need to perform the crucial task of maximising J_c over a wide range of applied fields and temperatures. As described in chapter 4, various APCs have been explored to tackle this problem. Due to the vast array of options at manufacturers disposal, it may sometimes be easier to first optimise those which are intrinsically present as a result of the growth process. As described in chapter 4, SuNAM attempt to maximise J_c by controlling the concentration of the Gd_2O_3 second phases in the grown tape to optimise the pinning density [8]. The easy-to-remove silver layer protecting the GBCO layer allows our SHPM to get into close proximity to superconducting layer, ensuring individual vortex resolution. Courtesy to this, we are able to quantitatively and qualitatively study the precise vortex pinning landscape and behaviour at low fields with SHPM. Correlating this with topographical and data, we can gain further insight to the complex pinning mechanisms in GBCO based HTS tapes.

<table>
<tr><td colspan="5">This declaration concerns the article entitled:</td></tr>
<tr><td colspan="5">Publication status</td></tr>
<tr><td>Draft ✓</td><td>Submitted</td><td>In review</td><td>Accepted</td><td>Published</td></tr>
<tr><td>Reference</td><td colspan="4">D. Collomb, M. Zhang, W. Yuan and S. J. Bending (2020)</td></tr>
<tr><td>Candidate's contribution to the paper</td><td colspan="4">The candidate performed all of the imaging, sample preparation, and transport measurements. S.J.B. performed sample alignment in the microscope. EDX and SEM was performed with help from technical staff with D.C. The imaging methodology used is not novel and has been developed before by S.J.B. Sample preparation and transport measurement was developed by the candidate. The candidate and S.J.B performed analysis work. The manuscript was written by the candidate with support and feedback from S.J.B.
• Formulation of ideas: 40%
• Design of methodology: 30%
• Experimental work: 95%
• Computational work: 90%
• Presentation of data in journal format: 95%</td></tr>
<tr><td>Statement from candidate</td><td colspan="4">This paper reports on original research I conducted during the period of my Higher Degree by Research candidature.</td></tr>
<tr><td>Signature</td><td colspan="2">  </td><td>Date</td><td>15/12/2020</td></tr>
</table>

8.1.1 Vortex imaging of high temperature superconducting tapes

nanomaterials

MDPI

Article

Imaging of Strong Nanoscale Vortex Pinning in GdBaCuO High Temperature Superconducting Tapes

David Collomb [1]*, Min Zhang [2], Weijia Yuan [2] and Simon J. Bending [1]

[1] University of Bath, Claverton Down, Bath, BA2 7AY, United Kingdom.;
[2] Applied Superconductivity Laboratory, Department of Electronics and Electrical Engineering, University of Strathclyde, Glasgow, G1 1XQ, United Kingdom.;
* Correspondence: dc805@bath.ac.uk.;

Received: date.; Accepted: date.; Published: date

Abstract: The high critical current density of second generation high temperature superconducting (2G-HTS) tapes is the result of the systematic optimisation of the pinning landscape for superconducting vortices through careful engineering of the size and density of defects and non-superconducting second phases. Here we use scanning Hall probe microscopy to make a vortex-resolved study of commercial GdBaCuO tapes in low fields for the first time and complement this work with "local" magnetisation and transport measurements. Magnetic imaging reveals highly disordered vortex patterns reflecting the presence of strongly pinning nanoscale Gd_2O_3 second phase inclusions in the superconducting film. However, we find that measured vortex profiles are unexpectedly broad, with full-width-half-maxima of typically 6μm, and exhibit almost no temperature-dependence in the range 10-85K. This suggests that individual vortex lines must be interacting with many different pinning sites and meander laterally over very considerable distances in order to pass through the maximum number of pinning centres. Deviations of our local magnetisation data from an accepted 2D Bean critical state model also indicate that critical state profiles relax quite rapidly by flux creep. Our measurements provide important information about the role second phase defects play in enhancing the critical current in these tapes and demonstrates the power of magnetic imaging as a complementary tool in the optimization of vortex pinning phenomena in 2G-HTS tapes.

Keywords: High Temperature Superconducting Tapes; Magnetic Imaging; Nanoscale Defects; Cuprates; Scanning Hall Microscopy

1. Introduction

Cuprate superconductors have been the subject of intense investigation ever since their discovery due to their promising application as the superconducting layer in high temperature superconducting (HTS) coated conductors, the second generation (2G) of which are known as 2G-HTS tapes. These typically have superconducting critical temperatures, T_c, greater than the boiling point of liquid nitrogen (77K), and high superconducting critical current densities, J_c. Such coated conductors hold great promise, with possible applications in electrical power transmission [1], fault current limiters [2], superconducting motors and generators [3], Maglev-based transport and superconducting magnetic energy storage [4, 5]. A major challenge for the adoption of HTS tapes in some of these applications is the need to overcome the rapid deterioration of J_c in high magnetic fields. If a supercurrent is applied in the mixed state of these type-II superconductors, when the superconductor is between the lower critical field, H_{c1}, and upper critical field, H_{c2}, magnetic flux lines treading the material will move as a result of the Lorentz force. This motion leads to finite energy dissipation, resulting in the loss of the zero resistance state. In practice these flux lines are pinned at normal 'defects' in the superconducting layer including impurities, second phases, grain

boundaries and dislocations. Since the Lorentz force scales linearly with supercurrent density, keeping these flux lines pinned at as very high currents requires careful engineering of the pinning sites, controlling their size and density to optimise the energy landscape for the maximum critical current density. Ideally, pinning centres should have sizes of the order of the vortex core diameter; if they are smaller than the superconducting coherence length, ξ, the vortex core may spread to other sites resulting in a reduction of the net pinning forces. There are several ways manufacturers can incorporate artificial pinning centers into cuprate superconductors. These include the addition of normal rare earth precipitates [6, 7], chemical modification through ion irradiation [8], surface deformation [9] and substrate surface decoration [10]. Advances in tape performance also must be combined with a low-cost and the ability to produce long lengths with high throughput, as reflected in a price-performance ratio [11]. The task is made particularly challenging due to the complex interplay between flux lines and the many different pinning sites that can be routinely introduced in 2G-HTS tapes. This makes it very challenging to predict the magnitude of pinning forces and J_c in advance and materials scientists must rely heavily on several complementary characterization methods to understand the roles played by different pinning centers. Advancing our understanding of the pinning potential landscape and behavior of flux lines within it will enable greater control of the maximum attainable J_c, and allow these tapes to get closer to their ultimate theoretical limit set by the pair breaking current density [12].

A large number of academic research groups and industrial manufacturers are developing high performance 2G-HTS tapes using different approaches [13]. Here we investigate commercial high J_c $GdBa_2Cu_3O_{7-\delta}$ (GBCO) based fabricated by the manufacturer SuNAM using reactive co-evaporation [14, 15]. These tapes have exceptional critical current densities well in excess of $1MAcm^{-2}$ at 77K under self-field conditions. In addition T_c lies in the range 92-95K, well above liquid nitrogen temperatures. This is achieved by careful tuning of BaO, CuO_x and Gd_2O_3 second phase inclusions produced during a deliberately Cu-rich deposition [16]. Applications for these tapes in motors, generators and magnet inserts require high J_c in high external fields, and to meet this need the microstructure of Gd_2O_3 nanoparticles is optimized to significantly raise the in-field J_c. However, if the density of pinning centres becomes too high their performance degrades again and the precise tuning of the Gd to Cu-Ba liquid ratio is required to attain optimal HTS tapes. Transmission electron microscopy (TEM) images of such tapes show uniformly dispersed, almost platelet-like Gd_2O_3 second phase inclusions in the best performing tapes [14, 15]. This contrasts with the more random and enlarged Gd_2O_3 nanoparticles found in worse performing in-field tapes. The establishment of the optimum growth conditions is very challenging requiring the microscopic characterisation of the vortex pinning landscape and its interpretation in terms of the nanoscale pinning centres known to be present.

Transport and magnetization measurements are two of the most common tools available to tape developers to characterise the ensemble-averaged pinning landscape at a macroscopic scale. In contrast, scanning probe microscopy techniques enable one to build a microscopic picture of the superconducting properties and represent ideal tools to study vortex behavior at discrete pinning centres [17]. Scanning Hall probe microscopy (SHPM) is a quantitative and non-invasive magnetic imaging technique has frequently been used to study supercurrent transport [18], ac losses [19], and flux penetration in cuprate superconductors at the microscale [20]. In this paper we use SHPM, supported by magnetization and electronic transport measurements, to obtain a microscopic picture the vortex pinning landscape at very low applied fields. We couple this with scanning electron microscopy (SEM) imaging to attempt to develop a detailed understanding of the role second phase inclusions play in pinning vortices and enhancing J_c. These studies reveal strong, and inhomogeneously distributed pinning sites throughout the GBCO film, but with dramatically broadened vortex profiles that exhibit negligible temperature dependence down to 10K. We attribute this to leading to large pinning forces resulting in the exceptionally high critical current densities in second generation HTS tapes. We tentatively suggest this is the result of the very strong pinning of individual vortex lines by multiple Gd_2O_3 nanoparticles, resulting in extensive lateral meandering on a scale of several micrometers as they traverse the film from bottom to top. Such a scenario would

clearly relay crucially on the shape and spatial distribution of pinning centres and provides important design rules for further enhancement of J_c in the future.

2. Materials and Methods

Magnetic imaging was performed by Scanning Hall Probe Microscopy (SHPM) in a commercial Oxford Instruments (OI) cryostat. A nanoscale Hall probe was patterned in a GaAs/AlGaAs heterostructure two-dimensional electron gas ~5μm from the gold-coated corner of a deep mesa etch acting as a makeshift Scanning Tunneling Microscope (STM) tip. The STM tip was used to approach the sensor to the sample surface and track it once the two were in close proximity. The spatial resolution of the Hall sensor was defined by the electronic wire width of the two intersecting Hall cross leads. A Hall probe with electronic width 500nm was used for the images obtained in figures 4, 5 and 7, while a Hall probe with electronic width 800nm was used for the images obtained in figure 6. To ensure that the Hall probe was in closest possible proximity to the superconducting layer, a 2μm thick protective Ag layer was removed from a 6mm length of 4mm wide 2G-HTS tape by wet chemical etching with ammonium peroxide. The tape was subsequently recoated with a Cr/Au (5nm/40nm) film to ensure good electrical contact between the sample and the STM tip and epoxied onto a silicon substrate. The Hall probe was mounted at an angle of approximately 1° with respect to the coated tape such that the STM tip is always the closest point to the tape surface [21]. A piezoelectric slick-slip driver and scanner tube facilitated the automated approach of the Hall probe towards the sample until a threshold current of 0.2nA was reached with the sample usually biased at +0.2V with respect to the grounded STM tip. The Hall probe was then lifted approximately 50nm above the sample surface for rapid 'flying-mode' imaging to produce a two-dimensional map of the magnetic induction. Several images were taken and averaged frame-by-frame to suppress the low frequency noise from the Hall probe. Different external magnetic fields could be applied from either a normal Cu wire coil wound around the cryostat or a superconducting magnet inside it. The scan range of the piezoelectric tube is strongly temperature dependent and varies from 8.5μm × 8.5μm to 22.4μm × 22.4μm between 10K and 88K. Local magnetometry was performed by parking the Hall sensor ~1 μm above a desired location on the superconducting sample and measuring the magnetic induction as an external field is swept around a hysteresis loop. At very large sample biases the high electric field associated with tall topographic features on the sample also modulates the response of the Hall sensor and the structural information obtained from such 'gating' images can then be directly correlated with magnetic information from the same location. In practice these images were generated by subtracting images captured at sample bias voltages of +2V and -2V, resulting in the removal of magnetic features and leaving only the topographic information of interest.

Electrical transport measurements were performed in a standard 4-point measurement configuration at temperatures down to 90K. Prior to Ag removal, two pairs of leads were soldered with a fixed spacing along a 16mm strip of 2G-HTS tape. These were subsequently contacted to the pads of a 20 pin ceramic package which was then attached to the end of a temperature-controlled sample holder designed to fit inside the OI cryostat. A constant current of 10mA was passed though the strip while the voltage was measured using a Keithley 182 nanovoltmeter as the temperature was swept at 0.1K/min using an OI ITC 503 temperature controller.

Field Effect Scanning Electron Microscopy (FE-SEM) at 5kV and 1kV and Energy Dispersive X-Ray Analysis (EDX) at 10kV were performed in a Joel JSM-6301F FE-SEM.

All data captured within this research project are openly available from the University of Bath Research Data Archive [22].

3. Results and discussion

3.1. Characterisation of the HTS tapes

An example of an as-received piece of tape covered by a 2μm thick Ag stabiliser layer is shown in Figure 1(a). The width of the HTS tape strip is 4mm while the thickness of the GBCO film below

the stabiliser layer is approximately 1.5μm. Once the stabiliser layer was etched away the dark, reflective and seemingly flat superconducting layer was exposed. Upon closer inspection of the surface of this layer with SEM and EDX (c.f. Figure S1) we find regions of sub-micrometre scale networks of non-superconducting CuO_x outgrowths with the lightly terraced yet much flatter superconducting GBCO layer in between (c.f., Fig. 1(b)).

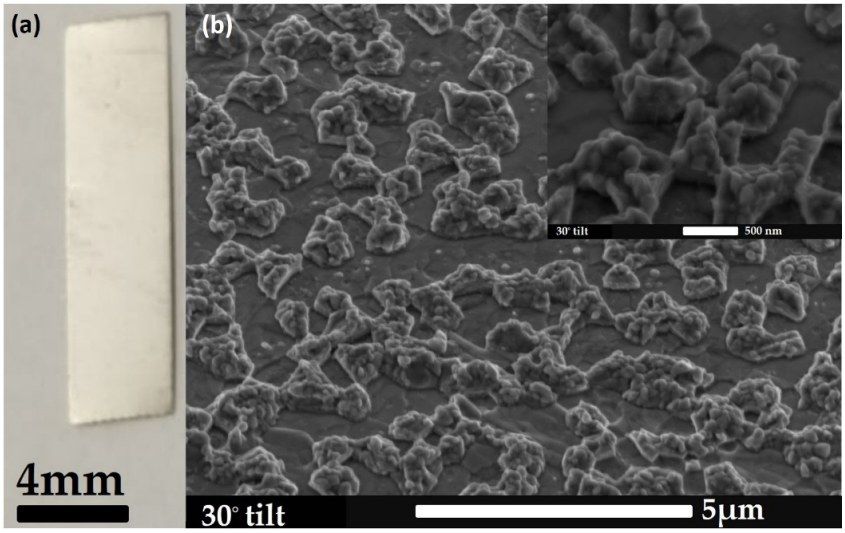

Figure 1. (a) Optical image of a strip of GBCO HTS tape covered with a 2μm thick Ag stabiliser layer.; (b) An SEM image of the surface of the tape after stabilizer removal at a 30 degree tilt angle. The inset shows a magnified SEM image of a region from the larger area of (b), showing the presence of CuO_x outgrowths from the upper layers of the superconducting film.

Temperature-dependent electronic transport measurements on a piece of tape with similar dimensions to the one in Figure 1(a) revealed a high mid-point resistive T_c of 93.4±0.2K, as shown in Figure 2. This falls within the range of previous measurements on similar types of tape [14, 15].

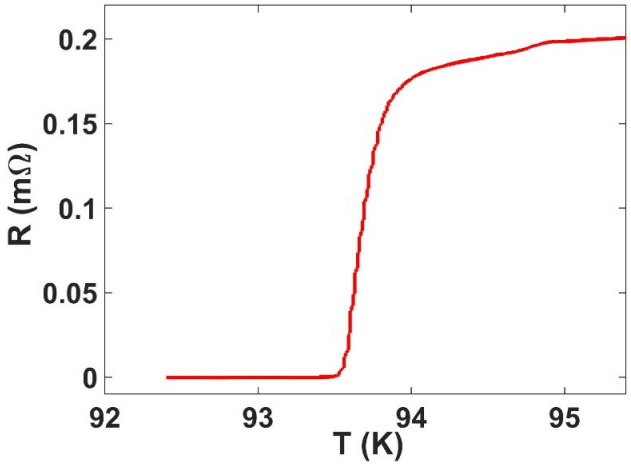

Figure 2. (**a**) Four-terminal resistance measured as a function of temperature showing a mid-point resistive transition at 93.4±0.2K.

J_c for our tapes has been estimated from local measurements of the magnetization using the parked SHPM Hall sensor, after fitting to a 'two-dimensional' critical state model developed by Brandt and Indenbom [23]. This describes the magnetic field penetration profile, B_z, in a zero field-cooled infinitely long type-II superconducting strip of width $2a$, and thickness d, under a constant perpendicular externally applied magnetic field. Within the assumptions of the model

(d<<2a) the critical current density can then be extracted as the sole unknown parameter. At an applied field H_a the magnetic field profile is described by,

$$B_z(y) = \begin{cases} 0 & |y| < b \\ B_c \tanh^{-1}\frac{\sqrt{y^2+b^2}}{c|y|} & b < |y| < a \\ B_c \tanh^{-1}\frac{c|y|}{\sqrt{y^2+b^2}} & |y| > a \end{cases}, \quad (1)$$

where $B_c=\mu_0 J_c d/\pi$, $c=\tanh(\mu_0 H_a/B_c)$ and $b=a/\cosh(\mu_0 H_a/B_c)$ is the boundary of the central flux free region. As the sweep direction of the applied field reverses again from H_{max}, $B_z(y)$ can be calculated from [23],

$$B_z^{\downarrow}(y, H_a, J_c) = B_z(y, H_{max}, J_c) - B_z(y, H_{max} - H_a, 2J_c). \quad (2)$$

The Hall probe was positioned approximately y=0.74mm from the center of the strip, and magnetisation loops captured using external field excursions H_{max}=±107mT from 10K up to 83K and H_{max}=±3.2mT from 81K up to 87.5K. The two different sweep ranges were used to ensure sufficient resolution in the hysteretic B-H loops across the full temperature range of interest. Example B-H loops and fits to the model are shown in Figures 3(a) and 3(c).The resulting estimations of J_c as a function of temperature are plotted in Figure 3(b) for higher field sweeps, and in Figure 3(d) for the lower field sweeps. The critical temperature can also be estimated from a linear extrapolation of J_c at high temperatures yielding a value of 90.2±0.2K, as indicated in Figure 3(d). The differences between the resistive T_c and magnetic estimations of T_c probably reflect small inhomogeneities in the film since the resistive measurement detects the strongest percolation path through the entire sample while the magnetisation data are only collected from the 'local' area near the Hall sensor. The estimated critical current density at 77K is within the range of previously estimated values obtained from transport measurements at the same temperature, with any difference likely to be due to the different in-field and self-field measurement conditions used [14, 15, 24]. Estimated J_c values for the smaller field range near Tc are systematically smaller than those for the larger sweep range reflecting the much lower sweep rates (approximately 30x lower) for these loops allowing much more time for the critical state to relax due, for example, to flux creep processes. These nevertheless represent exceptionally high critical current densities in comparison to other 2G-HTS tapes, reflecting the presence of very strong vortex pinning forces. A comparison between the data and the model fits in Figs. 3(a) and (b) reveals significant discrepancies, in particular at the points where the reverse flux repenetrates the sample. In practice the reverse flux penetrates much sooner than expected from the model and does not exhibit the very abrupt predicted onset. While our samples adequately satisfy the model assumption that d<<2a, the strips we measure are only of finite length with aspect ratio ~3:2 and the critical current is microscopically inhomogeneous on a scale of the distribution of artificial pinning centres. However, neither of these shortcomings seems able to explain the discrepancies with the fits which are more likely to be related to the relaxation of critical state profiles by flux creep. To illustrate this point in figures 3(e) and (f) we plot the magnetic induction profiles predicted by the model after increasing the applied field from zero to the maximum excursion, $\mu_0 H_{max}$=3.2mT, and after subsequent field reversal to -0.94mT respectively. Our measured data are quite closely represented by the dash-dot and dotted lines that have been superimposed to represent the smearing of the penetrating and repenetrating flux fronts due to flux creep. In fact the profile presented by these lines much more closerly mirrors the classical 3D Bean critical state behavior whereby dB_z/dy is a constant for a given sign of critical current density [23]. Similar behavior has been observed in local magnetization data measured on other types of 2G-HTS tapes [20], though not to the same extent as that seen here indicating a significantly faster relaxation rate in our samples. This in turn reflects the type, structure and topology of the specific pinning centres employed which lead to distinctly different creep barriers for different configurations.

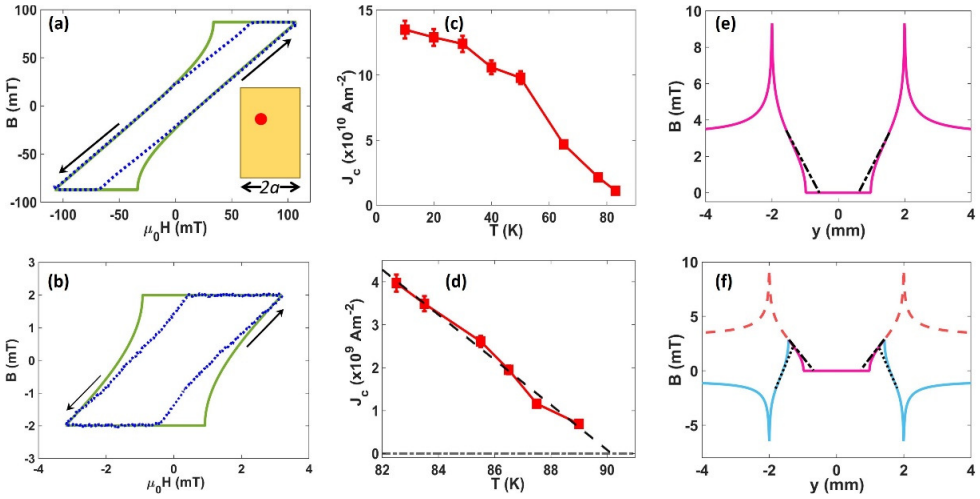

Figure 3. (a) B-H loop at 65K (dotted line) and a fit to the 2D critical state model (solid line). Arrows indicate the direction of the field sweep. The inset shows a sketch of the tape sample showing the position where local magnetometry measurements were performed (red dot); (b) B-H loop at 84K (dotted line) and a fit to the 2D critical state model (solid line). Arrows indicate the direction of the field sweep; (**c**) Temperature-dependent critical current density estimated from fitting magnetization loops swept out to ±107mT; (d) Temperature-dependent critical current density estimated from magnetization loops swept out to ±3.2mT. These data have been used to estimate the critical temperature from a linear extrapolation (dashed line) to J_c=0. (e) Magnetic field profile predicted by the 2D critical state model when the external field is increased from zero to $\mu_0.H_{max}$=3.2mT (J_c=5×10^9 A/m^2). The superimposed dash-dot line illustrates the actual behavior of the penetration front exhibited by our sample; (f) Model magnetic field profile after the applied field in (e) has been reduced again to $\mu_0.H_{max}$=-0.94mT (solid lines) The dashed red line shows the original penetration profile at the maximum applied field. The superimposed dotted line illustrates the actual behavior of the repenetration front exhibited by our sample.

3.2. Vortex pinning landscape in low fields

To further our understanding of the relationship between vortex pinning and the film microstructure we systematically captured a series of SHPM images of a sample of the 2G-HTS tape after field-cooling in small (<1mT) perpendicular magnetic fields. Figure 4 shows a series of three-dimensional renderings of vortex images captured at 77K after field-cooling from above T_c in several different fields [25]. We note that the applied fields stated are nominal values for the coil currents used and in practice the sample also sees contributions from the earth's field, nearby ferrous materials (e.g., the Hastelloy substrate of the tape [26]) and flux trapped in the windings of the superconducting magnet. As expected for a strong pinning film, vortex patterns are highly disordered and the number of first nearest neighbours frequently deviates from that expected for a perfect Abrikosov vortex lattice (i.e., six). In addition, specific sites are repeatedly occupied by a vortex after different field-cooling cycles suggesting that a few particularly strong pinning centres are present.

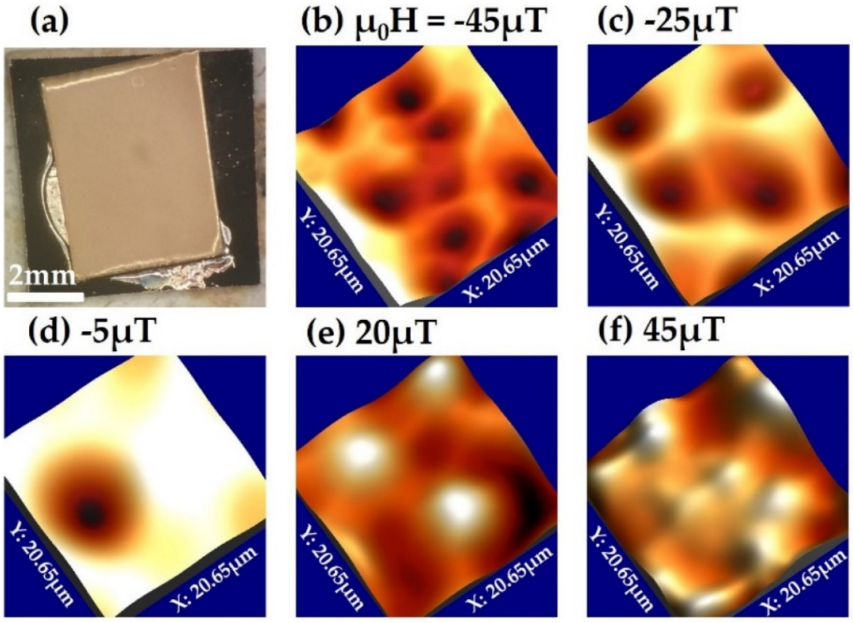

Figure 4. (a) Optical microscope image of the section of GBCO 2G-HTS tape imaged after the Ag stabiliser layer has been removed, and the sample then recoated with Cr/Au. The width, $2a = 4mm$, of the tape is given by its shortest length of 6mm; (b) – (f) Three dimensional renderings of SHPM vortex images captured on the GBCO tape after field-cooling to 77K from above T_c in perpendicular applied fields between -45μT and 45μT. The scan size is 20.7μm × 20.7μm. Vertical scales span 40μT (μ_0H=-45μT), 23μT (-25μT), 23μT (-5μT), 16μT (20μT) and 40μT (45μT).

Figures 5(a) and (b) examine the reproducibility of vortex patterns after repeatedly field-cooling the sample in the same applied field. As can be seen the vortex pattern is highly reproducible from one cooldown cycle to the next indicating that a small number of very strong pinning sites with a wide capture radius is dominating these frozen structures. This is in stark contrast to weakly pinning materials where such patterns tend to change dramatically between cooldowns due to statistical fluctuations in the freezing dynamics during the cooldown.

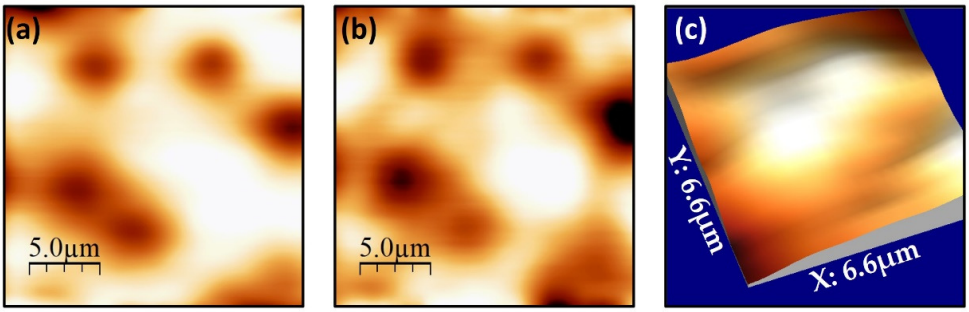

Figure 5. (a) and (b) SHPM images of vortices in a GBCO 2G=HTS tape after field-cooling to 77K from above T_c in the same applied perpendicular field of μ_0H≈-40μT. The vertical scales span 40μT and the scan size is 20.7μm × 20.7μm; (c) An expanded view of two very close white vortices in the center the sample after field-cooling to 77K in μ_0H≈95 μT, which were used to obtain a lower bound estimate of the pinning. The vertical scale spans 26μT.

A lower bound for the pinning force experienced by vortices has been estimated from two very close vortices in the image shown in Fig. 5(c). Assuming that both vortices are pinned with a force that matches or exceeds their mutual repulsion we compare this with an expression for

the force between two vortices in a bulk superconductor when the vortex-vortex separation, r, is much greater than the London penetration depth, λ_L. This is described by [27],

$$f_p^{v\to v} \approx \frac{\Phi_0^2}{2\pi\mu_0\lambda_L^2}\sqrt{\frac{\pi}{2\lambda_s r}}e^{\frac{-r}{\lambda_L}}, \qquad (3)$$

where Φ_o is the superconducting flux quantum. We estimate that two vortices in Fig. 5(c) are ~1.6μm apart, yields a lower bound on the pinning force of f_p~0.035μNm^{-1}. In practice of course, the spatial resolution of our imaging technique (~0.5μm) severely limits our ability to resolve two vortices at very close spacing and this number is inevitably a huge underestimate of typical pinning forces at this temperature. Moreover, it is knows that the vortex structure freezes in at a typical "irreversibility temperature" just below T_c where pinning forces become just strong enough to quench thermally activated vortex motion. Hence these vortex patterns are characteristic of even weaker pinning forces that apply much closer to T_c. A much more rigorous estimate of the average pinning force can be obtained from the relationship, $f_p \approx J_c \Phi_0$. Using the estimate of J_c at 77K from Fig. 3(d) we use this expression to estimate that pinning forces are approximately f_p~44μNm^{-1}, close to other high J_C cuprate materials and 2G-HTS tapes at similar fields [14, 15, 28, 29]. As expected this is several orders of magnitude larger than the force estimated from the separation of discrete vortices in SHPM images.

The quantitative nature of SHPM imaging also allows us to make a careful analysis of temperature-dependent vortex profiles which have been characterized in images of the type shown in Figures 6 (a). Fig. 6(b) illustrates linescans captured across the centre of one of these vortices at three different temperatures. Data for a number of different pinned vortices have been summarized in Figs. 6(c) and (d) in terms of the peak vortex heights and the full-width-half-maxima (FWHM) respectively. It is really striking that neither figure-of-merit shows any significant temperature dependence between 10K and 85K, with only a weak additional broadening of the vortices closer to T_c. Attempts to fit these profiles to the variational model predictions for type-II superconductors due to Clem fail completely, even if one assumes an unphysically large variational coherence length that breaks the assumption $\lambda_L >> \xi_v$ [30, 31]. In the limit that the measured FWHM of the vortex is governed by the diameter of the non-superconducting centre it is pinned on, these very large temperature-independent sizes would not be so surprising. However Gd_2O_3 nanoscale inclusions that are believed to dominate vortex pinning only have sizes of a few hundred nanometers [14, 15], orders of magnitude smaller than the vortex diameters we measure. This would suggest that individual flux lines are actually interacting with many nanoscale inclusions, meandering laterally over considerable distances in order to pass through as many artificial pinning centres as possible. The inset of Fig. 6(b) qualitatively illustrates this scenario.

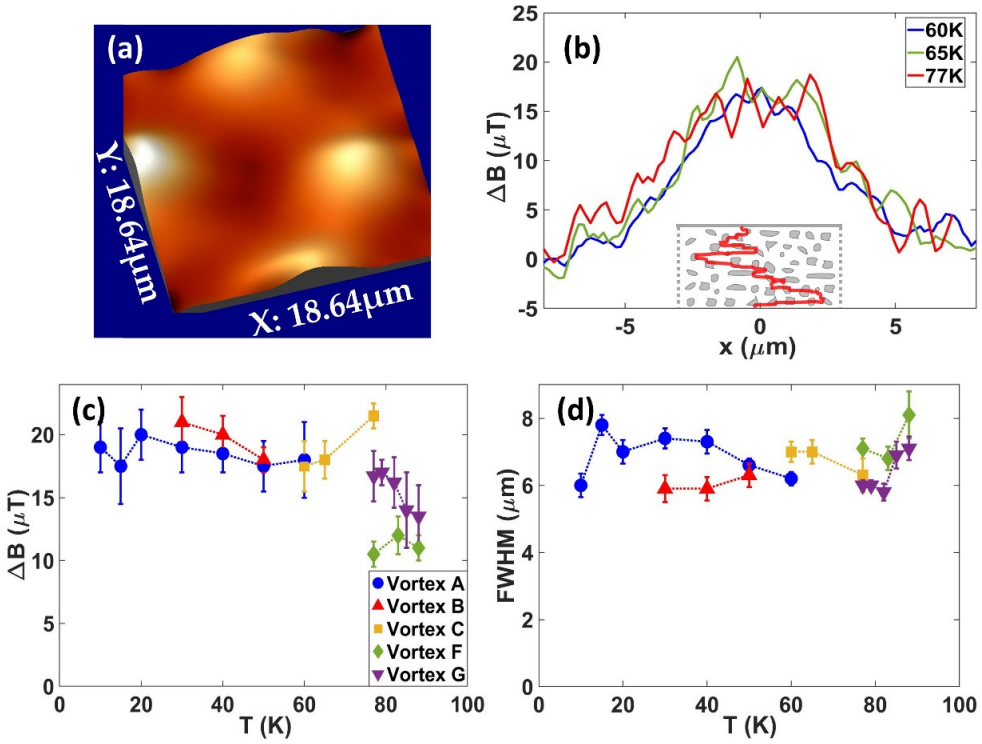

Figure 6. (a) Three dimensional rendering of an SHPM image of the vortex pattern after field-cooling to 65K μ_0H=25µT. The vertical scales span 19µT and the scan size is 18.6µm x 18.6; (b) Typical vortex profiled linescans across the centre of vortex C at three different temperatures. The inset shows a sketch of a flux line wiggling laterally within the tape to interact with as many of the pinning centres (grey) as possible; (c) Peak heights of vortex profiles as a function of temperature for several different pinned vortices; (d) FWHM of vortex profiles as a function of temperature for the same vortices shown in (c).

3.3. Correlating pinning sites

One of the challenges when it comes to developing 2G-HTS tapes is to understand which pinning objects in the superconducting film are dominating any increase in critical current. Previous TEM images of these SuNAM tapes has revealed both a high density of quite uniformly dispersed multilayers with a wide range of tilt angles Gd_2O_3 inclusions throughout the superconducting layer as well as much larger CuO_x outgrowths protruding from the top surface as shown in Fig. 1(b) [14, 15]. Since the latter are tend to have much larger lateral dimensions and are also non-superconducting, it is important to rule out that these are not also contributing significantly to the pinning of superconducting vortices. As these features are found at the tape surface they represent the main contribution to the surface topography and can be mapped using the "gating" imaging approach described in section 2. In this way we can search for correlations between location of the CuO_x outgrowths and the locations of strongly pinned vortices. Figures 7(a) shows examples of topographic maps that were captured just after the magnetic maps of Figures 7(b) (measured with a normal sample bias of 0.2V). Comparing the pairs of images we are unable to find any significant correlation between the largest topographical features and the characteristic vortex pinning locations. As clearly seen in linescans plotted in Figures 7(c), the vortex centres do not appear to bear any relationship with the measured topographic peaks (or the troughs), something that has been confirmed by generating a numerical cross-correlation of the images pairs. Hence we consider it very unlikely that these non-superconducting CuO_x outgrowths make a significant contribution to the vortex pinning landscape, and everything points to the fact that the

Gd_2O_3 nanoparticles distributed throughout the superconducting layer play the dominant role in maximising J_c.

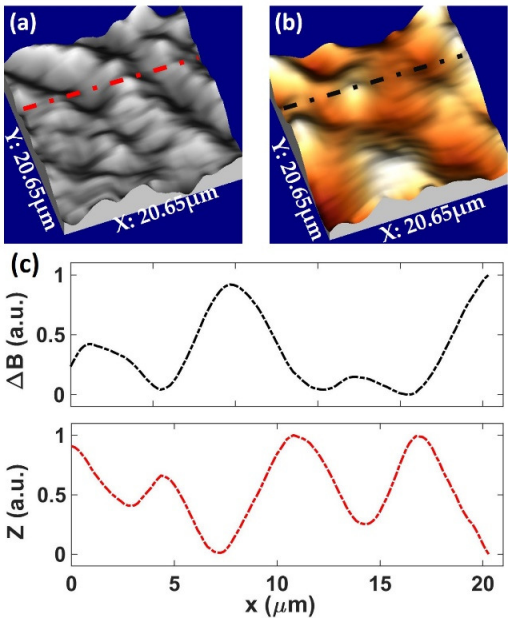

Figure 7. (a) Three dimensional rendering of a topographic 'gating' image captured at 77K.; (b) Three dimensional rendering of vortices at the same location as (a). Images were captured after field-cooling to 77K in μ_0H=25μT. The vertical scale for (b) spans 15μT. Scan sizes for all images are 20.7μm x 20.7μm. (c) shows linescans along the dashed-dotted lines superimposed on images (a) and (b).

5. Conclusions

Our results yield important new insights into nature of vortex pinning in commercial GdBaCuO high temperature superconducting tapes, providing new understanding that can be built on to further increase J_c in these tapes. Scanning Hall probe microscopy images reveal highly disordered vortex patterns reflecting a pinning landscape dominated by a small number of very strong pinning centres, most likely non-superconducting Gd_2O_3 second phase inclusions. Local magnetisation loops show surprising deviations from the predictions of widely accepted 2D Bean critical state model for infinite superconducting strips suggesting that penetration and repenetrating flux profiles relax rather rapidly due to flux creep. Indeed, we infer that our measured profiles are close to the predictions of the bulk 3D Bean critical state model with approximately constant values of dB_z/dy for a given sign of critical current density. An average pinning force per unit length of 44μNm^{-1} is estimated from our magnetisation data. Unexpectedly we measure extremely broad vortex profiles with FWHM of typically 6μm. Moreover, neither the vortex peak fields nor the FWHM shows significant temperature-dependence in the range 10-85K. These facts are very difficult to reconcile with the sizes of the dominant Gd_2O_3 pinning centres which are typically a few hundred nanometers in diameter. This suggests that individual vortex lines must be interacting with many different pinning sites and meander laterally over considerable distances in order to pass through as many artificial pinning centres as possible. This has important implications for the future development of HTS tapes using second phase pinning to increase J_c. Our work also reinforces the role magnetic imaging has as a powerful complementary tool for developing and optimizing high temperature superconducting tapes and opens up opportunities for further studies of flux pinning in GBCO tapes under self-field conditions [32]. In addition, ongoing improvements in the spatial resolution of magnetic imaging techniques [33, 34] will allow investigations to be performed with greater precision in order to resolve pinning sites in superconducting tapes across a much wider range of external fields and applied currents. This investigative approach would become even more powerful when

combined with simultaneous imaging of cross sections of the superconducting layer to more accurately correlate the locations of vortices and pinning sites.

Supplementary Materials: The following are available online at www.mdpi.com/xxx/s1; Figure S1: EDX analysis of the GdBaCuO layer surface.;

Author Contributions: Conceptualization, S.J.B.; W.Y.; M.Z. and D.C.; methodology, D.C. and S.J.B..; formal analysis, D.C. and S.J.B.; investigation, D.C.; resources, D.C. and S.J.B.; data curation, D.C.; writing—original draft preparation, D.C.; writing—review and editing, S.J.B.; visualization, D.C.; supervision, S.J.B.; project administration, S.J.B.; W.Y. and M.Z.; funding acquisition, S.J.B.; W.Y. and M.Z. All authors have read and agreed to the published version of the manuscript.

Funding: This research was funded by EPSRC in the UK under grant nos. EP/R007160/1 and the Nanocohybri COST Action CA-16218. DC is supported by a PhD studentship from Lloyds Register Foundation ICON (award nos. G0086). The APC was funded by the University of Bath.

Acknowledgments: We thank SuNAM for the provision of GdBaCuO high temperature superconducting tapes. We also thank electronics support from Joe Mills and acknowledge access to the University of Bath Nanofabrication Facility.

Conflicts of Interest: The authors declare no conflict of interest. The funders had no role in the design of the study.; in the collection, analyses, or interpretation of data.; in the writing of the manuscript, or in the decision to publish the results.

References

1. Xie, W.; Wei, B.; Yao, Z. Introduction of 35 kV km Level Domestic Second Generation High Temperature Superconducting Power Cable Project in Shanghai, China. *J. Supercond. Nov. Magn.* **2020**, 33, 1927-1931.
2. Noe, M.; Steurer, M. High-temperature superconductor fault current limiters: concepts, application, and development status. *Supercond. Sci. Technol.* **2007**, 20(3), R15-R29.
3. Haran, K.S.; Kalsi, S.; Arndt, T.; Karmaker, H.; Badcock, R.; Buckley, B.; Haugan, T.; Izumi, M.; Loder, D.; Bray, J.W.; Masson, P. High power density superconducting rotating machines-development status and technology roadmap. *Supercond. Sci. Technol.* **2017**, 30(12), 123002
4. Dong, F.; Huang, Z.; Hao, L.; Xu, X.; Jin. Z.; Shao, N. An on-board 2G HTS magnets system with cooling-power-free and persistent-current operation for ultrahigh speed superconducting maglevs. *Sci. Rep.* **2019**, 9(1), 1-12
5. Shiohara, Y.; Yoshzumi, M.; Takagi, Y.; Izumi, T. Future prospects of high T_c superconductors-coated conductors and their applications. *Physica C Supercond.* **2013**, 484, 1-5.
6. Yamasaki, H.; Yamada, H. Flux pinning properties of $YBa_2Cu_3O_{7-\delta}$ thin films containing a high density of nanoprecipitates: A comparative study to reveal size effects. *Physica C: Supercond.* **2017**, 542, pp.46-54.
7. MacManus-Driscoll, J.L.; Foltyn, S.R.; Jia, Q.X.; Wang, H.; Serquis, A.; Civale, L.; Maiorov, B.; Hawley, M.E.; Maley, M.P.; Peterson, D.E. Strongly enhanced current densities in superconducting coated conductors of $YBa_2Cu_3O_{7-x}$+ $BaZrO_3$. *Nat. Mater.* **2004**, *3*(7), pp.439-443.
8. Leroux, M.; Kihlstrom, K.J.; Holleis, S.; Rupich, M.W.; Sathyamurthy, S.; Fleshler, S.; Sheng, H.P.; Miller, D.J.; Eley, S.; Civale, L.; Kayani, A. Rapid doubling of the critical current of YBa2Cu3O7− δ coated conductors for viable high-speed industrial processing. *Appl. Phys. Lett.* **2015**, 107(19), p.192601.
9. Foltyn, S.R.; Civale, L.; MacManus-Driscoll, J.L.; Jia, Q.X.; Maiorov, B.; Wang, H.; Maley, M.; Materials science challenges for high-temperature superconducting wire. *Nat. Mater.* **2007**, *6*(9), pp.631-642.
10. Matsumoto, K.; Horide, T.; Osamura, K.; Mukaida, M.; Yoshida, Y.; Ichinose, A.; Horii, S. Enhancement of critical current density of YBCO films by introduction of artificial pinning centers due to the distributed nano-scaled Y_2O_3 islands on substrates. *Physica C: Supercond.* **2004**, 412, pp.1267-1271.
11. Fleshler, S.; Buczek, D.; Carter, B.; Cedrone, P.; DeMoranville, K.; Gannon, J.; Inch, J.; Li, X.; Lynch, J.; Otto, A.; Podtburg, E. Scale-up of 2G wire manufacturing at American Superconductor Corporation. *Physica C: Supercond.* **2009**, 469(15-20), pp.1316-1321.
12. Kwok, W.K.; Welp, U.; Glatz, A.; Koshelev, A.E.; Kihlstrom, K.J.; Crabtree, G.W. Vortices in high-performance high-temperature superconductors. *Rep. Prog. Phys.* **2016**, 79(11), p.116501.
13. Obradors, X.; Puig, T. Coated conductors for power applications: materials challenges. *Supercond. Sci. Technol.* **2014**, 27(4), p.044003.

14. MacManus-Driscoll, J.L.; Bianchetti, M.; Kursumovic, A.; Kim, G.; Jo, W.; Wang, H.; Lee, J.H.; Hong, G.W.; Moon, S.H. Strong pinning in very fast grown reactive co-evaporated $GdBa_2Cu_3O_7$ coated conductors. *APL Mater.* **2014**. *2*(8), p.086103.
15. Lee, J.H.; Lee, H.; Lee, J.W.; Choi, S.M.; Yoo, S.I.; Moon, S.H. RCE-DR, a novel process for coated conductor fabrication with high performance. *Supercond. Sci. Technol.* **2014**, 27(4), p.044018.
16. Dimos, D.; Chaudhari, P.; Mannhart, J. Superconducting transport properties of grain boundaries in $YBa_2Cu_3O_7$ bicrystals. *Phys. Rev. B*. **1990**, *41*(7), p.4038.
17. Kirtley, J.R. Fundamental studies of superconductors using scanning magnetic imaging. *Rep. Prog. Phys.* **2010**, 73(12), p.126501.
18. Dinner, R.B.; Moler, K.A.; Beasley, M.R.; Feldmann, D.M. Enhanced current flow through meandering grain boundaries in Y Ba 2 Cu 3 O 7− δ films. *Appl. Phys. Let.* **2007**, 90(21), p.212501.
19. Dinner, R.B.; Moler, K.A.; Feldmann, D.M.; Beasley, M.R. Imaging ac losses in superconducting films via scanning Hall probe microscopy. *Phys. Rev. B*. **2007**, 75(14), p.144503.
20. Marchiori, E.; Bending, S.J. Mapping the flux penetration profile in a 2G-HTS tape at the microscopic scale: deviations from a classical critical state model. *Supercond. Sci. Technol.* **2019**, 32(2), p.025009.
21. Bending, S.J. Scanning Hall probe microscopy of vortex matter. *Physica C: Supercond.* **2010**, 470(19), pp.754-757.
22. University of Bath Data Archive, DOI: pending
23. Brandt, E.H.; Indenbom, M. Type-II-superconductor strip with current in a perpendicular magnetic field. *Phys. Rev. B*. **1993**, 48(17), p.12893.
24. Talantsev, E.F.; Strickland, N.M.; Wimbush, S.C.; Brooks, J.; Pantoja, A.E.; Badcock, R.A.; Storey, J.G.; Tallon, J.L. The onset of dissipation in high-temperature superconductors: magnetic hysteresis and field dependence. *Sci. Rep.* **2018**, 8(1), pp.1-14.
25. Horcas, I.; Fernández, R.; Gomez-Rodriguez, J.M.; Colchero, J.; Gómez-Herrero, J.; Baro, A.M. WSXM: a software for scanning probe microscopy and a tool for nanotechnology. *Rev. Sci. Instrum*. **2007**, 78(1), p.013705.
26. Lu, J.; Choi, E.S.; Zhou, H.D. Physical properties of Hastelloy® C-276™ at cryogenic temperatures. *J. Appl. Phys.* **2003**, 103(6), p.064908.
27. Stoddart, S.T.; Bending, S.J.; Geim, A.K.; Henini, M. 1993. Quantum-resolved investigations of flux dynamics: collective and single vortex effects. Phys. Rev. Lett. 1993, 71(23), p.3854.
28. Llordes, A.; Palau, A.; Gázquez, J.; Coll, M.; Vlad, R.; Pomar, A.; Arbiol, J.; Guzman, R.; Ye, S.; Rouco, V.; Sandiumenge, F. Nanoscale strain-induced pair suppression as a vortex-pinning mechanism in high-temperature superconductors. *Nat. Mater.* **2012**. 11(4), pp.329-336.
29. Talantsev, E.F.; Pantoja, A.E.; Crump, W.P.; Tallon, J.L. Current distribution across type II superconducting films: a new vortex-free critical state. *Sci. Rep.* **2018**. 8(1), pp.1-9.
30. Clem, J.R. Simple model for the vortex core in a type II superconductor. *J. Low Temp. Phys.* **1975**, 18(5-6), pp.427-434.
31. Kirtley, J.R.; Kallin, C.; Hicks, C.W.; Kim, E.A.; Liu, Y.; Moler, K.A.; Maeno, Y.; Nelson, K.D. Upper limit on spontaneous supercurrents in Sr_2RuO_4. *Phys. Rev. B*. **2007**, 76(1), p.014526.
32. Talantsev, E.F.; Tallon, J.L. Universal self-field critical current for thin-film superconductors. *Nat. Commun.* **2015**, *6(1)*, 1-8.
33. Collomb, D.; Li, P.; Bending, S.J. Nanoscale graphene Hall sensors for high-resolution ambient magnetic imaging. *Sci. Rep.* **2019**, *9(1)*, pp.1-10.
34. Thiel, L.; Rohner, D.; Ganzhorn, M.; Appel, P.; Neu, E.; Müller, B.; Kleiner, R.; Koelle, D.; Maletinsky, P. Quantitative nanoscale vortex imaging using a cryogenic magnetometer. *Nat. Nanotechnol.* **2016**, 11(8), pp.677-81.

nanomaterials

MDPI

Article

Imaging of strong nanoscale vortex pinning in GdBaCuO high temperature superconducting tapes: Supplementary material

David Collomb [1]*, Min Zhang [2], Weijia Yuan [2] and Simon J. Bending [1]

[1] University of Bath, Claverton Down, Bath, BA2 7AY, United Kingdom.;
[2] Applied Superconductivity Laboratory, Department of Electronics and Electrical Engineering, University of Strathclyde, Glasgow, G1 1XQ, United Kingdom.;

1. EDX analysis of the GdBaCuO layer surface

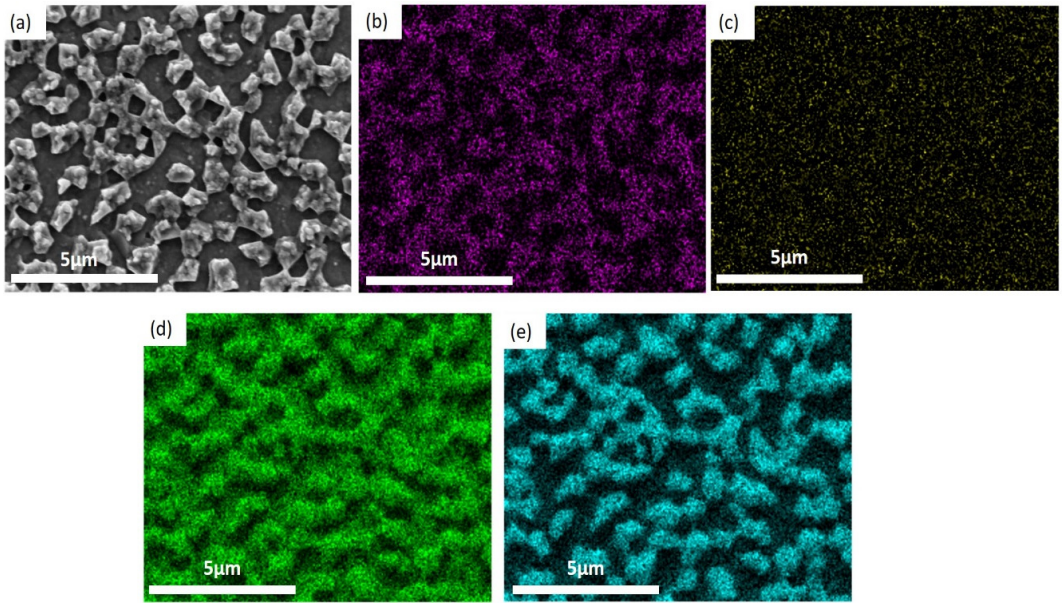

Figure S1. (**a**) Reference SEM image of the area where EDX was been performed.; (b) EDX map of Barium distribution of intensity.; (c) EDX map of Gadolinium distribution intensity.; (d) EDX map of Oxygen distribution of intensity.; (e) EDX map of Copper distribution of intensity.

8.1.2 Discussion on vortex imaging of high temperature superconducting tapes

Just by comparing images between these tapes and $RbEuFe_4As_4$ we can see the strong nature of certain pinning sites in these second generation HTS tapes. Unlike in $RbEuFe_4As_4$, repeatedly cooling the same field results in an almost identical vortex configuration, with differences likely being due to the piezo hysteresis as temperature is changed. This is further evidenced in the change in field, where in $RbEuFe_4As_4$ the vorticies pin in vastly different locations, whereas in the tapes similar positions are almost always occupied. Furthermore, the temperature dependence of the vortex profiles, tracked by measuring the full width half maximum and peak heights of the vortices, shows no trend. This is unlike in many other 'clean' superconducting thin films which exhibit a temperature dependence. This further highlights the strong pinning sites in the HTS layer of the tape. We note that the full width Hall maximums of these vortices are fairly large if assuming these are pinned on a cylindrical normal tube. This is more likely due to the large volumes across which the flux lines are bending between pinning sites along the c axis of the HTS layer. Despite there being normal CuO_z outgrowths as seen by topographical imaging, it is difficult to correlate this with the location of the pinned vortices, showing that Gd_2O_3 second phases buried throughout the superconducting layer are the likely primary contributor to the pinning. The SEM images of the surface of the tape alone show the complex nature of the material. We note that these outgrowths affect the ultimate attainable spatial resolution as essentially this limits our approach to a height equal to the gold conducting layer, plus the average height of the CuO outgrowths. However this is still not more than a micrometer in height and so we can comfortably resolve he vortices we observe in the text. Steps and other grain-like structures can be seen in the GBCO material, pointing to something beyond the simple picture of second phases being the primary pinning source. Although we cannot disconcern pinning sources in our research to full certainty, our work still provides a valuable first-look into the nature of these tapes to help dig deeper into what makes them so valuable for high critical current applications.

Similar experiments but under different self-field conditions can help gain further insight into the pinning properties. Furthermore, higher resolution imaging can help study how the vortex lattice and pinning regimes evolve as a function of higher fields and temperature, giving a further push for reasons to improve the spatial resolution of SHPM. The research into high temperature superconducting tapes is merely just beginning, thanks to the myriad of options at the disposal of tape manufacturers the effect of nanoengineering these materials has a large scope to study. We look forward to further material families being employed in such applications as well as their material engineering breakthroughs. 1

9 Conclusions and Future Outlook

9.1 Conclusions

9.1.1 Graphene-based Hall probe development and characterisation

Chemical vapour deposition has the powerful advantage of being a scaleable technology for high quality graphene growth [77]. However, the experiences described in chapter 6 show

that once the CVD graphene is processed into its final device state, the yield of successful devices is often rather low. Encapsulating the wet transferred CVD graphene is a very good alternative, providing better performance and representing the first step towards commercial production of graphene-based Hall probe devices. These results are now being built on to fabricate, and then improve, graphene-based SHPMs. The figures-of-merit and fabrication versatility do suggest that graphene-based Hall probes are likely to replace GaAs-based Hall sensors in commercial and research set-ups in the future, the major bottleneck for large scale commercial applications still being scaleability.

9.1.2 Vortex matter in HTS materials

The study of the ferromagnetic superconductor $RbEuFe_4As_4$ showed a rather significant effect on superconductivity arising from the magnetic ordering. We reveal that the exchange interaction between the superconducting and magnetic electrons is significant, weakening the superconductivity as the magnetic moments order as shown by our study of the penetration depth as a function of temperature. However, the exchange constant is not large enough to completely destroy superconductivity around the magnetic ordering temperature, thus the material remains superconducting down to 0K, while also exhibiting helimagnetism below 15K. As explored in this thesis, this is not the only material to exhibit this unexpected marriage of the two phenomena. The recent flow of studies on $RbEuFe_4As_4$ and its sister materials have established a renewed interest in studying spin-singlet hybrid superconductors, which exist in most part due to the optimum isolation between the magnetic and superconducting sublattices. As we learn more about these materials and their unique coexistence phenomena across a relatively large temperature range, this will advance our understanding of the mesoscopic interactions between superconductivity and magnetism, and could even inform the design of new superconducting-magnetic hybrid devices.

Research into HTS tapes currently spans numerous technologically-important aspects including solving the issue of effective superconducting joints, increasing the tolerance to high magnetic fields, improving the current carrying capacity, optimising the performance under mechanical stresses and strains and eliminating screening current-induced fields, to name just a few [171]. In this thesis we have chosen to tackle just one of these complex problems, namely investigating the properties of high current carrying capacity tapes incorporating nanoscale artificial pinning sites introduced as non-superconducting second phases during growth. We have shown a strong impact of these pinning sites on the superconducting vortices, giving rise to a highly inhomogeneous pinning landscape characterised by the formation of almost identical vortex patterns after repeated cooling, vortex hopping between different strong pinning sites and an unusual temperature dependence and field profile of vortices sitting at such sites. One can make simple comparisons between the vortex landscapes of $RbEuFe_4As_4$ and GdBaCuO studied in this thesis to further highlight how the two are on opposite ends of the vortex pinning spectrum. Estimations of the pinning forces and critical current density directly reflect the benefit of having such a landscape for superconducting applications. This also points out that less diversity of artificial pinning sites could well be more when it comes to selecting from the plethora of pinning sources when engineering artificial sites. Finally, this research work also illustrates that magnetic

imaging, especially imaging with very high spatial resolution, could become a key tool to accelerate the characterisation and further development of commercial 2G-HTS tapes.

9.2 Outlook for future work

9.3 Improvements to the SHPM technique

The future of SHPM must follow the same lines as those explored in this thesis; increased spatial resolution combined with improved minimum detectable fields. To see where this is likely to go next it is best to refer to chapter 2 and identify the trend exhibited by competing techniques in recent years. Scanning SQUID microscopy, NV centre scanning magnetometry and MFM all have the sensing element on the end of a sharp tip. While STM-tracking SHPM does incorporate a tip, the active component (the Hall cross) is still relatively far away from this, and the overall size of the sensor chip introduces limitations for the alignment and fine approach to the sample being imaged. One solution to this involves integrating the Hall probe on the apex of an AFM tip, and has been attempted a few times with modest success [172, 173, 174, 175]. While the spatial resolution can be much improved this way the device fabrication has proved to be a major challenge and often results in a reduction of the magnetic field resolution. The research work in this thesis exploiting the easy transferability of graphene to a wide range of substrates shows that this can be the basis of an Atomic Force Hall Probe Microscope (AFHPM) in which it is feasible to retain its high magnetic field resolution. Further advancements in the coating of AFM tips with graphene by Lanza et.al. also open up a pathway to retain the very high spatial resolution of AFM-based techniques, for example by using the previously-demonstrated draping technique due to Gregusova et. al. to pattern a nanoscale Hall cross [176, 175]. These developments should make SHPM highly competitive with NV scanning magnetometry for imaging under ambient conditions imaging and scanning SQUID microscopy under low temperature conditions. Finally, the addition of field excitation coils will enable the possibility to perform local susceptometry, with applications such as the manipulation of skyrmions and domain structures in magnetic materials, and non-destructive testing in a wide range of conducting materials.

As clearly demonstrated in this thesis, a high Hall coefficient is no use on its own if it is not combined with very low electronic noise. Hence, monolayer of few-layer graphene may not remain the best material for the Hall cross indefinitely. Materials such as Black Phosphorous and Indium Selenide could prove to be strong competitors to graphene, since both demonstrate very attractive low frequency noise figures, even at smaller wire widths [177, 178, 179]. Since the mechanisms of the noise may differ between materials, further research is needed to minimise their low frequency noise levels. However, at present there still remains much to do to optimise graphene Hall sensors. As discussed in chapters 3, multiple layers may be more beneficial for low noise applications where a lower Hall coefficient can be compensated for using ultra-low noise preamplifiers. Moreover, by designing the sensor system so that the few-layer Hall probe can be tuned to the lowest noise carrier density regions with a gate, the minimum detectable field can be further enhanced.

9.3.1 Further imaging

Due to current limitations on the performance of GaAs based SHPMs at room temperature, the SHPM technique has to date largely been limited to imaging superconducting materials. The development of SHPM sensors with improved room temperature SNRs opens many more applications such as; imaging and manipulation of Skyrmion systems [26], investigating novel magnetic 2D materials [180], antiferromagnetic devices for spintronic application [15], spin caloritronic materials [14] as well as more routine uses in industrial settings such as quality control during the manufacture of ferromagnetic data storage media (an application currently being performed by MFM [181]). The technique could even be used in the biosciences, such as for the identification and characterisation of magnetotactic bacteria [182].

Despite the focus of the development of scanning magnetometers towards room temperature and ambient conditions, to adapt Feynman's famous nanotechnology-related quote; *there is still plenty of room in the cold*. The familiarity of humans with superconductivity is still at an early stage of acquaintanceship, for example, even now aspects like the interplay between magnetism and superconductivity are only just becoming understood and the list of known high temperature superconductors is growing quickly. Building on the imaging work on $RbEuFe_4As_4$, described here, imaging in ferromagnetic-superconductors with coexisting out-of-plane magnetic moments such as $EuFe_2(As_{0.79}P_{0.21})_2$ could help us achieve a much more complete understanding of the interplay between magnetism and superconductivity. SHPM can achieve this by quantifying key superconducting parameters (e.g., the penetration depth and superfluid density) and ferromagnetic domain structures in Meissner-like and critical state-like regimes. The optimisation of vortex pinning for high J_c applications is still in its infancy. As the spatial resolution of magnetic imaging, topographic imaging and chemical characterisation tools increases, it will become easier to discern the various contributions to vortex pinning and identify which has the greater impact on the pining landscape. Furthermore, additional minor enhancements to imaging techniques, such as mapping under simultaneous transport current flow, will allow high temperature superconducting tapes to be studied under self-field conditions rather than just under external fields.

References

[1] Liye Xiao et al. "HTS power technology for future DC power grid". In: *IEEE Trans. Appl. Supercond* 23.3 (2013), p. 5401506.

[2] A Sykes et al. "Compact fusion energy based on the spherical tokamak". In: *Nuclear Fusion* 58.1 (2017), pp. 016–039.

[3] Yiyun Lu and Huiying Huang. "A novel HTS magnetic levitation dining table". In: *Physica C: Superconductivity and its Applications* 548 (2018), p. 1420.

[4] AK Geim and KS Novoselov. *The rise of graphene. naturematerials, 6: 183–191*. 2007.

[5] Junmo Kang et al. "Graphene transfer: key for applications". In: *Nanoscale* 4.18 (2012), pp. 5527–5537.

[6] Luca Banszerus et al. "Ultrahigh-mobility graphene devices from chemical vapor deposition on reusable copper". In: *Science advances* 1.6 (2015), e1500222.

[7] MP Smylie et al. "Anisotropic superconductivity and magnetism in single-crystal RbEuFe 4 As 4". In: *Physical Review B* 98.10 (2018), p. 104503.

[8] Jae-Hun Lee et al. "RCE-DR, a novel process for coated conductor fabrication with high performance". In: *Superconductor Science and Technology* 27.4 (2014), p. 044018.

[9] Antal Gasparics et al. "Magnetic imaging in non-destructive testing". In: *2010 International Conference on Mechanical and Electrical Technology*. IEEE. 2010, pp. 47–49.

[10] Jonathan Blackledge, Lorenzo Rosa, and Albert Boretti. "Nano-Magnetic Resonance Imaging (Nano-MRI) Gives Personalized Medicine a New Perspective". In: (2017).

[11] Simon J Bending. "Local magnetic probes of superconductors". In: *Advances in Physics* 48.4 (1999), pp. 449–535.

[12] Wolfgang Kuch. "Magnetic imaging". In: *Magnetism: a synchrotron radiation approach*. Springer, 2006, pp. 275–320.

[13] Xichao Zhang et al. "Skyrmion-electronics: writing, deleting, reading and processing magnetic skyrmions toward spintronic applications". In: *Journal of Physics: Condensed Matter* 32.14 (2020), p. 143001.

[14] Gerrit EW Bauer, Eiji Saitoh, and Bart J Van Wees. "Spin caloritronics". In: *Nature materials* 11.5 (2012), pp. 391–399.

[15] Tomas Jungwirth et al. "Antiferromagnetic spintronics". In: *Nature nanotechnology* 11.3 (2016), p. 231.

[16] AK Petford-Long and JN Chapman. "Lorentz microscopy". In: *Magnetic microscopy of nanostructures*. Springer, 2005, pp. 67–86.

[17] B Bartova et al. "Precipitates and magnetic domains in an annealed Co 38 Ni 33 Al 29 shape memory alloy studied by TEM". In: *EMC 2008 14th European Microscopy Congress 1–5 September 2008, Aachen, Germany*. Springer. 2008, pp. 391–392.

[18] Francis Bitter. "On inhomogeneities in the magnetization of ferromagnetic materials". In: *Physical review* 38.10 (1931), p. 1903.

[19] U Essmann and H Träuble. "The direct observation of individual flux lines in type II superconductors". In: *Physics letters A* 24.10 (1967), pp. 526–527.

[20] ZQ Qiu and Samuel D Bader. "Surface magneto-optic Kerr effect". In: *Review of Scientific Instruments* 71.3 (2000), pp. 1243–1255.

[21] Bevin Huang et al. "Layer-dependent ferromagnetism in a van der Waals crystal down to the monolayer limit". In: *Nature* 546.7657 (2017), pp. 270–273.

[22] Jeffrey McCord. "Progress in magnetic domain observation by advanced magneto-optical microscopy". In: *Journal of Physics D: Applied Physics* 48.33 (2015), p. 333001.

[23] St Egelkamp and L Reimer. "Imaging of magnetic domains by the Kerr effect using a scanning optical microscope". In: *Measurement Science and Technology* 1.1 (1990), p. 79.

[24] Alex De Lozanne. "Application of magnetic force microscopy in nanomaterials characterization". In: *Microscopy research and technique* 69.7 (2006), pp. 550–562.

[25] Miriam Jaafar et al. "Distinguishing magnetic and electrostatic interactions by a Kelvin probe force microscopy-magnetic force microscopy combination". In: *Beilstein journal of nanotechnology* 2.1 (2011), pp. 552–560.

[26] Arianna Casiraghi et al. "Individual skyrmion manipulation by local magnetic field gradients". In: *Communications Physics* 2.1 (2019), pp. 1–9.

[27] J Scott et al. "Electrostatic charging artefacts in Lorentz electron tomography of MFM tip stray fields". In: *Journal of Physics D: Applied Physics* 34.9 (2001), p. 1326.

[28] O Kazakova et al. "Frontiers of magnetic force microscopy". In: *Journal of Applied Physics* 125.6 (2019), p. 060901.

[29] John Clarke and Alex I Braginski. *The SQUID handbook. Vol. 1, Fundamentals and technology of SQUIDs and SQUID systems*. Wiley-VCH, 2004.

[30] S Chatraphorn et al. "Scanning SQUID microscopy of integrated circuits". In: *Applied physics letters* 76.16 (2000), pp. 2304–2306.

[31] RC Black et al. "Magnetic microscopy using a liquid nitrogen cooled YBa2Cu3O7 superconducting quantum interference device". In: *Applied physics letters* 62.17 (1993), pp. 2128–2130.

[32] A Finkler et al. "Scanning superconducting quantum interference device on a tip for magnetic imaging of nanoscale phenomena". In: *Review of Scientific Instruments* 83.7 (2012), pp. 073–702.

[33] EF Fleet et al. "HTS scanning SQUID microscopy of active circuits". In: *IEEE transactions on applied superconductivity* 9.2 (1999), pp. 4103–4106.

[34] Amit Finkler et al. "Self-aligned nanoscale SQUID on a tip". In: *Nano letters* 10.3 (2010), pp. 1046–1049.

[35] JM Taylor et al. "High-sensitivity diamond magnetometer with nanoscale resolution". In: *Nature Physics* 4.10 (2008), pp. 810–816.

[36] Myoengwon Lee, Jungbae Yoon, and Donghun Lee. "Atomic Scale Magnetic Sensing and Imaging Based on Diamond NV Centers". In: *Magnetometers-Fundamentals and Applications of Magnetism*. IntechOpen, 2019.

[37] Francesco Casola, Toeno van der Sar, and Amir Yacoby. "Probing condensed matter physics with magnetometry based on nitrogen-vacancy centres in diamond". In: *Nature Reviews Materials* 3.1 (2018), pp. 1–13.

[38] A Oral, SJ Bending, and M Henini. "Realtime scanning Hall probe microscopy". In: *Applied physics letters* 69.9 (1996), pp. 1324–1326.

[39] Munir Dede et al. "Scanning Hall probe microscopy (SHPM) using quartz crystal AFM feedback". In: *Journal of Nanoscience and Nanotechnology* 8.2 (2008), pp. 619–622.

[40] Alexander Grigorenko et al. "A one-dimensional chain state of vortex matter". In: *Nature* 414.6865 (2001), pp. 728–731.

[41] RF Broom and EH Rhoderick. "Studies of the intermediate state in thin superconducting films". In: *Proceedings of the Physical Society* 79.3 (1962), p. 586.

[42] Radivoje S Popovic. *Hall effect devices: magnetic sensors and characterization of semiconductors*. CRC Press, 2003.

[43] Alexander A Balandin. "Low-frequency 1/f noise in graphene devices". In: *Nature nanotechnology* 8.8 (2013), p. 549.

[44] LKJ Vandamme and AH De Kuijper. "Conductance noise investigations on symmetrical planar resistors with finite contacts". In: *Solid-State Electronics* 22.11 (1979), pp. 981–986.

[45] David Collomb, Penglei Li, and Simon J Bending. "Nanoscale graphene Hall sensors for high-resolution ambient magnetic imaging". In: *Scientific reports* 9.1 (2019), pp. 1–10.

[46] RS Popović. "Hall-effect devices". In: *Sensors and Actuators* 17.1-2 (1989), pp. 39–53.

[47] A Pross et al. *Second generation quantum well sensors for room-temperature scanning Hall probe microscopy*. 2005.

[48] Adarsh Sandhu et al. "Direct magnetic imaging of ferromagnetic domain structures by room temperature scanning Hall probe microscopy using a bismuth micro-Hall probe". In: *Japanese Journal of Applied Physics* 40.5B (2001), p. L524.

[49] Adarsh Sandhu et al. "High sensitivity InSb ultrathin film microHall sensors for bioscreening applications". In: *Japanese journal of applied physics* 43.7A (2004), p. L868.

[50] JK Gregory, SJ Bending, and A Sandhu. "A scanning Hall probe microscope for large area magnetic imaging down to cryogenic temperatures". In: *Review of scientific instruments* 73.10 (2002), pp. 3515–3519.

[51] HA Mohammed and SJ Bending. "Fabrication of nanoscale Bi Hall sensors by liftoff techniques for applications in scanning probe microscopy". In: *Semiconductor Science and Technology* 29.8 (2014), pp. 085–007.

[52] Adarsh Sandhu et al. "50 nm Hall sensors for room temperature scanning Hall probe microscopy". In: *Japanese Journal of Applied Physics* 43.2R (2004), p. 777.

[53] Philip Richard Wallace. "The band theory of graphite". In: *Physical review* 71.9 (1947), p. 622.

[54] Mildred S Dresselhaus and Gene Dresselhaus. "Intercalation compounds of graphite". In: *Advances in physics* 51.1 (2002), pp. 1–186.

[55] AH Castro Neto et al. "The electronic properties of graphene, 2009 Rev". In: *Mod. Phys* 81 (2009), p. 109.

[56] Tanmoy Das et al. "Graphene-based flexible and wearable electronics". In: *Journal of Semiconductors* 39.1 (2018), p. 011007.

[57] Goki Eda, Giovanni Fanchini, and Manish Chhowalla. "Large-area ultrathin films of reduced graphene oxide as a transparent and flexible electronic material". In: *Nature nanotechnology* 3.5 (2008), pp. 270–274.

[58] M Venkata Kamalakar et al. "Long distance spin communication in chemical vapour deposited graphene". In: *Nature communications* 6.1 (2015), pp. 1–8.

[59] Xiaoqiang Li et al. "18.5% efficient graphene/GaAs van der Waals heterostructure solar cell". In: *Nano Energy* 16 (2015), pp. 310–319.

[60] Emiliano Pallecchi et al. "Transport scattering time probed through rf admittance of a graphene capacitor". In: *Physical Review B* 83.12 (2011), p. 125408.

[61] Kentaro Nomura and Allan H MacDonald. "Quantum transport of massless Dirac fermions". In: *Physical review letters* 98.7 (2007), p. 076602.

[62] Giacomo Reina et al. "Promises, facts and challenges for graphene in biomedical applications". In: *Chemical Society Reviews* 46.15 (2017), pp. 4400–4416.

[63] Cory R Dean et al. "Boron nitride substrates for high-quality graphene electronics". In: *Nature nanotechnology* 5.10 (2010), pp. 722–726.

[64] Yan Zhang, Emilio E Mendez, and Xu Du. "Mobility dependent lowfrequency noise in graphene field effect transistors". In: *ACS nano* 5.10 (2011), pp. 8124–8130.

[65] V Panchal et al. "Small epitaxial graphene devices for magnetosensing applications". In: *Journal of Applied Physics* 111.7 (2012), 07E509.

[66] Yinxiao Yang and Raghunath Murali. "Impact of size effect on graphene nanoribbon transport". In: *IEEE Electron Device Letters* 31.3 (2010), pp. 237–239.

[67] Jan Dauber et al. "Reducing disorder in graphene nanoribbons by chemical edge modification". In: *Applied physics letters* 104.8 (2014), pp. 083–105.

[68] Guanxiong Liu et al. "Origin of 1/f noise in graphene multilayers: Surface vs. volume". In: *Applied Physics Letters* 102.9 (2013), p. 093111.

[69] Guanxiong Liu et al. "Graphene thickness-graded transistors with reduced electronic noise". In: *Applied Physics Letters* 100.3 (2012), p. 033103.

[70] Bruno Pellegrini. "1/f noise in graphene". In: *The European Physical Journal B* 86.9 (2013), p. 373.

[71] Atindra Nath Pal and Arindam Ghosh. "Ultralow noise field-effect transistor from multilayer graphene". In: *Applied Physics Letters* 95.8 (2009), pp. 082–105.

[72] Guangyu Xu et al. "Effect of spatial charge inhomogeneity on 1/f noise behavior in graphene". In: *Nano letters* 10.9 (2010), pp. 3312–3317.

[73] Yu-Ming Lin and Phaedon Avouris. "Strong suppression of electrical noise in bilayer graphene nanodevices". In: *Nano letters* 8.8 (2008), pp. 2119–2125.

[74] Hong Wang et al. "Two-dimensional heterostructures: fabrication, characterization, and application". In: *Nanoscale* 6.21 (2014), pp. 12250–12272.

[75] Rebeca Ribeiro-Palau et al. "Twistable electronics with dynamically rotatable heterostructures". In: *Science* 361.6403 (2018), pp. 690–693.

[76] Matthew Yankowitz et al. "van der Waals heterostructures combining graphene and hexagonal boron nitride". In: *Nature Reviews Physics* 1.2 (2019), pp. 112–125.

[77] André Dankert, Bogdan Karpiak, and Saroj P Dash. "Hall sensors batch-fabricated on all-CVD h-BN/graphene/h-BN heterostructures". In: *Scientific reports* 7.1 (2017), p. 15231.

[78] Morteza Kayyalha and Yong P Chen. "Observation of reduced 1/f noise in graphene field effect transistors on boron nitride substrates". In: *Applied Physics Letters* 107.11 (2015), pp. 113–101.

[79] GR Bhimanapati, NR Glavin, and Joshua Alexander Robinson. "2D boron nitride: synthesis and applications". In: *Semiconductors and Semimetals*. Vol. 95. Elsevier, 2016, pp. 101–147.

[80] Zhongwei Zhang et al. "Hexagonal boron nitride: a promising substrate for graphene with high heat dissipation". In: *Nanotechnology* 28.22 (2017), p. 225704.

[81] Luca Banszerus et al. "Identifying suitable substrates for high quality graphene-based heterostructures". In: *2D Materials* 4.2 (2017), pp. 025–030.

[82] Maxim A Stolyarov et al. "Suppression of 1/f noise in near ballistic hBNgraphene-hBN heterostructure field effect transistors". In: *Applied Physics Letters* 107.2 (2015), pp. 023–106.

[83] Kristen M Burson et al. "Direct imaging of charged impurity density in common graphene substrates". In: *Nano letters* 13.8 (2013), pp. 3576–3580.

[84] Jiamin Xue et al. "Scanning tunnelling microscopy and spectroscopy of ultra-flat graphene on hexagonal boron nitride". In: *Nature materials* 10.4 (2011), pp. 282–285.

[85] Dominik Bischoff et al. "Reactive-ion-etched graphene nanoribbons on a hexagonal boron nitride substrate". In: *Applied Physics Letters* 101.20 (2012), pp. 203–103.

[86] Filippo Pizzocchero et al. "The hot pick up technique for batch assembly of van der Waals heterostructures". In: *Nature communications* 7 (2016), pp. 118–94.

[87] L Wang et al. "One-dimensional electrical contact to a two dimensional material". In: *Science* 342.6158 (2013), pp. 614–617.

[88] B-Y Tsaur and GM Metze. "Molecular beam epitaxy of GaAs and AlGaAs on Si". In: *Applied physics letters* 45.5 (1984), pp. 535–536.

[89] JD Albar et al. "An atomic carbon source for high temperature molecular beam epitaxy of graphene". In: *Scientific reports* 7.1 (2017), pp. 1–8.

[90] Xiangping Chen, Lili Zhang, and Shanshan Chen. "Large area CVD growth of graphene". In: *Synthetic Metals* 210 (2015), pp. 95–108.

[91] Sukang Bae et al. "Roll-to-roll production of 30-inch graphene films for transparent electrodes". In: *Nature nanna2015selectiveotechnology* 5.8 (2010), p. 574.

[92] Jan Dauber et al. "Ultra-sensitive Hall sensors based on graphene encapsulated in hexagonal boron nitride". In: *Applied Physics Letters* 106.19 (2015), pp. 193–501.

[93] Atindra Nath Pal, Ageeth A Bol, and Arindam Ghosh. "Large low-frequency resistance noise in chemical vapor deposited graphene". In: *Applied Physics Letters* 97.13 (2010), p. 133504.

[94] Andreas Isacsson et al. "Scaling properties of polycrystalline graphene: a review". In: *2D Materials* 4.1 (2016), p. 012002.

[95] Zenas A Van Veldhoven et al. "Electronic properties of CVD graphene: The role of grain boundaries, atmospheric doping, and encapsulation by ALD". In: *physica status solidi (b)* 253.12 (2016), pp. 2321–2325.

[96] Lene Gammelgaard et al. "Graphene transport properties upon exposure to PMMA processing and heat treatments". In: *2D Materials* 1.3 (2014), pp. 035–005.

[97] Jinsung Kwak et al. "Oxidation behavior of graphene-coated copper at intrinsic graphene defects of different origins". In: *Nature Communications* 8.1 (2017), p. 1549.

[98] T Uwanno et al. "Fully dry PMMA transfer of graphene on h-BN using a heating/cooling system". In: *2D Materials* 2.4 (2015), p. 041002.

[99] Min-Kyu Joo et al. "Large-scale graphene on hexagonal-BN Hall elements: prediction of sensor performance without magnetic field". In: *ACS nano* 10.9 (2016), pp. 8803–8811.

[100] Bogdan Karpiak, André Dankert, and Saroj P Dash. "Gate-tunable Hall sensors on large area CVD graphene protected by h-BN with 1D edge contacts". In: *Journal of Applied Physics* 122.5 (2017), pp. 054–506.

[101] Tymoteusz Ciuk et al. "Low-noise epitaxial graphene on SiC Hall effect element for commercial applications". In: *Applied Physics Letters* 108.22 (2016), pp. 223–504.

[102] S Sonusen et al. "Single layer graphene Hall sensors for scanning Hall probe microscopy (SHPM) in 3 to 300 K temperature range". In: *Applied Surface Science* 308 (2014), pp. 414–418.

[103] Le Huang et al. "Ultra sensitive graphene Hall elements". In: *Applied Physics Letters* 104.18 (2014), pp. 183–106.

[104] Chiu-Chun Tang et al. "Characteristics of a sensitive microHall probe fabricated on chemical vapor deposited graphene over the temperature range from liquid-helium to room temperature". In: *Applied Physics Letters* 99.11 (2011), pp. 112–107.

[105] Zhenxing Wang et al. "Encapsulated graphene based Hall sensors on foil with increased sensitivity". In: *physica status solidi (b)* 253.12 (2016), pp. 2316–2320.

[106] H Kamerlingh Onnes. "Further experiments with Liquid Helium G. On the electrical resistance of Pure Metals etc. VI. On the Sudden Change in the Rate at which the Resistance of Mercury Disappears". In: *Koninklijke Nederlandse Akademie van Weteschappen Proceedings Series B Physical Sciences* 14 (1911), pp. 1911–1912.

[107] Natuurkundig Laboratorium. *Communications from the Physical Laboratory of the University of Leiden: Supplement*. 1931.

[108] Thomas Sheahen. *Introduction to high-temperature superconductivity*. Springer Science & Business Media, 1994.

[109] F London. "Royal Society of London". In: *Proceedings A149* 71 (1935).

[110] A Meshkovskii and Al Shalnikov. "* POVERKHNOSTNYE YAVLENIYA U SVERKHPROVODNIKOV V PROMEZHUTOCHNOM SOSTOYANII". In: *ZHURNAL EKSPERIMENTALNOI I TEORETICHESKOI FIZIKI* 17.10 (1947), pp. 851–861.

[111] Vitaly L Ginzburg and Lev D Landau. "On the theory of superconductivity". In: *On Superconductivity and Superfluidity*. Springer, 2009, pp. 113–137.

[112] John Bardeen, Leon N Cooper, and J Robert Schrieffer. "Microscopic theory of superconductivity". In: *Physical Review* 106.1 (1957), p. 162.

[113] RE Glover III and M Tinkham. "Transmission of superconducting films at millimeter-microwave and far infrared frequencies". In: *Physical Review* 104.3 (1956), p. 844.

[114] D Feinberg. "Theory of the tilted vortex lattice in Josephson-coupled layered superconductors". In: *Physica C: Superconductivity* 194.1-2 (1992), pp. 126–140.

[115] John R Clem. "Simple model for the vortex core in a type II superconductor". In: *Journal of low temperature physics* 18.5-6 (1975), pp. 427–434.

[116] Philip W Anderson. "Theory of flux creep in hard superconductors". In: *Physical Review Letters* 9.7 (1962), p. 309.

[117] Co Po Bean. "Magnetization of hard superconductors". In: *Physical review letters* 8.6 (1962), p. 250.

[118] Roland Hott. "Application fields of high-temperature superconductors". In: *High Temperature Superconductivity 2*. Springer, 2004, pp. 35–48.

[119] AP Drozdov et al. "Conventional superconductivity at 203 kelvin at high pressures in the sulfur hydride system". In: *Nature* 525.7567 (2015), pp. 73–76.

[120] Jun Nagamatsu et al. "Superconductivity at 39 K in magnesium diboride". In: *nature* 410.6824 (2001), pp. 63–64.

[121] Yoichi Kamihara et al. "Iron-based layered superconductor La [O1-x F x] FeAs (x= 0.05- 0.12) with T c= 26 K". In: *Journal of the American Chemical Society* 130.11 (2008), pp. 3296–3297.

[122] Jian-Feng Ge et al. "Superconductivity above 100 K in single-layer FeSe films on doped SrTiO 3". In: *Nature materials* 14.3 (2015), pp. 285–289.

[123] O Chmaissem et al. "Neutron powder diffraction study at room temperature and at 10 K of the crystal structure of the 133 K superconductor HgBa2Ca2Cu3O8+ δ". In: *Physica C: Superconductivity* 217.3-4 (1993), pp. 265–272.

[124] JL MacManus-Driscoll et al. "Strong pinning in very fast grown reactive co-evaporated GdBa2Cu3O7 coated conductors". In: *APL Materials* 2.8 (2014), p. 086103.

[125] Pia Jensen Ray. "Structural investigation of La 2-x Sr x CuO 4". In: (2015).

[126] VS Vinila et al. "Ceramic Nanocrystalline Superconductor Gadolinium Barium Copper Oxide (GdBaCuO) at Different Treating Temperatures". In: *Journal of Crystallization Process and Technology* 2014 (2014).

[127] Gianni Blatter et al. "Vortices in high-temperature superconductors". In: *Reviews of Modern Physics* 66.4 (1994), p. 1125.

[128] ZZ Sheng and AM Hermann. "Bulk superconductivity at 120 K in the TlCa/BaCuO system". In: *Nature* 332.6160 (1988), p. 138.

[129] PJ Curran et al. "Tuning the structure of the Josephson vortex lattice in Bi 2 Sr 2 CaCu 2 O 8+ δ single crystals with pancake vortices". In: *Scientific reports* 8.1 (2018), pp. 1–10.

[130] SR Foltyn et al. "Materials science challenges for high-temperature superconducting wire". In: *Materials For Sustainable Energy: A Collection of Peer-Reviewed Research and Review Articles from Nature Publishing Group*. World Scientific, 2011, pp. 299–310.

[131] Y Yamada et al. "Epitaxial nanostructure and defects effective for pinning in Y (RE) Ba 2 Cu 3 O 7- x coated conductors". In: *Applied Physics Letters* 87.13 (2005), p. 132502.

[132] K Tsuchiya et al. "Critical current measurement of commercial REBCO conductors at 4.2 K". In: *Cryogenics* 85 (2017), pp. 1–7.

[133] Seung Hyun Moon. "HTS development and industrialization at SuNAM". In: *1st Workshop on Accelerator Magnets in HTS (Hamburg, Germany)*. 2014.

[134] XD Wu et al. "Large critical current densities in YBa2Cu3O7- x thin films made at high deposition rates". In: *Applied Physics Letters* 57.5 (1990), pp. 523–525.

[135] D Dimos, P Chaudhari, and J Mannhart. "Superconducting transport properties of grain boundaries in YBa 2 Cu 3 O 7 bicrystals". In: *Physical Review B* 41.7 (1990), p. 4038.

[136] X Jin et al. "Magnetic pinning effect in high Tc superconductor GdBaCuO". In: *Physica C: Superconductivity* 185 (1991), pp. 2193–2194.

[137] David R Nelson and VM Vinokur. "Boson localization and pinning by correlated disorder in high-temperature superconductors". In: *Physical review letters* 68.15 (1992), p. 2398.

[138] BH Stafford et al. "Tilted BaHfO3 nanorod artificial pinning centres in REBCO films on inclined substrate deposited-MgO coated conductor templates". In: *Superconductor Science and Technology* 30.5 (2017), p. 055002.

[139] WA Fertig et al. "Destruction of Superconductivity at the Onset of Long-Range Magnetic Order in the Compound ErRh 4 B 4". In: *Ten Years of Superconductivity: 1980–1990*. Springer, 1993, pp. 57–60.

[140] CT Wolowiec, BD White, and MB Maple. "Conventional magnetic superconductors". In: *Physica C: Superconductivity and its Applications* 514 (2015), pp. 113–129.

[141] SS Saxena et al. "Superconductivity on the border of itinerant-electron ferromagnetism in UGe 2". In: *Nature* 406.6796 (2000), pp. 587–592.

[142] Guanghan Cao et al. "Superconductivity and ferromagnetism in EuFe2 (As1- xPx) 2". In: *Journal of Physics: Condensed Matter* 23.46 (2011), p. 464204.

[143] Katsuyoshi Komatsu et al. "Experimental evidence for violation of the fluctuation-dissipation theorem in a superspin glass". In: *Physical review letters* 106.15 (2011), p. 150603.

[144] C Julian Chen. *Introduction to scanning tunneling microscopy*. Vol. 4. Oxford University Press on Demand, 1993.

[145] Rafael B Dinner, MR Beasley, and Kathryn A Moler. "Cryogenic scanning Hall-probe microscope with centimeter scan range and submicron resolution". In: *Review of scientific instruments* 76.10 (2005), p. 103702.

[146] P Blake et al. "Making graphene visible". In: *Applied physics letters* 91.6 (2007), p. 063124.

[147] Yuan Huang et al. "Reliable exfoliation of large-area high-quality flakes of graphene and other two-dimensional materials". In: *ACS nano* 9.11 (2015), pp. 10612–10620.

[148] Mingguang Chen et al. "Advances in transferring chemical vapour deposition graphene: a review". In: *Materials Horizons* 4.6 (2017), pp. 1054–1063.

[149] Alongkorn Pimpin and Werayut Srituravanich. "Review on micro-and nanolithography techniques and their applications". In: *Engineering Journal* 16.1 (2012), pp. 37–56.

[150] Bharat Bhushan. *Springer handbook of nanotechnology*. Springer, 2017.

[151] Franz Laermer and Andrea Schilp. *Method of anisotropically etching silicon*. US Patent 5,501,893. 326 1996.

[152] Andrea C Ferrari and Denis M Basko. "Raman spectroscopy as a versatile tool for studying the properties of graphene". In: *Nature nanotechnology* 8.4 (2013), p. 235.

[153] Ramy Nashed et al. "Ultra-high mobility in dielectrically pinned CVD graphene". In: *IEEE Journal of the Electron Devices Society* 4.6 (2016), pp. 466–472.

[154] Norman Colthup. *Introduction to infrared and Raman spectroscopy*. Elsevier, 2012.

[155] Guanghong Zeng et al. "Nanomechanics of Amyloid Materials Studied by Atomic Force Microscopy". In: *Atomic Force Microscopy Investigations into Biology-From Cell to Protein*. InTech, 2012.

[156] Sina Ebnesajjad and Cyrus Ebnesajjad. *Surface treatment of materials for adhesive bonding*. William Andrew, 2013.

[157] Brian T Schaefer et al. "Magnetic field detection limits for ultraclean graphene Hall sensors". In: *Nature Communications* 11.1 (2020), pp. 1–8.

[158] Guibin Song, Mojtaba Ranjbar, and Richard A Kiehl. "Operation of graphene magnetic field sensors near the charge neutrality point". In: *Communications Physics* 2.1 (2019), pp. 1–8.

[159] L Banszerus et al. "Extraordinary high room-temperature carrier mobility in graphene-WSe _2 heterostructures". In: *arXiv preprint arXiv:1909.09523* (2019).

[160] LN Bulaevskii et al. "Coexistence of superconductivity and magnetism theoretical predictions and experimental results". In: *Advances in Physics* 34.2 (1985), pp. 175–261.

[161] Jin-Ke Bao et al. "Single crystal growth and study of the ferromagnetic superconductor RbEuFe4As4". In: *Crystal Growth & Design* 18.6 (2018), pp. 3517–3523.

[162] Kazuki Iida et al. "Coexisting spin resonance and long-range magnetic order of Eu in EuRbFe 4 As 4". In: *Physical Review B* 100.1 (2019), p. 014506.

[163] VS Stolyarov et al. "Unique interplay between superconducting and ferromagnetic orders in EuRbFe 4 As 4". In: *Physical Review B* 98.14 (2018), p. 140506.

[164] A. E. Koshelev. "Suppression of superconducting parameters by correlated quasi-two-dimensional magnetic fluctuations". In: *Phys. Rev. B* 102 (5 Aug. 2020), p. 054505. DOI: 10.1103/PhysRevB.102.054505. URL: https://link.aps.org/doi/10.1103/PhysRevB.102.054505.

[165] Kyle M Shen and JC Seamus Davis. "Cuprate high-Tc superconductors". In: *Materials today* 11.9 (2008), pp. 14–21.

[166] ZL Feng et al. "A Practical Processing Method for the Fabrication of NdBCO Seed Crystals and High-Performance Single-Domain GdBCO Bulk Superconductors". In: *Journal of Superconductivity and Novel Magnetism* (2020), pp. 1–10.

[167] H Kutami et al. "Progress in research and development on long length coated conductors in Fujikura". In: *Physica C: Superconductivity* 469.15-20 (2009), pp. 1290–1293.

[168] M Lao et al. "Critical current anisotropy of GdBCO tapes grown on ISD–MgO buffered substrate". In: *Superconductor Science and Technology* 28.12 (2015), p. 124002.

[169] Alok K Jha and Kaname Matsumoto. "Superconductive REBCO thin films and their nanocomposites: the role of rare-earth oxides in promoting sustainable energy". In: *Frontiers in Physics* 7 (2019), p. 82.

[170] Samuel C Johnson et al. "Selecting Favorable Energy Storage Technologies for Nuclear Power". In: *Storage and Hybridization of Nuclear Energy*. Elsevier, 2019, pp. 119–175.

[171] Hideaki Maeda and Yoshinori Yanagisawa. "Recent developments in high-temperature superconducting magnet technology". In: *IEEE Transactions on applied superconductivity* 24.3 (2013), pp. 1–12.

[172] AJ Brook et al. "Integrated piezoresistive sensors for atomic force-guided scanning Hall probe microscopy". In: *Applied physics letters* 82.20 (2003), pp. 3538–3540.

[173] AJ Brook et al. "Micromachined III-V cantilevers for AFM-tracking scanning Hall probe microscopy". In: *Journal of Micromechanics and Microengineering* 13.1 (2002), p. 124.

[174] BK Chong et al. "Scanning Hall probe microscopy on an atomic force microscope tip". In: *Journal of Vacuum Science & Technology A: Vacuum, Surfaces, and Films* 19.4 (2001), pp. 1769–1772.

[175] D Gregušová et al. "On-tip sub-micrometer Hall probes for magnetic microscopy prepared by AFM lithography". In: *Ultramicroscopy* 109.8 (2009), pp. 1080–1084.

[176] M Lanza et al. "Graphene-Coated Atomic Force Microscope Tips for Reliable Nanoscale Electrical Characterization". In: *Advanced Materials* 25.10 (2013), pp. 1440–1444.

[177] Mengjiao Li et al. "High Mobilities in Layered InSe Transistors with Indium-Encapsulation-Induced Surface Charge Doping". In: *Advanced Materials* 30.44 (2018), p. 1803690.

[178] Junhong Na et al. "Few-layer black phosphorus field-effect transistors with reduced current fluctuation". In: *ACS nano* 8.11 (2014), pp. 11753–11762.

[179] Xuefei Li et al. "Mechanisms of current fluctuation in ambipolar black phosphorus field-effect transistors". In: *Nanoscale* 8.6 (2016), pp. 3572–3578.

[180] Bevin Huang et al. "Layer-dependent ferromagnetism in a van der Waals crystal down to the monolayer limit". In: *Nature* 546.7657 (2017), pp. 270–273.

[181] G Persch and H Strecker. "Applications of magnetic force microscopy in magnetic storage device manufacturing". In: *Ultramicroscopy* 42 (1992), pp. 1269–1274.

[182] David Le Sage et al. "Optical magnetic imaging of living cells". In: *Nature* 496.7446 (2013), pp. 486–489.